

Optimization-based robust control for high-performance torque vectoring in electric vehicles operated by induction traction motors

Von der Fakultät für Elektrotechnik und Informationstechnik
der Rheinisch-Westfälischen Technischen Hochschule Aachen
zur Erlangung des akademischen Grades eines Doktors
der Ingenieurwissenschaften genehmigte Dissertation

vorgelegt von

Diplom-Informatiker Diplom-Wirtschaftsingenieur
Zheng Hu
aus Jiangsu Provinz in China

Berichter: Univ.-Prof. Dr.-Ing. habil. Dr. h. c. Kay Hameyer
Univ.-Prof. Dr.-Ing. Axel Mertens

Tag der mündlichen Prüfung: 08. Feb. 2017

Diese Dissertation ist auf den Internetseiten der Universitätsbibliothek online verfügbar

Aachener Schriftenreihe zur
Elektromagnetischen Energiewandlung

Band 24

Zheng Hu

**Optimization-based robust control for high-
performance torque vectoring in electric vehicles
operated by induction traction motors**

Shaker Verlag
Aachen 2017

Bibliographic information published by the Deutsche Nationalbibliothek

The Deutsche Nationalbibliothek lists this publication in the Deutsche Nationalbibliografie; detailed bibliographic data are available in the internet at <http://dnb.d-nb.de>.

Zugl.: D 82 (Diss. RWTH Aachen University, 2017)

Aachener Schriftenreihe zur Elektromagnetischen Energiewandlung

Herausgeber:

Univ.-Prof. Dr.-Ing. habil. Dr. h.c. Kay Hameyer
Institut für Elektrische Maschinen
RWTH Aachen
52056 Aachen

Copyright Shaker Verlag 2017

All rights reserved. No part of this publication may be reproduced, stored in a retrieval system, or transmitted, in any form or by any means, electronic, mechanical, photocopying, recording or otherwise, without the prior permission of the publishers.

Printed in Germany.

ISBN 978-3-8440-5209-1

ISSN 1861-3799

Shaker Verlag GmbH • P.O. BOX 101818 • D-52018 Aachen

Phone: 0049/2407/9596-0 • Telefax: 0049/2407/9596-9

Internet: www.shaker.de • e-mail: info@shaker.de

Deutsche Kurzfassung

Aufgrund hoher Kundenanforderungen an den Sicherheitsgrad im Automobil haben Sicherheitsfunktionen in Fahrzeugen eine besondere Bedeutung. Dazu gehört die Torque-Vectoring-Funktion als eine aktive Sicherheitsfunktion, die mittels asymmetrischer Antriebskräfte an beiden Fahrzeugseiten ein zusätzliches Giermoment erzeugt, um das Lenkverhalten entweder zu verbessern oder zu korrigieren. Im Vergleich zu konventionellen Fahrzeugen haben Elektrofahrzeuge den Vorteil, dass diese Funktion ohne spezifisches Differentialgetriebe realisiert werden kann. Darüber hinaus zeichnet sich ein elektrisches Antriebssystem durch hochdynamische Drehmomenterzeugung aus. Die gesamte Torque-Vectoring-Funktion in Elektrofahrzeugen beinhaltet die Regelungen der elektrischen Antriebe, der mechanischen Antriebsstränge und der Fahrquerdynamik. Um eine leistungsstarke Applikation zu implementieren, ergeben sich die Herausforderungen, dass die physikalischen Begrenzungen und die Unsicherheiten des Systems berücksichtigt werden müssen und gleichzeitig die Regeldynamik gewährleistet wird. Um einen zufriedenstellenden Kompromiss zu erzielen, wird die modellbasierte Prädiktivregelung (MPC) als theoretische Grundlage für diese Dissertation ausgewählt, in der Anwendung untersucht und umgesetzt.

Die kritischen Regelungsprobleme in elektrischen Antriebssystemen, einschließlich der bei Asynchronmotoren (ASM), lassen sich durch die Parametervariation der ASM, die Totzeit und die Strom- und Spannungsbegrenzung des Systems darstellen. Um die Parametervariation zu behandeln, werden zwei Lösungsansätze implementiert. Im ersten Ansatz wird die Methodik der Min-Max-Regelung verwendet. Das Regelsystem wird als ein lineares parameter-variiertes (LPV) System mit polytopischen Unsicherheiten vorgesehen. Die Robustheit des Systems wird dadurch gewährleistet, dass das Optimierungsproblem des schlimmsten Falls (an einem Vertex des Polytopes) durch eine Lyapunov-Funktion begrenzt und behandelt wird. Um eine echtzeitfähige Anwendung zu realisieren, wird der Optimierungsvorgang durch multiparametrische semidefinite Programmierung (mp-SDP) offline durchgeführt. Online wird ein effizienter Suchvorgang durch den Quadtree-Search-Algorithmus vorgenommen. Der andere Ansatz basiert auf sogenannter Tube-MPC-Methodik. Statt eines LPV-Systems wird das lineare zeitinvariante (LTI) System verwendet. Die Abweichung zwischen dem LTI-System und dem realen System wird durch einen robusten positiven invarianten (RPI) Satz begrenzt. Durch die Bestimmung des minimalen RPI (mRPI) Satzes werden sowohl die Robustheit als auch die Optimalität erzielt. Neben den Parameterunsicherheiten werden die Systembegrenzungen behandelt. Im Gegensatz zu anderen Ansätzen, in denen die Strom- und Spannungsbegrenzungen direkt als Nebenbedingung des Optimierungsproblems vorgegeben sind, werden in dieser Arbeit die Systembegrenzungen nach der Umformulierung durch das Drehmoment

repräsentiert. Der Vorteil besteht darin, dass keine Approximation für die Darstellung der Nebenbedingungen vorgenommen werden muss und dadurch die Optimalität des Systems erhöht wird. Im mechanischen Antriebsstrang wird die primäre Regelungsaufgabe durch aktive Drehschwingungsdämpfung des übertragenen Antriebsmomentes dargestellt. Durch einen MPC-Regler mit einer Feedback-Kompensation kann die Drehschwingung an der Seitenwelle wesentlich unterdrückt werden. Um die Torque-Vectoring-Funktion zu vervollständigen, werden die Gierratenregelung als Hauptkomponente und die Reifenschlupfregelung als Hilfskomponente implementiert. Durch die Reifenschlupfregelung kann das Durchdrehen der Räder reduziert werden. Darüber hinaus wird eine Betriebsstrategie implementiert, welche abhängig von Fahrbahnsituationen eine zuverlässige Soll-Gierrate vorgibt. Da im Fahrzeugsystem lediglich Standardsensoren verfügbar sind, wird eine Strategie implementiert, die die nicht messbaren Signale abschätzt und sie der Regelssoftware zur Verfügung stellt.

Die oben genannten Subsysteme werden integriert und an einem Hardware-in-the-Loop-Prüfstand (HiL) validiert. Dazu werden die in ISO 7401 spezifizierten Fahrmanöver durchgeführt. Die Ergebnisse zeigen, dass die implementierte Funktion in der Lage ist, nicht nur das Lenkverhalten des Fahrzeugs zu verbessern, sondern auch die Fahrstabilität bis zu den Systembegrenzungen zu gewährleisten.

Danksagung

Die vorliegende Dissertation entstand während meiner Tätigkeit als wissenschaftlicher Mitarbeiter am Institut für Elektrische Maschinen der RWTH Aachen.

Mein besonderer Dank gilt dem Leiter des Instituts, Herrn Univ.-Prof. Dr.-Ing. habil. Dr. h. c. Kay Hameyer, für die Betreuung dieser Arbeit und seine fördernde Unterstützung, sowie für den Freiraum, den er mir einräumte, bei der Bearbeitung des Themas. Als Nächstes bedanke ich mich bei Herrn Univ.-Prof. Dr.-Ing. Axel Mertens für seine engagierte Übernahme des Korreferats und das entgegengebrachte Interesse an dieser Arbeit.

Weiterhin gebührt mein Dank den Mitgliedern meiner Prüfungskommission, Herrn Univ.-Prof. Dr.-Ing. Dr. med. Steffen Leonhardt, für die Übernahme des Prüfungsvorsitzes, und Herrn Univ.-Prof. Dr. sc. techn. Renato Negra.

Mein Dank gilt auch allen Assistenten des Instituts sowie Frau Petra Jonas-Astor, Frau Isabel Mainz und Frau Denise Boukamp für Hilfe, Entlastung und Beistand.

Nicht vergessen will ich alle wissenschaftlichen Hilfskräften, Studien-, Bachelor- und Masterarbeiter, die stets engagiert zum Gelingen dieser Arbeit beigetragen haben.

Der mechanischen und elektrischen Werkstatt des Instituts danke ich für die Unterstützung beim Prüfstands Aufbau meiner Arbeit. Für die stete Hilfsbereitschaft und schnelle unkomplizierte Unterstützung danke ich besonders Herrn Jörg Paustenbach.

Bedanken möchte ich mich auch bei allen Freunden, Bekannten und Verwandten, die mich auf meinem Weg begleitet haben.

Schließlich bedanke ich mich noch ganz herzlich bei meinen Eltern für die Ermöglichung des Studiums nach Deutschland. Besonders hervorheben möchte ich hier noch meinen väterlichen Freund, Herrn Prof. Dr. Wolfgang Kaefer, der mir stets wertvolle Ratschläge für mein Leben und meine Karriere gegeben hat und leider im Februar 2014 verstorben ist. Ohne deren Unterstützung wäre ich nicht soweit gekommen. Dafür widme ich ihnen diese Arbeit.

Aachen, im März 2017

Zheng Hu

Contents

1	Introduction	1
1.1	Torque vectoring and E-mobility	1
1.2	Motivation	2
1.3	Outline of the work	3
2	Torque vectoring in electric vehicles	7
2.1	Functionality	7
2.2	Vehicle configuration	8
2.3	Requirements and specifications	10
2.3.1	Functional requirements and test standards	10
2.3.2	Boundary conditions	11
2.3.3	Software specifications	11
3	State of the art and novelties of the work	15
3.1	MPC history and concept	15
3.2	Technical reviews	17
3.2.1	Electrical drive control	17
3.2.2	Oscillation damping control	19
3.2.3	Vehicle dynamics control	20
3.3	Objectives and contributions	21
4	Theoretical backgrounds of model predictive control	23
4.1	Backgrounds	23
4.1.1	Standard convex optimization problems	23
4.2	Basic principles of model predictive control	25
4.2.1	MPC startup	25
4.2.2	State estimation and disturbance modeling	26
4.3	Constrained model predictive control	29
4.3.1	On-line optimization problem	30

4.3.2	Multi-parametric QP	31
4.4	Robust model predictive control	32
4.4.1	Min-max control	32
4.4.2	Tube-based MPC	38
4.5	Summary	47
5	Robust current control in induction machines	49
5.1	Dynamic modeling of electric drive system	49
5.1.1	Modeling of induction machines	49
5.1.2	Uncertainties	52
5.2	Classical control approach	53
5.3	Robust current control in consideration of parameter variation	55
5.3.1	Min-max current control	55
5.3.2	Tube-based robust model predictive current control	63
5.4	Constraint handling for the electric drive systems	72
5.5	Overview of the control approach	76
5.6	Simulation and experimental results	76
5.6.1	Simulation results	77
5.6.2	Experimental results	82
5.7	Summary	88
6	Active damping control in the mechanical drivetrain	89
6.1	Modeling of elastic mechanical drivetrain	89
6.1.1	Mechanical structure	89
6.1.2	Oscillation analysis	90
6.1.3	Parameter variation	92
6.2	Dynamic active damping control	94
6.3	Simulative and experimental results	96
6.4	Summary	99

7	High-performance torque vectoring control	101
7.1	Vehicle modeling	101
7.1.1	Coordinate systems	101
7.1.2	Tire modeling	105
7.1.3	Linear single track model	111
7.1.4	Dual track model	115
7.2	Vehicle dynamics control	117
7.2.1	Tire slip control	117
7.2.2	Inversed tire model	119
7.2.3	Yaw rate control	121
7.3	Operation strategy	125
7.3.1	Determination of reference yaw rate	125
7.3.2	Cross slope correction	128
7.3.3	Friction limit	130
7.4	Parameter estimation	130
7.5	Summary	139
8	Integration and Validation of the entire application	141
8.1	Simulation approaches	141
8.2	Results and evaluations	143
9	Conclusions and perspectives	153
A	Definitions and notations of optimization problems	157
B	Technical data of electric drivetrain	160
C	Measurement of the characteristic curve of the stator inductance	164
D	Dynamic torque constraint calculation	165
E	Technical data of mechanical drivetrain	166

F	Technical data of the hypothetical vehicle	167
F.1	The Magic Formula Tire Model: Full Set of Equations	168
F.1.1	Longitudinal Tire Force	168
F.1.1.1	Main Equations	168
F.1.1.2	Main Parameters	168
F.1.1.3	Auxiliary Parameters	169
F.1.2	Lateral Tire Force	169
F.1.2.1	Main Equations	169
F.1.2.2	Main Parameters	170
F.1.2.3	Auxiliary Parameters	170
F.1.3	Scaling of the Friction Coefficient	170
G	Derivation of the computations in the operation strategy	172
G.1	Derivation of system matrices of the EKF	172
G.2	Analytical calculation of the vehicle lateral velocity \hat{v}_y^V	173
H	Test maneuvers	174
H.1	Lateral Transient Response Test (ISO 7401)	174
H.2	Sine-Steer Test (ISO 7401)	174
H.3	Sine-steer Test with dwell input (UN 13-H)	174
I	Estimation results	176
I.1	Lateral transient response test	176
I.2	Sine-steer test	177
I.3	Sine-steer with dwell test	179
J	Abbreviation	181
K	Nomenclature	185
	Bibliography	191
	Lebenslauf	211

1 Introduction

In the modern automotive market, design, active vehicle safety and dynamic performance are amongst the most critical factors that influence consumers in their decision to purchase a particular vehicle - especially when premium brands are considered [47]. Safety systems for automotive context can be categorized by passive safety and active safety. Passive safety systems, such as seat belts or airbags, aim at moderating the implications of the occupants' health in an accident. In contrast, active safety systems prevent vehicles from accidents and thus minimize the severity effect [185]. Currently, driver assistance systems based on intelligent sensor technology monitoring the vehicle surroundings as well as driving behaviors are the primary means for the active safety technology. They are achieved commonly by control systems that deliberately influence the dynamic vehicle behavior, such that collision is avoided. As a consequence, the chance that accidents occur is lowered.

The first active safety system that entered the stage of serial production is the Anti-lock Braking System (ABS) developed by the German supplier company Bosch in the late 1970's. It is dedicated to preserving the vehicle's tractability during full braking by inhibiting the wheels to lock and preventing skidding. Therewith, the tire's ability to produce a lateral force is maintained [163].

The next major innovation in active safety systems came to market in the 1990's, again designed by Bosch. The Electronic Stability Control (ESC) measures the steering wheel angle and vehicle velocity. On that basis it estimates the trajectory the driver wishes to follow. If the vehicle deviates from this path, wheel-individual and targeted braking interventions would support the driver in negotiating the vehicle back on the desired path [29].

Also during the 1990's, Honda and Mitsubishi were the first to introduce an Active Yaw Rate Control (AYC) or Torque Vectoring (TV) system in commercially available vehicles [170, 91]. These systems employed an electronically controllable differential, which facilitated the asymmetric distribution of engine torque among the wheels individually. Therefore, a reduction of the under-steering tendency could be accomplished, which results in an enhanced cornering behavior. However, due to the considerable extra costs raised by the auxiliary components [143], such TV systems developed into a niche product for high performance sport vehicles [148], [21], [91].

1.1 Torque vectoring and E-mobility

The recent changes in the automotive industry have reset TV to modern attention. Environmental and political constraints force the car manufacturers to increase the number of emission-reduced or emission-free vehicles to the market. As a

reaction, the E-mobility is prevailing again after over hundred years. E-mobility describes a category of vehicles, which partially or even fully rely on electrified drivetrains, and utilize electro-chemical batteries as energy storage devices. For TV applications, those Electric Vehicles (EVs) are interested because of their featured wheel individual drives unlike conventional vehicles with Internal Combustion Engines (ICE). This class of vehicles requires no additional mechanical components such as expensive active differentials. Indeed, TV can be implemented conveniently by using additional software components and building on the existing power-train architecture as well as sensors made available through the aforementioned ABS and ESC systems.

Another advantage of EV compared to ICE vehicles regarding to TV is the high torque dynamics. As an approximate value, the torque response time of an ICE is around 1 – 2 seconds, while the electromagnetic torque of electrical machines (EMs) can be produced in several milliseconds depending on the machine design and the control strategy [95].

1.2 Motivation

TV applications require high dynamic torque distribution to adjust the drive trajectory in time. According to this requirement, the motivation of the present work is therefore to fully utilize the advantages of EM by means of advanced control approaches.

In order to realize asymmetric torque distribution in EV, we adopted a configuration in which two identically constructed Induction Motors (IMs) are mounted on the same axle. In such a way, the wheels can be controlled individually to attain a distributed propulsion system. The IM was firstly constructed by Nikola Tesla in 1883. However, it was sluggishly spread due to its asynchronous property and therefore unsatisfying controllability. Thanks to the vector control, also called Field Oriented Control (FOC) theory [183], proposed in the 1980's, as well as the development of power electronics technology during the recent decades, the industrial applications of adjustable speed and high dynamic IM drives become realistic. IM is nowadays prevalently used in electric drive systems because of its simple and reliable structure, low material and manufacturing cost. On these reasons, IMs are adopted in the EVs, such as Tesla Model S and Model X.

The simplest way to implement TV applications including entire drivetrain control is employing the classical Proportional Integral (PI) controller. However, in the present work, the studied system presents a system of high order. To achieve high control performance, several PI controllers have to be applied, which constitute a multilayer cascaded control structure. One of the drawbacks of such control approach is, that the time constant of the inner control loop is contributed to the outer control loop. To obtain a good control performance, the time constants of the inner control loop and the subsequent external control loop should differ by a factor of at least 7 – 10 [56]. Therefore, the dynamics achieved by cascading PI

controllers cannot meet the requirement of high dynamic drive applications [117]. Another drawback of PI controllers is represented by the conditioned optimality of the control system. The control parameters can be systematically optimized by optimum methods such as modulus and symmetrical optimum [168]. Indeed, the optimization can be restrictedly designed for a certain operation range, which will be discussed in detail later.

Furthermore, the control approaches to be implemented should be sufficiently robust against undesirable disturbances and system uncertainties. Among approaches with PI controller such issues are tackled by means of precontrols or feedforward compensation techniques to meet the control quality [117]. Another technique is the so-called adaptive control, in which the behavior of the controller is modified in response to system changes [155]. However, the parameter adjustment mechanism of the controller slows down the system convergence when compared to the normal feedback loop. Moreover, the adaptive control design depends strongly on the uniqueness of the system, for this reason the proofs for stability are difficult to be attained.

In consideration of both criteria hereinbefore, the principle of optimization-based control theory, so-called model predictive control (MPC), is decided to be the fundamental of the present work. The basic idea of MPC is to define an objective function regarding the control objective, and to minimize this objective function by means of solving diverse mathematical optimization problems. The system constraints and the uncertainties are incorporated into the optimization problem as well. In such a way, both the dynamics and the robustness can be ensured to a certain degree. MPC algorithms are based on a solid mathematical foundation of convex optimization theories, which are elusive at times. In addition to that, the implementation is often complicated. Nevertheless, the control structure is simple, the control design is universal. Therefore, the controller can oftentimes be easily generalized to different systems.

1.3 Outline of the work

The studied control system is composed of a current control in the IM, an active damping control in the mechanical drivetrain, and a TV control in the vehicle. They constitute a complicated system and interact with each other. Therefore, a systematical development and testing procedure is required. The V-model, which is prevailing and often used as standard of automotive system development in Germany, is employed as the development procedure for the present work. Figure 1.1 illustrates the V-model concerning this work.

The entire development procedure is divided into system and software (SW) development. On the left hand side of the V-model, the steps in the verification phase are described, while on the right hand side the test processes denoting the validation phase are given. The system and the SW components are specified and designed before the implementation. After the implementation, the smallest

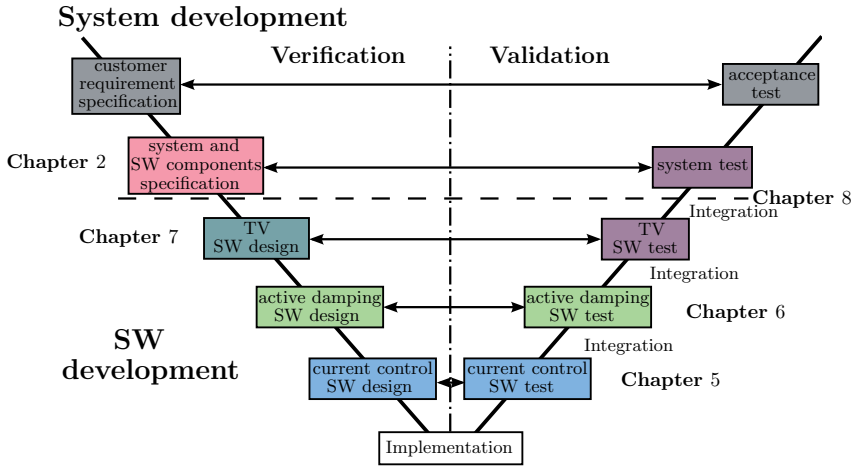


Figure 1.1: Development procedure of the present work.

subsystem/component is first validated and then integrated into the system over it. In this sequence, the location of the defects can be conveniently identified. Furthermore, as shown in the figure, the verification step and the validation step on the same level communicate with each other. This interaction avoids the downward flow of the defects and enables efficient verification and validation processes.

Based on this development procedure, the present work is outlined as follows: In chapter 2, the system verification is discussed. First, the functionality of TV system is introduced. Second, a system analysis is performed by discussion of the proper vehicle configuration for the TV application. Moreover, system requirements and architecture as well as SW specifications are defined. In order to state the up-to-date technologies based on optimization methodologies, which deal with the same control system, the state-of-the-art methods are schematically reviewed in chapter 3. Compared to these methods, the contributions of the present work are highlighted. In chapter 4, the theoretical backgrounds of the convex optimization methodology are introduced. Different MPC algorithms are detailed, which are based on diverse optimization problems and are applied to the SW design and implementation. The SW development is introduced in a bottom-up sequence: In chapter 5, the development of the current control in IMs is discussed. Two different robust current control approaches are implemented and validated. The mechanical drivetrain is described in chapter 6. Due to its oscillation behavior, an active damping control approach is implemented and validated. In chapter 7, the vehicle dynamic system is analyzed. Moreover, the design of operation strategy, control approaches and parameter estimation are clarified. The TV application and the entire system are validated on a Hardware-in-the-Loop (HiL) test bench introduced in chapter 8. Finally, this work is completed in chapter 9 and provides a

perspective of the possible future work.

2 Torque vectoring in electric vehicles

In this chapter, an introduction will be given in section 2.1 to illustrate how TV works. In order to apply and validate TV in a physical system, topology and configuration of EV are analyzed and defined for the present work in section 2.2. In section 2.3, the functional requirements on the control design as well as the software specifications are given.

2.1 Functionality

TV, or more precisely active torque vectoring, can be implemented in EV with two or four EMs, which produce individually engine torques transferred to the tires. Therefore, no expensive active differential is required in contrast to ICE vehicles. The principle and the effect of TV are well illustrated in Figure 2.1.

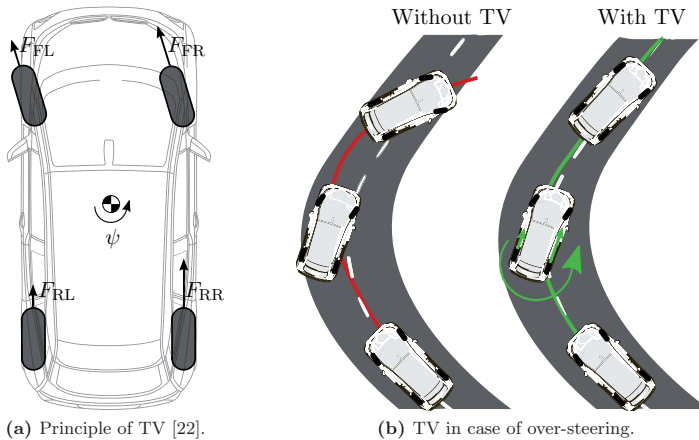


Figure 2.1: Illustration of TV application.

As shown in Figure 2.1a, the principle of TV diverges slightly from the one of ESC. The only difference consists in the way of yaw moment generation. TV exploits the possibility of producing additional yaw moment by applying asymmetric tire forces on either vehicle side [91]. This additional yaw moment is oriented in a way to either support or to correct the driver's steering effort, always having a preferably neutral steering behavior in mind.

TV substantially facilitates the steering behavior of vehicles without deteriorating drive dynamics, since the additional yaw moment is caused by the asymmetric drive forces. Consequently, EVs with TV can achieve a faster cornering compared to ICE vehicles.

Additionally, in certain critical situations, for instance over- or under-steering, TV acts on adjusting the vehicle behavior before the driver senses that the vehicle escapes the desired trajectory and overreacts in such a situation. In Figure 2.1b the effect of TV in case of over-steering is presented. When the vehicle without TV deviates from the desired trajectory, it can be very probably operated by the over-strained driver into an instable state. In summary, asymmetric torque distribution of TV facilitates the vehicle safety, vehicle performance, vehicle agility [91] and vehicle maneuverability.

2.2 Vehicle configuration

Amongst the wide range of available vehicle designs a hypothetical compact class car design is chosen for the present work.

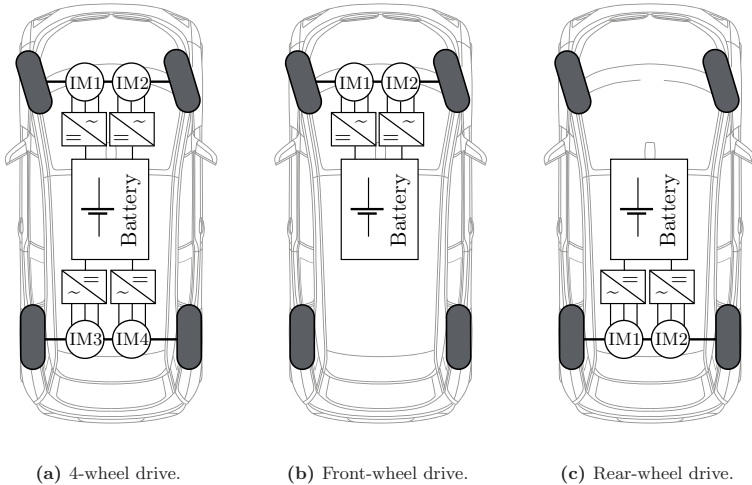


Figure 2.2: Possible topologies without differential for TV applications.

Figure 2.2 shows the possible topologies for TV applications in EV.

4-Wheel Drive (4WD) concept requires four EMs, while the other both concepts need two EMs respectively. Therefore, EVs with 4WD are more expensive and heavier, which means increased consumption and less drive range as well in case of the same energy storage and the same power class.

The installation of EMs in 4WD-EV is more complicated when compared to the resting two topologies with 2 EMs. The front axle contains the steering system, which makes the installation of Front-Wheel Drive (FWD) EVs different from that of Rear-Wheel Drive (RWD) EVs. However, the complexity of both cases can be roughly considered as identical.

Implementation of TV application in 4WD EVs is more complicated, since the torque is individually distributed to each wheel. In comparison to RWD EVs, the steering wheel angel has to be taken into account in TV application for FWD EVs due to the steering system on the front axle.

It has to be analyzed, in which topology the TV application can be applied better. An active TV application is implemented by exerting additional longitudinal forces on the tires. Because of the side forces, the adhesion limit is at first reached on the front wheels in under-steering vehicles. Therefore, there are less possibilities for applying longitudinal forces in FWD EV. Moreover, in case of acceleration, the rear wheels get higher force limitation because of axle load transfer and consequently more vehicle load on the rear wheels. The same explanation can be given for situations of upslope curving [81].

FWD vehicles show an under-steering behavior which does not cause instability [129]. In contrast, RWD vehicles may become unstable in certain situations, e.g. acceleration when cornering or on wet and icy surfaces. 4WD vehicles behave best performance in adverse road conditions, since the full amount of vehicle forces is available for friction.

In summary, the aforementioned topologies are collected in Table 2.1.

Criteria	4WD-EV	FWD-EV	RWD-EV
Cost	–	+	+
Mass/drive range	–	+	+
Installation complexity	–	+	+
SW complexity	–	○	+
TV adaptability	+	○	+
Vehicle behavior / stability	+	+	–

Table 2.1: Evaluation of vehicle topologies.

Based on the evaluations mentioned above, the RWD topology is employed in the present work, since on the one hand it is well featured for TV application and the disadvantage of vehicle behavior and, on the other hand stability in certain situations can be overcome by means of TV.

In addition, to execute a TV application effectively, the drive motors should be designed in such a way, so that it copes with driving resistances, acceleration resistances and additional drive forces required by TV at the same time. The

technical data of the hypothetical vehicle are given in Appendix F, which is mainly based on the available data of the BMW i3 [22]. The IM applied in this thesis is not specified for automotive applications, in other words, the ratio between drive speed and drive torque does not match the one at the wheels. Therefore, no transmission with fixed ratio is possible. Consequently, diverse ratios are defined in the present work for the speed and the torque, respectively. The ratios are determined according to the rated torque of the IM and the maximum force on the tires, as well as the maximum speed of the IM and the assumed maximum vehicle velocity. They can be found in Appendix F as well.

2.3 Requirements and specifications

Since TV serves as an application enhancing drive performance and it ensures vehicle stability, high level software reliability is required. For this reason, the safety aspects associated with the control design are addressed and discussed in this section. Moreover, software specifications are defined in this section to guide the implementation and the later validation.

2.3.1 Functional requirements and test standards

Based on the functionality of TV introduced in the previous section the following functional requirements should be fulfilled:

- ▷ TV is capable of enhancing the steering dynamic of the vehicle by means of an additional yaw moment, so that an abrupt avoidance of obstacles can be achieved.
- ▷ TV can recognize and correct the behavioral deviation in time.
- ▷ TV should not overreact, so that the driver is not terrified and the vehicle instability should not be led.
- ▷ TV should take physical limitations into account and diminish the risk of skidding.

In order to validate these functional requirements, meaningful test cases should be defined. In this work, only standardized test maneuvers are applied, which cause diverse critical drive situations. The test maneuvers are listed as follows:

- ▷ lateral transient response test (ISO 7401) [3]
- ▷ sine-steer test (ISO 7401) [3] and
- ▷ sine-steer test with dwell (National Highway Traffic Safety Administration (NHTSA)) [5].

Detailed information about these test maneuvers are referred to in Appendix H.

2.3.2 Boundary conditions

Albeit TV application can enhance the vehicle stability, no arbitrary drive situation has to be considered for the software design. To gain a physically meaningful design a 'normal' driver is assumed, who represents statistically 95% of all drivers and driving situations [129]. The following conditions are specified in the present work:

- ▷ TV will be activated for a speed larger than 30 km/h.
- ▷ TV strategy is based on driving traction forces. Therefore, TV is deactivated if the brake pedal is applied.
- ▷ A normal driver steers smaller than 90° with the corresponding lateral acceleration of 2 m/s^2 . In the present work, the maximum lateral acceleration is defined by 7 m/s^2 .
- ▷ The maximum admissible change of the steering wheel angle is $300^\circ/\text{s}$ in case of small friction coefficient μ and $400^\circ/\text{s}$ in case of large μ .
- ▷ The maximum vehicle sideslip angle is 6° .
- ▷ A normal driver reacts to the vehicle movement change not earlier than one second [31]. Therefore, the maximum execution time of TV is 1 s.
- ▷ The vehicle behaves linearly by means of the Linear Single Track Model (LSTM) in 95% of all times.

Some of these conditions are adopted from the requirements of ESC design described in [86]. These conditions arise from the response of normal drivers and vehicle stability. They are considered as the thresholds in the control design.

2.3.3 Software specifications

Figure 2.3 illustrates the software structure of the implementation of this work. The control of high dynamic torque distribution for TV consists of electrical drive control (1), oscillation damping control of the mechanical drivetrain (2), vehicle dynamic control containing yaw rate control (3) as well as the operation strategy (4) in consideration of the driver demand (5).

To attain a TV application employed in EVs, we assume only the commonly in production vehicles used sensor equipments being available for the control approaches. Signals and values transferred amongst the software modules are depicted in Table 2.2.

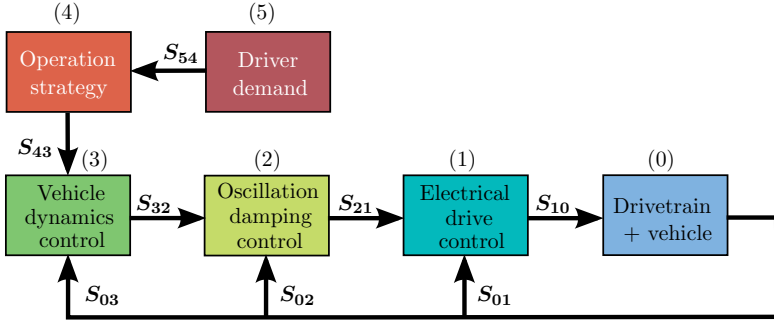


Figure 2.3: Software structure.

Signal	Quantity	Unit	Description
S_{01}	I_{abc}	A	Stator current of the IM
	Ω_r	rpm	Mechanical rotor speed of the IM
S_{02}	Ω_r	rpm	Mechanical rotor speed of the IM
	Ω_{wheel}	rpm	Wheel speed
S_{03}	$\dot{\psi}$	rad/s	Yaw rate of the EV
	a_y	m/s ²	Lateral acceleration of the EV
S_{10}	T_{el}	Nm	Electromagnetic torque of the IM
S_{21}	T_{el}^*	Nm	Electromagnetic torque reference value
S_{32}	T_{shaft}^*	Nm	Shaft torque reference value
S_{43}	$\dot{\psi}^*$	rad/s	Yaw rate reference value
	p_{gp}	%	Gas pedal position
S_{54}	p_{brk}	%	Brake pedal position
	δ_H	rad	Steering wheel angle

Table 2.2: Signal specification.

Operation strategy

Depending on the current drive situation, an intelligent operation strategy computing a reference yaw rate should be implemented, which takes driver demands and vehicle states as well as road effects (friction, cross slope) into account. For improved handling the computed yaw rate set point changes the vehicle's under-steering behavior towards a neutral one.

Furthermore, due to limited measurable quantities, An observer is required, which estimates all control-relevant information, such as tire forces, lateral velocity, longitudinal slip, tire slip angle and road friction coefficient, etc.

Vehicle dynamics control

In order to enhance vehicle agility by means of vehicle dynamics control, an intelligent strategy for facilitating the full use of the tire's potential to produce a force should be implemented. Another reason for implementing this strategy is to mitigate the risk of skidding. It is achieved in such a manner, that the 'weaker' tire is taken into account and an excessive slipping can be therefore avoided.

To monitor the physical limitation of tires mentioned above, the nonlinearity of tires has to be considered in the control design. For this reason, an inversed tire model should be implemented, which translates the required longitudinal tire forces into corresponding slip values based on the vehicle velocity and the friction coefficient. Moreover, depending on the drive situation the tire radii vary, which can impact the computation of physical limitations. Therefore, a function should be introduced to provide the dynamic tire radii.

Additionally, according to the boundary conditions a control logic should be implemented to determine under which circumstances the control strategy becomes active or inactive.

Oscillation damping control

Due to the oscillation behavior of drive shafts, a damping control is necessary to ensure the performance of torque transmission. Since the measurable quantities are merely the rotor speed of the machine and the wheel speed, an observer should be implemented to estimate the actual shaft torque.

Electrical drive control

Both drive motors are considered as actuator in the entire TV system. To achieve a high dynamic torque distribution, the current control in IM is essential. In order to transform the torque requirement from the damping control into the reference value of the current control, the nonlinearity magnetic property should be identified. Furthermore, over-current and -voltage issues should be considered for safety reasons.

Summary

As illustrated in Figure 2.3, these software modules constitute a cascade structure. Hence, the implementation of TV will be performed thereafter by an introduction

from the innermost control loop (between module 1 and module 0 in the figure) to the outermost control loop (between module 3 - and module 0 in the figure). This corresponds to the bottom-up sequence in the V-model. The validation of the entire TV system is performed on a HiL test bench, which will be detailed in chapter 8.

3 State of the art and novelties of the work

As has been mentioned, the MPC framework is decided as fundamental solution in the present work. In the previous chapter, the general problem was specified onto the functional level. In this chapter, an overview is given on solving the problem on the technical level. The historical background and conceptual idea of MPC are introduced in section 3.1. In section 3.2 the state of the art techniques of solving the subproblems specified in section 2.3.3 are discussed. In section 3.3 the objectives and academic contributions of the present work are presented.

3.1 MPC history and concept

The idea of model predictive control and receding horizon control has been developed since the 1960s [119]. MPC made its first appearance in industrial applications in the petrochemical process industry in the 1970s [160]. This field of applications was a natural starting point, as the hundreds of inputs and outputs being present in typical systems inhibited the application of classical control theory. It was shown in [158] that MPC is an effective way to handle multi-variable constrained control problems. Furthermore, the large time constants involved in many chemical processes allowed the control system a sufficient amount of time to process challenging computations inherent to MPC.

As suggested by its name, MPC is a predictive control strategy, where the predictions on the future system state are derived from a prediction model based on the physical system. The basic concept of MPC is to solve an open-loop constrained optimization problem at each time instant and implement only the first control action of the solution.

Figure 3.1 illustrates the concept of MPC methodology. Starting from the system's current state at any time instant k , MPC seeks to find an optimal control sequence over the control horizon N_u with $\mathbf{U} = [u_{k|k}^T, u_{k+1|k}^T, \dots, u_{k+N_u-1|k}^T]^T$ which drives the deviation of the system output $y_{k+i|k}$ to the reference towards zero. This is achieved implicitly by solving an open-loop control problem over a finite or an infinite prediction horizon N_p . It is assumed that after N_u steps the control action remains constant and after N_p steps the system converges to the reference. Although \mathbf{U} contains a sequence of optimal control actions for the next N_p steps, only the control action for the next time instant u_k is applied to the system by $u^* = u_{k|k}$. The rest of the control actions are discarded. At the next time instant $k+1$, the system state is updated in accordance to either measurement or estimation. The system is therefore shifted one step ahead and such procedure is repeated over the same prediction horizon N_p , which yields the next optimal control value for $u^* = u_{k+1|k+1}$. Therefore,

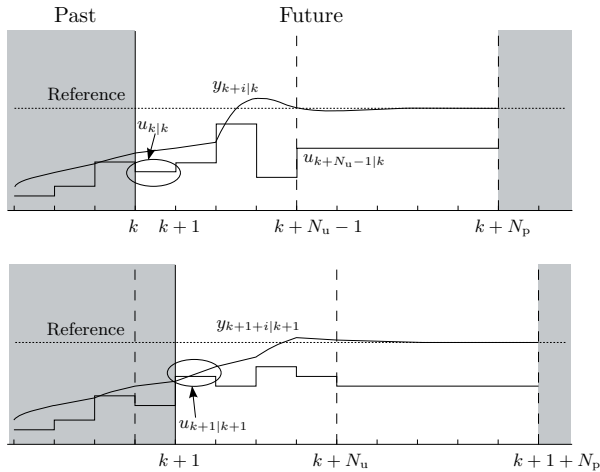


Figure 3.1: Receding horizon control.

MPC is also referred to as Receding Horizon Control (RHC). [159] and [157] give extensive general information about MPC methodology.

MPC has been intensively developed during the last three decades [152, 130, 109] and it becomes one of the most important advances in the processing industry, especially in chemical process control such as petrochemical, pulp and paper control. However, the procedure of determining the optimal control action represented by solving a mathematical optimization problem requires relatively large computational effort in comparison to classic control methods. Hence, the application of MPC was restricted to low dynamic systems.

With the development of micro-controller techniques in the last few decades, MPC is increasingly discussed for high dynamic control applications. In [116, 118], MPC was firstly systematically proposed for power electronics and electrical drive control. Since then, an increasing number of MPC strategies have been adopted in this area. In [93, 184, 94] the applications of MPC in power electronics and alternative current (ac) drives are comprehensively depicted. Simultaneously, the theories of MPC stability, feasibility, optimality as well as robustness are developed. The proofs are oftentimes investigated strategy-dependently. Nevertheless, the general theories are explained and derived in [156, 36, 125, 119, 122, 112, 23]. Since most MPC strategies handle discrete time systems, they can be easily employed in the modern Digital Signal Processor (DSP) systems. MPC shows several apparent advantages, such as design simplicity, explicit inclusion of design criteria and constraints, high dynamics and inherent robustness. Furthermore, MPC strategies are essentially based on optimization problems, wherefore the development of MPC theories has not been accomplished yet and can be still expanded hereafter.

3.2 Technical reviews

In this section, state of the art techniques, primarily optimization-based MPC approaches are introduced, which are used to tackle similar problems as in this work. This technical review places emphasis on the applications of MPC in diverse physical systems. The theoretical control issues associated with control design will be discussed in the corresponding sections respectively.

3.2.1 Electrical drive control

Since the 1980s the FOC has been developed for the practical use of ac machines and represents nowadays the state of the art [183]. In most cases, the requirements of drive applications can be met by dint of field-oriented cascaded PI controllers. Nevertheless, due to the drawbacks of such approaches introduced in section 1.2, new approaches are searched for high dynamic drive systems. The development of MPC theories in the last three decades stimulates the applications of MPC in electrical drive systems.

In [105], it was firstly proposed to apply MPC for the current control in IM. The idea of vector control was used to obtain decoupled linear systems for the d- and q-axis quantities. The underlying optimization problem of MPC can be moved off-line and solved by means of multi-parametric Quadratic Programming (mp-QP), which was derived in [18]. In this manner, MPC in consideration of system constraints can be applied for high dynamic systems, such as current control in IM, in real-time. In [46], MPC was applied for speed control in IM. The performances of the MPC controller and the conventional PI controller were compared. In [60], the cascade structure of FOC with PI controllers was introduced for continuous-time MPC. Depending on the control structure, an observer was applied to the system with an integral term to diminish the impact of disturbance. In [61], the disturbance issue was further investigated. Integrators were embedded in both inner and outer loop control systems to completely reject the disturbance and thus enhance the robustness of the entire system. Furthermore, the current constraint of IM was formulated in such a way, that d-current was assumed to be constant and the constraint of q-current can be therefore derived from the maximum admissible dq-current.

In [45], observers were employed for the purpose of sensorless control of MPC in IM. An adaptive full-order observer was implemented to estimate the stator currents and rotor flux. The dynamics and the robustness of MPC against parameter uncertainties as well as load changes were studied in that work. In [44], the advantage of MPC concerning dynamics and robustness was emphasized by means of comparison to the conventional PI controllers.

[58] proposed a predictive speed control for electrical drives without cascade structure. A single optimization problem was formulated in the control design by means of minimum-time control problem for a double integrator. The computational effort was reduced significantly by using Finite-Control-Set MPC (FCS-MPC), which is based on enumeration of switching possibilities of the inverter.

In [132], the issue of delay time compensation was discussed for MPC approaches in IM. Delay time compensation was obtained in such a way, that instead of one step prediction in FCS-MPC, two steps are considered to improve the system performance against delay time.

In the last two approaches, the controller tackles directly with the finite possible switching states of combinations of the inverter over the prediction horizon, and generates ready-to-use switching states for the inverter without translating voltage space vectors by using modulators. In contrast to other aforementioned MPC approaches combined with modulation techniques named Continuous Control Set MPC (CCS-MPC), these approaches have a relatively simple architecture because no modulator is required and it is well-designed for digital power inverter control systems.

Among those FCS-MPC schemes, the one based on enumeration is one of the most well established and widely adopted method. In [102], the application of enumeration-based FCS-MPC approach in power converters was introduced in detail. The drawback of such approaches is that the general problem to be optimized is NP-hard and it is practically only applicable for a limited number of switching sequences and length of the prediction horizon due to its exhaustive computation. For the sake of complexity reduction, some modified enumeration-based strategies eliminate certain switching sequences, which violate the upper limit of switch change per sampling period, from the candidate set [151].

As an alternative, FCS-MPC based on extrapolation is tailored for emulating a long prediction horizon while being computationally efficient [70, 69]. The basic idea of extrapolation-based FCS-MPC is to compute control sequences over the switching horizon that is significantly shorter than the prediction horizon, which is determined by linearly extrapolating the promising state trajectory within their constraints. However, the accuracy is compromised. There are other emerging strategies targeted at enabling long-horizon FCS-MPC such as move-blocking [94] and event-based horizon strategies [65].

In [66, 67], a long prediction horizon of FCS-MPC was achieved by setup and solving a Constrained Finite-Time Optimal Control (CFTOC) problem. This problem can be reformulated into an integer least-squares problem and efficiently solved by the sphere decoding algorithm. Such approach was evaluated and compared with other FCS-MPC methods in [68] in respect of control performance and computational complexity. Although this algorithm can be improved by further complexity-reducing techniques, it cannot meet the real-time requirement in the present work.

In summary, due to the expensive on-line computational effort and the notable current as well as torque ripples [35], CCS-MPC is decided to form the basis of this work for the development of new electrical drive control approaches.

3.2.2 Oscillation damping control

The topic of oscillation damping in electrical drive systems was handled in [128]. It was studied, which physical parameters/mechanical factors can impact the dominant eigenvalue of the mechanical system. Based on this investigation, the controllers are designed in terms of a physical meaning. By means of the controllers, these influencing parameters can be mathematically modified by manipulating the control parameters. The drawback of this approach was the stationary torque deviation. In [175], diverse approaches with cascaded PI controllers and different additional feedbacks were reviewed for electrical drive systems with elastic joint. The classic pole-placement method was applied to calculate control parameters. The concept of additional feedbacks frees the pole-placement and therefore improved the control performance of such linear controllers.

A comparison of different damping control approaches was given in [180]. The performance of the classic PI controller was unsatisfying due to constricted pole-placement, while PI controllers with additional feedbacks and generalized predictive control (GPC), which is a sort of MPC, require high computational efforts. In [43], an oscillation damping control by means of Explicit MPC (EMPC) was proposed for a two-mass drive system with elastic coupling. The system constraints were considered in the control design. By means of multi-parametric Quadratic Programming (mp-QP), the most computational effort was moved off-line and the on-line computation was represented by the search for the optimal control action stored in a lookup table. The simulation and experiment results showed quite satisfying control performance. The robustness of EMPC against parameter variation in electrical drive systems with elastic coupling was studied in [178]. Results showed that by a proper selection of control parameters, a robust and reliable control strategy can be obtained.

In [188], the so-called EMPC-PI switching control, was applied for the vibration suppression with shaft torque limitation in electrical drive systems. By means of this approach, the high requirements for the control module memory caused by Look Up Tables (LUTs) containing off-line solutions can be avoided, which makes this approach more attractive for industrial applications.

To ensure the control performance of MPC-based approaches, an observer has to be implemented, which estimates the unmeasurable state variables such as shaft torque and varying system parameters. In [176], an adaptive Nonlinear Extended Kalman Filter (NEKF) was introduced. It was aimed to design an adaptation strategy to obtain higher dynamic observer in case of parameter variation. The initial values of observer parameters were selected by using genetic algorithm. Based on these values, the adaptation strategy was proposed in form of a mathematical formula associated with a so-called correction factor. Although good performance was observed in the experimental results, no mathematical derivation was given for the determination of this adaptation formula. In [177], a systematical analysis was given to present the control performance of the electrical drive system with elastic coupling by means of nonadaptive and adaptive EKF. The results showed that the application of the adaptation mechanism facilitated a faster convergence to the real values.

3.2.3 Vehicle dynamics control

In [91], the control objective of active TV was investigated and TV applications were categorized as follows: First of all, the reference yaw rate $\dot{\psi}$, which is determined by steering wheel angle and vehicle velocity, is selected as control objective. Such strategy is used in most TV systems [150, 32, 153, 62, 51, 135]. Another common alternative is to control the combination of yaw rate and vehicle sideslip angle β as applied in [64, 191, 179, 92, 38]. Besides both concepts, longitudinal vehicle velocity v_x and tire slip λ can be applied as the control objective as well [140, 135, 37]. As in most applications the yaw rate is determined as the control objective in the present work as well.

The conventional control approaches of vehicle dynamics control, or rather active yaw rate/moment control, are based on Proportional Integral Derivative (PID) technique. The control structure consists of a feedforward controller combined with PID controller and multi-parametric gain scheduling depending on vehicle velocity and estimated vehicle behavior [74]. The drawback of such approaches is the weak robustness against variation of vehicle parameters [74].

In order to improve the stability and robustness of the system, the concept of sliding mode control [53] was introduced to the yaw rate control of TV. By means of this technique, the system insensitivity to parameter variations and external perturbations is kept on the so-called sliding surface. In [135], two different formulations of two second-order sliding model control was proposed. However, the first- and second-order sliding mode control approaches have the drawbacks, that the robustness can be ensured restrictedly or the performance is significantly affected by signal discretization and actuation dynamics [74]. Therefore, integral sliding mode control was introduced in [74], and it showed a good tracking performance with a smooth control action.

In [55], an optimization-based TV control was proposed. The control objective is to minimize the control errors of forces on the vehicle's Center of Gravity (CoG). The optimization problem was formulated in a Semi-Definite Programming (SDP). However, due to the computational burden, only simulation results were presented. In [98] the driver's effects was involved in the control design as uncertainties in order to enhance the drive-in-the-loop stability. The robust \mathcal{H}_∞ control method was applied in that work. Analogous to the previous approach, the on-line computational effort was expensive, since the feasible solution was found by an iterative algorithm including underlying optimization problems. In [172, 173, 96], the control objective was formulated by a quadratic objective function with linear constraints, which can be numerically solved by quadratic programming (QP) solvers. Although efficient numerical solver was employed in [96] and experimental results were presented, the on-line computation was still emphasized.

In [171], the limitation of lateral acceleration was investigated to stabilize the vehicle behavior during cornering. By means of comparing the required and minimum feasible turning radii according to the actual velocity and applied steering command, it was able to be checked if the vehicle was stable. In critical cases, the controller

braked the vehicle in such a way, so that the feasible minimum radius was reduced and the required radius became stable. Based on this knowledge, the system constraints are explicitly expressed and incorporated in the control design [172]. The system constraints consist of yaw rate, vehicle sideslip angle, longitudinal slips on the drive wheels as well as the motor torque.

So far, diverse yaw rate control approaches are discussed for vehicle dynamics control. It is important to note that most TV applications are merely implemented by yaw rate control. In these approaches [185, 192, 91], the control variables of the yaw rate loop – mostly an asymmetric longitudinal tire force distribution – was translated into corresponding wheel torques directly applied to the wheel shafts. A major drawback of those systems is their inability to systematically consider the conditions of excessive tire slip, which leads to a degenerated control performance [165]. Another disadvantage of a lacking tire slip control is the potential force oscillations on the tires, especially at low speed.

3.3 Objectives and contributions

The main objective of the present work is represented by the implementation of the specifications defined in section 2.3.3 and the validation of the software according to the functional requirements, which was given in section 2.3.1. Besides, advanced control approaches will be pursued, which enhance the performance of the entire system in such a manner, so that a good trade-off between robustness and optimality can be achieved.

Most of the aforementioned optimization-based approaches are based on the robust nature of MPC to attain so-called robust control performance. However, no mathematical derivation can be given here to guarantee the global robustness of the control system. In other works, systematical incorporation of the system uncertainties was introduced. However, the algorithms introduced were based on numerical solution of optimization problems, which impedes its real-time application in dynamic systems. Furthermore, in order to achieve a feasible optimal control action in consideration of system constraints, the constrained MPC method with underlying QP problem was applied in many other works. However, due to the property of some system constraints, which are not able to be expressed in the standard form of the QP problem, an approximation has to be accepted, which yields that the system resource cannot be fully utilized. This causes the deterioration of the system optimality.

Therefore, it will be studied in the present work to further exploit the potential benefit of MPC theories and how to apply these theories to the control system/subsystems. Moreover, systematical analysis of system uncertainties and constraints, which can influence control performance, will be performed. In summary, to the best knowledge of the author, the novel contributions of the present work are highlighted by

- ▷ implementation of the min-max control theory and an efficient search algorithm for current control in IM to enhance the system's robustness,
- ▷ adaptation and implementation of the tube-based MPC theory for current control in IM in order to guarantee the robustness and simultaneously reduce the computational effort,
- ▷ handling the system constraints in IM without any approximation, so that the system optimality is not deteriorated,
- ▷ applying the explicit MPC in combination with a torque compensation to obtain a high dynamic damping control in mechanical drivetrain systems,
- ▷ implementation of an optimization-based robust tire slip control to prevent skidding and to provide the TV application an offset-free slip.
- ▷ implementation of a comprehensive operation strategy to ensure the TV performance in different drive situations.

In the next chapter, the topic will be concentrated more on MPC theories on the mathematical level.

4 Theoretical backgrounds of model predictive control

In this chapter, an overview is given to introduce the fundamentals of MPC employed in the present work. Since the basic idea of MPC is to specify the control problem by means of a mathematical optimization problem, the definitions of convex optimization are introduced in section 4.1. To understand the optimization problems introduced in this chapter, some definitions and notations of the key elements consisting the MPC approaches are given in Appendix A. In section 4.2, the basic formulation of MPC and its extended descriptions are explained. One of the significant advantages of MPC is to incorporate the system constraints and uncertainties explicitly in the optimization problems. Depending on the way, how these issues are handled, different optimization problems can be defined, which are discussed in section 4.3 and section 4.4.

4.1 Backgrounds

An optimization problem is a mathematical description of a problem, which helps find the best solution out of all feasible solutions. Therefore, MPC with underlying optimization problem is able to achieve a good performance once the optimization problem is properly set up.

4.1.1 Standard convex optimization problems

In this section, formulations of different convex optimization problems are given. The general form of a convex optimization problem is described by minimizing an objective function with constraints as follows:

$$\begin{aligned} \min_{\mathbf{x}} \quad & f_0(\mathbf{x}) \\ \text{s.t.} \quad & f_i(\mathbf{x}) \leq 0, \quad i = 1, \dots, m \\ & \mathbf{a}_j^\top \mathbf{x} = \mathbf{b}_j, \quad j = 1, \dots, p, \end{aligned} \tag{4.1}$$

where f_0, \dots, f_m are convex functions. To obtain a convex optimization problem the following requirements have to be fulfilled [27]:

- ▷ the objective function is convex,
- ▷ the inequality constraint functions are convex and
- ▷ the equality constraint functions are affine.

Linear Program (LP)

One of the most widely used convex optimization problem is linear program, which is defined by

$$\begin{aligned} \min_{\mathbf{x}} \quad & \mathbf{c}^T \mathbf{x} + d \\ \text{s.t.} \quad & \mathbf{A} \mathbf{x} \leq \mathbf{b}, \\ & \mathbf{A}_{\text{eq}} \mathbf{x} = \mathbf{b}_{\text{eq}}, \end{aligned} \tag{4.2}$$

where $d \in \mathbb{R}$, the vectors $\mathbf{c} \in \mathbb{R}^n$, $\mathbf{b} \in \mathbb{R}^m$, $\mathbf{b}_{\text{eq}} \in \mathbb{R}^p$, the matrices $\mathbf{A} \in \mathbb{R}^{m \times n}$ and $\mathbf{A}_{\text{eq}} \in \mathbb{R}^{p \times n}$. In most cases, the constant d is removed from the objective function, since it affects neither the optimal solution nor the feasible set. The linear constraints in (4.2) describes a polyhedron \mathcal{P} . Therefore, LP is an optimization of a linear objective over \mathcal{P} .

Quadratic Program (QP)

The convex optimization problem is called quadratic program if the problem is formulated by:

$$\begin{aligned} \min_{\mathbf{x}} \quad & \frac{1}{2} \mathbf{x}^T \mathbf{Q} \mathbf{x} + \mathbf{c}^T \mathbf{x}, \\ \text{s.t.} \quad & \mathbf{A} \mathbf{x} \leq \mathbf{b}, \\ & \mathbf{A}_{\text{eq}} \mathbf{x} = \mathbf{b}_{\text{eq}}, \end{aligned} \tag{4.3}$$

where the matrix $\mathbf{Q} \in \mathbb{S}_+^n$, which means it is symmetric positive definite. The vectors $\mathbf{c} \in \mathbb{R}^n$, $\mathbf{b} \in \mathbb{R}^m$, $\mathbf{b}_{\text{eq}} \in \mathbb{R}^p$. The matrices $\mathbf{A} \in \mathbb{R}^{m \times n}$ and $\mathbf{A}_{\text{eq}} \in \mathbb{R}^{p \times n}$. As in (4.2), the feasible set of QP is a polyhedron \mathcal{P} , over which a convex quadratic function is minimized.

Semidefinite Program (SDP)

A further convex optimization problem is semidefinite program, which has the general form

$$\begin{aligned} \min_{\mathbf{x}} \quad & \mathbf{c}^T \mathbf{x} \\ \text{s.t.} \quad & \mathbf{F}(\mathbf{x}) \succeq 0, \end{aligned} \tag{4.4}$$

where vector $\mathbf{c} \in \mathbb{R}^n$ and $\mathbf{F}(\mathbf{x}) \succeq 0$ denotes a *Linear Matrix Inequality* (LMI).

Definition 4.1.1 (Linear Matrix Inequality [42]) *A linear matrix inequality in the variable $x \in \mathbb{R}^n$ is an expression of the form*

$$\mathbf{F}(\mathbf{x}) = \mathbf{F}_0 + \sum_{i=1}^m x_i \mathbf{F}_i \succeq 0, \tag{4.5}$$

where \mathbf{F}_i with $i \in \{0, \dots, m\}$ are symmetric matrices in $\mathbb{R}^{n \times n}$.

The LMIs describe a positive semidefinite cone, over which a linear objective function in (4.4) is minimized. In case that all matrices F_i are diagonal, the LMI is equivalent to a set of n linear inequalities, which means the optimization problem expressed in (4.4) returns to a LP in (4.2).

4.2 Basic principles of model predictive control

In this section, the concept and the fundamental elements of MPC are introduced.

4.2.1 MPC startup

Prediction model

The prediction model is considered as the basis of MPC design. In the following a discrete-time Linear Time Invariant (LTI) unconstrained system without dead time in the simplified form is considered at first:

$$\begin{aligned}\mathbf{x}_{k+1} &= \mathbf{A}\mathbf{x}_k + \mathbf{B}\mathbf{u}_k \\ \mathbf{y}_k &= \mathbf{C}\mathbf{x}_k + \mathbf{D}\mathbf{u}_k,\end{aligned}\tag{4.6}$$

where $\mathbf{x}_k, \mathbf{x}_{k+1} \in \mathbb{R}^n$, $\mathbf{u}_k \in \mathbb{R}^m$ and $\mathbf{y}_k \in \mathbb{R}^p$ are the state, input and output vectors of the system with k denoting the time instant, respectively. $\mathbf{A} \in \mathbb{R}^{n \times n}$, $\mathbf{B} \in \mathbb{R}^{n \times m}$, $\mathbf{C} \in \mathbb{R}^{p \times n}$ and $\mathbf{D} \in \mathbb{R}^{p \times m}$ are state matrix, input matrix, output matrix and feedforward matrix, respectively. In order to control the outlined system, the following assumption should be fulfilled:

Assumption 4.2.1 (Controllability) *The objective system is controllable, in other words, controllability matrix $[\mathbf{B} \ \mathbf{A}\mathbf{B} \ \mathbf{A}^2\mathbf{B} \ \dots \ \mathbf{A}^{n-1}\mathbf{B}]$ has full rank.*

Objective function

Regarding to different MPC algorithms, various objective functions are proposed. The objective function J is also known as cost function. In the most control problems, the reference value should be tracked. Therefore, the following objective (cost) function is applied for the purpose of reference tracking

$$J = \sum_{i=1}^{N_p} (\mathbf{r}_{k+i} - \hat{\mathbf{y}}_{k+i})^T \mathbf{Q} (\mathbf{r}_{k+i} - \hat{\mathbf{y}}_{k+i}) + \sum_{i=0}^{N_u-1} \mathbf{u}_{k+i}^T \mathbf{R} \mathbf{u}_{k+i},\tag{4.7}$$

where N_p and N_u represent the prediction and control horizon length, respectively. The prediction horizon can be much longer than the control horizon. \mathbf{r}_{k+i} , $\hat{\mathbf{y}}_{k+i}$ and \mathbf{u}_{k+i} are the reference, predicted output and control vectors at time instant $k+i$, where $\mathbf{u}_{k+i} = \mathbf{u}_{k+N_u-1}$ for $N_u \leq i < N_p$. \mathbf{Q} , \mathbf{R} are symmetric positive definite weighting matrices, which penalize the tracking offset and control effort, respectively. The control law is computed by minimizing J at each time instant.

Control law

From (4.6) the predictions in next N_p steps at time k are computed by

$$\mathbf{Y} = \begin{bmatrix} \mathbf{CA} \\ \mathbf{CA}^2 \\ \vdots \\ \mathbf{CA}^{N_p} \end{bmatrix} \hat{\mathbf{x}}_k + \begin{bmatrix} \mathbf{CB} & \dots & 0 \\ \mathbf{CAB} & \dots & 0 \\ \vdots & \ddots & \vdots \\ \mathbf{CA}^{N_p-1}\mathbf{B} & \dots & \mathbf{CA}^{N_p-N_u+1}\mathbf{B} \end{bmatrix} \mathbf{U}, \quad (4.8)$$

where the vectors $\mathbf{Y} = [\mathbf{y}_{k+1}^T \dots \mathbf{y}_{k+N_p}^T]^T \in \mathbb{R}^h$ and $\mathbf{U} = [\mathbf{u}_k^T \dots \mathbf{u}_{k+N_u-1}^T]^T \in \mathbb{R}^l$ with $h \triangleq pN_p$ and $l \triangleq mN_u$. Equation (4.8) can be expressed by

$$\mathbf{Y} = \mathbf{\Psi}\hat{\mathbf{x}}_k + \mathbf{\Theta}\mathbf{U}. \quad (4.9)$$

By substituting (4.9) into (4.7), the cost function (4.7) is rearranged to

$$J = (\mathbf{W} - \mathbf{\Psi}\hat{\mathbf{x}}_k)^T \mathbf{Q}(\mathbf{W} - \mathbf{\Psi}\hat{\mathbf{x}}_k) - 2\mathbf{U}^T \mathbf{\Theta}^T \mathbf{Q}(\mathbf{W} - \mathbf{\Psi}\hat{\mathbf{x}}_k) + \mathbf{U}^T (\mathbf{\Theta}^T \mathbf{Q} \mathbf{\Theta} + \mathbf{R}) \mathbf{U}, \quad (4.10)$$

where $\mathbf{W} \triangleq [\mathbf{r}_{k+1}^T \dots \mathbf{r}_{k+N_p}^T]^T \in \mathbb{R}^h$. Independent on the case, whether $\hat{\mathbf{x}}_k$ is corrected by the observer or not, this value is known at time instant k . Therefore, the only unknown variable of the cost function at time instant k is \mathbf{U} . In the absence of the constraints, an analytical solution exists by which the optimum yields

$$\begin{aligned} \frac{\partial J}{\partial \mathbf{U}} &\stackrel{!}{=} 0 \\ \mathbf{U}^* &= (\mathbf{\Theta}^T \mathbf{Q} \mathbf{\Theta} + \mathbf{R})^{-1} \mathbf{\Theta}^T \mathbf{Q}(\mathbf{W} - \mathbf{\Psi}\hat{\mathbf{x}}_k). \end{aligned} \quad (4.11)$$

Thus, the optimal control action at the next time instant is determined by applying the first element of \mathbf{U}^* :

$$\mathbf{u}_k = \mathbf{u}_k^*, \quad (4.12)$$

which is applied as input to system (4.6), while the resting part of the control actions is discarded. At the next time instant $k+1$ the optimization (4.11) is shifted one step ahead and the whole procedure is repeated with the updated information. Therefore, MPC is also called Receding Horizon Control.

4.2.2 State estimation and disturbance modeling

As aforementioned, in order to minimize the objective function, it is assumed that all state variables are known. In reality however, the system states are always either unmeasurable or measured with noises. Thus, MPC is often combined with an estimator / observer. Furthermore, disturbance and uncertainties occur, which lead to undesired tracking offset. To tackle these issues, a Kalman filter with extended disturbance modeling is introduced in the following.

A LTI system in consideration of noises can be modeled by

$$\begin{aligned} \mathbf{x}_{k+1} &= \mathbf{A}\mathbf{x}_k + \mathbf{B}\mathbf{u}_k + \mathbf{w}_k \\ \mathbf{y}_k &= \mathbf{C}\mathbf{x}_k + \mathbf{v}_k, \end{aligned} \quad (4.13)$$

where \mathbf{w} and \mathbf{v} represent the process and measurement noises respectively. \mathbf{w} is the process noise, which is a zero mean multivariate normal distribution with covariance \mathbf{Q}_k defined by

$$\mathbf{Q}_k = \text{E} [\mathbf{w}_k \mathbf{w}_k^T]. \quad (4.14)$$

\mathbf{v} is the zero mean Gaussian white noise and has the covariance

$$\mathbf{R}_k = \text{E} [\mathbf{v}_k \mathbf{v}_k^T]. \quad (4.15)$$

In Figure 4.1, the structure of a Kalman filter is illustrated. The estimation model of a Kalman filter is expressed according to the system matrices by

$$\begin{aligned} \hat{\mathbf{x}}_{k+1|k} &= \mathbf{A}\hat{\mathbf{x}}_{k|k} + \mathbf{B}\mathbf{u}_k \\ \hat{\mathbf{y}}_k &= \mathbf{C}\hat{\mathbf{x}}_{k|k-1}. \end{aligned} \quad (4.16)$$

It is assumed, that the system is observable, and it can be examined by means of Hautus Lemma given in [174].

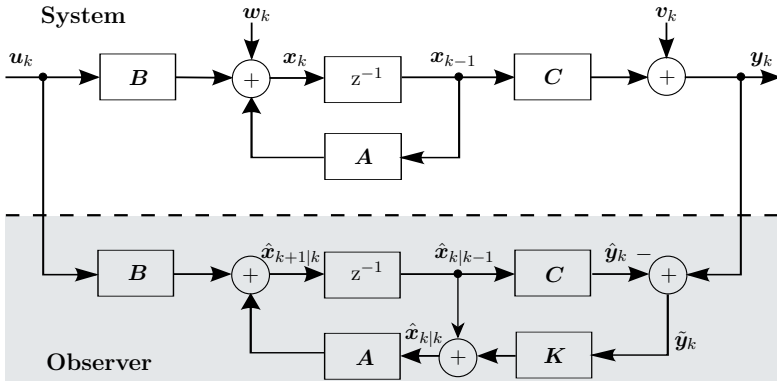


Figure 4.1: Block diagram of discrete-time Kalman filter.

The principle of a Kalman filter is to correct the estimated state value at time instant k by means of the measurement residual:

$$\hat{\mathbf{x}}_{k|k} = \hat{\mathbf{x}}_{k|k-1} + \mathbf{K}_k(\mathbf{y}_k - \mathbf{C}\hat{\mathbf{x}}_{k|k-1}) \quad (4.17)$$

where \mathbf{K} denotes the Kalman gain and $\tilde{\mathbf{y}}_k = \mathbf{y}_k - \mathbf{C}\hat{\mathbf{x}}_{k|k-1}$ represents the measurement residual. The Kalman gain is obtained by

$$\mathbf{K}_k = \mathbf{P}_{k|k-1}\mathbf{C}\mathbf{S}_k^{-1}, \quad (4.18)$$

where $\mathbf{P}_{k|k-1}$ is the predicted estimate covariance and calculated by

$$\mathbf{P}_{k|k-1} = \mathbf{A}\mathbf{P}_{k-1|k-1}\mathbf{A}^T + \mathbf{Q}_k, \quad (4.19)$$

and \mathbf{S}_k describes the residual covariance and is given by

$$\mathbf{S}_k = \mathbf{C}\mathbf{P}_{k|k-1}\mathbf{C}^T + \mathbf{R}_k. \quad (4.20)$$

The correction of estimate covariance is expressed by

$$\mathbf{P}_{k|k} = (\mathbf{I} - \mathbf{K}_k\mathbf{C})\mathbf{P}_{k|k-1}. \quad (4.21)$$

Therefore, the estimation procedure is recursive and can be summarized as shown in Figure. 4.2.

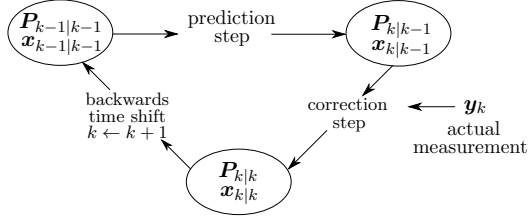


Figure 4.2: Estimation procedure of Kalman filter.

In [131], the nominal Kalman filter is extended with unmeasured disturbance models to suppress tracking error due to the disturbance. To simplify expressions, the predicted values are replaced by $\hat{\mathbf{x}}_{k+1}$. The state-space representation is given as follows:

$$\begin{aligned} \begin{bmatrix} \hat{\mathbf{x}}_{k+1} \\ \hat{\mathbf{d}}_{k+1} \end{bmatrix} &= \begin{bmatrix} \mathbf{A} & \mathbf{E} \\ \mathbf{0} & \mathbf{I} \end{bmatrix} \begin{bmatrix} \hat{\mathbf{x}}_k \\ \hat{\mathbf{d}}_k \end{bmatrix} + \begin{bmatrix} \mathbf{B} \\ \mathbf{0} \end{bmatrix} \mathbf{u}_k \\ \mathbf{y}_k &= \begin{bmatrix} \mathbf{C} & \mathbf{G} \end{bmatrix} \begin{bmatrix} \hat{\mathbf{x}}_k \\ \hat{\mathbf{d}}_k \end{bmatrix}, \end{aligned} \quad (4.22)$$

where the variable \mathbf{d} denotes the unmeasured disturbance. It is assumed, that the unmeasured disturbance in the system has much lower dynamics and can therefore be considered as constant within the prediction horizon, i.e. $\hat{\mathbf{d}}_{k+1} = \hat{\mathbf{d}}_k$.

The matrices \mathbf{E} and \mathbf{G} describe the kind and the dynamics of the disturbance respectively. In case that the output disturbance is dominant, which means $\hat{\mathbf{d}}_k = \mathbf{y}_k - \mathbf{C}\hat{\mathbf{x}}_k$, matrix \mathbf{G} is set by \mathbf{I} . Alternatively, If the input disturbance is determining, matrix \mathbf{E} is simply configured by \mathbf{B} , since $\hat{\mathbf{x}}_{k+1} = \mathbf{A}\hat{\mathbf{x}}_k + \mathbf{B}(\mathbf{u}_k + \hat{\mathbf{d}}_k)$. In this way, the estimated disturbance is compensated in the corresponding position, i.e. to input or output variable.

Besides the importance of both kinds of disturbances, another criteria which has to be considered is the selection of the critical constraint for the system. In case

that the input constraint should not be violated, the output disturbance has to be modeled and compensated to the system output to avoid the modification of the input value decided by the controller. Same principle holds for output constraint as well. In the present work, the nominal Kalman filter is applied to the controllers by default. It will be explicitly mentioned if any extension such as disturbance modeling exists.

4.3 Constrained model predictive control

Almost all real-world physical systems have their constraints, whether they are input, output or state limits. As has been stated, one advantage of MPC when compared to PI controllers is the incorporation of system constraints in the control design. Hence, MPC provides a good instrument to handle constrained system control.

In PI control approaches, the system constraints are handled by means of the saturation of the corresponding values and anti-windup mechanism, which suppresses output overshooting. However, saturation is not the best way for optimal control approaches. The reasons for this are clarified in the following.

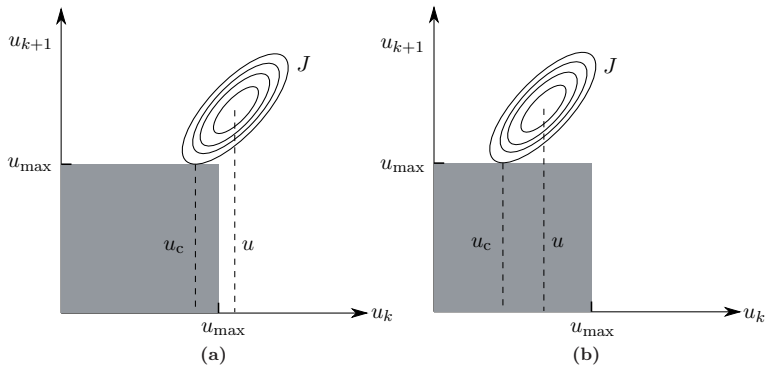


Figure 4.3: Computation of control signals with and without incorporation of input constraints [33].

Figure 4.3 illustrates the difference between saturation and constraint incorporation in MPC. To give a direct insight to the expression, the MPC problem is defined with a control horizon in two steps. The annular curves represent the values of cost function J . Figure 4.3a shows the scenario, in which $u_k, u_{k+1} > u_{\max}$. By means of saturation, u_k is forced to its limiting value u_{\max} , while by constraint consideration u_c is applied to reach the minimum of J . In the case of Figure 4.3b, the value of the next control action u_k does not violate the constraint and is therefore applied to the system. However, the input u_{k+1} exceeds the limit after u_k is applied. As

a consequence, the value of the cost function deviates from the one of the optimal solution in consideration of constraints, where u_c is applied to the system.

4.3.1 On-line optimization problem

The example shown in Figure 4.3 gives a good explanation, why constraints have to be considered in MPC design to ensure the optimality. Now the unconstrained optimization problem of MPC is recalled. Minimizing the cost function described in (4.10) is equivalent to the following problem:

$$\min_U J' = \frac{1}{2}U^T \mathbf{H}U + \mathbf{c}^T U, \quad (4.23)$$

where $\mathbf{H} = \Theta^T \mathbf{Q} \Theta + \mathbf{R}$ and $\mathbf{c} = -\Theta^T \mathbf{Q}(\mathbf{W} - \Psi \hat{\mathbf{x}}_k)$. It can be easily obtained that the Hessian matrix \mathbf{H} is symmetric positive semi-definite. Thereby, the optimization problem is specified as a convex optimization. The control horizon is set by two steps. In this example there exists a unique globally optimum.

The optimization problem of MPC (4.23) under consideration of constraints is then depicted as follows:

$$\begin{aligned} \min_U \quad & \frac{1}{2}U^T \mathbf{H}U + \mathbf{c}^T U \\ \text{s.t.} \quad & \mathbf{G}U \leq \mathbf{b} + \mathbf{E}\hat{\mathbf{x}}_k, \end{aligned} \quad (4.24)$$

where the vectors \mathbf{G} , \mathbf{b} and \mathbf{E} depend on the constraint formulation. For constant constraints \mathbf{E} is zero. Since the box-constraint can be converted to a one-sided form, this form is generally valid for all inequality constraint expressions. Therefore, the optimization problem with constraints is a standard QP as expressed in (4.3). Since the problem changes at each time instant k (the matrix \mathbf{c}^T and the constraints are state-dependent), an on-line solution is required for MPC to solve the problem at each time instant.

Commonly, the QP problems are solved by efficient numerical solvers based on active set methods or interior-point methods. With active set methods, only the active constraints are considered at each iteration step. Therefore, the active set varies slightly from step to step. One remarkable disadvantage of the active set algorithms is, that the algorithm may become inefficient near to the optimum point. With interior-point or Primal Dual (PD) interior-point methods, the QP is converted to a Lagrangian. The constraints are replaced by barrier functions. By means of Karush-Kuhn-Tucker (KKT) conditions [27] the system is converted to nonlinear equations, whereat at each iteration the system is linear. Thus, the computation can be accomplished by iterative linear algebraic solvers. The PD interior-point methods feature fast convergent properties. However, the on-line computational effort for obtaining the control law is tremendous despite of the efficient numerical solvers. Apparently, this does not meet the real-time requirement in the present work. Therefore, in the following, the approach proposed in [18] is introduced to attain a real-time application of MPC for constrained LTI systems.

4.3.2 Multi-parametric QP

In the on-line optimization of problem (4.24), the value of $\hat{\mathbf{x}}_k$ is given at each time instant k for the solution. Therefore, the control law $\mathbf{u} = \mathbf{u}(k)$ is defined implicitly as a function of $\hat{\mathbf{x}}_k$. To reduce the computational effort, the explicit MPC is introduced. The explicit MPC based on mp-QP, which is proposed in [18]. The QP is solved for all feasible states \mathbf{x} off-line, to find the control law $\mathbf{u} = \mathbf{u}(\mathbf{x})$ explicitly. According to the current value of $\mathbf{x}(k)$, the solution is calculated on-line in the explicit form.

The standard QP can be converted into mp-QP in such a way, that state variables are treated as a vector of parameters. According to the system constraints, the space of the parameters can be represented by a set of regions, which are convex polyhedral and in which the QP is feasible. By solving the optimization problem the control law can be expressed piecewisely with respect to the vector of the parameters. It is proved that the linear MPC controller is a continuous piecewise affine function of the parameters [18].

To introduce the algorithm of mp-QP, we consider at first the QP of regulation problem with measurable state variables and the cost function

$$\tilde{J} = \mathbf{x}_{k+N_p}^T \mathbf{P} \mathbf{x}_{k+N_p} + \sum_{i=0}^{N_p-1} (\mathbf{x}_{k+i}^T \mathbf{Q} \mathbf{x}_{k+i} + \mathbf{u}_{k+i}^T \mathbf{R} \mathbf{u}_{k+i}). \quad (4.25)$$

From (4.25) we obtain the following QP:

$$\begin{aligned} V(\mathbf{x}) = \min_{\mathbf{U}} \quad & \frac{1}{2} \mathbf{U}^T \mathbf{H} \mathbf{U} + \mathbf{x}_k^T \mathbf{F} \mathbf{U} \\ \text{s.t.} \quad & \mathbf{G} \mathbf{U} \leq \mathbf{b} + \mathbf{E} \mathbf{x}_k. \end{aligned} \quad (4.26)$$

By defining $\mathbf{z} = \mathbf{U} + \mathbf{H}^{-1} \mathbf{F}^T \mathbf{x}_k$ and substituting it in (4.26), we obtain an equivalent problem:

$$\begin{aligned} V_z(\mathbf{x}) = \min_{\mathbf{z}} \quad & \frac{1}{2} \mathbf{z}^T \mathbf{H} \mathbf{z} \\ \text{s.t.} \quad & \mathbf{G} \mathbf{z} \leq \mathbf{b} + \mathbf{S} \mathbf{x}_k, \end{aligned} \quad (4.27)$$

where $\mathbf{S} \triangleq \mathbf{E} + \mathbf{G} \mathbf{H}^{-1} \mathbf{F}^T$ and $V_z(\mathbf{x}) = V(\mathbf{x}) + \frac{1}{2} \mathbf{x}_k^T \mathbf{F} \mathbf{H}^{-1} \mathbf{F}^T \mathbf{x}_k$. Compared to (4.26) the parameter vector \mathbf{x}_k in (4.27) appears only on the right hand side of the inequality. In [18], it is proved that \mathbf{z} is also an affine function of parameter vector \mathbf{x} . Since it fulfills both primal and dual feasibility, the constraints can be converted to linear inequalities of the parameter vector. According to these inequalities, the parameter vector space can be partitioned into a set of convex polyhedral regions called critical regions, in each of these regions the problem is feasible. They are described by

$$\mathcal{CR}_i = \{\mathbf{x} \in \mathbb{R}^n \mid \mathbf{H}_i \mathbf{x} \leq \mathbf{K}_i\}. \quad (4.28)$$

Finally, the optimum solution can be obtained as a piecewise affine function in the following form:

$$\mathbf{u}^* = \mathbf{f}_i \mathbf{x} + \mathbf{g}_i. \quad (4.29)$$

4.4 Robust model predictive control

Besides the system constraint handling, another essential advantage of MPC is to deal with the system uncertainties. Possible sources of uncertainties are represented by modeling mismatch, unknown parameter variation in the system, at last but not least the external disturbances. These uncertainties can be considered in the MPC design to achieve a good trade-off between robustness and optimality. In this section, two different concepts concerning *Robust Model Predictive Control* (RMPC) will be introduced.

4.4.1 Min-max control

The robust MPC with explicit incorporated system uncertainties based on min-max optimization, also called min-max MPC, was firstly introduced 1996 in [100]. The plant model is described as a *Linear Parameter-Varying* (LPV) system with polytopic uncertainties. The objective function is formulated as a quadratic Lyapunov function in infinite horizon and minimized by solving the LMIs on-line. This approach is improved in [39] and corrected in [123] by applying parameter-dependent Lyapunov functions. In such a way, the control performance is improved since the conservativeness of the optimization problem is reduced. In [34] and [85], the RMPC subjected to input saturation is presented. RMPC in finite horizon was introduced 2004 in [49]. The parameter-dependent Lyapunov function is divided into two parts: the first $N - 1$ steps and the terminal step. In [146] the performance of the RMPC in finite horizon was further improved by defining Lyapunov function for each prediction step.

Fundamental method

In general, the system uncertainty can be incorporated in the optimization problems by means of two methods. One is modeling the uncertainty by adding a disturbance to the system as described in the following equation:

$$\mathbf{x}_{k+1} = \mathbf{A}\mathbf{x}_k + \mathbf{B}\mathbf{u}_k + \mathbf{G}\mathbf{w}_k, \quad \mathbf{w}_k \in \mathbb{W}, \quad (4.30)$$

where \mathbf{w}_k is the unknown disturbance and \mathbb{W} is the disturbance constraint set. Another method is modeling the uncertainty as a polyhedron, which is named polytopic uncertainty [16]. The system is described as a LPV system by:

$$\begin{aligned} \mathbf{x}_{k+1} &= \mathbf{A}(\theta)\mathbf{x}_k + \mathbf{B}(\theta)\mathbf{u}_k \\ \mathbf{y}_k &= \mathbf{C}\mathbf{x}_k \\ [\mathbf{A}(\theta), \mathbf{B}(\theta)] &\in \Omega, \end{aligned} \quad (4.31)$$

where Ω is a convex hull (polytopic set) defined by

$$\Omega = \text{Co}\{[\mathbf{A}_1, \mathbf{B}_1], [\mathbf{A}_2, \mathbf{B}_2], \dots, [\mathbf{A}_L, \mathbf{B}_L]\}. \quad (4.32)$$

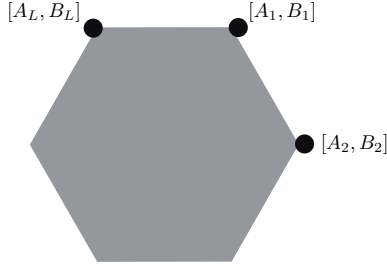


Figure 4.4: Two dimensional polytopic uncertainty.

$[A_l, B_l]$ denote the vertices of the convex hull with $l \in \mathbb{L}$. Therefore, for any $[A(\theta), B(\theta)] \in \Omega$ there exists

$$[A(\theta), B(\theta)] = \sum_{l=1}^L \theta_l [A_l, B_l], \quad \forall \theta_l \in \Theta, \quad (4.33)$$

where Θ is the unit simplex with $\Theta = \{\sum_{l=1}^L \theta_l = 1, \theta_l \geq 0\}$. Figure 4.4 illustrates a simple two-dimensional example of polytopic uncertainty.

For simplicity, it is imposed hereinafter that the control horizon and the prediction horizon are N ($N_p = N_u = N$). Therefore, the cost function of finite horizon min-max control is defined by

$$J_k(\mathbf{x}, U) = \|\mathbf{x}_{k+N}\|_{\mathbf{P}}^2 + \sum_{i=0}^{N-1} \{\|\mathbf{x}_{k+i}\|_{\mathbf{Q}}^2 + \|\mathbf{u}_{k+i}\|_{\mathbf{R}}^2\}. \quad (4.34)$$

The optimal control laws are obtained by minimizing this cost function in the worst case

$$J_k^*(\mathbf{x}_k) = \min_{U=\{\mathbf{u}_k \dots \mathbf{u}_{k+N-1}\}} \max_{\theta \in \Theta} J_k(\mathbf{x}_k, U, \theta), \quad (4.35)$$

wherefore it is also called min-max control.

In [100], it is proved that if the following inequality is satisfied

$$V(\mathbf{x}_{k+i+1|k}) - V(\mathbf{x}_{k+i|k}) \leq -\mathbf{x}_{k+i|k}^T \mathbf{Q} \mathbf{x}_{k+i|k} - \mathbf{u}_{k+i|k}^T \mathbf{R} \mathbf{u}_{k+i|k} \quad (4.36)$$

for any $[A_{k+i}, B_{k+i}] \in \Omega$ and all $\mathbf{x}_{k+i|k}$, $\mathbf{u}_{k+i|k}$ at time instant k , the cost function of infinite horizon min-max control has an upper bound

$$\max_{[A_{k+i}, B_{k+i}] \in \Omega, i \geq 0} J_{\infty}(k) \leq V(\mathbf{x}_{k|k}), \quad (4.37)$$

where $V(\mathbf{x}_{k|k}) = \mathbf{x}^T \mathbf{P} \mathbf{x}$ describing a quadratic Lyapunov function. Therefore, (4.35) can be represented by:

$$\min_{\gamma, \mathbf{S}} \gamma \quad (4.38)$$

$$\text{s.t. } \begin{bmatrix} 1 & \mathbf{x}_k^T \\ \mathbf{x}_k & \mathbf{S} \end{bmatrix} \succeq 0 \quad (4.39)$$

with $\mathbf{x}^T \mathbf{P} \mathbf{x} < \gamma$ and $\mathbf{S} = \gamma \mathbf{P}^{-1}$. The inequality (4.36) can be replaced by the LMI

$$\begin{bmatrix} \mathbf{S} & (\mathbf{A}_l \mathbf{S} + \mathbf{B}_l \mathbf{Y})^T & \mathbf{S} \mathbf{Q}^{\frac{1}{2}} & \mathbf{Y}^T \mathbf{R}^{\frac{1}{2}} \\ \mathbf{A}_l \mathbf{S} + \mathbf{B}_l \mathbf{Y} & \mathbf{S} & 0 & 0 \\ \mathbf{Q}^{\frac{1}{2}} \mathbf{S} & 0 & \gamma \mathbf{I} & 0 \\ \mathbf{R}^{\frac{1}{2}} \mathbf{Y} & 0 & 0 & \gamma \mathbf{I} \end{bmatrix} \succeq 0, \quad (4.40)$$

$l = 1, \dots, L$

where $\mathbf{Y} = \mathbf{F} \mathbf{S}$ and $\mathbf{u}_{k+i|k} = \mathbf{F} \mathbf{x}_{k+i|k}$. Thus, the unconstrained min-max control problem can be transformed to the optimization of a linear objective (4.38) subject to LMIs (4.39), (4.40).

Moreover, the satisfaction of inequality (4.36) implicates that

$$\mathbf{x}_{k+i+1|k}^T \mathbf{P} \mathbf{x}_{k+i+1|k} \leq \mathbf{x}_{k+i|k}^T \mathbf{P} \mathbf{x}_{k+i|k}, \quad i = 0, \dots, N-1, \quad (4.41)$$

since $Q \succ 0$ and $R \succeq 0$. Therefore, there exists an invariant ellipsoid at each time instant k defined by

$$\mathbb{E} = \{ \mathbf{z} \mid \mathbf{z}^T \mathbf{S}^{-1} \mathbf{z} \leq 1 \}, \quad (4.42)$$

where \mathbf{z} denotes the worst case

$$\max_{[\mathbf{A}_{k+i}, \mathbf{B}_{k+i}] \in \Omega, i=1 \dots N} \mathbf{x}_{k+i|k}^T \mathbf{S} \mathbf{x}_{k+i|k}. \quad (4.43)$$

This invariant ellipsoid is illustrated in Figure 4.5. It gives the feasible domain of all $\mathbf{x}_{k+i}, i = 1, \dots, N$, which means that all predicted states across the prediction horizon at time instant k should be located within this ellipsoid.

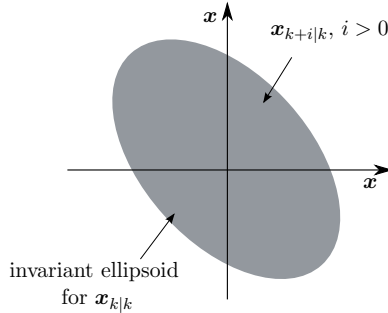


Figure 4.5: Illustration of invariant ellipsoid.

Considering the input constraint of the system, the following inequality should be satisfied

$$|(\mathbf{u}_{k+i|k})_j| \leq (\mathbf{u}_{\max})_j, \quad i = 1, \dots, N, \quad j = 1, \dots, m. \quad (4.44)$$

Since $\mathbf{u}_{k+i|k} = \mathbf{F}\mathbf{x}_{k+i|k}$, it yields

$$\begin{aligned} \max_{i \geq 0} \|(\mathbf{u}_{k+i|k})_j\|_2^2 &= \max_{i \geq 0} \|(\mathbf{F}\mathbf{x}_{k+i|k})_j\|_2^2 \\ &\leq \max_{\mathbf{z} \in \mathbb{E}} \|(\mathbf{Y}\mathbf{S}^{-1}\mathbf{z})_j\|_2^2 \\ &\leq \|\mathbf{Y}\mathbf{S}^{-\frac{1}{2}}\|_2^2 \\ &\leq (\mathbf{Y}\mathbf{S}^{-1}\mathbf{Y}^T)_{jj}, \quad j = 1, \dots, m. \end{aligned} \quad (4.45)$$

By means of Schur-complements the input constraint (4.45) is transformed in the following LMI:

$$\begin{bmatrix} \mathbf{X} & \mathbf{Y} \\ \mathbf{Y}^T & \mathbf{S} \end{bmatrix} \succeq 0, \quad \mathbf{X}_{jj} \leq \mathbf{u}_{j,\max}^2, \quad j = 1, \dots, m, \quad (4.46)$$

where m represents the dimension of the input vector. In analogy, the following LMIs are given for state and output constraints:

$$\begin{bmatrix} \mathbf{S} & (\mathbf{A}_l\mathbf{S} + \mathbf{B}_l\mathbf{Y})^T \\ \mathbf{A}_l\mathbf{S} + \mathbf{B}_l\mathbf{Y} & \Gamma_x \end{bmatrix} \succeq 0, \quad (4.47)$$

$(\Gamma_x)_{rr} \leq x_{r,\max}^2, \quad r = 1, \dots, n, \quad l = 1, \dots, L$

$$\begin{bmatrix} \mathbf{S} & (\mathbf{A}_l\mathbf{S} + \mathbf{B}_l\mathbf{Y})^T \mathbf{C}^T \\ \mathbf{C}(\mathbf{A}_l\mathbf{S} + \mathbf{B}_l\mathbf{Y}) & \Gamma_y \end{bmatrix} \succeq 0, \quad (4.48)$$

$(\Gamma_y)_{ss} \leq y_{s,\max}^2, \quad s = 1, \dots, p, \quad l = 1, \dots, L$

and they can be extended to the optimization problem (4.38). In (4.47) and (4.48), n and p denote the dimension of input and output vector, respectively. To summarize, the constrained min-max control problem based on LMIs is defined as a SDP problem:

$$\begin{aligned} &\min_{\gamma, \mathbf{S}, \mathbf{Y}, \mathbf{X}, \Gamma} \gamma \\ \text{s.t.} & \quad (4.39), (4.40), (4.46), (4.47), (4.48). \end{aligned} \quad (4.49)$$

According to this optimization problem, the fundamental min-max controller proposed in [100] is implemented by means of the following algorithm:

Algorithm 1 Kothare's RMPC [100]

-
- 1: Measure the state \mathbf{x}_k at time instant k
 - 2: Compute the optimization problem (4.49) and obtain the optimized parameters $\{\gamma^*, \mathbf{S}^*, \mathbf{Y}^*, \mathbf{X}^*, \Gamma^*\}$
 - 3: Apply $\mathbf{u}_k^* = \mathbf{Y}^* \mathbf{S}^{*-1} \mathbf{x}_k$ in the system
 - 4: Set $k \leftarrow k + 1$ and restart over.
-

Optimality improvement

So far, the min-max method introduced presents an approach with open-loop feasible domain determination, since the invariant ellipsoid (see (4.42)) is calculated at each time instant k with prediction horizon $N = 0$. Therefore, this approach has high conservativeness. In order to enhance the optimality, a min-max control approach based on close-loop predictions is introduced in [146] and [42], which is considered as a special case of extended invariance concept introduced in [110].

In this approach, the invariant ellipsoid for each prediction step $\mathbb{E}_{k+i|k} = \mathbf{x}_{k+i|k}^T \mathbf{S}_{k+i} \mathbf{x}_{k+i|k}$ is studied, which means that instead of unique \mathbf{S}_k , a sequence of \mathbf{S}_{k+i} should be determined. In order to ensure the property of invariant ellipsoid described in (4.42), (4.43) and Figure 4.5, a so-called *robust one-step set* [97] should be fulfilled, which means

$$\mathbf{x}_{k+i+1|k} \in \mathbb{E}_{k+i+1|k} \text{ if } \mathbf{x}_{k+i|k} \in \mathbb{E}_{k+i|k}. \quad (4.50)$$

The conditions are given as follows:

$$\begin{aligned} \mathbf{S}_{k+i}^{-1} - (\mathbf{A}_{k+i} + \mathbf{B}_{k+i} \mathbf{F}_{k+i})_l^T \mathbf{S}_{k+i+1} (\mathbf{A}_{k+i} + \mathbf{B}_{k+i} \mathbf{F}_{k+i})_l &\geq 0, \quad \forall l = 1, \dots, L \\ \mathbf{S}_{k+i} - \mathbf{S}_{k+i+1} &\geq 0 \\ \mathbf{F}_{k+i} \mathbf{x} &\in \mathbb{U}, \quad \forall \mathbf{x} \in \mathbb{E}_{k+i|k} \\ \mathbb{E}_{k+i|k} &\subset \mathbb{X}. \end{aligned} \quad (4.51)$$

The sufficient conditions of (4.51) in the LMI formulation are given by

$$\begin{aligned} &\begin{bmatrix} \mathbf{S}_{k+i} & (\mathbf{A}_l \mathbf{S}_{k+i} + \mathbf{B}_l \mathbf{Y}_{k+i})^T \\ \mathbf{A}_l \mathbf{S}_{k+i} + \mathbf{B}_l \mathbf{Y}_{k+i} & \mathbf{S}_{k+i+1} \end{bmatrix} \succeq 0, \quad l = 1, \dots, L \\ &\mathbf{S}_{k+i} - \mathbf{S}_{k+i+1} \geq 0 \\ &\begin{bmatrix} \mathbf{X} & \mathbf{Y}_{k+1} \\ \mathbf{Y}_{k+1}^T & \mathbf{S}_{k+1} \end{bmatrix} \succeq 0, \quad \mathbf{X}_{jj} \geq u_{j,\text{inf}}^2, \quad j = 1, \dots, m \\ &\begin{bmatrix} \mathbf{S}_{k+i} & (\mathbf{A}_l \mathbf{S}_{k+1} + \mathbf{B}_l \mathbf{Y}_{k+1})^T \\ \mathbf{A}_l \mathbf{S}_{k+1} + \mathbf{B}_l \mathbf{Y}_{k+1} & \Gamma_x \end{bmatrix} \succeq 0, \quad (\Gamma_x)_{ss} \geq x_{s,\text{inf}}^2, \\ &\hspace{15em} s = 1, \dots, n, \quad l = 1, \dots, L, \end{aligned} \quad (4.52)$$

where $u_{j,\text{inf}} = \min \{u_{j,\text{min}}, u_{j,\text{max}}\}$ and $x_{m,\text{inf}} = \min \{x_{m,\text{min}}, x_{m,\text{max}}\}$.

However, conditions (4.52) guarantee only the property (4.50) for $i \in \{1, \dots, N-1\}$. In order to ensure the general feasibility over the infinite horizon, further LMI to fulfill $\mathbf{x}_{k+1|k} \in \mathbb{E}_{k+1|k}$ and $\mathbf{x}_{k+N+i|k} \in \mathbb{E}_{k+N+i|k}$, $i \geq 1$ should be defined as well. The LMI, which satisfies the former condition, is straightforward:

$$\begin{bmatrix} 1 & (\mathbf{A}_l \mathbf{x}_k + \mathbf{B}_l \mathbf{u}_k)^\top \\ \mathbf{A}_l \mathbf{x}_k + \mathbf{B}_l \mathbf{u}_k & \mathbf{S}_{k+1} \end{bmatrix} \succeq 0, \quad l = 1, \dots, L. \quad (4.53)$$

Here, the input and state constraints for time instant $k+1$ should be satisfied, which means

$$\mathbf{u}_{\min} \leq \mathbf{u}_k \leq \mathbf{u}_{\max} \quad \text{and} \quad \mathbf{x}_{\min} \leq \mathbf{x}_{k+1} \leq \mathbf{x}_{\max}. \quad (4.54)$$

Both constraints are summarized in one LMI with

$$\mathbf{G}_b(\mathbf{x}_{k+1}, \mathbf{u}_k) - \mathbf{h}_b \geq 0, \quad (4.55)$$

where \mathbf{G}_b and \mathbf{h}_b are the matrices corresponding to (4.54).

In order to ensure that all states beyond the prediction horizon are located in the terminal region $\mathbb{E}_{k+N|k}$, the standard robust stability requirement, similar as the one given in (4.40) for one prediction step, is imposed:

$$\left[\begin{array}{cccc} \mathbf{S}_{k+N} & (\mathbf{A}_l \mathbf{S}_{k+N} + \mathbf{B}_l \mathbf{Y}_{k+N})^\top & (\mathbf{Q}^{\frac{1}{2}} \mathbf{S}_{k+N})^\top & (\mathbf{R}^{\frac{1}{2}} \mathbf{Y}_{k+N})^\top \\ \mathbf{A}_l \mathbf{S}_{k+N} + \mathbf{B}_l \mathbf{Y}_{k+N} & \mathbf{S}_{k+N} & 0 & 0 \\ \mathbf{Q}^{\frac{1}{2}} \mathbf{S}_{k+N} & 0 & \gamma_N \mathbf{I} & 0 \\ \mathbf{R}^{\frac{1}{2}} \mathbf{Y}_{k+N} & 0 & 0 & \gamma_N \mathbf{I} \end{array} \right] \succeq 0, \quad l = 1, \dots, L. \quad (4.56)$$

Moreover, the worst case of the cost function (4.34) in finite horizon can be formulated by:

$$\begin{aligned} \max_{\theta \in \Theta} J_k(\mathbf{x}, \mathbf{U}) &= \max_{[\mathbf{A}_{k+i}, \mathbf{B}_{k+i}] \in \Omega, i=1 \dots N} \|\mathbf{x}_{k+N|k}\|_{\mathbf{P}}^2 + \sum_{i=0}^{N-1} \|\mathbf{x}_{k+i|k}\|_{\mathbf{Q}}^2 + \|\mathbf{u}_{k+i|k}\|_{\mathbf{R}}^2 \\ &= \|\mathbf{x}_k\|_{\mathbf{Q}}^2 + \|\mathbf{u}_k\|_{\mathbf{R}}^2 + \max_{\mathbf{x}_{k+N|k} \in \mathbb{E}_{k+N|k}} \|\mathbf{x}_{k+N|k}\|_{\mathbf{P}}^2 \\ &\quad + \sum_{i=1}^{N-1} \max_{\mathbf{x}_{k+i|k} \in \mathbb{E}_{k+i|k}} \|\mathbf{x}_{k+i|k}\|_{\mathbf{Q}}^2 + \|\mathbf{F}_{k+i} \mathbf{x}_{k+i|k}\|_{\mathbf{R}}^2. \end{aligned} \quad (4.57)$$

According to (4.57) the upper bound of the cost function γ in the worst case is composed of

$$\gamma_0 \geq \|\mathbf{x}_k\|_{\mathbf{Q}}^2 + \|\mathbf{u}_k\|_{\mathbf{R}}^2, \quad (4.58a)$$

$$\gamma_N \geq \|\mathbf{x}_{k+N|k}\|_{\mathbf{P}}^2, \quad (4.58b)$$

$$\gamma_i \geq \|\mathbf{x}_{k+i|k}\|_{\mathbf{Q}}^2 + \|\mathbf{u}_{k+i|k}\|_{\mathbf{R}}^2. \quad (4.58c)$$

Therefore, instead of minimizing the unique γ in (4.49) the sum of the upper bounds $\gamma_0 + \sum_{i=1}^{N-1} \gamma_i + \gamma_N$ should be optimized. As a consequence, the following LMI are given as further constraints:

$$\begin{bmatrix} \gamma_0 & \mathbf{x}_k^T & \mathbf{u}_k^T \\ \mathbf{x}_k & \mathbf{Q}^{-1} & \mathbf{0} \\ \mathbf{u}_k & \mathbf{0} & \mathbf{R}^{-1} \end{bmatrix} \succeq 0, \quad (4.59a)$$

$$\begin{bmatrix} \mathbf{S}_{k+i} & (\mathbf{Q}^{\frac{1}{2}} \mathbf{S}_{k+i})^T & (\mathbf{R}^{\frac{1}{2}} \mathbf{Y}_{k+i})^T \\ \mathbf{Q}^{\frac{1}{2}} \mathbf{S}_{k+i} & \gamma_i \mathbf{I} & \mathbf{0} \\ \mathbf{R}^{\frac{1}{2}} \mathbf{Y}_{k+i} & \mathbf{0} & \gamma_i \mathbf{I} \end{bmatrix} \succeq 0, \quad \forall i \in \{1, \dots, N-1\}. \quad (4.59b)$$

The optimization problem is summarized as follows:

$$\begin{aligned} \min_{\substack{u_k, \gamma_0, \gamma_1, \dots, \gamma_{N-1}, X, \Gamma \\ s_1, s_2, \dots, s_N, y_1, y_2, \dots, y_N}} \quad & \gamma_0 + \sum_{i=1}^{N-1} \gamma_i + \gamma_N \\ \text{s.t.} \quad & (4.52), (4.53), (4.55), (4.56), (4.59). \end{aligned} \quad (4.60)$$

Besides this prediction-step-dependent extension, the conservativeness can be further reduced by parameter-dependent extension as well, and this strategy is introduced in [42]. The evaluation result in [42] shows that the optimality of the approach including both refinements is only slightly better than the one with prediction-step-dependent extension, whereas the computational effort increases significantly due to additional LMI constraints. Therefore, the approach with only prediction-horizon-dependent extension is applied in the present work.

4.4.2 Tube-based MPC

Another method to cope with system uncertainties is called tube-based robust model predictive control, which is initially proposed in [106]. In the following, the state feedback tube-based robust MPC with underlying regulation problem is introduced.

State feedback tube-based robust MPC

First issue to be discussed is the derivation of the optimal control from initial state \mathbf{x}_0 across the prediction horizon N . The system is described by a constrained, discrete-time linear system with a bounded, additive disturbance, which is given by

$$\mathbf{x}_{i+1} = \mathbf{A}\mathbf{x}_i + \mathbf{B}\mathbf{u}_i + \mathbf{w}_i, \quad (4.61)$$

where $\mathbf{x}_i \in \mathbb{R}^n$, $\mathbf{u}_i \in \mathbb{R}^m$ and $\mathbf{w}_i \in \mathbb{R}^n$ denote the state, the input and the disturbance at the time instant $i \in \{0, \dots, N-1\}$, while \mathbf{x}_{i+1} the successor state of the system at the next time instant. To simplify the description, (4.61) is expressed by

$$\mathbf{x}^+ = \mathbf{A}\mathbf{x} + \mathbf{B}\mathbf{u} + \mathbf{w} \quad (4.62)$$

with the following system constraints

$$\mathbf{x} \in \mathbb{X}, \mathbf{u} \in \mathbb{U}, \mathbf{w} \in \mathbb{W}, \quad (4.63)$$

where $\mathbb{X} \subset \mathbb{R}^n$, $\mathbb{U} \subset \mathbb{R}^m$ and $\mathbb{W} \subset \mathbb{R}^n$ are all polyhedral sets containing the origin. The disturbance set \mathbb{W} is as stated unknown but bounded. Furthermore, a nominal system without exogenous disturbance is considered in the control design, which is given as follows:

$$\bar{\mathbf{x}}^+ = \mathbf{A}\bar{\mathbf{x}} + \mathbf{B}\bar{\mathbf{u}}, \quad (4.64)$$

where $\bar{\mathbf{x}}$ and $\bar{\mathbf{u}}$ denote the state and input value of the nominal system.

In [126], the robust attractivity and robust exponential stability of a robust positively invariant set have been proven. These theories are fundamentals of tube-based robust MPC. As proposed in [111], the applied control law consists of two separated parts: the first part is a feedforward control with input calculated from the nominal system (4.64), and the second part is a linear feedback control of the error between the real state \mathbf{x} and the nominal state $\bar{\mathbf{x}}$, which is formulated by

$$\mathbf{e} := \mathbf{x} - \bar{\mathbf{x}}. \quad (4.65)$$

Therefore, the control law can be expressed as

$$\mathbf{u} = \bar{\mathbf{u}} + \mathbf{K}\mathbf{e} = \bar{\mathbf{u}} + \mathbf{K}(\mathbf{x} - \bar{\mathbf{x}}). \quad (4.66)$$

$\mathbf{K} \in \mathbb{R}^{m \times n}$ in (4.66) is called disturbance rejection control parameter and it is obtained under the condition that $\mathbf{A}_K := \mathbf{A} + \mathbf{B}\mathbf{K}$ is Hurwitz.

In [126], the relationship between systems (4.62) and (4.64) is given. It is proposed, if the set Ω is robust positively invariant for the system $\mathbf{x}^+ = \mathbf{A}_K\mathbf{x} + \mathbf{w}$ with $\mathbf{x} \in \bar{\mathbf{x}} \oplus \Omega$, $\mathbf{u} = \bar{\mathbf{u}} + \mathbf{K}(\mathbf{x} - \bar{\mathbf{x}})$, then $\mathbf{x}^+ \in \bar{\mathbf{x}}^+ \oplus \Omega$ for any admissible disturbance $\mathbf{w} \in \mathbb{W}$, where $\bar{\mathbf{x}}^+$, $\bar{\mathbf{x}}^+$ satisfy the formulation of systems (4.62) and (4.64), respectively. This proposition indicates that the control law (4.66) keeps the state of the real system \mathbf{x}^+ close to the state of the nominal system $\bar{\mathbf{x}}^+$. In other words, for any admissible disturbance $\mathbf{w} \in \mathbb{W}$, if $\mathbf{x}_0 \in \bar{\mathbf{x}}_0 \oplus \Omega$, then $\mathbf{x}_i \in \bar{\mathbf{x}}_i \oplus \Omega$, where \mathbf{x}_0 and $\bar{\mathbf{x}}_0$ are initial states of the real and the nominal systems, while \mathbf{x}_i and $\bar{\mathbf{x}}_i$ are the states of (4.62) and (4.64) at time instant i , respectively. Therefore, the system constraints of the nominal system can be tightened by

$$\bar{\mathbf{x}}_i \in \bar{\mathbb{X}} := \mathbb{X} \ominus \Omega, \quad i \in \{0, \dots, N-1\}, \quad (4.67)$$

$$\bar{\mathbf{u}}_i \in \bar{\mathbb{U}} := \mathbb{U} \ominus \mathbf{K}\Omega, \quad i \in \{0, \dots, N-1\} \text{ and} \quad (4.68)$$

$$\bar{\mathbf{x}}_N \in \bar{\mathbb{X}}_f. \quad (4.69)$$

$\bar{\mathbb{X}}_f$ denotes terminal constraint set and it ensures the stability as well as the feasibility. Furthermore, $\bar{\mathbb{X}}_f$ has to satisfy the assumptions discussed in [125] and [87]. With these tightened constraints, the optimization problem is set up as follows:

$$\min J(\bar{\mathbf{X}}, \bar{\mathbf{U}}) = \sum_{i=0}^{N-1} \{ \|\bar{\mathbf{x}}_i\|_Q^2 + \|\bar{\mathbf{u}}_i\|_R^2 \} + \|\bar{\mathbf{x}}_N\|_P^2 \quad (4.70)$$

$$\text{s.t. (4.67), (4.68), (4.69).}$$

In [126], a modified optimal control problem $\mathcal{P}_N^*(\mathbf{x})$ has been proposed, which aims to minimize $J_N^*(\mathbf{x})$ and thus it is unnecessary to keep the coincidence between initial states of the nominal system and the real system. The main difference between the conventional optimal control problem (4.70) and the modified optimal control problem (4.71) is that the latter one applies $\bar{\mathbf{x}}_0$ instead of the complete sequence of the states $\bar{\mathbf{X}}$ as a decision variable:

$$J_N^*(\mathbf{x}) = \min_{\bar{\mathbf{x}}_0, \bar{\mathbf{U}}} \{J_N(\bar{\mathbf{x}}_0, \bar{\mathbf{U}}) \mid \bar{\mathbf{U}} \in \mathcal{U}(\bar{\mathbf{x}}_0), \bar{\mathbf{x}}_0 \in \mathbf{x} \oplus (-\Omega)\}, \quad (4.71)$$

where $\bar{\mathbf{U}}$ is the control sequence containing control actions from the initial state to the current state. $\mathcal{U}(\bar{\mathbf{x}}_0)$ is the admissible nominal control set, which is depicted by

$$\mathcal{U}(\bar{\mathbf{x}}_0) := \{\bar{\mathbf{U}} \mid \bar{\mathbf{u}}_i \in \mathbb{U}, \bar{\phi}(i; \bar{\mathbf{U}}, \bar{\mathbf{x}}_0) \in \bar{\mathbb{X}}\}, \text{ for } i = 0, \dots, N-1, \bar{\phi}(N; \bar{\mathbf{U}}, \bar{\mathbf{x}}_0) \in \bar{\mathbb{X}}_f. \quad (4.72)$$

Moreover, the state feedback control law is defined by

$$\kappa^*(\mathbf{x}) := \bar{\mathbf{u}}_0^*(\mathbf{x}) + \mathbf{K}(\mathbf{x} - \bar{\mathbf{x}}_0^*(\mathbf{x})), \quad (4.73)$$

where \mathbf{x} is the current state, $\bar{\mathbf{u}}_0^*(\mathbf{x})$ and $\bar{\mathbf{x}}_0^*(\mathbf{x})$ are obtained by solving the modified optimal control problem $\mathcal{P}_N^*(\mathbf{x})$ described in (4.71). Clearly, the relationship between domains of region of attraction for the real system \mathcal{X} and the nominal system $\bar{\mathcal{X}}$ satisfies $\mathcal{X} = \bar{\mathcal{X}} \oplus \Omega$.

Figure 4.6 illustrates the tube of the state trajectory. The dotted line represents the trajectory of the nominal system, whereas the gray line describes the real states trajectory. Because of the disturbance sequence \mathbf{w} , system states trajectory \mathbf{x} stays inside of the sets sequence $\{\Omega(0), \Omega(1), \dots\}$, where $\Omega(i) = \bar{\mathbf{x}}_0^*(\mathbf{x}_i) \oplus \Omega$, which builds the tube around the nominal state trajectory as shown in the figure, and it ensures the feasibility and accuracy of the objective system.

The parameter determination of tube-based RMPC consists of several elements. Among of them, calculating the terminal set $\bar{\mathbb{X}}_f$, choosing the disturbance rejection

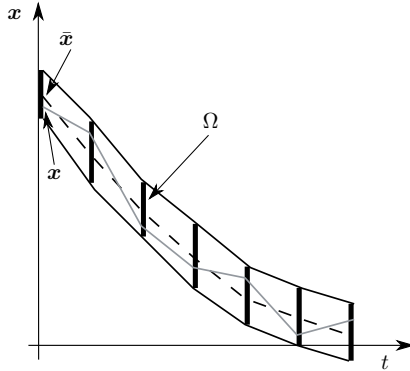


Figure 4.6: Illustration of principle of tube-based RMPC.

control parameter \mathbf{K} and computing the approximated minimal Robust Positively Invariant (mRPI) set of Ω are the most important issues. To calculate these control parameters, it is assumed that the other control parameters, such as weighting matrices, are predefined. In the following, fundamental theories and algorithms are given, according to which these parameters are obtained.

Calculation of the terminal set $\bar{\mathbb{X}}_f$

The terminal set $\bar{\mathbb{X}}_f$ should satisfy the following axiom [125]:

$$\begin{aligned} \mathbf{A}_K \bar{\mathbb{X}}_f &\subset \bar{\mathbb{X}}_f, \\ \bar{\mathbb{X}}_f &\subset \mathbb{X} \ominus \Omega, \\ \mathbf{K} \bar{\mathbb{X}}_f &\subset \mathbb{U} \ominus \mathbf{K} \Omega. \end{aligned} \quad (4.74)$$

Meanwhile, the terminal constraint set $\bar{\mathbb{X}}_f$ is a constraint admissible positively invariant set under the control law $\kappa(\bar{\mathbf{x}}) = \mathbf{K}_{\text{LQR}} \bar{\mathbf{x}}$, where \mathbf{K}_{LQR} is the gain of a linear quadratic regulator (LQR) without considering constraints. Therefore, the system (4.64) can be written as

$$\bar{\mathbf{x}}^+ = \mathbf{A}_{\text{LQR}} \bar{\mathbf{x}}, \quad (4.75)$$

where $\mathbf{A}_{\text{LQR}} := \mathbf{A} + \mathbf{B} \mathbf{K}_{\text{LQR}}$ represents the state matrix of the nominal system controlled by the unconstrained optimal infinite horizon controller \mathbf{K}_{LQR} . Besides, the nominal system is completed with the constraints stated in (4.67) and (4.68), i.e.

$$\begin{aligned} \bar{\mathbf{x}} \in \bar{\mathbb{X}} &= \mathbb{X} \ominus \Omega \\ \mathbf{K}_{\text{LQR}} \bar{\mathbf{x}} \in \bar{\mathbb{U}} &= \mathbb{U} \ominus \mathbf{K} \Omega. \end{aligned} \quad (4.76)$$

To procure a sufficiently large region, the terminal set $\bar{\mathbb{X}}_f$ should be determined by the maximal Robust Positively Invariant set (MRPI). The MRPI Ω_∞ is mathematically defined by

$$\Omega_\infty(\mathbf{A}_{\text{LQR}}, \mathbf{K}_{\text{LQR}}, \bar{\mathbb{X}}, \bar{\mathbb{U}}) := \{\mathbf{x} \in \mathbb{R}^n \mid \mathbf{A}_{\text{LQR}}^i \mathbf{x} \in \bar{\mathbb{X}}, \mathbf{K}_{\text{LQR}} \mathbf{A}_{\text{LQR}}^i \mathbf{x} \in \bar{\mathbb{U}}, \forall i \geq 0\}. \quad (4.77)$$

Before the MRPI is calculated, the predecessor set $\mathbb{P}(\Omega)$ for a set Ω has first to be defined, which is given in [25] by

$$\mathbb{P}(\Omega) := \{\mathbf{x} \in \bar{\mathbb{X}} \mid \mathbf{A}_{\text{LQR}} \mathbf{x} \in \Omega, \mathbf{K}_{\text{LQR}} \mathbf{A}_{\text{LQR}} \mathbf{x} \in \bar{\mathbb{U}}\}. \quad (4.78)$$

Furthermore, the target set Ω , tightened state constraint set $\bar{\mathbb{X}}$ and tightened input constraint set $\bar{\mathbb{U}}$ can be transformed into a H-polyhedral representation by

$$\begin{aligned} \Omega &= \{\mathbf{x} \in \mathbb{R}^n \mid \mathbf{H}_\Omega \mathbf{x} \leq k_\Omega\}, \\ \bar{\mathbb{X}} &= \{\mathbf{x} \in \mathbb{R}^n \mid \mathbf{H}_x \mathbf{x} \leq k_x\} \text{ and} \\ \bar{\mathbb{U}} &= \{\mathbf{u} \in \mathbb{R}^m \mid \mathbf{H}_u \mathbf{u} \leq k_u\}. \end{aligned} \quad (4.79)$$

Considering the definition of predecessor of a set Ω in (4.78), $\mathbb{P}(\Omega)$ can be naturally represented in H-polyhedron by

$$\mathbb{P}(\Omega) = \left\{ \mathbf{x} \in \mathbb{R}^n \mid \begin{bmatrix} \mathbf{H}_\Omega \mathbf{A}_{\text{LQR}} \\ \mathbf{H}_x \\ \mathbf{H}_u \mathbf{K}_{\text{LQR}} \end{bmatrix} \mathbf{x} \leq \begin{bmatrix} k_\Omega \\ k_x \\ k_u \end{bmatrix} \right\} \quad (4.80)$$

as well. However, the predecessor representation in (4.80) may contain redundant inequalities, which have to be discarded. Otherwise, the computational complexity becomes extremely high, or demands significant computational effort. Computing the minimum representation of a polyhedron \mathcal{P} means solving a LP for all half-spaces, which defines its non-minimal representation [25]. The algorithm to compute the MRPI set Ω_∞ is proposed in [71] and applied in [97]:

Algorithm 2 Computation of MRPI set Ω_∞

- 1: set $i = 0$
 - 2: set $\Omega_0 = \bar{\mathbb{X}}$
 - 3: let the intersection of set $\mathbb{P}(\Omega)$ and set Ω_0 be Ω_1
 - 4: **while** $\Omega_{i+1} \neq \Omega_i$ **do**
 - 5: $i = i + 1$
 $\Omega_{i+1} = \mathbb{P}(\Omega_i) \cap \Omega_i$
 - 6: **end while**
 - 7: **return** $\Omega_\infty = \Omega_{i+1}$
-

However, Algorithm 2 may not be terminated in finite time. In [71], several necessary conditions are stated to guarantee the finite termination of Algorithm 2, which are revisited below:

Theorem 4.4.1 (Finite determination of MRPI set [71]) *The MRPI set is finitely determined if the following assumptions hold:*

1. *System matrix \mathbf{A} is asymptotically stable.*
2. *The pair (\mathbf{A}, \mathbf{C}) is observable, i.e. the system is observable.*
3. *The output constraint set \mathbb{Y} is bounded and includes origin.*

Disturbance rejection controller

The robustness of a tube-based robust MPC is essentially based on the disturbance rejection controller \mathbf{K} , which determines the size and shape of the RPI set Ω describing the difference between the real and the nominal states. Additionally, the disturbance rejection controller is also a trade-off between disturbance rejection capability and control performance. The simplest way to obtain the disturbance rejection controller \mathbf{K} is to choose the unconstrained LQR gain \mathbf{K}_{LQR} as \mathbf{K} . However, the unconstrained LQR gain can not satisfy the requirement of \mathbf{K}

explicitly: First, the presence of an admissible RPI set Ω should be ensured. In this way, the tightened constraint sets $\bar{\mathbb{X}}$ and $\bar{\mathbb{U}}$ are not empty. Second, the size of Ω should be minimized [11]. In [8] and [11], a method to determine the disturbance rejection controller \mathbf{K} is presented, which is based on minimizing the size of a constrained admissible ellipsoidal invariant set in accordance to the closed-loop system with $\mathbf{u} = \mathbf{K}\mathbf{x}$. The ellipsoidal invariant set is defined by

$$\mathbb{E}(\mathbf{P}) := \{\mathbf{x} \in \mathbb{R}^n \mid \mathbf{x}^T \mathbf{P} \mathbf{x} \leq 1\}, \quad (4.81)$$

where \mathbf{P} is a positive definite matrix. $\mathbb{E}(\mathbf{P})$ is uniquely defined by \mathbf{P} and allows the utilization of LMI-based optimization method to find the control law. Moreover, the state constraint set \mathbb{X} and the input constraint set \mathbb{U} can be written into the normalized H-representation by

$$\begin{aligned} \mathbb{X} &= \{\mathbf{x} \in \mathbb{R}^n \mid |f_i^T \mathbf{x}| \leq 1, i = 1, \dots, L\}, \\ \mathbb{U} &= \{\mathbf{x} \in \mathbb{R}^m \mid |g_j^T \mathbf{u}| \leq 1, j = 1, \dots, J\}, \end{aligned} \quad (4.82)$$

where L and J denote the number of facets of corresponding constraint sets. To obtain the minimized ellipsoidal $\mathbb{E}(\mathbf{P})$ regarding to the control law $\mathbf{u} = \mathbf{K}\mathbf{x}$, the state constraint, input constraint, invariance constraint should be satisfied simultaneously. To satisfy the state constraint, $\mathbb{E}(\mathbf{P})$ must be fully contained in \mathbb{X} , which means

$$\max_{i=1, \dots, L} |f_i^T \mathbf{x}| \leq 1, \forall \mathbf{x} \in \mathbb{E}(\mathbf{P}). \quad (4.83)$$

Moreover, (4.83) can be represented by $f_i^T \mathbf{P}^{-1} f_i \leq 1$ [26]. By means of Schur complement, the state constraint is transformed into LMI formulation:

$$\begin{bmatrix} 1 & f_i^T \\ f_i & \mathbf{P} \end{bmatrix} \succeq 0, i = 1, \dots, L. \quad (4.84)$$

In the similar way, the input constraint can be transformed into LMI formulation as well. However, in order to guarantee a sufficiently large tightened input constraint set $\bar{\mathbb{U}}$, it is beneficial to introduce an additional relaxation parameter $\rho \in (0, 1]$, which determines the size of tightened constraint set. Therefore, the input constraint is reformulated by

$$|g_j^T \mathbf{K}\mathbf{x}| \leq \rho, j = 1, \dots, J, \forall \mathbf{x} \in \mathbb{E}(\mathbf{P}), \quad (4.85)$$

which can be expressed by a set of LMIs

$$\begin{bmatrix} \rho^2 & g_j^T \mathbf{K} \\ \mathbf{K}^T g_j & \mathbf{P} \end{bmatrix} \succeq 0, j = 1, \dots, J. \quad (4.86)$$

In addition to the state and input constraints, the invariance constraint should be considered because of the presence of the exogenous disturbance \mathbf{w} . The invariance constraint is presented by

$$(\mathbf{x}^+)^T \mathbf{P}(\mathbf{x}^+) \leq 1, \forall \mathbf{x} \in \mathbb{E}(\mathbf{P}), \forall \mathbf{w} \in \mathbb{W}. \quad (4.87)$$

It is given in [26], that constraint (4.87) is satisfied if there exists a parameter α fulfilling

$$\begin{aligned} \left((\mathbf{A}_K \mathbf{x} + \mathbf{w}_v)^T \mathbf{P} (\mathbf{A}_K \mathbf{x} + \mathbf{w}_v) - 1 \right) - \alpha (\mathbf{x}^T \mathbf{P} \mathbf{x} - 1) \leq 0, \\ \forall \mathbf{w}_v \in \mathbb{W}_v, \end{aligned} \quad (4.88)$$

where \mathbb{W}_v is the set of vertices in \mathbb{W} . The parameter α is the factor, which describes the contraction from $\mathbb{E}(\mathbf{P})$ to the mapped ellipsoid $\mathbb{E}(\mathbf{P})^+$. The value of α denotes the size difference between $\mathbb{E}(\mathbf{P})$ and $\mathbb{E}(\mathbf{P})^+$, i.e. large α means that $\mathbb{E}(\mathbf{P})$ and $\mathbb{E}(\mathbf{P})^+$ approach the same size. The inequality (4.88) can be rewritten into LMI by

$$\alpha \begin{bmatrix} \mathbf{P} & \mathbf{0} \\ \mathbf{0} & -\mathbf{I} \end{bmatrix} - \begin{bmatrix} \mathbf{A}_K^T \mathbf{P} \mathbf{A}_K & \mathbf{A}_K^T \mathbf{P} \mathbf{w}_v \\ \mathbf{w}_v^T \mathbf{P} \mathbf{A}_K^T & \mathbf{w}_v^T \mathbf{P} \mathbf{w}_v - \mathbf{I} \end{bmatrix} \succeq 0, \forall \mathbf{w}_v \in \mathbb{W}_v. \quad (4.89)$$

It can be reformulated by

$$\begin{bmatrix} \alpha \Delta & \mathbf{0} & \Delta^T \mathbf{A}^T + \Phi^T \mathbf{B}^T \\ \mathbf{0} & \mathbf{I} - \alpha & \mathbf{w}_v^T \\ \mathbf{A} \Delta + \mathbf{B} \Phi & \mathbf{w}_v & \Delta \end{bmatrix} \succeq 0, \forall \mathbf{w}_v \in \mathbb{W}_v, \quad (4.90)$$

where $\Delta = \mathbf{P}^{-1}$ and $\Phi = \mathbf{K} \mathbf{P}^{-1}$.

The computation of the disturbance rejection controller \mathbf{K} is represented by minimizing the associated invariant ellipsoid $\mathbb{E}(\mathbf{P})$, whose size is proportional to $\det(\mathbf{P}^{-1})$. As suggested in [8] and [11], the disturbance rejection controller can be obtained by solving the following optimization problem:

$$\begin{aligned} \min_{\Delta, \Phi, \gamma} \quad & \gamma \\ \text{s.t.} \quad & \begin{bmatrix} \gamma & f_i^T \Delta^T \\ f_i \Delta & \Delta \end{bmatrix} \succeq 0, i = 1, \dots, L \\ & \begin{bmatrix} \rho^2 & g_j^T \Phi \\ \Phi^T g_j & \Delta \end{bmatrix} \succeq 0, j = 1, \dots, J. \end{aligned} \quad (4.91)$$

To guarantee the admissibility of the solution, γ should satisfy $0 < \gamma \leq 1$. The disturbance rejection control parameter \mathbf{K} is then calculated by $\mathbf{K} = \Phi \Delta^{-1}$. Moreover, the parameter α is chosen in such a manner that $0 \leq \alpha \leq \alpha_\infty$ can be satisfied, where α_∞ is the solution of (4.89) with $\mathbf{A}_K = \mathbf{A} + \mathbf{B} \mathbf{K}_{LQR}$ and $\mathbf{P} = \mathbf{P}_{LQR}$.

Approximation of mRPI set

The explicit computation of the mRPI set \mathcal{F}_∞ is only possible if the system is nilpotent [108]. Nevertheless, several methods have been proposed to calculate the approximation of the mRPI set of Ω , such as the ones presented in [63] and in [19]. In [154], an invariant outer approximation of mRPI set algorithm is proposed, which solves the problem remained in the former works. The following assumption is given to calculate the approximation of the mRPI set:

Assumption 4.4.1 (Properties of disturbance set) *The disturbance set \mathbb{W} is convex, compact and includes origin in interior.*

Definition 4.4.1 (ε -Approximation [154]) *Given a scalar $\varepsilon > 0$ and a set $\Omega \subset \mathbb{R}^n$, the set $\Omega_\varepsilon \subset \mathbb{R}^n$ is an outer ε -approximation of set Ω if $\Omega \subset \Omega_\varepsilon \subset \Omega \oplus \varepsilon\mathbb{B}^n$ and it is an inner ε -approximation if $\Omega_\varepsilon \subset \Omega \subset \Omega_\varepsilon \oplus \varepsilon\mathbb{B}^n$, where \mathbb{B}^n denotes the unit ball in \mathbb{R}^n .*

Regarding the calculation of the set \mathcal{F}_∞ , the set \mathcal{F}_s is essential and this set is defined by

$$\mathcal{F}_s := \bigoplus_{i=0}^{s-1} \mathbf{A}^i \mathbb{W}, \quad \mathcal{F}_0 := \{0\}. \quad (4.92)$$

Moreover, \mathcal{F}_s is convex and compact if \mathbb{W} is convex and compact. As suggested in [99], the accurate mRPI set \mathcal{F}_∞ is defined by

$$\mathcal{F}_\infty := \bigoplus_{i=0}^{\infty} \mathbf{A}^i \mathbb{W}. \quad (4.93)$$

Furthermore, it is proposed in [14], that \mathcal{F}_∞ exists and is unique over the class of the closed RPI sets. However, it is not sufficient to apply (4.93) to compute the mRPI set. In [101], a plausible method is proposed to obtain an invariant outer approximation of \mathcal{F}_∞ .

Theorem 4.4.2 (Relationship between \mathcal{F}_∞ and \mathcal{F}_s [99]) *If \mathbf{A} is Hurwitz, then there exists a compact set $\mathcal{F}_\infty \subset \mathbb{R}^n$ with following properties:*

1. *Origin is contained in the set \mathcal{F}_s in its interior. Besides, $\mathcal{F}_s \subset \mathcal{F}_\infty, \forall s \in \mathbb{N}^+$.*
2. *\mathcal{F}_s approaches to \mathcal{F}_∞ if s approaches to ∞ , i.e. for any $\varepsilon > 0$ there exists $s \in \mathbb{N}^+$ that $\mathcal{F}_\infty \subset \mathcal{F}_s \oplus \varepsilon\mathbb{B}^n$.*
3. *\mathcal{F}_∞ is robust positively invariant.*

Theorem 4.4.3 [101] *If the system matrix \mathbf{A} is Hurwitz and \mathbb{W} contains origin in its interior, then there exists a finite integer $s \in \mathbb{N}^+$ and an associated scalar $\alpha \in (0, 1]$ satisfying*

$$\mathbf{A}^s \mathbb{W} \subset \alpha \mathbb{W}. \quad (4.94)$$

The scaled set $\mathcal{F}(\alpha, s)$ is a RPI set and outer approximation of the mRPI set \mathcal{F}_∞ and defined by

$$\mathcal{F}(\alpha, s) := (1 - \alpha)^{-1} \mathcal{F}_s, \quad (4.95)$$

where (α, s) satisfies (4.94).

In order to approach the outer approximation set $\mathcal{F}(\alpha, s)$ to the accurate mRPI set \mathcal{F}_∞ , s is chosen sufficiently large or α is selected sufficiently small. The smallest values of α and s are defined by

$$\alpha^0(s) := \min \{ \alpha \in \mathbb{R} \mid \mathbf{A}^s \mathbb{W} \subset \alpha \mathbb{W} \} \quad (4.96a)$$

$$s^0(\alpha) := \min \{ s \in \mathbb{N}^+ \mid \mathbf{A}^s \mathbb{W} \subset \alpha \mathbb{W} \}, \quad (4.96b)$$

where $\alpha^0(\cdot)$ and $s^0(\cdot)$ satisfy (4.94), respectively. Subsequently, the support function is introduced to improve the algorithm, which is relevant in the set-based control theory.

Definition 4.4.2 (Support function [27]) *The support function of a set $\mathbb{W} \subset \mathbb{R}^n$ is defined by*

$$h_{\mathbb{W}}(\alpha) := \sup_{\mathbf{w} \in \mathbb{W}} \alpha^T \mathbf{w}. \quad (4.97)$$

Support function defines the evaluation of set \mathbb{W} with $\alpha \in \mathbb{R}^n$. If \mathbb{W} is a zonotope, i.e. the image of a cube is under an affine mapping [73], the computation of the support function is trivial. Then \mathbb{W} can be characterized by the affine mapping described by $\Phi \in \mathbb{R}^{n \times n}$ and $\mathbf{c} \in \mathbb{R}^n$ as follows

$$\mathbb{W} = \{ \Phi \mathbf{x} + \mathbf{c} \mid \|\mathbf{x}\|_\infty \leq \eta \}. \quad (4.98)$$

Substituting (4.98) in the support function (4.97), it yields

$$\begin{aligned} h_{\mathbb{W}}(\alpha) &:= \sup_{\mathbf{w} \in \mathbb{W}} \alpha^T \mathbf{w} \\ &= \max_{\|\mathbf{x}\|_\infty \leq \eta} \alpha^T \Phi \mathbf{x} + \alpha^T \mathbf{c} = \eta \|\Phi^T \alpha\|_\infty + \alpha^T \mathbf{c}. \end{aligned} \quad (4.99)$$

Besides, the disturbance set \mathbb{W} can be written into the *H-formulation* [99] by

$$\mathbb{W} = \{ \mathbf{w} \in \mathbb{R}^n \mid \mathbf{H}_w \mathbf{w} \leq k_w \}. \quad (4.100)$$

Moreover, the equation (4.94) is satisfied if and only if

$$h_{\mathbb{W}} \left((\mathbf{A}^s)^T f_i \right) \leq \alpha k_i, \quad \forall i = 1, \dots, I, \quad (4.101)$$

where $\mathbf{H}_w = [f_1, f_2, \dots, f_I]^T$ and $k_w = [k_1, k_2, \dots, k_I]^T$. Applying this definition, $\alpha^0(s)$ can be calculated by

$$\alpha^0(s) = \max_{i=1, \dots, I} \frac{h_{\mathbb{W}} \left((\mathbf{A}^s)^T f_i \right)}{k_i}. \quad (4.102)$$

However, the outer approximation \mathcal{F}_s is included in the polyhedral set $\mathcal{P} = \{ \mathbf{x} \in \mathbb{R}^n \mid \mathbf{H}_p \mathbf{x} \leq \mathbf{d}_p \}$ if and only if

$$\sum_{i=1}^{s-1} h_{\mathbb{W}} \left((\mathbf{A}^i)^T g_j \right) \leq \alpha d_j, \quad \forall j = 1, \dots, J, \quad (4.103)$$

where $\mathbf{H}_p = [g_1, \dots, g_J]^T$ and $\mathbf{d}_p = [d_1, \dots, d_J]^T$ [154]. Subsequently, $\mathcal{F}(\alpha, s)$ is the robust positively invariant *outer* ε -approximation of the mRPI set \mathcal{F}_∞ if the following condition is fulfilled:

$$\varepsilon \geq \alpha(1 - \alpha)^{-1} \max_{\mathbf{x} \in \mathcal{F}_s} \|\mathbf{x}\| = \alpha(1 - \alpha)^{-1} \min_{\gamma} \{\gamma \mid \mathcal{F}_s \subset \gamma \mathbb{B}^n\}, \quad (4.104)$$

where $\alpha \in (0, 1]$, $s \in \mathbb{N}^+$. It is sufficient to define $M(s)$ with

$$M(s) := \min_{\gamma} \{\gamma \in \mathbb{R} \mid \mathcal{F}_s \subset \gamma \mathbb{B}_\infty^n\}, \quad (4.105)$$

where \mathbb{B}_∞^n denotes the ∞ -norm unit ball in \mathbb{R}^n . $M(s)$ can be calculated by

$$M(s) = \max_{i=1, \dots, n} \left\{ \sum_{k=0}^{s-1} h_{\mathbb{W}} \left(\left(\mathbf{A}^k \right)^T \mathbf{e}_i \right), \sum_{k=0}^{s-1} h_{\mathbb{W}} \left(- \left(\mathbf{A}^k \right)^T \mathbf{e}_i \right) \right\}, \quad (4.106)$$

where \mathbf{e}_i denotes the i th basis vector in \mathbb{R}^n [154]. Then, the relationship among α , $M(s)$ and ε is given by

$$\alpha(1 - \alpha)^{-1} \mathcal{F}_s \subset \varepsilon \mathbb{B}_\infty^n \quad \text{if and only if} \quad \alpha \leq \frac{\varepsilon}{\varepsilon + M(s)}. \quad (4.107)$$

Finally, an efficient algorithm, which is proposed in [154], is given as follows:

Algorithm 3 computation of a RPI *outer* ε -approximation to the mRPI set \mathcal{F}_∞

- 1: set $s = 1$
 - 2: set $\alpha = \alpha^0(1)$
 - 3: compute $M(1)$
 - 4: **while** $\alpha > \frac{\varepsilon}{\varepsilon + M(s)}$ **do**
 - 5: $s = s + 1$
 - 6: $\alpha = \alpha^0(s)$
 - 7: compute $M(s)$
 - 6: **end while**
 - 7: **return** $\Omega_\infty = \Omega_{i+1}$
-

4.5 Summary

In this chapter, the theoretical backgrounds of the MPC approaches applied in the present work are introduced. The constrained MPC approaches with multi-parametric Quadratic Programming (mp-QP) deal with the optimization problems with incorporated system constraints. The min-max control and tube MPC approaches are used to handle the system with parameter variation. In the next chapter, these approaches are adapted to the control system of the IM and validated on the test bench.

5 Robust current control in induction machines

In the present work, a three-phase squirrel-cage IM driven by a two-level voltage source inverter (VSI) is applied as traction system for the high-performance torque vectoring control. Based on the principles of MPC introduced in chapter 4, the control strategies and synthesis for the electric drivetrain is discussed in this chapter. The system modeling and relevant issues, which are critical to control design, are given in section 5.1. In section 5.2, the classic current control approach for IM is introduced and compared to the proposed approaches. In section 5.3, the proposed control approaches are discussed in details. In section 5.4, a novel concept is given, according to which the constraints of IM can be handled in a convenient way. Based on these approaches, the simulation and experimental results are presented in section 5.6.

5.1 Dynamic modeling of electric drive system

In order to define the optimization problem for the control design, the physical system is first described by a model. In the present work, for the purpose of a robust current control, the fundamental wave model of the IM is applied.

5.1.1 Modeling of induction machines

For simplified IM modeling, it is a common practice to transform all variables in the three-phase system into an orthogonal two-axis reference frame. The most frequently used methods are Clarke-transformation and Park-transformation. Clarke-transformation aims to translate a three-phase system in a stationary orthogonal two-axis frame, which is formulated by:

$$\begin{bmatrix} x_\alpha \\ x_\beta \end{bmatrix} = \sqrt{\frac{2}{3}} \begin{bmatrix} 1 & -\frac{1}{2} & -\frac{1}{2} \\ 0 & \frac{\sqrt{3}}{2} & -\frac{\sqrt{3}}{2} \end{bmatrix} \begin{bmatrix} x_a \\ x_b \\ x_c \end{bmatrix}, \quad (5.1)$$

where x_a, x_b, x_c denote the electrical or magnetic variables in the three-phase system, e.g. current, voltage as well as flux linkage. Here, only the simplified Clarke-transformation is introduced and the system being transformed is a balance (symmetrical) system. Moreover, all the transformations are based on the power invariant principle in the present work. The inverse Clarke-transformation is given by

$$\begin{bmatrix} x_a \\ x_b \\ x_c \end{bmatrix} = \sqrt{\frac{2}{3}} \begin{bmatrix} 1 & 0 \\ -\frac{1}{2} & \frac{\sqrt{3}}{2} \\ -\frac{1}{2} & -\frac{\sqrt{3}}{2} \end{bmatrix} \begin{bmatrix} x_\alpha \\ x_\beta \end{bmatrix}. \quad (5.2)$$

Park-transformation transfers the three-phase sinusoidal variables of IM into arbitrary rotating two-axis variables with the help of a rotating speed defined by the reference frame. Besides, Park-transformation is also called dq-transformation, which denotes the fundamental goal of this transformation. The currents in the d- and q-axis are referred to as flux-generating and torque-generating currents, respectively. The mathematical formulation of Park-transformation is shown as follows:

$$\begin{bmatrix} x_d \\ x_q \end{bmatrix} = \sqrt{\frac{2}{3}} \begin{bmatrix} \cos(\theta) & \cos(\theta - \frac{2\pi}{3}) & \cos(\theta + \frac{2\pi}{3}) \\ -\sin(\theta) & -\sin(\theta - \frac{2\pi}{3}) & -\sin(\theta + \frac{2\pi}{3}) \end{bmatrix} \begin{bmatrix} x_a \\ x_b \\ x_c \end{bmatrix}. \quad (5.3)$$

In analogy, the inverse of Park-transformation is

$$\begin{bmatrix} x_a \\ x_b \\ x_c \end{bmatrix} = \sqrt{\frac{2}{3}} \begin{bmatrix} \cos(\theta) & -\sin(\theta) \\ \cos(\theta - \frac{2\pi}{3}) & -\sin(\theta - \frac{2\pi}{3}) \\ \cos(\theta + \frac{2\pi}{3}) & -\sin(\theta + \frac{2\pi}{3}) \end{bmatrix} \begin{bmatrix} x_d \\ x_q \end{bmatrix}. \quad (5.4)$$

Here θ is the position angle of the reference frame related to the α -axis, which is defined by:

$$\theta = \omega_k t + \theta_0, \quad (5.5)$$

where θ_0 can be chosen freely. In order to assign the q-axis corresponding to the real axis and d-axis to the negative imaginary axis, we choose θ_0 as $-\frac{\pi}{2}$. ω_k is the rotational angular speed of arbitrary coordinate system, which is usually defined in the following four ways:

1. $\omega_k = 0$: inactive coordinate system, i.e. the coordinate system is aligned to the stator;
2. $\omega_k = \omega_r$: coordinate system rotating with rotor speed;
3. $\omega_k = \omega_s$: coordinate system rotating with synchronous speed;
4. $\omega_k = \omega_{\mu}$: coordinate system rotating with rotor flux linkage.

The dq-reference frame can be either rotational with an arbitrary speed or stationary with respect to the three-phase system. The detailed rotational frame theory can be found in [104, 147].

Based on the aforementioned theories, the differential voltage equations of induction motor in d-q axis are presented in Laplace domain as [103]:

$$\begin{bmatrix} u_{sq} \\ u_{sd} \\ u'_{rq} \\ u'_{rd} \end{bmatrix} = \begin{bmatrix} (R_s + sL_s) & \omega L_s & sL_m & \omega L_m \\ -\omega L_s & (R_s + sL_s) & \omega L_m & sL_m \\ sL_m & (\omega - \omega_r) L_m & (R'_r + sL'_r) & (\omega - \omega_r) L'_r \\ -(\omega - \omega_r) L_m & sL_m & -(\omega - \omega_r) L'_r & (R'_r + sL'_r) \end{bmatrix} \begin{bmatrix} i_{sq} \\ i_{sd} \\ i'_{rq} \\ i'_{rd} \end{bmatrix}, \quad (5.6a)$$

where

$$L_s = L_{s\sigma} + L_m, \quad (5.6b)$$

$$L'_r = L'_{r\sigma} + L_m. \quad (5.6c)$$

Subscripts r and s denote the parameters of rotor and stator respectively. L_m is the mutual inductance. $L_{s\sigma}$ and $L'_{r\sigma}$ represent the leakage flux of stator and rotor respectively. The rotor values are referred to the stator side and identified by the apostrophe symbol. The aforementioned four different coordinate systems are chosen according to various control objectives of IM [117, 174]. To simplify the description, the reference frame for system modeling is chosen to be aligned with the rotor speed in electrical degrees ω_r . Besides, because the applied IM is a squirrel-cage motor, the rotor voltages u'_{rd} and u'_{rq} are both zero. Taking these conditions into account, the model of the IM can be reformulated as:

$$\begin{bmatrix} u_{sq} \\ u_{sd} \\ 0 \\ 0 \end{bmatrix} = \begin{bmatrix} (R_s + sL_s) & \omega L_s & sL_m & \omega L_m \\ -\omega L_s & (R_s + sL_s) & \omega L_m & sL_m \\ sL_m & 0 & (R'_r + sL'_r) & 0 \\ 0 & sL_m & 0 & (R'_r + sL'_r) \end{bmatrix} \begin{bmatrix} i_{sq} \\ i_{sd} \\ i'_{rq} \\ i'_{rd} \end{bmatrix}. \quad (5.7)$$

Different to the machine modeling, for the purpose of control, the rotor flux oriented reference frame is chosen in the control design. Based on this reference frame, (5.7) is reformulated by

$$\begin{aligned} u_{sd} &= R_s i_{sd} + \sigma L_s \frac{di_{sd}}{dt} + (1 - \sigma) L_s \frac{di_\mu}{dt} - \omega_\mu \sigma L_s i_{sq} \\ u_{sq} &= R_s i_{sq} + \sigma L_s \frac{di_{sq}}{dt} + (1 - \sigma) L_s \omega_\mu i_\mu + \omega_\mu \sigma L_s i_{sd}, \end{aligned} \quad (5.8)$$

where σ denotes the leakage factor, and i_μ the magnetizing current for the mutual flux linkage generation. i_μ has the following relationship to the stator current in the d-axis:

$$i_\mu + \tau_r \frac{di_\mu}{dt} = i_{sd}, \quad (5.9)$$

where τ_r represents the rotor time constant with $\tau_r = \frac{L'_r}{R'_r}$. Subsequently, the electromagnetic torque in the rotor flux oriented reference frame is described by

$$T_{el} = \frac{pL_m^2}{L'_r} i_\mu i_{sq}, \quad (5.10)$$

where p is the pole pair number. Besides, the mechanical dynamic of EMs can be generally depicted by

$$J_r \frac{d}{dt} \Omega_r = T_{el} - T_{load}, \quad (5.11)$$

where Ω_r is the mechanical speed of rotor with $\Omega_r = \frac{\omega_r}{p}$. J_r is the rotor inertia and T_{load} is the load torque.

5.1.2 Uncertainties

As has been introduced, there are uncertainties in the system. These uncertainties can deteriorate the control performance and therefore should be considered in the control design. The system uncertainties in IM are represented essentially by variation of stator and rotor resistances by temperature, magnetic saturation and time delay.

Resistance variation

The operation temperature in IM changes due to the heating caused by losses [1]. Consequently, the ohmic resistance varies with the operation temperature and can be calculated by

$$R(T) = R_0 \cdot (1 + \alpha_{\text{Cu}}(T - T_0)). \quad (5.12)$$

R_0 represents the resistance at temperature T_0 , which is commonly defined at 20 °C. T is the operation temperature. α_{Cu} denotes the temperature coefficient of resistance for copper and this value is 0.393 %/K [181]. Depending on the operation condition and the insulation class of IM, the operation temperature T can reach up to 200 °C. The lowest operation temperature considered in the present work lies around -30 °C. Therefore, in the present study, the variation of ohmic resistance is defined by $R \in [0.8R_0, 2R_0]$ for the control design, which covers the entire operation temperature range of IM.

Magnetic saturation

Another type of uncertainty, which can significantly impact the control performance, is the magnetic saturation effect. It means that the magnetic permeability μ , which describes the relationship between the magnetizing field strength H and the magnetic field density B by $\mu = \frac{B}{H}$, decreases with increasing H . For more detailed information about saturation magnetization the readers are referred to [89]. In Figure 5.1 the nonlinear magnetic property is illustrated.

This figure implies that in IM, the inductance varies with the magnetizing current. For the purpose of high performance control, the relationship between mutual inductance and magnetizing current should be identified. In [137], the approach of experimental identification of the characteristic line, which is applied in the present work, is introduced. The measured characteristic line of stator inductance to magnetizing current applied in this work is given in Figure C.1. According to this characteristic line, the variation of the mutual inductance is defined by $L_m \in [0.5L_m^n, 2L_m^n]$, where L_m^n denotes the value from the data sheet.

Time delay

Time delays can lead to overshooting or even results in instability of the entire system. Particularly for high dynamic control such as MPC, time delays are

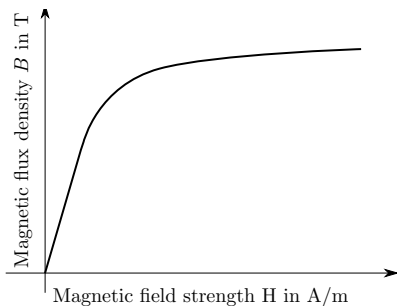


Figure 5.1: Illustration of magnetic saturation.

frequently the main cause of performance degradation and instability [88]. More informations about stability analysis of control systems with time delays are referred to [134, 50].

In electric drive systems the critical time delay is mainly the dead time due to the *Digital Signal Processor* (DSP). Essentially, DSP consists of sampling delay by *Analog-Digital* (AD) conversion, which is equal to the half of the pulse interval, and the calculation time of the DSP [136]. Therefore, the delay of SVM in a two-level VSI is calculated by

$$T_d = \frac{1}{2f_{\text{PWM}}} + T_s. \quad (5.13)$$

The sampling time of the current control loop in the present work is $T_s = 0.1$ ms and the carrier frequency of the inverter $f_{\text{PWM}} = 3200$ Hz. Consequently, the dead time of the electrical drive system $T_d = 3T_s$ is defined in this work.

5.2 Classical control approach

In industrial applications, the PI controller is widely applied for electric drive systems. Particularly, the classical FOC approach, which uses PI current controller is a standard control scheme for IM. Unlike to the system modeling, the controller is based on the reference frame aligned to the rotating rotor flux ω_μ .

Current control with PI controller

The plant for the current control in IM is described in (5.8). In order to decouple the d- and q-axis, the *Electromotive Force* (EMF) terms on both axes are compensated in such a way, that

$$\begin{aligned} u_{Rd} &= R_s i_{sd} + \sigma L_s \frac{di_{sd}}{dt} \\ u_{Rq} &= R_s i_{sq} + \sigma L_s \frac{di_{sq}}{dt}, \end{aligned} \quad (5.14)$$

with

$$\begin{aligned} u_{Rd} &= u_{sd} - (1 - \sigma)L_s \frac{di_\mu}{dt} + \omega_\mu \sigma L_s i_{sq} \\ u_{Rq} &= u_{sq} - (1 - \sigma)L_s \omega_\mu i_\mu - \omega_\mu \sigma L_s i_{sd}. \end{aligned} \quad (5.15)$$

It is evident that the current plant (5.14) with EMF-compensation in (5.14) behaves as PT₁ element and it is convenient to be handled by the PI controller. The control parameters can be tuned by means of magnitude optimum, or sometimes called modulus optimum, which is introduced in [168]. The block diagram of the current control loop on both axes are summarized in Figure 5.2.

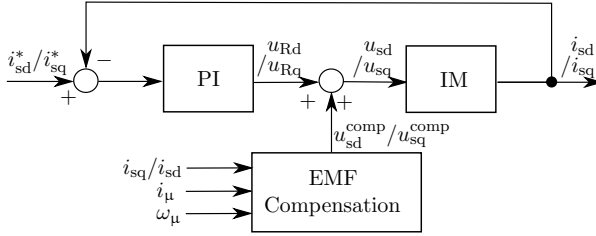


Figure 5.2: Block diagram of current control loop with PI controller.

Flux control with PI controller

The plant of the rotor flux control is depicted in (5.9). It is a typical PT₁-element similar to the d-current plant. Since the time constant of the current control loop is much smaller than the rotor time constant, the time constant of the plant can be approximately represented by τ_r . Same as the current controller, the control parameters of the flux controller are tuned by magnitude optimum. The block diagram of the flux control loop is described in Figure 5.3.

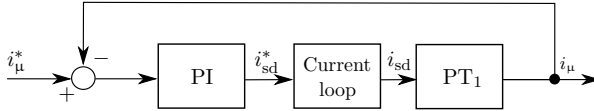


Figure 5.3: Block diagram of flux control loop with PI controller.

Rotor flux estimation

In order to compensate the EMF term described in (5.15) and to control the rotor flux as well as for Park-transformation, the magnetizing current i_μ and the rotor flux angular speed ω_μ must be known. The calculation of the magnetizing current

is based on the inverse flux model expressed in (5.9). The electric angular speed of rotor flux is derived by

$$\omega_{\mu} = \omega_r + \frac{\dot{i}_{sq}}{\tau_r i_{\mu}}. \quad (5.16)$$

Finally, the structure of the entire current and flux control in IM is summarized in Figure 5.4.

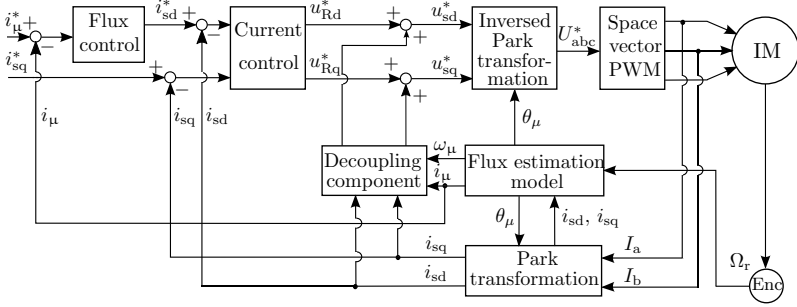


Figure 5.4: Block diagram of FOC with cascaded PI controllers.

5.3 Robust current control in consideration of parameter variation

According to the knowledge introduced in section 5.1, in order to attain a high-performance current control, the system uncertainties are not negligible. Traditionally, the system uncertainties, which can be estimated by an observer, are extended in the prediction model as disturbance in MPC. Their effects are fed back to the controller as input or output compensation. This concept was introduced in section 4.2.2. However, current overshooting can occur due to parameter mismatch, particularly the inductance mismatch caused by saturation in high current level, which makes the problem more critical. To deal with this problem, two different robust current control approaches implemented in the present work are introduced in the following.

5.3.1 Min-max current control

The first approach is to use the min-max control method introduced in section 4.4.1. We briefly recall the idea of this control method: A system with uncertainties is described as a LPV system with polytopic uncertainties, in which the extreme values of the parameters are represented by the vertices. The optimization is geared to minimizing the worst case (at the vertices) of the objective function. In such a

and the system can be then described as:

$$\begin{aligned} \mathbf{x}_{k+1} &= \mathbf{A}(\theta)\mathbf{x}_k + \mathbf{B}(\theta)\mathbf{u}_k \text{ with} \\ [\mathbf{A}(\theta) \ \mathbf{B}(\theta)] &\in \text{Co}\{[\mathbf{A}_1 \ \mathbf{B}_1], [\mathbf{A}_2 \ \mathbf{B}_2], [\mathbf{A}_3 \ \mathbf{B}_1], [\mathbf{A}_4 \ \mathbf{B}_2]\}. \end{aligned} \quad (5.18)$$

Since the introduced min-max optimization only deals with the regulation problem, which means that the system converges to the zero point in steady-state. The reference tracking problem of IM has to be reformulated, and the reformulated state space representation is given by:

$$\begin{bmatrix} \Delta \mathbf{x}_{k+1} \\ \mathbf{x}_{k+1} - \mathbf{r}_{k+1} \end{bmatrix} = \begin{bmatrix} \mathbf{A}(\theta) & \mathbf{0} \\ \mathbf{A}(\theta) & \mathbf{I} \end{bmatrix} \begin{bmatrix} \Delta \mathbf{x}_k \\ \mathbf{x}_k - \mathbf{r}_k \end{bmatrix} + \begin{bmatrix} \mathbf{B}(\theta) \\ \mathbf{B}(\theta) \end{bmatrix} \Delta \mathbf{u}_k, \quad (5.19)$$

where \mathbf{r} represents the reference value and it is considered as constant within the prediction horizon, $\Delta \mathbf{x}_k = \mathbf{x}_k - \mathbf{x}_{k-1}$. Therefore, the min-max optimization problem of current control for the system (5.19) can be set up according to (4.60).

It is important to note that, to obtain the control laws, a set of SemiDefinite Programming (SDP) problems as well as Linear Programming (LP) problems have to be solved at each time instant, which cannot meet the real-time requirement of current control in IM and therefore can not be applied directly. To tackle this problem, the expensive computational efforts are moved to an off-line process by the following approach.

Explicit min-max MPC using approximated multi-parametric SDP

In [15], an off-line solution of min-max constrained optimization problem in the case of L_1 - and L_∞ -norms by using multi-parametric Linear Programming (mp-LP) is proposed. In [186] and [187], the concept of asymptotically invariant ellipsoids describing the time-varying terminal constraint set was introduced. A sequence of explicit control laws corresponding to these ellipsoids is constructed off-line by solving SDP. Based on the current state, the ellipsoid and the control law are searched on-line. To simultaneously improve the feasibility and optimality of the min-max controller, the control law of the large ellipsoid is obtained in a backward manner with the knowledge of the control laws associated with included ellipsoids [48]. In [13] and [145], further performance improvement of the invariant ellipsoid-based off-line min-max control is given.

Instead of solving SDP off-line based on the invariant ellipsoids, the original optimization problem can be formulated as multi-parametric or rather as approximated multi-parametric SemiDefinite Programming (mp-SDP). [75] gives a solution of the mp-SDP. However, the finite termination property cannot be guaranteed by mp-SDP due to the variation of the optimal solution of a SDP problem according to the parameter vector [42]. Therefore, in [17] and [142], algorithms based on approximated mp-SDP are introduced. Instead of ellipsoids, the state-space is partitioned into triangle regions. The binary search tree algorithm is used for such approaches. To improve the on-line search efficiency, the orthogonal

search tree is applied in [90] for multi-parametric Quadratic Programming (mp-QP) by substituting the triangle regions with quadratic ones. The similar idea using k-d tree is adopted to solve approximated mp-SDP in [40] and [41]. In [83], the quad-tree search algorithm for approximated mp-SDP is implemented and presented.

A standard mp-SDP problem is formulated as follows:

$$\begin{aligned} \min_{\mathbf{z}} J(\mathbf{z}, \mathbf{x}) \\ \text{s.t. } F(\mathbf{z}, \mathbf{x}) \geq 0, \end{aligned} \quad (5.20)$$

where \mathbf{z} denotes the new variable for the optimization problem to be solved and \mathbf{x} the state variable. Either the upper bounds of the cost functions or the actuating variable can be approximated for the application of the off-line optimization. In the present work, the actuating variable approximation is determined and therefore $\mathbf{z}(\mathbf{x}) = \mathbf{u}_k$.

The basic idea of approximated mp-SDP is to construct a piecewise affine function of \mathbf{z} according to the state space vector parameters. The state space is partitioned into several regions, in each region a control law in linear form is applied. The regions are defined as quadrat in this work and expressed as follows:

$$\begin{aligned} \mathcal{B}_r &= \{\mathbf{x} \in \mathbb{R}^n : \mathbf{H}_r \mathbf{x} \leq \mathbf{d}_r\} \\ \mathbf{H}_r &= \begin{bmatrix} \mathbf{I} \\ -\mathbf{I} \end{bmatrix}, \mathbf{d}_r = \begin{bmatrix} h_u \\ -h_l \end{bmatrix}, \forall r \in \mathbb{I}. \end{aligned} \quad (5.21)$$

\mathcal{B}_r describes the unique quadrat, $\mathbf{I} \in \mathbb{R}^{n \times n}$ is the unit matrix, h_u and h_l are the upper and lower limits, \mathbb{I} is the index set of the quadrats.

Since it is impossible to find the optimal solution for each point in the quadrat, the approximated solution is targeted, and this value can be calculated by choosing several sample points. In order to obtain the approximated linear solution (control law) in each quadrat, which is represented by

$$\hat{\mathbf{z}}(\mathbf{x}) = \hat{\mathbf{K}}_r \mathbf{x} + \hat{\mathbf{g}}_r, \forall \mathbf{x} \in \mathcal{B}, \quad (5.22)$$

the vertices of the quadrat $\mathbf{V} = \{v_1, v_2, \dots, v_M\}$ are employed as sample points with $M = 2^n$. For each vertex v_i of the quadrat, the SDP problem (4.49) is solved to obtain the optimal solution $\mathbf{z}^*(v_i)$. Based on the optimal solutions at the vertices, the suboptimal solution (5.22) can be obtained by minimizing the following optimization problem

$$\begin{aligned} \min_{\hat{\mathbf{K}}_r, \hat{\mathbf{g}}_r} \sum_{i=1}^M (\mathbf{z}^*(v_i) - (\hat{\mathbf{K}}_r v_i + \hat{\mathbf{g}}_r))^T \mathbf{H}_1 (\mathbf{z}^*(v_i) - (\hat{\mathbf{K}}_r v_i + \hat{\mathbf{g}}_r)) \\ \text{s.t. } \mathbf{F}((\hat{\mathbf{K}}_r v_i + \hat{\mathbf{g}}_r), v_i) \geq 0, i \in \{1, \dots, M\}, \end{aligned} \quad (5.23)$$

where $H_1 \succ 0$ denotes the weighting matrix for the optimization.

In order to check the accuracy of the approximated solutions, some points are selected as sample. Typically, the vertices, the middle points of the edges and

the middle point of the quadrat are used. They are called the face points. The approximation error of each face point is given by the L_2 -norm of the solution deviation defined by

$$\epsilon_z(\mathbf{x}) = \|\mathbf{z}^*(\mathbf{x}) - \hat{\mathbf{z}}(\mathbf{x})\|_{H_2}^2, \quad \forall \mathbf{x} \in \mathcal{B}, \quad (5.24)$$

where $H_2 \succ 0$ describes the weighting factor of the error. The maximum error of the face points represents the approximation error of the quadrat

$$\hat{\epsilon}_z = \max_{\mathbf{x} \in \mathbb{X}^d} \epsilon_z(\mathbf{x}), \quad (5.25)$$

where \mathbb{X}^d represents the set of the face points. This approximation error should not exceed the error tolerance named absolute error and denoted by ϵ_a . This absolute error, which is normally very small, is defined to guarantee the quantitative accuracy of the suboptimal solutions. However, in certain critical regions, it is unnecessary to achieve such a high accuracy. To reduce the computational effort, a relative error is introduced as follows:

$$\epsilon_z^r(\mathbf{x}) = \frac{\epsilon_z(\mathbf{x})}{\|\mathbf{z}^*(\mathbf{x})\|_{H_2}^2}. \quad (5.26)$$

The relative error of the quadrat is the maximum error of the face points:

$$\hat{\epsilon}_z^r = \max_{\mathbf{x} \in \mathbb{X}^d} \epsilon_z^r(\mathbf{x}) \leq \frac{\hat{\epsilon}_z}{\min_{\mathbf{x} \in \mathbb{X}^d} \|\mathbf{z}^*(\mathbf{x})\|_{H_2}^2}. \quad (5.27)$$

Therefore, the final error tolerance is described by the maximum of the absolute error and the upper bound of the relative error related to the absolute value:

$$\epsilon_t = \max \left(\epsilon_a, \epsilon_r \cdot \min_{\mathbf{x} \in \mathbb{X}^d} \|\mathbf{z}^*(\mathbf{x})\|_{H_2}^2 \right), \quad (5.28)$$

where ϵ_r defines the tolerance of the relative error. If the approximation error exceeds the error tolerance, the quadrat is partitioned into sub-quadrats, and the entire process is repeated, until the approximation error is reduced to a value lower than the tolerance.

To diminish the impact of disturbances such as measurement noise, a minimum quadrat should be defined with the size S_{\min} . In this quadrat, the system is able to converge to the origin point in spite of disturbance. In order to ensure the system stability, a terminal set \mathcal{E}_0 encompassing the origin is proposed in [186], in which the standard mp-SDP problem is solved instead. This mp-SDP problem is formulated as follows [42]:

$$\begin{aligned} & \min_{\beta, \mathbf{S}, \mathbf{Y}} \beta \\ \text{s.t.} \quad & \begin{bmatrix} \mathbf{S} & (\mathbf{A}_l \mathbf{S} + \mathbf{B}_l \mathbf{Y})^T & \mathbf{S} \mathbf{Q}^{\frac{1}{2}} & \mathbf{Y}^T \mathbf{R}^{\frac{1}{2}} \\ \mathbf{A}_l \mathbf{S} + \mathbf{B}_l \mathbf{Y} & \mathbf{S} & \mathbf{0} & \mathbf{0} \\ \mathbf{Q}^{\frac{1}{2}} \mathbf{S} & \mathbf{0} & \beta \mathbf{I} & \mathbf{0} \\ \mathbf{R}^{\frac{1}{2}} \mathbf{Y} & \mathbf{0} & \mathbf{0} & \beta \mathbf{I} \end{bmatrix} \geq 0, \quad \mathbf{S} \geq \delta \mathbf{I}, \quad l = 1, \dots, L, \end{aligned} \quad (5.29)$$

where δ and β are nonnegative scalar quantities. By solving (5.29) the feedback matrix $\mathbf{F} = \mathbf{Y}\mathbf{S}^{-1}$ ensures the system stability for any state inside the terminal set $\mathbf{x}_k \in \mathcal{E}_0$. On the one hand, the parameter δ should be set to a large value to ensure the feasibility. On the other hand, it should be not too large to influence the accuracy. In [42], the rule is given by defining the value as twice of the size of the minimum quadrat: $\delta = 2\Delta\mathbf{x}_{\min}$.

The off-line optimization process is summarized in Algorithm 4, whereas a user defined initial box of parameter $\mathcal{B} \subset \mathbb{R}^n$ with vertices $\{v_1, v_2, \dots, v_M\}$ is introduced. It is an artificial bound of the state space in consideration of the state constraints.

In the present work, the optimization problems are solved by invoking the Multi-Parametric Toolbox (MPT) [82] and optimization toolbox YALMIP [120]. As a result of the off-line optimization, the state-space is partitioned into a set of regions, which can be structured in the form of a quad tree.

In the following, the algorithm of the on-line computation is introduced. For this purpose, a simple example is given in Figure 5.6.

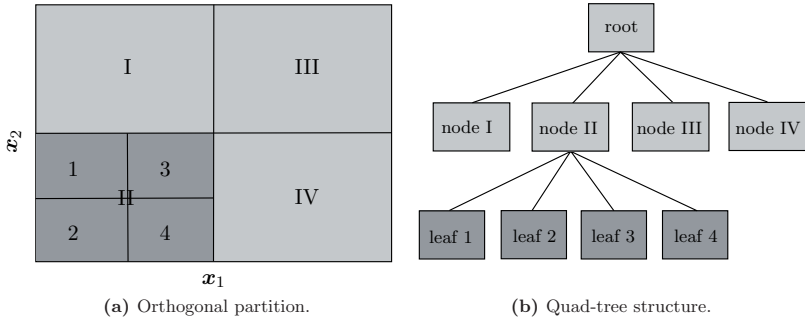


Figure 5.6: Orthogonal partition and quad tree search.

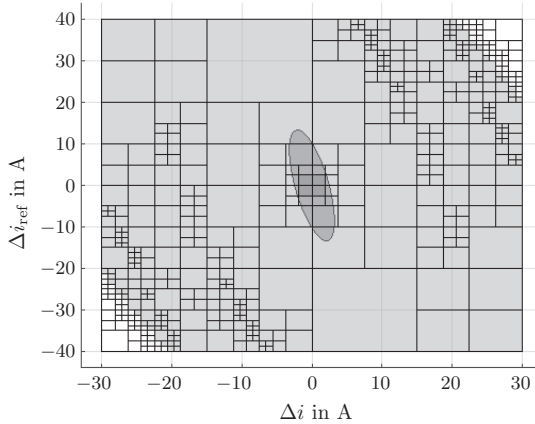
Figure 5.6 shows an example of a two-dimensional parameter vector. Following the off-line optimization procedure described in Algorithm 4, the state-space is partitioned into several critical regions as illustrated in Figure 5.6a. According to the principle of the off-line optimization, these regions are able to be structured in a quad tree as given in Figure 5.6b. The sub-quadrats included in one quadrat are considered as children of this quadrat in the tree structure. All quadrats including children are represented by the nodes in the tree. The quadrats without children are the leaves of the tree, in which the factor $\hat{\mathbf{K}}_r$ and $\hat{\mathbf{g}}_r$ of the approximated solution are stored. Therefore, the on-line computation effort is represented by identifying in which leaf the actual state is located and by specifying the appropriate control law according to the factor $\hat{\mathbf{K}}_r$, $\hat{\mathbf{g}}_r$ as well as the actual state value. The on-line computation process is described in Algorithm 5 by means of the efficient quad tree search.

Algorithm 4 Explicit min-max MPC by means of approximated mp-SDP [42]

- 1: Initialize the set of unpartitioned regions $\mathbb{Z} = \{\bar{\mathcal{B}}\}$, and the set of partitioned regions $\mathbb{P} = \{\}$.
 - 2: Select the region $\mathcal{B}_r \in \mathbb{Z}$, if $\mathbb{Z} = \emptyset$ then terminate.
 - 3: Solve the SDP problems (4.60) for each vertex v_i , $i \in [1, M]$
 - ▷ If all solutions are feasible go to step 4
 - ▷ If all solutions are infeasible go to step 2
 - ▷ Otherwise, go to step 7
 - 4: If $0 \in \mathcal{B}_r$, i.e. origin is contained in the region, solve the SDP problem (5.29) with $\delta = 2\Delta\mathbf{x}_{\min}$ in order to get the feedback matrix \mathbf{F}_0 around the origin.
 - ▷ If $\mathcal{B}_r \subset \mathcal{E}_0$ then $\mathbb{P} = \mathbb{P} \cup \mathcal{B}_r$, $\mathbb{Z} = \mathbb{Z} \setminus \mathcal{B}_r$ and go to step 2
 - ▷ Otherwise, go to step 7
 - 5: Compute the parameter $\hat{\mathbf{K}}_r$ and $\hat{\mathbf{g}}_r$ of the approximated solution (5.22) by solving the problem (5.23)
 - ▷ If no feasible solution is found, go to step 7
 - ▷ Otherwise, go to step 6
 - 6: Compute the approximation error $\hat{\epsilon}_z$ according to (5.24) and (5.25), determine the tolerance ϵ_t for \mathcal{B}_r
 - ▷ If $\hat{\epsilon}_z \leq \epsilon_t$, then $\mathbb{P} = \mathbb{P} \cup \mathcal{B}_r$, $\mathbb{Z} = \mathbb{Z} \setminus \mathcal{B}_r$ and go to step 2
 - ▷ Otherwise, go to step 7
 - 7: Compute the size of \mathcal{B}_r by multiplying the edge lengths of the quadratic region.
 - ▷ If the size is smaller than the predefined minimum quadrat size S_{\min} , then $\mathbb{P} = \mathbb{P} \cup \mathcal{B}_r$, $\mathbb{Z} = \mathbb{Z} \setminus \mathcal{B}_r$ and go to step 2
 - ▷ Otherwise, go to step 8
 - 8: Partition \mathcal{B}_r into $K = 2^n$ equal-sized sub-quadrats \mathcal{B}_i , $i \in [1, K]$. Perform $\mathbb{Z} = \mathbb{Z} \cup \{\mathcal{B}_1, \dots, \mathcal{B}_K\}$ and go to step 2
-

Algorithm 5 Orthogonal search algorithm

- 1: Measure or estimate the state \mathbf{x}_k at time instant k .
- 2: Search the quadrat including \mathbf{x}_k from the top of the tree.
 - ▷ If the quadrat is node, search the child of this node including \mathbf{x}_k , i.e. $\mathbf{H}_r - \mathbf{d}_r \leq 0$.
 - ▷ If the quadrat is not node, access the parameter $\hat{\mathbf{K}}_r$ and $\hat{\mathbf{g}}_r$, determine the control law by $\mathbf{u}_k^* = \hat{\mathbf{K}}_r \mathbf{x} + \hat{\mathbf{g}}_r$.
- 3: Apply \mathbf{u}_k^* into system.
- 4: Set $k \leftarrow k + 1$ and restart over.

**Figure 5.7:** Orthogonal partition.

The off-line optimization results of the min-max robust current control implemented in this work are presented in Figure 5.7 and Figure 5.8. Since the controllers on both axes are designed exactly in the same way, only one of the both cases is discussed in the following. The state space vector is partitioned orthogonally and illustrated in Figure 5.7. The dark gray region containing the origin represents the terminal ellipsoid calculated by the optimization. The gray regions represent the regions, in which the vector parameters are feasible. Depending on the error tolerances defined for the approximation, the regions are divided either coarse or fine. In the present work, the state space is partitioned in 416 feasible quadrats. All the regions are structured in a quadratic tree including the relationships to their super- and subregions.

In Figure 5.8a the approximated control laws are presented in the state space. It is evident that according to the vector parameters, the control laws build up a continuous piece-wise affine function. The relative error between the approximated

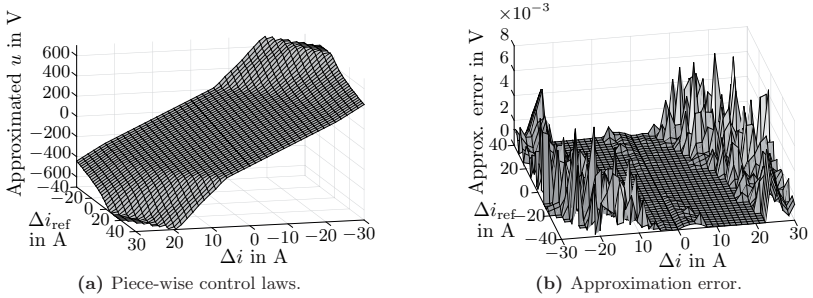


Figure 5.8: Off-line optimization result.

mp-SDP solutions and the original SDP solutions is given in Figure 5.8b. The errors due to the approximation are negligible.

Furthermore, as shown in Figure 5.5, a Kalman filter is used to reduce the impact of the measurement disturbance of stator current. With the help of KF, the edge length of the facets of the minimum quadrat $\delta = 2\Delta x_{\min}$ can be limited to a small value.

5.3.2 Tube-based robust model predictive current control

The min-max control approach incorporates the system uncertainties into the optimization problem solved by invoking a sequence of mp-SDP and mp-QP, which leads to expensive computational costs. As a drawback, the control parameters cannot be tuned conveniently: For each process of the control parameter tuning, the off-line optimization has to be performed once, which may take several hours. Therefore, the tube-based MPC is studied.

Figure 5.9 gives the structure of the entire control system. The tube-based robust current control for reference tracking, with Kalman filter, with predictor and with the reference modification is discussed in the following.

Reference tracking problem

In order to apply the tube-based MPC to the current control in IM, the standard formulation introduced in section 4.4.2 for regulation problems has to be adapted in such a way, that the reference tracking problems can be dealt with. In [9], [114], [115] and [10] an efficient method to deal with the non zero target steady state is presented. The formulation in (4.62) is extended by

$$\begin{aligned} \mathbf{x}^+ &= \mathbf{A}\mathbf{x} + \mathbf{B}\mathbf{u} + \mathbf{w} \\ \mathbf{y} &= \mathbf{C}\mathbf{x} + \mathbf{D}\mathbf{u} + \mathbf{v}, \end{aligned} \quad (5.30)$$

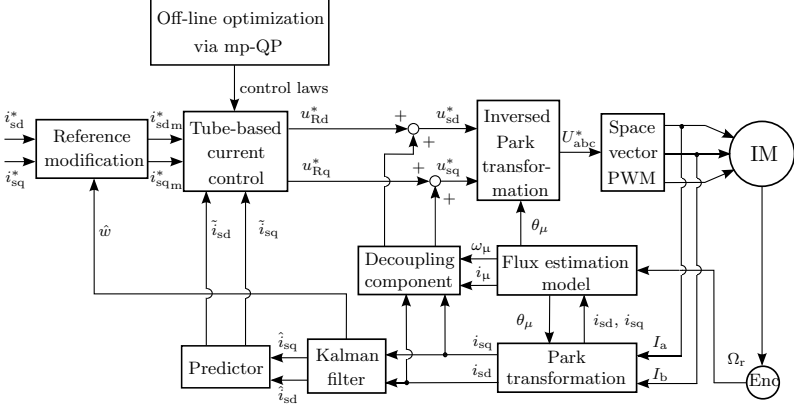


Figure 5.9: Block diagram of tube-based robust current control in IM.

where $\mathbf{y} \in \mathbb{R}^p$ and $\mathbf{v} \in \mathbb{R}^p$ are system output and unknown output disturbance, respectively. As has been discussed, the optimization problem is built and solved regarding to the nominal system. Therefore, the reference can be robustly tracked if the steady state of the nominal system is admissible. The constraints to be fulfilled are the modified constraints:

$$\bar{\mathbf{X}} = \mathbf{X} \ominus \Omega, \bar{\mathbf{U}} = \mathbf{U} \ominus \mathbf{K}\Omega. \quad (5.31)$$

In [141] a related theory is proposed to realize the offset-free steady state. The estimated steady state error is caused by the steady state disturbance and measurement noises.

Lemma 5.3.1 (Offset-free steady state [141]) *Consider a linear discrete-time system*

$$\begin{aligned} \mathbf{x}^+ &= \mathbf{A}\mathbf{x} + \mathbf{B}\mathbf{u} \\ \mathbf{y} &= \mathbf{C}\mathbf{x}, \end{aligned}$$

if and only if

$$\text{rank} \begin{bmatrix} \mathbf{I} - \mathbf{A} & -\mathbf{B} \\ \mathbf{C} & \mathbf{0} \end{bmatrix} = n + p, \quad (5.32)$$

where n and p are the dimensions of \mathbf{x} and \mathbf{y} , then there exists a steady state $(\mathbf{x}_s, \mathbf{u}_s)$ without offset for any given set point \mathbf{y}_s .

More specifically, the idea of Lemma 5.3.1 is extended for system (5.30). A given set point \mathbf{y}_s and steady state $\mathbf{s}_s := (\mathbf{x}_s, \mathbf{u}_s)$ satisfy:

$$\begin{bmatrix} \mathbf{A} - \mathbf{I} & \mathbf{B} \\ \mathbf{C} & \mathbf{D} \end{bmatrix} \begin{bmatrix} \mathbf{x}_s \\ \mathbf{u}_s \end{bmatrix} = \begin{bmatrix} \mathbf{0} \\ \mathbf{y}_s \end{bmatrix}, \quad (5.33)$$

which can be simplified into:

$$\mathbf{E}\mathbf{s}_s = \mathbf{F}\mathbf{y}_s. \quad (5.34)$$

Furthermore, for any given set point \mathbf{y}_s , there exists more than one admissible steady state \mathbf{s}_s . To characterize the set of admissible steady states, the related Lemma is introduced in [8]:

Lemma 5.3.2 *Suppose the pair (\mathbf{A}, \mathbf{B}) is stabilizable, a solution to problem (5.33) can be parameterized by:*

$$\begin{aligned} \mathbf{s}_s &= \mathbf{M}_\theta \theta, \\ \mathbf{y}_s &= \mathbf{N}_\theta \theta, \end{aligned} \quad (5.35)$$

where $\theta \in \mathbb{R}^{n_\theta}$ is a parameter vector to characterize solutions. $\mathbf{M}_\theta \in \mathbb{R}^{(n+m) \times n_\theta}$ and $\mathbf{N}_\theta \in \mathbb{R}^{p \times n_\theta}$ are suitable matrices.

Let \mathbb{X}_s denote the admissible steady state set and it is meanwhile polyhedron which is given by

$$\mathbb{X}_s := \{ \mathbf{x}_s \in \bar{\mathbb{X}} : \exists \mathbf{u}_s \in \bar{\mathbb{U}} \mid (\mathbf{A} - \mathbf{I})\mathbf{x}_s + \mathbf{B}\mathbf{u}_s = \mathbf{0} \}. \quad (5.36)$$

Lemma 5.3.3 (Uniqueness of the steady state [8]) *As it is proposed in Lemma 5.3.1, a given admissible set point \mathbf{s}_s has a unique steady state $\mathbf{s}_s = (\mathbf{x}_s, \mathbf{u}_s)$ if and only if the rank of \mathbf{E} is equal to $n + m$.*

Then for the nominal system

$$\begin{aligned} \bar{\mathbf{x}}^+ &= \mathbf{A}\bar{\mathbf{x}} + \mathbf{B}\bar{\mathbf{u}} \\ \bar{\mathbf{y}} &= \mathbf{C}\bar{\mathbf{x}} + \mathbf{D}\bar{\mathbf{u}}, \end{aligned} \quad (5.37)$$

with control law

$$\mathbf{u} = \bar{\mathbf{u}} + \mathbf{K}(\mathbf{x} - \bar{\mathbf{x}}), \quad (5.38)$$

and subjects to the constraints (5.31), there exists an admissible steady state $\mathbf{s}_s = (\mathbf{x}_s, \mathbf{u}_s)$ satisfying the tightened nominal system constraints

$$\mathbf{s}_s = (\mathbf{x}_s, \mathbf{u}_s) \in \bar{\mathbb{S}} := \bar{\mathbb{X}} \times \bar{\mathbb{U}}. \quad (5.39)$$

In order to attain an offset-free reference tracking, the essential invariant set for tracking is solved for the tube-based RMPC design, which is defined in the following.

Definition 5.3.1 (Invariant set for tracking [10]) *Let \mathbf{x}^e denote the extended state $(\mathbf{x}, \theta) \in \mathbb{R}^{n+n_\theta}$ and $\mathbf{K}_c \in \mathbb{R}^{m \times n}$ the control gain, and $\mathbf{A} + \mathbf{B}\mathbf{K}_c$ the Hurwitz. Then, a set $\Omega_t^e \subset \mathbb{R}^{n+n_\theta}$ is an admissible invariant set for tracking if for all $(\mathbf{x}, \theta) \in \Omega_t^e$, $\mathbf{x} \in \bar{\mathbb{X}}$, $\mathbf{K}_c \mathbf{x} + \mathbf{K}_\theta \theta \in \bar{\mathbb{U}}$ and $((\mathbf{A} + \mathbf{B}\mathbf{K}_c)\mathbf{x} + \mathbf{B}\mathbf{K}_\theta \theta, \theta) \in \Omega_t^e$, where $\mathbf{K}_\theta := [-\mathbf{K}_c \ \mathbf{I}] \mathbf{M}_\theta$.*

Definition 5.3.2 (Projection of a set [20]) *The projection of a set $\mathbb{A} \subset \mathbb{R}^{n+p}$ onto the x -space \mathbb{R}^n is defined as*

$$\text{Proj}_x(\mathbb{A}) := \left\{ \mathbf{x} \in \mathbb{R}^n \mid \exists \mathbf{y} \in \mathbb{R}^p \text{ such that } \begin{bmatrix} \mathbf{x} \\ \mathbf{y} \end{bmatrix} \in \mathbb{A} \right\}. \quad (5.40)$$

Definitions 5.3.1 and 5.3.2 yield that for an initial state $(\mathbf{x}_0, \theta) \in \Omega_t^e$, the state sequence of system $\mathbf{x}^+ = \mathbf{A}\mathbf{x} + \mathbf{B}\mathbf{u}$ controlled by $\mathbf{u} = \mathbf{u}_s + \mathbf{K}_c(\mathbf{x} - \mathbf{x}_s)$, where $(\mathbf{x}_s, \mathbf{u}_s) = \mathbf{M}_\theta\theta$ satisfies $\mathbf{x}_i \in \text{Proj}_x(\Omega_t^e), \forall k \geq 0$ and tends to \mathbf{x}_s . Moreover, Definition 5.3.1 consents the separation of optimal control and the robust constraint satisfaction.

According to aforementioned theories, the original optimization problem (4.70) is reformulated. The artificial steady state $\bar{\mathbf{s}}_s = (\bar{\mathbf{x}}_s, \bar{\mathbf{u}}_s)$ is considered as a decision variable of the optimization problem. This way, the artificial steady state can be represented by $\bar{\mathbf{s}}_s = \mathbf{M}_\theta\bar{\theta}$. As a consequence, the parameter $\bar{\theta}$ is incorporated as a decision variable into the optimization problem, i.e. into the objective function:

$$J_N(\mathbf{x}, \theta; \bar{\mathbf{x}}_0, \bar{\mathbf{u}}, \bar{\theta}) := \sum_{i=0}^{N-1} L(\bar{\mathbf{x}}_i, \bar{\mathbf{x}}_s, \bar{\mathbf{u}}_i, \bar{\mathbf{u}}_s) + J_f(\bar{\mathbf{x}}_N, \bar{\mathbf{x}}_s) + J_r(\bar{\theta}, \theta), \quad (5.41)$$

with the modified stage cost

$$L(\bar{\mathbf{x}}_i, \bar{\mathbf{x}}_s, \bar{\mathbf{u}}_i, \bar{\mathbf{u}}_s) := \|\bar{\mathbf{x}}_i - \bar{\mathbf{x}}_s\|_Q^2 + \|\bar{\mathbf{u}}_i - \bar{\mathbf{u}}_s\|_R^2, \quad (5.42)$$

and modified terminal cost

$$J_f(\bar{\mathbf{x}}_N, \bar{\mathbf{x}}_s) := \|\bar{\mathbf{x}}_N - \bar{\mathbf{x}}_s\|_P^2, \quad (5.43)$$

also the steady state offset cost

$$J_r(\bar{\theta}, \theta) := \|\bar{\theta} - \theta\|_T^2, \quad (5.44)$$

where \mathbf{T} is named steady state offset weighting matrix, which is positive definite. It incorporates the deviation between the artificial steady state and the given steady state into the cost function. Subsequently, the resulting optimization problem is summarized by

$$\begin{aligned} & \min_{\bar{\mathbf{x}}, \bar{\mathbf{u}}, \bar{\theta}} J_N(\mathbf{x}, \mathbf{x}_s; \bar{\mathbf{x}}, \bar{\mathbf{u}}, \bar{\theta}) \\ & \text{s.t. } \bar{\mathbf{x}} \in \mathbf{x} \oplus -\Omega \\ & \quad \bar{\mathbf{x}}_i \in \bar{\mathbb{X}} = \mathbb{X} \ominus \Omega \\ & \quad \bar{\mathbf{u}}_i \in \bar{\mathbb{U}} = \mathbb{U} \ominus \mathbf{K}\Omega \\ & \quad (\bar{\mathbf{x}}_{N_p}, \bar{\theta}) \in \Omega_t^e, \end{aligned} \quad (5.45)$$

where \mathbf{x}_s is the desired steady state and $\bar{\mathbf{u}}$ the control sequence. The solutions of the optimization problem are optimal nominal initial state $\bar{\mathbf{x}}^*(\mathbf{x}, \mathbf{x}_s)$, optimal control sequence $\bar{\mathbf{u}}^*(\mathbf{x}, \mathbf{x}_s) := \{\bar{\mathbf{u}}^*(0; \mathbf{x}, \mathbf{x}_s), \bar{\mathbf{u}}^*(1; \mathbf{x}, \mathbf{x}_s), \dots, \bar{\mathbf{u}}^*(N-1; \mathbf{x}, \mathbf{x}_s)\}$ and $\theta^*(\mathbf{x}, \mathbf{x}_s)$. The control law applied into the system is defined by

$$\kappa_N^*(\mathbf{x}, \mathbf{x}_s) := \bar{\mathbf{u}}^*(0; \mathbf{x}, \mathbf{x}_s) + \mathbf{K}(\mathbf{x} - \bar{\mathbf{x}}^*(\mathbf{x}, \mathbf{x}_s)). \quad (5.46)$$

To guarantee the robust stability and to satisfy the robust constraints of the closed-loop system, the following conditions should be fulfilled before the optimized control law is generated [8], [11]:

1. \mathbf{Q} , \mathbf{R} are positive definite.
2. There exists a constant $\sigma > 0$ such that $\sigma \mathbf{T} \geq \mathbf{M}_x^T \mathbf{M}_x$, where $\mathbf{M}_x = [\mathbf{I} \ \mathbf{0}] \mathbf{M}_\theta$.
3. The feedback control gain \mathbf{K} guarantees that the $\mathbf{A}_K = \mathbf{A} + \mathbf{B}\mathbf{K}$ is Hurwitz.
4. \mathbf{K}_c and \mathbf{P} fulfill that $\mathbf{A} + \mathbf{B}\mathbf{K}_c$ is Hurwitz, \mathbf{P} is positive definite, and $\mathbf{P} - (\mathbf{A} + \mathbf{B}\mathbf{K}_c)^T \mathbf{P} (\mathbf{A} + \mathbf{B}\mathbf{K}_c) = \mathbf{Q} + \mathbf{K}_c^T \mathbf{R} \mathbf{K}_c$.
5. The set $\Omega \subset \mathbb{X}$ is an admissible robust positively invariant set for the system $\mathbf{x}^+ = \mathbf{A}_K \mathbf{x} + \mathbf{w}$, i.e. $\mathbf{A}_K \Omega \oplus \mathbb{W} \subset \Omega$ and $\mathbf{K} \Omega \subset \mathbb{U}$.
6. The set Ω_t^e is an invariant set for tracking the nominal system subjected to tightened constraints $\bar{\mathbb{X}}$ and $\bar{\mathbb{U}}$.

Furthermore, the proposed controller asymptotically steers the system to the neighborhood of the desired state, which is testified in [9]. For further interests readers are referred to [9].

Based on these conditions, the admissible steady state $\mathbf{s}_s = (\mathbf{x}_s, \mathbf{u}_s)$ is defined. The new parameter vector $\mathbf{x}^* = [\mathbf{x} \ \mathbf{x}_s]^T$ and input vector $\mathbf{u}^* = [\mathbf{u} \ \mathbf{u}_s]^T$ are introduced for the tube-based current control. Therefore, the system matrices for the control design are defined by

$$\mathbf{A}^* = \begin{bmatrix} 1 - T_s \frac{R_s}{\sigma(1+\sigma_1)L_m} & 0 \\ 0 & 1 \end{bmatrix}; \quad \mathbf{B}^* = \begin{bmatrix} T_s \frac{1}{\sigma(1+\sigma_1)L_m} \\ 0 \end{bmatrix}. \quad (5.47)$$

However, considering the measurement noise as well as the limitation of directly measuring of the states, an observer shares great importance compared with reference tracking in the control design. Therefore, a Kalman filter is employed for the tube-based MPC such as the min-max current control. In order to apply the Kalman filter to the control approach, the following adaptation is implemented.

Tube MPC extended with observer

The observer system is formulated by:

$$\begin{aligned} \hat{\mathbf{x}}^+ &= \mathbf{A}\hat{\mathbf{x}} + \mathbf{B}\hat{\mathbf{u}} + \mathbf{K}_{\text{KF}}(\mathbf{y} - \hat{\mathbf{y}}), \\ \hat{\mathbf{y}} &= \mathbf{C}\hat{\mathbf{x}}, \end{aligned} \quad (5.48)$$

where $\hat{\mathbf{x}}^+ \in \mathbb{R}^n$, $\hat{\mathbf{x}} \in \mathbb{R}^n$ and $\hat{\mathbf{y}} \in \mathbb{R}^p$ are estimated successor state, system state and system output of observer system. To distinguish from the disturbance rejection

control parameter \mathbf{K} , the Kalman gain is denoted by \mathbf{K}_{KF} . The estimation error \mathbf{e}_e between the actual state and estimated state is defined by

$$\mathbf{e}_e := \mathbf{x} - \hat{\mathbf{x}}. \quad (5.49)$$

Besides, the estimation error satisfies

$$\mathbf{e}_e^+ = \mathbf{A}_{\text{KF}}\mathbf{e}_e + \mathbf{w}_{ee}, \quad (5.50)$$

where $\mathbf{w}_{ee} := \mathbf{w} - \mathbf{K}_{\text{KF}}\mathbf{v}$ and $\mathbf{A}_{\text{KF}} := (\mathbf{A} - \mathbf{K}_{\text{KF}}\mathbf{C})$. Here, \mathbf{w}_{ee} is bounded by the set \mathbb{W}_{ee} , which is derived and defined by

$$\mathbb{W}_{ee} := \mathbb{W} \oplus (-\mathbf{K}_{\text{KF}}\mathbb{V}). \quad (5.51)$$

Suppose that the matrix \mathbf{A}_{KF} is Hurwitz, then there exists a robust positively set Ω_{ee} for system (5.50) with

$$\mathbf{A}_{\text{KF}}\Omega_{ee} \oplus \mathbb{W}_{ee} \subset \Omega_{ee}. \quad (5.52)$$

Considering the fundamental characteristics of robust positively invariant sets, $\mathbf{x}_i \in \hat{\mathbf{x}}_i \oplus \Omega_{ee}$ for $\forall k \in \mathbb{N}$ is satisfied, if $\mathbf{e}_e(0) = \mathbf{x}_0 - \hat{\mathbf{x}}_0 \in \Omega_{ee}$ [10]. Besides, the nominal system is same as described in (4.64). Instead, the control law is defined by

$$\mathbf{u} = \bar{\mathbf{u}} + \mathbf{K}\mathbf{e}_c, \quad (5.53)$$

where \mathbf{e}_c is defined by $\mathbf{e}_c := \hat{\mathbf{x}} - \bar{\mathbf{x}}$ and it denotes the control error between the estimated and the nominal states. Similar to the estimation error, control error \mathbf{e}_c satisfies

$$\mathbf{e}_c^+ = \mathbf{A}_{\text{KF}}\mathbf{e}_c + \mathbf{w}_{ec}, \quad (5.54)$$

where $\mathbf{w}_{ec} := \mathbf{K}_{\text{KF}}\mathbf{C}\mathbf{e}_e + \mathbf{K}_{\text{KF}}\mathbf{v}$. Furthermore, \mathbf{w}_{ec} is bounded by the set \mathbb{W}_{ec} , which is defined by

$$\mathbb{W}_{ec} := \mathbf{K}_{\text{KF}}\mathbf{C}\Omega_{ee} \oplus (\mathbf{K}_{\text{KF}}\mathbb{V}). \quad (5.55)$$

Taking into account of the assumption that \mathbf{A}_{KF} is Hurwitz, there exists a robust positively invariant set Ω_{ec} , which satisfies:

$$\mathbf{A}_{\text{KF}}\Omega_{ec} \oplus \mathbb{W}_{ec} \subset \Omega_{ec}. \quad (5.56)$$

Similarly, if $\mathbf{e}_c(0) = \hat{\mathbf{x}}_0 - \bar{\mathbf{x}}_0 \in \Omega_{ec}$ and $\mathbf{e}_e(0) \in \Omega_{ee}$, then $\hat{\mathbf{x}}_i \in \bar{\mathbf{x}}_i \oplus \Omega_{ec}$ for $\forall i \in \mathbb{N}$. Moreover, $\mathbf{x}_i \in \bar{\mathbf{x}}_i \oplus \Omega$, $\forall i \in \mathbb{N}$, where $\Omega = \Omega_{ec} \oplus \Omega_{ee}$. However, the following assumptions should be satisfied to guarantee the feasibility and admissibility using the nominal system [127]:

1. There exist \mathbf{K} , \mathbf{K}_{KF} , a robust positively invariant set Ω_{ee} for system (5.50) as well as a robust positively invariant set Ω_{ec} for system (5.54), which ensures that the tightened constraint $\mathbb{X} \ominus \Omega$ and $\mathbb{U} \ominus \mathbf{K}\Omega$ are not empty.
2. The initial states of actual system \mathbf{x}_0 , observer $\hat{\mathbf{x}}_0$ and nominal system $\bar{\mathbf{x}}_0$ lie inside the state constraint set \mathbb{X} . The initial value of estimation error $\mathbf{e}_e(0)$ and control error $\mathbf{e}_c(0)$ lie in Ω_{ee} and Ω_{ec} respectively.

3. The states $\bar{\mathbf{x}}$ and control sequence $\bar{\mathbf{u}}$ satisfy the tightened state and input constraints, respectively.

Theorem 5.3.1 ([127]) *Suppose that the aforementioned assumptions hold, then the states and control input satisfy the origin constraints, i.e. $\mathbf{x}_i \in \bar{\mathbb{X}}$ and $\mathbf{u}_i = \bar{\mathbf{u}}_i + \mathbf{K}(\hat{\mathbf{x}}_i - \bar{\mathbf{x}}_i), \forall i \in \mathbb{N}$.*

Considering the error Ω_{ec} and Ω_{ee} , the optimization problem (5.45) is refined with the observer system. The optimization problem is restructured as

$$\begin{aligned} \min_{\bar{\mathbf{x}}, \bar{\mathbf{u}}, \theta} \quad & J_N(\hat{\mathbf{x}}, \mathbf{x}_s; \bar{\mathbf{x}}, \bar{\mathbf{u}}, \bar{\theta}) \\ \text{s.t.} \quad & \bar{\mathbf{x}} \in \hat{\mathbf{x}} \oplus (-\Omega_{ec}) \\ & \bar{\mathbf{x}}_i \in \bar{\mathbb{X}} = \mathbb{X} \ominus \Omega \\ & \bar{\mathbf{u}}_i \in \bar{\mathbb{U}} = \mathbb{U} \ominus \mathbf{K}\Omega \\ & (\bar{\mathbf{x}}_N, \theta) \in \Omega_t^e, \end{aligned} \quad (5.57)$$

where $\hat{\mathbf{x}}$ and \mathbf{x}_s are the output of the observer and desired steady state, respectively. $\bar{\mathbf{u}}$ is the control sequence. The solutions of the optimization problem are the optimal initial nominal state $\bar{\mathbf{x}}^*(\hat{\mathbf{x}}, \mathbf{x}_s)$, optimal control sequence $\bar{\mathbf{u}}^*(\hat{\mathbf{x}}, \mathbf{x}_s) := \{\bar{\mathbf{u}}^*(0; \hat{\mathbf{x}}, \mathbf{x}_s), \bar{\mathbf{u}}^*(1; \hat{\mathbf{x}}, \mathbf{x}_s), \dots, \bar{\mathbf{u}}^*(N-1; \hat{\mathbf{x}}, \mathbf{x}_s)\}$ and $\theta^*(\hat{\mathbf{x}}, \mathbf{x}_s)$. The control law applied to the system is specified by

$$\kappa_N^*(\hat{\mathbf{x}}, \mathbf{x}_s) := \bar{\mathbf{u}}^*(0; \hat{\mathbf{x}}, \mathbf{x}_s) + \mathbf{K}(\hat{\mathbf{x}} - \bar{\mathbf{x}}^*(\hat{\mathbf{x}}, \mathbf{x}_s)). \quad (5.58)$$

Reference modification

Since the system contains uncertainty \mathbf{w} , which tends to a steady value \mathbf{w}_∞ , tracking error can be generated. This issue should be avoided by the control design. In [9], a method of tracking error cancellation for systems with the assumption $\mathbf{D} = \mathbf{0}$ is proposed. As an extension, the corresponding steady state output \mathbf{y}_∞ in general case ($\mathbf{D} \neq \mathbf{0}$) is derived in this work and expressed by

$$\begin{aligned} \mathbf{y}_\infty = \mathbf{C}\mathbf{x}_\infty + \mathbf{D}\mathbf{u}_\infty + \mathbf{v}_\infty = & [\mathbf{I} + \mathbf{C}(\mathbf{I} - \mathbf{A}\mathbf{K})^{-1}\mathbf{K}_{KF} + \mathbf{D}\mathbf{K}(\mathbf{I} - \mathbf{A}\mathbf{K})^{-1}\mathbf{K}_{KF}] \\ & \cdot (\mathbf{C}\mathbf{e}_e(\infty) + \mathbf{v}_\infty) + \mathbf{s}, \end{aligned} \quad (5.59)$$

where $\mathbf{s} = \mathbf{C}\bar{\mathbf{x}}_\infty + \mathbf{D}\bar{\mathbf{u}}_\infty$ denotes the desired set point. Obviously, there exists an offset leading to $\mathbf{y}_\infty \neq \mathbf{s}$. For the purpose of canceling the offset to guarantee $\mathbf{y}_\infty = \mathbf{s}$, a modified reference \mathbf{s}_n is computed by

$$\mathbf{s}_n = \mathbf{s} - \mathbf{F}(\mathbf{C}\mathbf{e}_e(\infty) + \mathbf{v}_\infty), \quad (5.60)$$

where $\mathbf{F} = \mathbf{I} + \mathbf{C}(\mathbf{I} - \mathbf{A}\mathbf{K})^{-1}\mathbf{K}_{KF} + \mathbf{D}\mathbf{K}(\mathbf{I} - \mathbf{A}\mathbf{K})^{-1}\mathbf{K}_{KF}$. Moreover, the steady state value $\mathbf{C}\mathbf{e}_e(\infty) + \mathbf{v}_\infty$ can be obtained from the observer. Finally, the modified reference \mathbf{s}_n at each time instant can be computed by the following equation:

$$\mathbf{s}_n(i) = \mathbf{s} - \mathbf{F}(\mathbf{y}_i - \mathbf{C}\hat{\mathbf{x}}_i), \quad i = 0, \dots, N. \quad (5.61)$$

Predictor for dead time compensation

For high dynamic control, dead time can yield overshooting or even can result in instability. In [169] and [121], the approaches of dead-time compensation for RMPC are proposed. The principle is to use an extra system model defined as the predicted system to predict the system states and handle the dead time issue. In [162] and [161], the methods of dead time compensation for tube-based RMPC are proposed. Furthermore, the explicit dead-time compensation is described in [162], which is applied in the control design in this work.

At first, a general form of the dead time compensation method is introduced. An uncertain discrete linear system with dead time is described by

$$\begin{aligned} \mathbf{x}_{k+1} &= \mathbf{A}\mathbf{x}_k + \mathbf{B}\mathbf{u}_{k-d} + \mathbf{w}_k \\ \mathbf{y}_k &= \mathbf{C}\mathbf{x}_k, \end{aligned} \quad (5.62)$$

where \mathbf{x}_k is the state at time instant k with $k \geq d$, \mathbf{u}_{k-d} the control input with dead time d , \mathbf{w}_k the unknown but bounded disturbance and \mathbf{y}_k the current output.

Besides, the constraints are represent by polyhedrons \mathbb{X} , \mathbb{U} and \mathbb{W} as aforementioned. Due to the existing dead-time d , the control input \mathbf{u}_k affects the system state \mathbf{x}_{k+d} . A simple prediction for \mathbf{x}_{k+d} at time instant k is given by

$$\tilde{\mathbf{x}}_k := \mathbf{x}_{k+d|k} = \mathbf{A}^d \mathbf{x}_k + \sum_{l=1}^d \left[\mathbf{A}^{l-1} \mathbf{B} \mathbf{u}_{k-l} \right]. \quad (5.63)$$

Thus, the prediction system is represented by

$$\tilde{\mathbf{x}}_{k+1} = \mathbf{A}\tilde{\mathbf{x}}_k + \mathbf{B}\mathbf{u}_k. \quad (5.64)$$

Equation (5.64) denotes the nominal system without dead-time but at d steps ahead. Moreover, the disturbance should be considered in the system, and it leads to the deviation between the prediction at k_{th} step $\tilde{\mathbf{x}}_k$ and the real state appearing after d steps \mathbf{x}_{k+d} . Therefore, the dead-time compensation for systems with predicted bounded disturbance is presented by

$$\tilde{\mathbf{x}}_k = \mathbf{A}^d \mathbf{x}_k + \sum_{l=1}^d \left[\mathbf{A}^{l-1} \mathbf{B} \mathbf{u}_{k-l} \right] + \sum_{l=1}^d \mathbf{A}^{l-1} \mathbf{w}_{k+d-l}. \quad (5.65)$$

Subsequently, the complete model of the nominal system with dead time compensation and disturbance is given by

$$\tilde{\mathbf{x}}_{k+1} = \mathbf{A}\tilde{\mathbf{x}}_k + \mathbf{B}\mathbf{u}_k + \tilde{\mathbf{w}}_k, \quad (5.66)$$

where $\tilde{\mathbf{w}}_k$ is the entire disturbance of the system across d steps from time instant k and this value can be derived by substituting (5.63) into (5.66)

$$\begin{aligned} \tilde{\mathbf{w}}_k &:= \mathbf{w}_{k+d|k} \\ &= \tilde{\mathbf{x}}_{k+1} - \mathbf{A}\tilde{\mathbf{x}}_k - \mathbf{B}\mathbf{u}_k \\ &= \mathbf{A}^d (\mathbf{x}_{k+1} - \mathbf{A}\mathbf{x}_k - \mathbf{B}\mathbf{u}_{k-d}). \end{aligned} \quad (5.67)$$

Since the estimated states from the observer are fed back to the controller as system states, the formulation of $\tilde{\mathbf{w}}_k$ in (5.67) is re-arranged to

$$\tilde{\mathbf{w}}_k = \mathbf{A}^d (\hat{\mathbf{x}}_{k+1|k} - \mathbf{A}\hat{\mathbf{x}}_k - \mathbf{B}\mathbf{u}_{k-d}). \quad (5.68)$$

Furthermore, a prediction error \mathbf{e}_p is introduced:

$$\mathbf{e}_p(k) = \hat{\mathbf{x}}_k - \tilde{\mathbf{x}}_{k-d} \quad (5.69)$$

with $\tilde{\mathbf{x}}_{k-d} = \mathbf{A}^d \hat{\mathbf{x}}_{k-d} + \sum_{l=1}^d \mathbf{A}^{l-1} \mathbf{B}\mathbf{u}_{k-d-l}$. Therefore, \mathbf{e}_p can be depicted by

$$\mathbf{e}_p(k) = \mathbf{A}^{d-1} \mathbf{w}_{k-d} + \mathbf{A}^{d-2} \mathbf{w}_{k-d+1} + \dots + \mathbf{w}_{k-1}. \quad (5.70)$$

Since the disturbance \mathbf{w} and the prediction error \mathbf{e}_p are both bounded [162], the bounded set \mathbb{E} is defined by

$$\mathbb{E} = \mathbf{A}^{d-1} \mathbb{W} \oplus \mathbf{A}^{d-2} \mathbb{W} \oplus \dots \oplus \mathbb{W}. \quad (5.71)$$

Obviously, the predicted state $\tilde{\mathbf{x}}_k$ is bounded by $\tilde{\mathbb{X}}$ defined by $\tilde{\mathbb{X}} := \mathbb{X} \ominus \mathbb{E}$. Similar to the tube-based RMPC with reference tracking, a tube-based RMPC is adapted for dead-time compensation with the objective function

$$J_N(\tilde{\mathbf{x}}, \theta; \bar{\mathbf{x}}_k, \mathbf{u}, \bar{\theta}) = \sum_{i=0}^{N-1} L(\bar{\mathbf{x}}_{k+i}, \bar{\mathbf{x}}_s, \bar{\mathbf{u}}_{k+i}, \bar{\mathbf{u}}_s) + J_f(\bar{\mathbf{x}}_{k+N}, \bar{\mathbf{x}}_s) + J_r(\bar{\theta}, \theta). \quad (5.72)$$

The resulting optimization problem, which considers dead-time compensation as well as reference tracking, can be presented as follows:

$$\begin{aligned} & \min_{\tilde{\mathbf{x}}_k, \bar{\mathbf{u}}, \bar{\theta}} J_N(\tilde{\mathbf{x}}, \mathbf{x}_s; \bar{\mathbf{x}}, \bar{\mathbf{u}}, \bar{\theta}) \\ & \text{s.t. } \tilde{\mathbf{x}}_k \in \tilde{\mathbb{X}} \oplus (-\Omega_n) \\ & \quad \tilde{\mathbf{x}}^+ = \mathbf{A}\tilde{\mathbf{x}} + \mathbf{B}\bar{\mathbf{u}} \\ & \quad \bar{\mathbf{x}}_k \in \tilde{\mathbb{X}} = \mathbb{X} \ominus \mathbb{E} \ominus \Omega_n \\ & \quad \bar{\mathbf{u}}_k \in \bar{\mathbb{U}} = \mathbb{U} \ominus \mathbf{K}\Omega_n \\ & \quad (\bar{\mathbf{x}}_{k+N}, \bar{\theta}) \in \Omega_t^e, \end{aligned} \quad (5.73)$$

where Ω_n is an admissible invariant set satisfying $(\mathbf{A} + \mathbf{BK})\Omega_n \oplus \tilde{\mathbb{W}} \subset \Omega_n$. Therefore, the corresponding control law for the dead-time free controller is given by

$$\mathbf{u}_{k+i} = \kappa(\tilde{\mathbf{x}}_{k+i}) = \bar{\mathbf{u}}_{k+i}^* + \mathbf{K}(\tilde{\mathbf{x}}_{k+i} - \bar{\mathbf{x}}_k^*(k+i)). \quad (5.74)$$

Furthermore, the offset error has to be removed. The steady state output value can be separated into two parts: One is the steady state value of the predicted state, and the other is the offset term. It is represented by

$$\mathbf{y}_\infty = \mathbf{C}\tilde{\mathbf{x}}_s + \mathbf{F}\mathbf{w}_\infty, \quad (5.75)$$

where $\mathbf{F} = \mathbf{C} \left[(\mathbf{I} - \mathbf{A} - \mathbf{BK})^{-1} \mathbf{A}^d + \sum_{l=1}^d \mathbf{A}^{l-1} \right]$ [162]. Since the disturbance is unknown, an observer is required to estimate the disturbance at each time instant. In

the present work, the Kalman filter with extended disturbance modeling is applied. The state space representation is given by

$$\begin{aligned} \begin{bmatrix} \hat{\mathbf{x}}_{k+1} \\ \hat{\mathbf{w}}_{k+1} \end{bmatrix} &= \begin{bmatrix} \mathbf{A} & \mathbf{I} \\ \mathbf{0} & \mathbf{I} \end{bmatrix} \begin{bmatrix} \hat{\mathbf{x}}_k \\ \hat{\mathbf{w}}_k \end{bmatrix} + \begin{bmatrix} \mathbf{B} \\ \mathbf{0} \end{bmatrix} \mathbf{u}_{k-d} \\ \hat{\mathbf{y}}_k &= \begin{bmatrix} \mathbf{C} \\ \mathbf{0} \end{bmatrix} \begin{bmatrix} \hat{\mathbf{x}}_k \\ \hat{\mathbf{w}}_k \end{bmatrix}. \end{aligned} \quad (5.76)$$

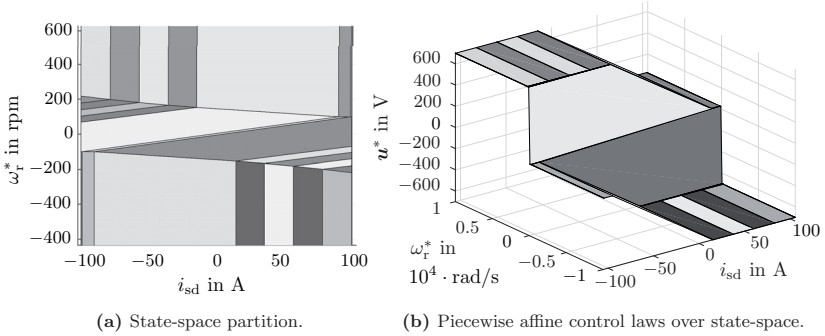


Figure 5.10: State-space partition.

Similar to the min-max current control, the tube-based current MPC on one axis is presented. Figure 5.10 shows the results of the off-line optimization. There are 29 partitioned critical regions presented in Figure 5.10a, in each of these regions a control law is given. The piecewise affine control laws over the state space are illustrated in Figure 5.10b.

5.4 Constraint handling for the electric drive systems

So far we discussed about the robust current control without system constraints. In the following, the constraint handling in IM is studied. The system constraints of IM are given by the maximum admissible stator current which depends on the thermal classification of the motor's insulation system, and the maximum available dc link voltage of the inverter. Both have to be considered for safety reasons in the control design. The stator current and voltage limits, without consideration of over-modulation by means of Space Vector Modulation (SVM), can be represented in the dq-frame by a circle and an ellipse, whose expressions are introduced later. This means, that the constraints are depicted by quadratic inequalities, which do not fulfill the standard QP form anymore and therefore have to be rearranged.

The simplest way of constraint handling for IM is to apply a constant limiting values. In [105], three box-constrained inequalities are given for the d-current, torque and

rotor flux. In [7, 113, 78, 58, 77], the constraint of the q-current is formulated assuming that the d-current is constant. The problem of such approaches is that the feasible regions of the system are not comprehensively considered. It causes that the optimality can not be guaranteed, or the optimal control is only available for a particular operating area. In [79], a penalty of stator current is introduced in the cost function to prevent over-current. It is only applicable for the finite set direct control based on enumeration, since there are finite combinations of control values. In case of optimal control problems with continuous control variables, the optimality is deteriorated. Another approach is to convert the spherical constraint curves into polygons by approximation [182]. The quadratic inequality can thereby be replaced by a set of linear inequalities. In [124], the current constraint is defined by an adjustable inequality regarding the actual value of the d-current and the reference value of the q-current. The voltage constraint is depicted by a polygon with the radius of direct current (dc) link voltage of the inverter. However, the accuracy of approximation is strongly dependent on the degree of the polygon. Therefore, a trade-off between approximation accuracy and computational effort should be considered in the control design.

In the following, a novel method, which is proposed in [84], is introduced. We recall the voltage equations of IM described in (5.14) and (5.15). The system constraints in IM are described by

$$\begin{aligned} i_{sd}^2 + i_{sq}^2 &\leq I_{dq,\max}^2 \\ u_{sd}^2 + u_{sq}^2 &\leq U_{dq,\max}^2, \end{aligned} \quad (5.77)$$

where $I_{dq,\max}$ and $U_{dq,\max}$ are the maximum admissible stator current and available inverter voltage converted into the dq-frame, respectively. It is evident that (5.77) does not match the linear inequality specified in (4.3). To transform the quadratic inequality system constraints to linear ones, the torque limit of the system is considered. The maximum available torque can be determined by the following equations

$$I_{dq,\max}^2 = i_{sd}^2 + i_{sq}^2 \quad (5.78a)$$

$$U_{dq,\max}^2 = (\omega_{\mu} L_s i_{sd})^2 + (\sigma \omega_{\mu} L_s i_{sq})^2 \quad (5.78b)$$

$$i_{sd} = \frac{\omega_n}{\omega_r} i_{sd,n} \quad (5.78c)$$

$$T_{el} = \frac{pL_m^2}{L_r} i_{sd} i_{sq}. \quad (5.78d)$$

$i_{sd,n}$ denotes the rated d-current. Since the voltage limit is only considerable in the field weakening area, where the voltage drops on stator and rotor resistances are negligible compared to the induced voltage due to rotation. Therefore, the voltage boundary line described in (5.8) and (5.77) can be simplified in form of (5.78b). In this equation, the d-current i_{sd} is used instead of the magnetizing current i_{μ} , since the excess of current limitation in transient states should be considered as well, which is discussed later. In the present work, the conventional constant rotor flux method with field weakening in (5.78c) is applied for the torque limit calculation.

In consideration of (5.78a), (5.78c) and (5.78d) in the basic speed area and (5.78b), (5.78c) and (5.78d) in the field weakening area, the system constraint represented by the torque limit is described by $-\bar{T}_{el} \leq T_{el} \leq \bar{T}_{el}$, where

$$\bar{T}_{el} = \begin{cases} \frac{pL_m^2}{L_r} i_{sd,n} \sqrt{T_{dq,max}^2 - i_{sd,n}^2}, & \omega_r \leq \omega_n \\ \frac{pL_m^2}{L_r} \frac{\omega_n}{\omega_r} i_{sd,n} \sqrt{\left(\frac{U_{dq,max}}{\sigma\omega_u L_s}\right)^2 - \left(\frac{\omega_n}{\sigma\omega_r} i_{sd,n}\right)^2}, & \omega_r \geq \omega_n. \end{cases} \quad (5.79)$$

The first torque limit formulation in (5.79) describes the rated torque of IM, which has a constant value and is only available in the basic speed area. In the field weakening area, the maximum torque depends on the actual rotor speed ω_r and ω_μ , which represents the synchronous frame speed at the operating point regarding the actual rotor speed with the maximum torque requirement. This dynamic torque limit is specified in the second formulation in (5.79). However, as described in (5.16), ω_μ is not directly given in the control. For this reason, ω_μ has to be replaced by ω_r by means of an analytical solution of (5.78b), (5.78c), (5.78d) and (5.16). The torque constraint formulation in field weakening area is thereby only with respect to ω_r , when this solution is replaced in the second formulation in (5.79). For a given rotor speed ω_r , the torque limit is determined by solving a fourth-order polynomial equation. The derivation of the dynamic torque limit in consideration of the rotor speed and magnetic saturation is given in Appendix D.

In addition, it has to be noticed that the voltage limit (5.78b) is represented by i_{sd} . In case of field weakening operation, the magnetizing current i_μ drops slower than i_{sd} in transient states. As a consequence, the actual EMF in the q-axis

$$\epsilon_q = \sigma\omega_\mu L_s i_{sd} + (1 - \sigma)\omega_\mu L_s i_\mu \quad (5.80)$$

resulted primarily by i_{sd} and i_μ , is larger than the one calculated solely from i_{sd} . Due to this reason, the applied voltage exceeds the voltage limit in transient procedures in the field weakening area. This issue can be suppressed by applying i_μ in the voltage limit calculation and using a rotor flux controller, whereas current overshooting in the d-axis arises in transient procedures and the current limit may be exceeded. In contrast, the impact of resulted over-voltage issue in transient procedures is limited by the available dc link voltage of the inverter as has been discussed. Therefore, the approach with flux controller is abandoned in this work.

Since the system constraints are related to the torque limit after the reformulation, which can be considered as input of the outer loop system of control loop, a constrained speed MPC will be demonstrated to validate the concept of constraint handling. The prediction model of speed loop is described by

$$\omega_r(k+1) = \omega_r^c(k) + T_s \frac{p}{J_r} T_{el}(k), \quad (5.81)$$

in which T_{load} has been already compensated to the actual rotor speed $\omega_r(k)$ represented by $\omega_r^c(k)$. The sample time T_s is fixed to the same value as in the current loop by $T_s = 0.1$ ms.

Based on the theories of multi-parametric Quadratic Programming (mp-QP) introduced in section 4.3.2, we recall the QP problem in form of (4.26). Considering our reference tracking problem with reference \mathbf{r} and applying the reformulated constraint description (5.79) yield

$$\begin{aligned} \min_U \quad & \left\{ \frac{1}{2} \mathbf{U}^T \mathbf{H} \mathbf{U} + [\hat{\mathbf{x}}_k^T \ \mathbf{r}_k^T] \mathbf{F} \mathbf{U} \right\} \\ \text{s.t.} \quad & \begin{bmatrix} \mathbf{I} \\ -\mathbf{I} \end{bmatrix} \mathbf{U} \leq \mathbf{E} \begin{bmatrix} \bar{T}_{\text{el}}(k) \\ \bar{T}_{\text{el}}(k) \end{bmatrix}, \end{aligned} \quad (5.82)$$

where the inequality constraint is linear but time-varying. Therefore, the parameter vector is extended by

$$\tilde{\mathbf{x}}_k = \left[\hat{\mathbf{x}}_k \ \mathbf{r}_k \ \bar{T}_{\text{el}}(k) \ \bar{T}_{\text{el}}(k) \right]^T. \quad (5.83)$$

Finally, the optimization problem is set up by

$$\begin{aligned} \min_U \quad & \left\{ \frac{1}{2} \mathbf{U}^T \mathbf{H} \mathbf{U} + \tilde{\mathbf{x}}_k^T \tilde{\mathbf{F}} \mathbf{U} \right\} \\ \text{s.t.} \quad & \begin{bmatrix} \mathbf{0} \\ \mathbf{0} \\ \mathbf{I} \\ -\mathbf{I} \end{bmatrix} \mathbf{U} \leq \tilde{\mathbf{E}} \tilde{\mathbf{x}}_k. \end{aligned} \quad (5.84)$$

Figure 5.11 shows the off-line optimization solution of the constrained speed MPC. The solution consists of control laws defined in 20 polyhedral regions in \mathbb{R}^3 state-space. Figure 5.11a illustrates the state-space partition projected to the two-dimensional subspace $[\omega_r \ \bar{T}_{\text{el}}]$, where the reference is set by $\mathbf{r} = 150$ rad/s. The piece-wise affine control laws projected on this subspace are shown in Figure 5.11b. The simulation and experiment results are presented in section 5.6.

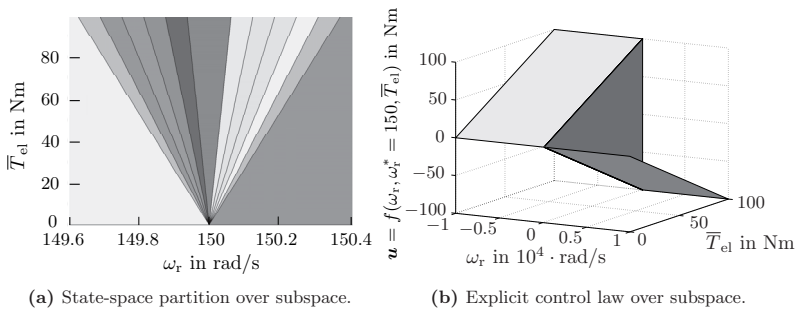


Figure 5.11: Off-line optimization results.

5.5 Overview of the control approach

In this chapter, the system parameter variations and constraints are considered in the robust current control design of IM in such a way, that they are incorporated into the optimization problems. According to the problem description, two different robust current controllers are implemented: The first controller is based on the min-max optimization using multi-parametric SemiDefinite Programming (mp-SDP) and the second one is based on the minimal Robust Positively Invariant (mRPI) set. The system constraints of stator current and voltage are reformulated and transferred to the torque constraint, which is moved to the outer control loop. Therefore, no explicit constraint handling is required in the current control loop. In the present work, only relaxed boxed constraints, which cover the real physical range, are defined for the current control design. The entire control structure is shown in Figure 5.12.

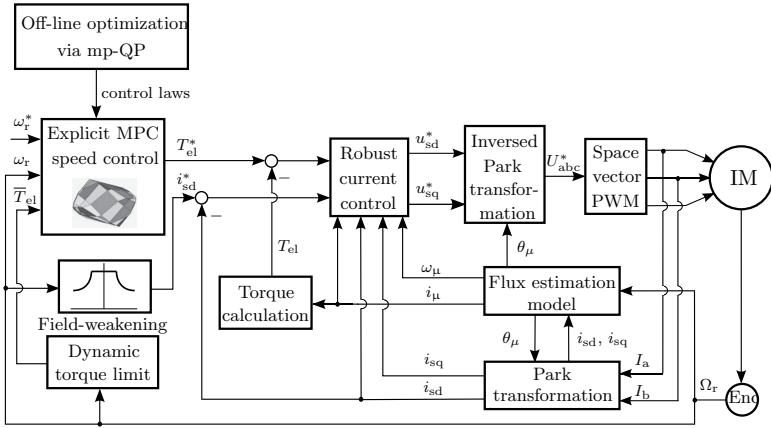


Figure 5.12: Overview of the robust current control in IM with constraint handling.

5.6 Simulation and experimental results

In this section, the discussed control approaches are validated. The machine parameters and the data of the test bench are given in Appendix B. Due to the hardware limit, some parameters are newly defined. The reason is given in section 5.6.2. All control approaches are implemented and simulated in MATLAB/Simulink. The performance of the following three approaches are compared:

- ▷ nominal model predictive current control with Kalman filter extended by

disturbance modeling introduced in section 4.2.2, which is named as NMPCC subsequently;

- ▷ robust min-max model predictive current control implemented in section 5.3.1, which is named as RM3PCC, and
- ▷ tube-based model predictive current control designed in section 5.3.2, which is named as TMPCC.

Moreover, for the real-time application, the dSPACE DSP system is applied, which is introduced in section 5.6.2. The sample time of the current control loop is defined by $T_s = 0.1$ ms for both the simulation and the experiment.

5.6.1 Simulation results

Robust current control

To present the performance of robust current control in consideration of parameter mismatch, four test cases are chosen for the simulation. In the first case, the parameters in the system and controller are identical. In the second case, the actual resistance is higher than the one applied to the controller, which corresponds to the scenario at high operating temperature. In the third and the last cases, the mutual inductance set by the controller is set to half and twice of the actual one, respectively.

Figure 5.13 shows the current responses of different control approaches in the d- and q-axis. The reference value is set in form of a step change with $i_{sd}^* = 10$ A and $i_{sq}^* = 10$ A, respectively. The rotor speed is kept constant at 1000 rpm. r_s and l_m are the normalized ohmic resistance and mutual inductance in the controller based on the motor's data sheet information. The simulation results of all four cases are presented in Figures 5.13a - 5.13d, respectively.

In Figure 5.13a, it is apparent that in the case without parameter mismatch, all three control approaches have achieved a similar good performance without overshooting. In the second case, the system controlled by NMPCC has a small overshooting due to resistance mismatch, while RM3PCC and TMPCC show a similar performance as in the first case. In the third case, the system performances of NMPCC and RM3PCC are impacted in the transient procedure, in which the overshooting of NMPCC is essentially larger than the one of RM3PCC. In opposition to that, TMPCC behaves comparably well as before. In Figure 5.13d the performance of NMPCC is further deteriorated. A significant overshooting amounting 50% takes place. In contrast, a good system performance is exhibited by RM3PCC as well as by TMPCC.

Furthermore, the off-line and the on-line computational efforts of TMPCC are significantly reduced in comparison to RM3PCC. Depending on the computing capacity of the computer used, as a reference, only several minutes are required for TMPCC to get the off-line control laws instead of several hours for RMPCC. The

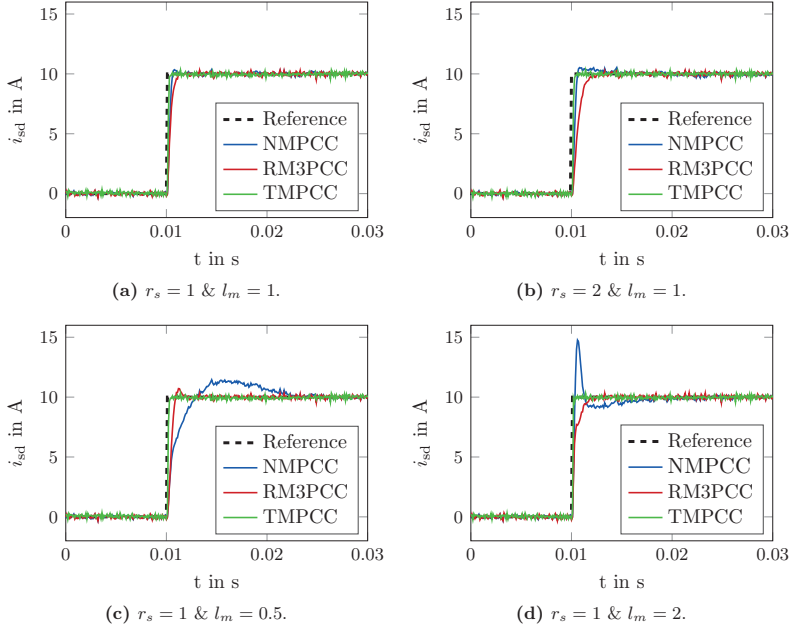


Figure 5.13: Simulation results.

tuning process of control parameters becomes therefore more comfortable. Moreover, there are 29 partitioned regions for TMPCC, whereas 416 regions are generated for RM3PCC. That means, the implementation of advanced search algorithms for the on-line computation is no longer necessary for the TMPCC.

Figure 5.14 illustrates the result of dead time compensation. As predefined in section 5.1.2, the dead time $T_d = 0.3$ ms, which means $d = 3$. The TMPCC with predictor introduced in section 4.4.2 named DCTMPCC is presented here as example. It is important to note, that the impact of the dead time is well diminished by extension of the predictor in the control structure. It helps to improve the performance and to ensure the system stability.

Constraint handling

The aim here is to validate and to evaluate the method of constraint handling in IM using MPC introduced in section 5.4. Therefore, it is focused on the optimum utilization of the system resource under the new constraint condition. Figure 5.15 illustrates the off-line computation results of the torque limit, which is stored in a look-up table and applied to the on-line computation.

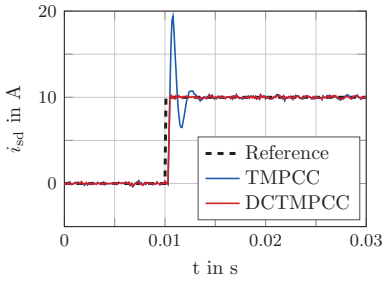


Figure 5.14: Dead time compensation.

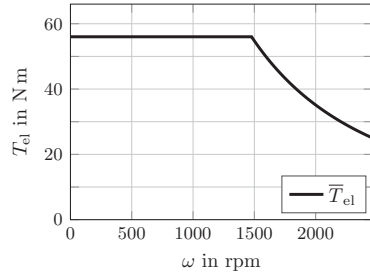


Figure 5.15: Torque limitation.

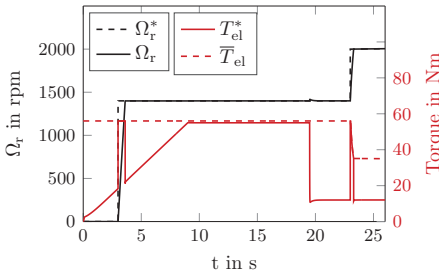
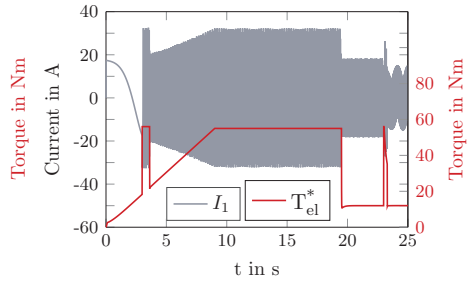
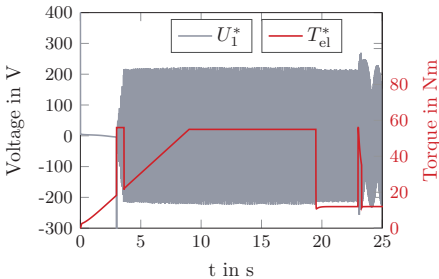
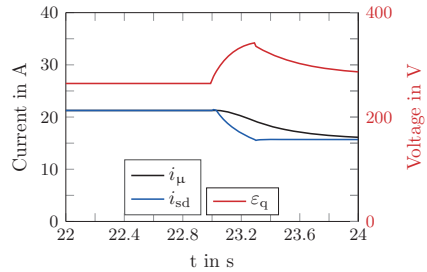
Figure 5.16: $\Omega_r - T_{el}^*$.Figure 5.17: $I_1 - T_{el}^*$.Figure 5.18: $U_1 - T_{el}^*$.

Figure 5.19: Voltage overshooting in transient.

The simulation runs as follows: Initially, the reference rotor speed is changed abruptly to 1400rpm, whereat the load ramps up from 0Nm to 55Nm within the first 9s. After 10s, the load torque falls to 12Nm. A few seconds later, the reference speed is increased to 2000rpm in step form, which is in the field-weakening area.

To evaluate the optimality of the controller, the reference torque applied by the controller is considered. As shown in Figure 5.16, the MPC controller applies the maximum torque to be limited to 56 Nm in the base speed area, as long as the reference speed is not reached. Once the reference speed is reached, the required drive torque drops to the actual value of the load torque and follows this value thereafter. In the phase of speed increase from 1400 rpm to 2000 rpm, which is mainly in the field weakening area, the reference torque coincides with the curve shown in Figure 5.15 in the field weakening area. As soon as the transient procedure is finished, the reference torque is reduced to the load torque again.

Figure 5.17 shows the stator current change in the simulation. According to Table B.3, the admissible amplitude of the phase current \hat{I}_{abc} corresponding to $I_{dq,max}$ is calculated to be 32.7 A. The maximum current by dint of the $\frac{\omega_n}{\omega_r}$ method described in (5.78c) is delivered when the maximum torque is required in the base speed area. As shown in Figure 5.17, the amplitude of the current is well limited to \hat{I}_{abc} by using the torque constraint.

The admissible amplitude of the phase voltage \hat{U}_{abc} being 231 V is calculated in the same way as by \hat{I}_{abc} . As mentioned in section 5.4, the voltage limit is relevant in the field weakening area. The maximum voltage is demanded in the case of the maximum torque requirement in the field weakening area. In Figure 5.18, it is presented that the maximum voltage is reached at the rated operation point. However, during the transient procedure in the field weakening with the maximum torque requirement, the stator voltage exceeds the limit value, which is shown in Figure 5.19 as shark fins in shape. The clarification of this phenomenon was given in section 5.4 and is confirmed by Figure 5.19.

In the following, the comparisons between proposed approach and PI controller as well as Explicit Model Predictive Control (EMPC) with approximated constraints are given. To compare the dynamics of the proposed EMPC controller and the PI controller, the following reference speeds are applied as example in sequence with decreasing step changes: 500 rpm, 600 rpm, 650 rpm, 675 rpm and 680 rpm. The offsets from each reference value change are reduced step by step. The parameters of the PI current and speed controllers are tuned by means of magnitude and symmetric optimum, respectively. The IM is driven without load. Figure 5.20 - Figure 5.24 show the step responses with different step changes, respectively. The PI controller achieves a comparable dynamic as the proposed EMPC in the case of large reference change. Because of the significant control deviation, the maximum permissible torque is applied by the PI controller as shown in Figure 5.20. However, this manipulated value of the PI controller reduces when the reference change becomes smaller: The smaller the step change is, the smaller is the reference torque applied by the PI controller, which is illustrated in Figures 5.21 - 5.24. In general, the parameter optimization of PI controllers can only be designed within a constricted operation range. In contrast, the proposed approach applies the maximum permissible torque independent on the size of reference change to obtain the high dynamic.

To present the advantage of the proposed EMPC approach compared to the EMPC with approximated constraints, the following constraints are defined for the latter

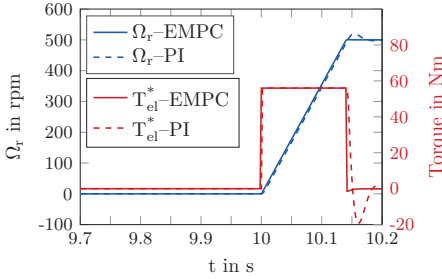


Figure 5.20: Step change = 500 rpm.

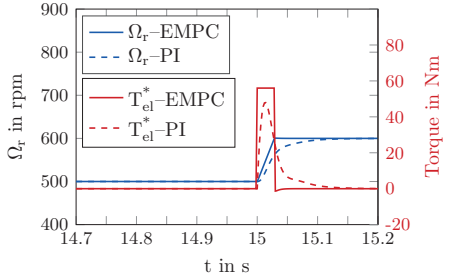


Figure 5.21: Step change = 100 rpm.

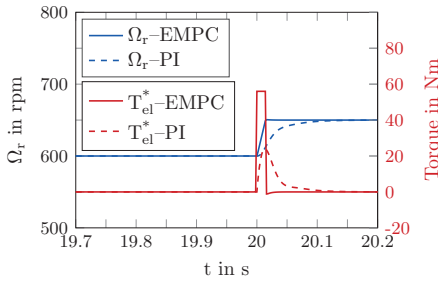


Figure 5.22: Step change = 50 rpm.

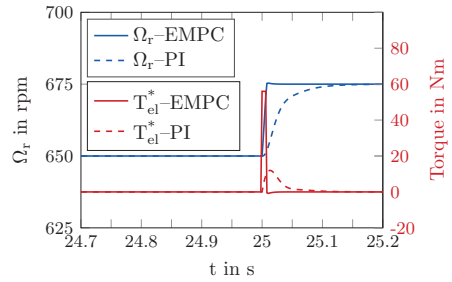


Figure 5.23: Step change = 25 rpm.

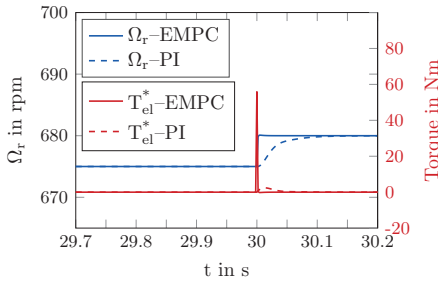


Figure 5.24: Step change = 5 rpm.

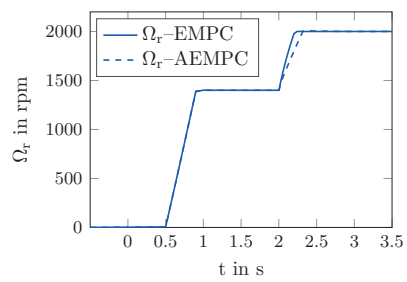


Figure 5.25: Dynamics comparison.

approach

$$\begin{aligned}
 & 0 \leq i_{sd} \leq i_{sd,n} \\
 & -\sqrt{I_{dq,\max}^2 - i_{sd,n}^2} \leq i_{sq} \leq \sqrt{I_{dq,\max}^2 - i_{sd,n}^2} \\
 & -\frac{U_{dq,\max}}{\sqrt{2}} \leq u_{sd} \leq \frac{U_{dq,\max}}{\sqrt{2}} \\
 & -\sqrt{U_{dq,\max}^2 - u_{sd}^{*2}} \leq u_{sq} \leq \sqrt{U_{dq,\max}^2 - u_{sd}^{*2}}.
 \end{aligned} \tag{5.85}$$

The stator current in the d-axis i_{sd} is limited by the rated current and is larger or equal to zero. The q-current i_{sq} is constrained by the positive and negative value of the rated current in the q-axis. Since the stator voltage in the d-axis is much smaller than the one in the q-axis at high speed due to the leakage factor, it is constrained by a constant value, whereas the constraint of the q-component voltage is determined by the maximum voltage and the actual reference voltage in the d-axis. For this reason, both the current and voltage constraints are approximated by rectangular polygons. Because the dq-components of stator current and voltage are decoupled, two EMPC controllers are able to be separately implemented to reduce the dimension of the state space. The torque constraint of the speed controller is given by the rated torque. After the off-line optimization, 29 polyhedral regions in \mathbb{R}^3 state space are defined for each EMPC current controller.

The simulation result of the proposed EMPC approach and the EMPC with the approximated constraints defined in (5.85) is presented in Figure 5.25. In the beginning, the reference speed is set by 1400 rpm, which is in the base speed area. In this area, the system is only constrained by the current inequalities. Because the stator current in the d-axis remains at its rated value. It means that the maximum torque is reachable for both approaches. Therefore, there is no difference associated with system dynamics between both approaches as shown in Figure 5.25. Subsequently, the reference speed is increased to 2000 rpm. This value lies in the field weakening area and the voltage constraints should be thus considered. In the optimization of EMPC with approximated constraints, only the area inside the voltage rectangle is feasible, whereas the feasible area of the proposed approach is represented by the voltage ellipse defined by the original voltage description derived from (5.8) and (5.77). In this particular case, less system resources can be used by the EMPC with approximated constraints. Due to this issue, the system dynamic is deteriorated by the approximation as shown in Figure 5.25. As aforementioned, the performance can be improved if the approximation is more accurate. However, since the dq-components are no more decoupled due to the inequality formulations, the hexagonal approximations of current and voltage constraints leads to 1057 polyhedral regions. Thereby, the on-line computational effort is increased significantly, whereat the feasible area is still smaller than the proposed approach.

5.6.2 Experimental results

Test bench configuration

The aforementioned simulation cases are practically validated by measurements on a laboratory test bench, which is set up as illustrated in Figure 5.26.

The test bench consists of the following main components with their functions described as:

- ▷ drive motor: Siemens IM with model type 1LA5186-4AA10 (Table B.2)

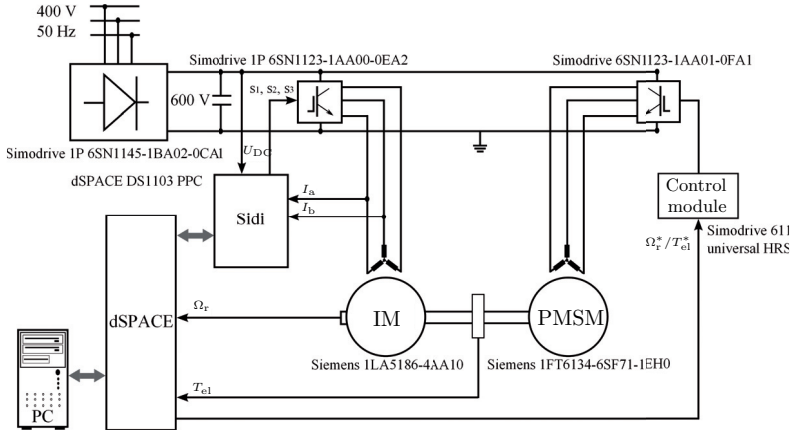


Figure 5.26: Schematic illustration of the test bench setup for the current control in IM.

controlled by the software implemented in this work running on dSPACE system DS1103 (Table B.9)

- ▷ load machine: Siemens Permanent-Magnet Synchronous Motor (PMSM) with model type 1FT6134-6SF71 (Table B.4) controlled by Siemens control program running on the control module 6SN1118-1NH01-0AA1 (Table B.8)
- ▷ two-level VSI: Simodrive 6SN1123-1AA00-0EA2 (Table B.6) drives the IM; and Simodrive 6SN1123-1AA01-0FA1 (B.7) drives the PMSM. Both systems use the same dc link voltage supplied by the supply module 6SN1145-1BA02-0CA1 (Table B.5)
- ▷ Simodrive-dSPACE-interface (Sidi) board: the switching signals from dSPACE modulator using SVPWM are implemented by Sidi onto the inverter. The signals of measured stator currents and dc link voltage are sent from here to the dSPACE IO system. Moreover, the over-current and -voltage signals are sent from here to the dSPACE system for the safety function.
- ▷ encoder: Heidenhain encoder with model type ROD 420 (Table B.10) measures the rotational speed of the drive motor. The speed of PMSM is measured by EQN1325 integrated in the machine.
- ▷ torquemeter: HBM T10F (Table B.11) measures the torque produced by the drive motor.

Due to the over-current protection on the Sidi board, the original rated current of the IM can not be reached. Therefore, the rated operating point is redefined in the present work with the data given in Table B.3.

Robust current control

The experimental results of robust current control are shown in Figure 5.27.

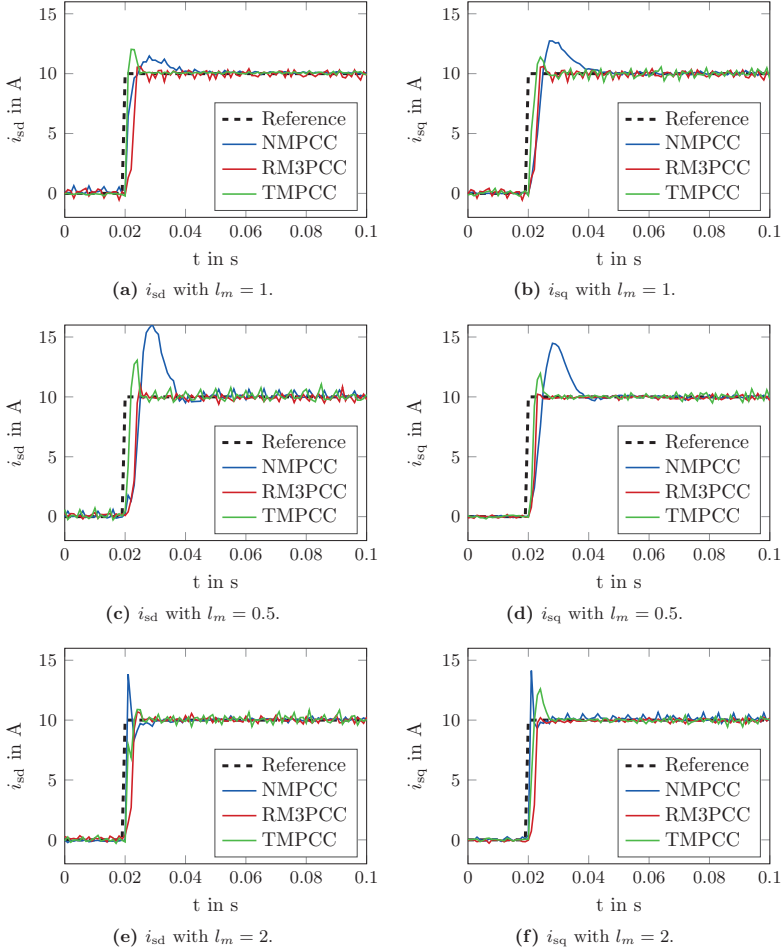


Figure 5.27: Experimental results.

Slightly different from the simulation presented before, only the mutual inductance mismatch is implemented for the controller on the test bench. The reason for this is that the variation of the mutual inductance affects the current control performance more significant than the stator resistance according to the simulation results. The

results in Figure 5.27 are comparable to the ones in the simulation (see Figure 5.13). Figure 5.28 illustrates the difference between the simulation and the experiment results in the d-axis with $l_m = 1$ as example. In order to synchronize the start time, the experimental result is shifted 0.1 s backwards. The legend texts sRM3PCC and sTMPCC mean the simulation results. The overshooting and the response time of the current in the experiment shown in Figure 5.28 is larger than those in the simulation. The reason for this is the dead time in the physical system, which is not modelled in the simulation shown in Figure 5.13.

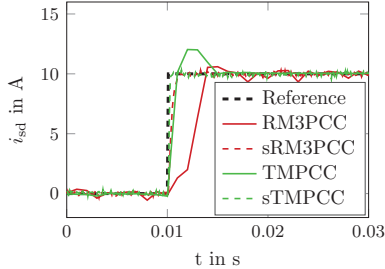


Figure 5.28: Comparison of simulative and experimental results: i_{sd} with $l_m = 1$.

According to the simulative and the experimental results, NMPCC for IM is robust against parameter mismatch and variation. However, it is not easy to prove, that if the robustness can be guaranteed over the entire operation range by means of this approach. Furthermore, the system performance degrades in case of parameter variation. To achieve a high robustness based on this scheme, the system dynamic has to be sacrificed. Meanwhile, since the proposed approaches systematically incorporate the system uncertainties into the formulation of the optimization problems, a universal robustness can be guaranteed for the control system.

Constraint handling

The following three test results concerning constraint handling are presented: The first test validates the current limit by means of the proposed method in a start up process; the second test validates the optimality of the proposed method; the last test delivers the measurement results compared to the simulation results.

In the start up test a load torque of 13 Nm is imposed to the IM. Then, the reference speed is changed to 1000 rpm. As shown in Figure 5.29a the reference torque demanded by the speed controller jumps to the maximum available torque at the same time. The reference torque falls to the value equal to the load torque after the transient procedure is terminated. Meanwhile, as shown in Figure 5.29b, the stator current is well limited during the entire process, particularly in the transient procedure of the startup. The amplitude of the stator current shown in the figure

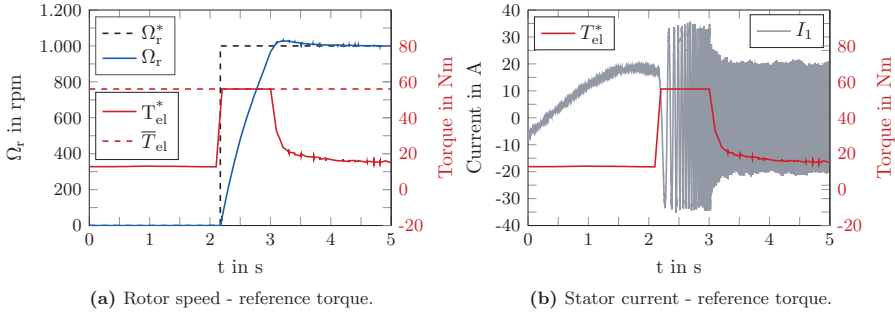


Figure 5.29: Start up.

is below 35 A. Due to measurement noises, it is slightly higher than the theoretical limit.

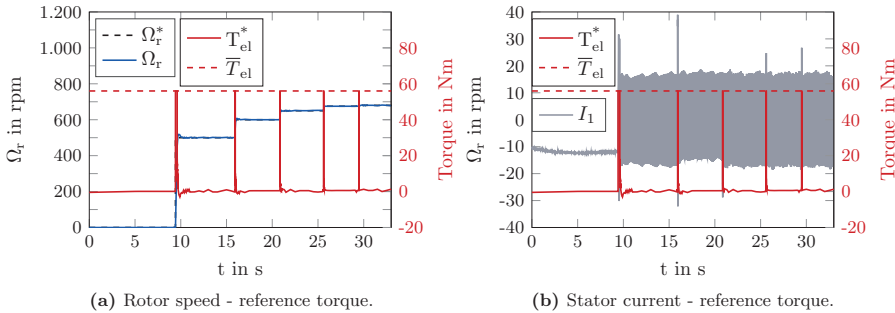


Figure 5.30: Diverse speed requirements.

In the second test, the IM is operated as in the simulation with different step variants to check the optimality of the control approach. In Figure 5.30a, it is evident that despite of the diminished reference changes, the maximum admissible torque is enforced for each transient procedure. It confirms that the maximum system resource is required no matter how large the control offset is. This implicates the optimality of the control algorithm. The stator current curve is illustrated in Figure 5.30b. The current is limited to the admissible current except in the second transient procedure. However, the current limit is exceeded for about 5 ms and the peak value is about 39 A. Usually, the admissible peak current of power electronics and EMs is much higher compared to the one for continuous operations. Therefore, the exceeding in this case will not plague the hardware and is uncritical. In case of the maximum torque requirement for long durations, no over-current arises, which was depicted by the first test in Figure 5.29b.

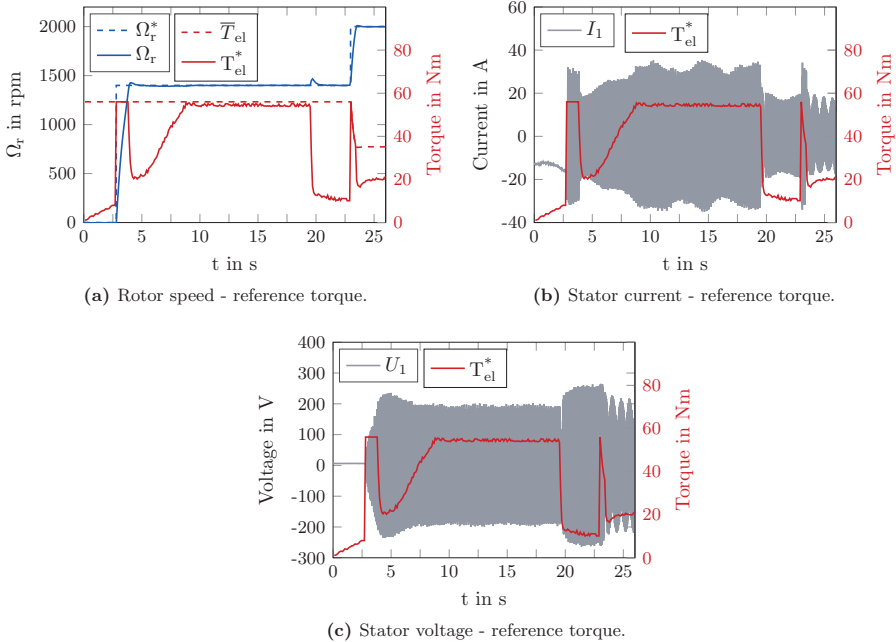


Figure 5.31: Drive cycle.

In the last test, the similar drive cycle is performed as in the simulation. The load torque ramps from the beginning until 55 Nm. The reference speed is set to 1400 rpm, same as in the simulation. After the steady state is reached, the load is changed from 55 Nm to 12 Nm. After a few seconds the reference speed is set to be 2000 rpm, as in the simulation.

In Figure 5.31, the experimental results are shown in comparison to the simulation results. In the first phase, roughly within the first 2.8 seconds in Figure 5.31a, the reference torque follows the load because no control offset exists. As soon as the reference speed changes to 1400 rpm, the speed controller enforces the reference torque to the maximum torque in order to reach the reference value as quickly as possible. Once the reference value is met, the reference torque drops to the current load torque and increases with it. At about the 20th second, the load drops to 12 Nm. After the reference speed is set to 2000 rpm, the reference torque rises firstly to 56 Nm and then follows the torque limit curve, since entering the field weakening area until the reference speed is reached. This measurement result coincides with the simulation result presented before.

The stator current curve in one phase is presented in Figure 5.31b. As the maximum

admissible torque is required at the 3rd second, the stator current reaches its limit. From the 9th second to the 19th second, the stator current remains around the current limit, as the load is approximately equal to the maximum torque. In the next procedure of the maximum torque requirement, the stator current increases to the limit and then is reduced because of the field weakening operation. Thus, the current limit via torque limit is validated.

The reference values of the stator voltage are described in Figure 5.31c. Since the IM is in standstill at the beginning, the stator voltage results mainly from the voltage drop of the stator resistor in the d-axis, which is marginal compared to its limit value. Due to the small speed overshooting shown in Figure 5.31a, the voltage limit is reached at approximately the 5th second. Because of the load reduction at the 20th second, the rated speed is exceeded, so that the maximum voltage is reached again. Due to the maximum torque requirement in the field weakening area around the 23rd second, the reference voltage exceeds the maximum admissible voltage, which confirms the explanation in Figure 5.19 and agrees with the simulation result.

Finally, the validated constraint handling method can be applied in the overlying active damping controller introduced in the next chapter.

5.7 Summary

The robust current control for IM is discussed and implemented in this chapter. In order to obtain high control performance, the optimization-based robust constrained MPC methods are applied. To attain a good trade-off between robustness and optimality, two approaches are implemented in this work: the approach based on the min-max optimization and the one based on the minimal Robust Positively Invariant (mRPI) set. The system constraints are incorporated into the optimization problem as well and solved by the multi-parametric Quadratic Programming (mp-QP). The experimental results shows that the control performance of the IM is enhanced by those approached when compared to the classical control approaches. In order to implemented the TV application, the controlled traction motor should be integrated into the mechanical system as actuator. In the next chapter, this integration and the control approach in the mechanical drivetrain are presented.

6 Active damping control in the mechanical drivetrain

By combining the robust current control approaches as introduced in chapter 5 with the torque equation 5.10, a desired electromagnetic torque is produced by the induction traction motor and then transmitted to the mechanical drivetrain. In vehicles, traction motors are combined by elastic mechanical transmission elements, which induce torsional oscillations on the mechanical drive shaft in the course of the torque transmission. This issue may deteriorate the drivability and the comfort. Particularly critical is the situation, when the resonance frequency of the mechanical drivetrain is stimulated by issues such as the unbalance mass of the system. In this case, the oscillation of the drive torque leads to jerking of the bodywork, which may have a comparable large resonance frequency. Moreover, the torque oscillation on the drive shaft may in turn impact the IM and causes current and voltage oscillations. This degrades the control performance of the electric drivetrain and may even lead to undesired cutoff of the electric traction motor.

In this chapter, the properties of the mechanical drivetrain are introduced in section 6.1. In section 6.2, a dynamic active damping control is introduced, designed and implemented in order to suppress torque oscillations in the crucial low frequency range. The test bench setup as well as the results are presented in section 6.3.

6.1 Modeling of elastic mechanical drivetrain

6.1.1 Mechanical structure

The mechanical drivetrain system in EVs is composed of the rotor of the electric traction motor, the input and the output gear, the wheel rim, the tire belt, the vehicle mass as well as the mechanical couplings among them. The behavior of the entire system can be idealized as a six-mass-oscillator and can be modeled as a spring-damper-mass system. Such a mechanical drivetrain model is illustrated in Figure 6.1.

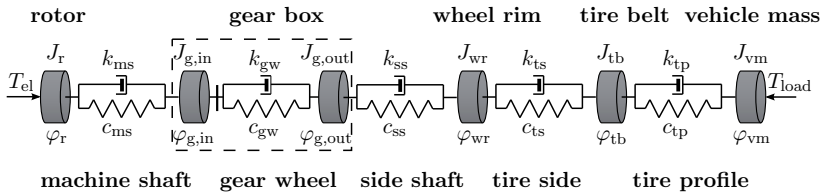


Figure 6.1: Illustration of the mechanical drivetrain system.

In the figure, J and φ denote the moment of inertia and the position angle of the masses. Symbols k and c represent the damping coefficient and the torsional stiffness of the mechanical joints, respectively. Moreover, r_g embodies the gear ratio. In this way, the kinetics of the system are described by

$$J_r \cdot \ddot{\varphi}_r = T_{el} - c_{ms} \cdot (\varphi_r - \varphi_{g,in}) - k_{ms} \cdot (\dot{\varphi}_r - \dot{\varphi}_{g,in}), \quad (6.1a)$$

$$J_{g,in} \cdot \ddot{\varphi}_{g,in} = c_{ms} \cdot (\varphi_r - \varphi_{g,in}) + k_{ms} \cdot (\dot{\varphi}_r - \dot{\varphi}_{g,in}) - \frac{c_{gw}}{r_g} \cdot \left(\frac{\varphi_{g,in}}{r_g} - \varphi_{g,out} \right) - \frac{k_{gw}}{r_g} \cdot \left(\frac{\dot{\varphi}_{g,in}}{r_g} - \dot{\varphi}_{g,out} \right), \quad (6.1b)$$

$$J_{g,out} \cdot \ddot{\varphi}_{g,out} = c_{gw} \cdot \left(\frac{\varphi_{g,in}}{r_g} - \varphi_{g,out} \right) + k_{gw} \cdot \left(\frac{\dot{\varphi}_{g,in}}{r_g} - \dot{\varphi}_{g,out} \right) - c_{ss} \cdot (\varphi_{g,out} - \varphi_{wr}) - k_{ss} \cdot (\dot{\varphi}_{g,out} - \dot{\varphi}_{wr}), \quad (6.1c)$$

$$J_{wr} \cdot \ddot{\varphi}_{wr} = c_{ss} \cdot (\varphi_{g,out} - \varphi_{wr}) + k_{ss} \cdot (\dot{\varphi}_{g,out} - \dot{\varphi}_{wr}) - c_{ts} \cdot (\varphi_{wr} - \varphi_{tb}) - k_{ts} \cdot (\dot{\varphi}_{wr} - \dot{\varphi}_{tb}), \quad (6.1d)$$

$$J_{tb} \cdot \ddot{\varphi}_{tb} = c_{ts} \cdot (\varphi_{wr} - \varphi_{tb}) + k_{ts} \cdot (\dot{\varphi}_{wr} - \dot{\varphi}_{tb}) - c_{tp} \cdot (\varphi_{tb} - \varphi_{vm}) - k_{tp} \cdot (\dot{\varphi}_{tb} - \dot{\varphi}_{vm}), \quad (6.1e)$$

$$J_{vm} \cdot \ddot{\varphi}_{vm} = c_{tp} \cdot (\varphi_{tb} - \varphi_{vm}) + k_{tp} \cdot (\dot{\varphi}_{tb} - \dot{\varphi}_{vm}) - T_{load}. \quad (6.1f)$$

6.1.2 Oscillation analysis

In [128], the parameters of a real mechanical drivetrain are presented. Based on these parameters, the oscillation behavior of the system is analyzed. Its eigenvalues are calculated and collected in Table 6.1.

Position	Eigenvalue	Frequency (Hz)	Damping factor
–	$-0 \pm j0$	0	–1
side shaft	$-0.225 \pm j47.4$	7.55	0.00473
tire profile	$-16.8 \pm j404$	64.4	0.0416
tire side	$-43.9 \pm j684$	109	0.0642
machine shaft	$-18.3 \pm j2580$	411	0.00708
gearbox	$-468 \pm j23400$	3725	0.02

Table 6.1: Eigenvalues of the six-mass-oscillator.

Furthermore, the Bode diagram describing the oscillation behavior is shown in Figure 6.2. From Table 6.1 and Figure 6.2 it can be identified, that the dominant resonance frequency of the system lies on the side shaft. Mostly, this frequency is much smaller than the other resonance frequencies. As a consequence, vehicle jerking takes place during the startup procedure, which is called Ferraria effect. Therefore, the major task of the control strategy is to suppress oscillations with the dominant resonance frequency on the side shaft.

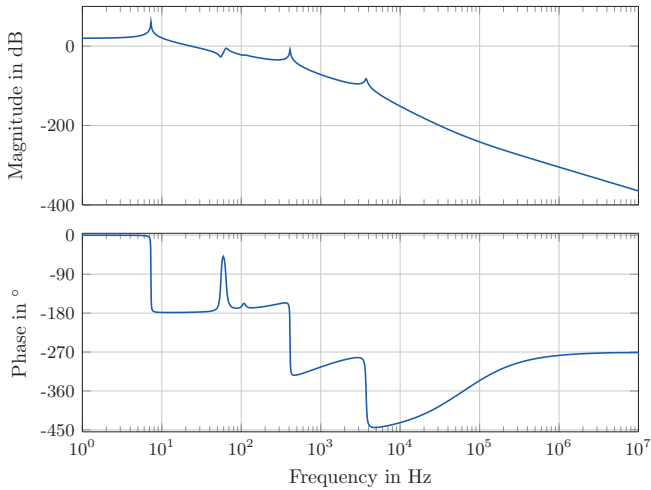


Figure 6.2: Bode diagram of the six-mass-oscillator.

It is worthy to note, that the original studied system (6.1) has a high order and is therefore hardly suitable for the control design. In order to simplify the system and describe it better controllable without significantly changing the properties, the order reduction method proposed by Laschet is used [107]. Figure 6.3 shows an example of the order reduction.

The Laschet's order reduction works as follows:

$$J'_1 = J_1 + \frac{c_1}{c_1 + c_2} \cdot J_2, \quad (6.2a)$$

$$J'_3 = J_3 + \frac{c_2}{c_1 + c_2} \cdot J_2, \quad (6.2b)$$

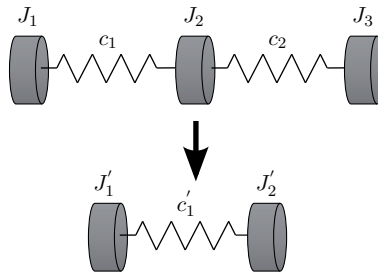


Figure 6.3: An example of Laschet's order reduction.

$$c'_1 = \frac{c_1 \cdot c_2}{c_1 + c_2}. \quad (6.2c)$$

The moment of inertia associated with the mass to be eliminated is distributed to the adjacent masses in accordance to the relationship of the torsional stiffness. The joints composed of two stiffnesses are summarized by one. Because of the gear ratio, it is important to notice, that the damping coefficients, torsional stiffnesses as well as the inertias on the right hand side of the gear wheel (see Figure 6.1) have to be transformed by

$$\tilde{J} = J/r_g^2, \quad (6.3a)$$

$$\tilde{c} = c \cdot r_g^2, \quad (6.3b)$$

$$\tilde{k} = k \cdot r_g^2, \quad (6.3c)$$

if they are referred to the left hand side of the gear wheel. Furthermore, the sequence of the order reduction has to be performed in such a way, that the mass on the mechanical joint with the highest resonance frequency is firstly reduced. In this sequence, the six-mass-oscillator is reduced to a two-mass-oscillator composed of a rotor, a vehicle mass and a drive shaft. This system has a comparable resonance frequency as the original one to be suppressed. The physical values of these components are modified according to Laschet's order reduction and represented by J_r^* , J_{vm}^* , c_{ss}^* and k_{ss}^* . In this way, the new undamped resonance frequency is calculated by

$$\omega_0^* = \sqrt{\frac{c_{ss}^*}{J_r^*} + \frac{c_{ss}^*}{J_{vm}^*}} \quad (6.4)$$

and the damping factor

$$\zeta^* = \frac{k_{ss}^*}{2} \sqrt{\frac{1}{J_r^* \cdot c_{ss}^*} + \frac{1}{J_{vm}^* \cdot c_{ss}^*}}. \quad (6.5)$$

In Figure 6.4, the reduced two-mass-oscillator is compared to the original one in regard to the oscillation behavior.

After the order reduction, the dominant resonance frequency of the two-mass-oscillator differs slightly from the original one: The frequency drops from 7.55 Hz to 7.48 Hz. Moreover, there is a marginal change of the magnitude in the bode diagram corresponding to the damping factor. Despite of these facts, the result of the order reduction is still considered to be acceptable and suited for the control design.

6.1.3 Parameter variation

Another issue, which has to be discussed for the control design, is the impact of the parameter variation on the resonance frequency. As an example, the inertia of the vehicle mass varies with the load situation. Due to this reason, the parameters

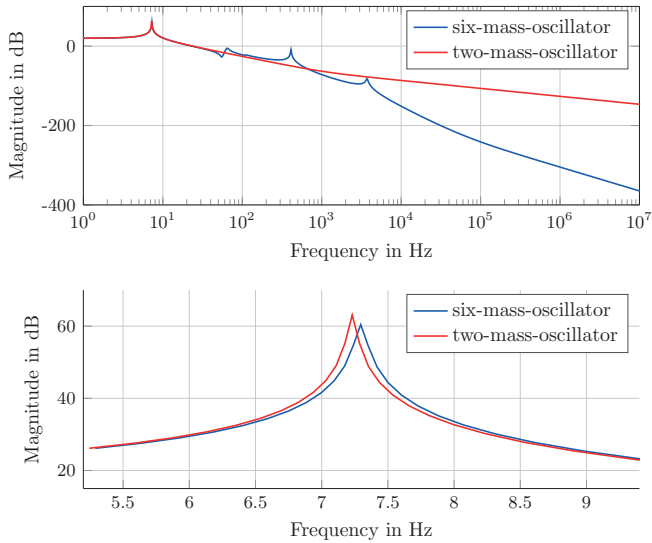


Figure 6.4: Amplitude response of the six-mass-oscillator and the reduced two-mass-oscillator.

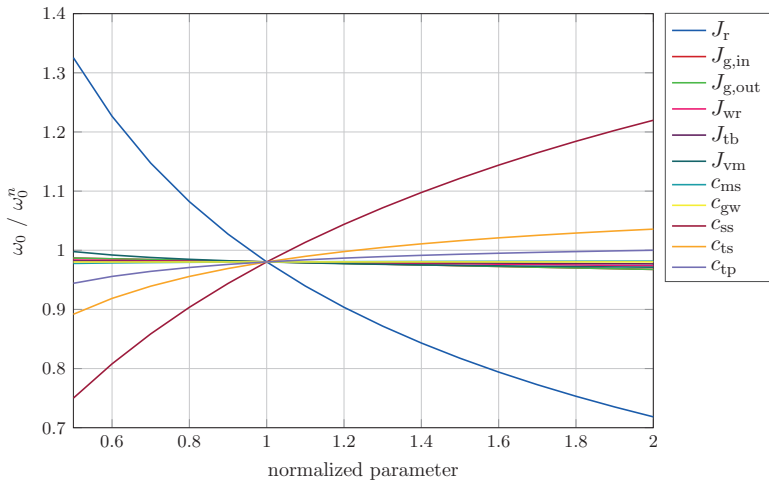


Figure 6.5: Resonance frequency variation due to parameter variation.

in the six-mass-oscillator are analyzed. In Figure 6.5, the relationship between the

parameter variation and the change of the resonance frequency is illustrated.

The x- and y-axis denote the normalized physical values and resonance frequencies, respectively. The parameters, whose variations significantly impact the resonance frequency, are J_r^* and c_{ss} . Both parameters are able to be identified precisely and do not change during operation. As a consequence, no parameter variation has to be considered in the control design.

6.2 Dynamic active damping control

Based on the reduced two-order-oscillator model, a dynamic active damping control is implemented. Since the rotational speeds of both the rotor and the wheel are measured in the real system, the kinetic equations containing angle positions are reformulated. The state-space representation of the reformulated system is defined by

$$\begin{bmatrix} \dot{\omega}_r \\ \dot{\omega}_w \\ \dot{T}_{ss} \\ \dot{T}_{load} \end{bmatrix} = \begin{bmatrix} 0 & 0 & -\frac{1}{J_r^*} & 0 \\ 0 & 0 & \frac{1}{J_{vm}^*} & -\frac{1}{J_{vm}^*} \\ c_{ss}^* & -c_{ss}^* & -k_{ss}^* \left(\frac{1}{J_r^*} + \frac{1}{J_{vm}^*} \right) & k_{ss}^* \\ 0 & 0 & 0 & 0 \end{bmatrix} \cdot \begin{bmatrix} \omega_r \\ \omega_w \\ T_{ss} \\ T_{load} \end{bmatrix} + \begin{bmatrix} \frac{1}{J_r^*} \\ 0 \\ \frac{k_{ss}^*}{J_r^*} \\ 0 \end{bmatrix} \cdot T_{el}, \quad (6.6)$$

where ω_w denotes the wheel speed, c_{ss}^* and k_{ss}^* the modified stiffness and damping coefficient on the side shaft and T_{ss} the transmitted drive torque on the side shaft.

According to the expression of the control laws introduced in section 4.3.2, the control action determined by Explicit Model Predictive Control (EMPC) in each critical region is proportional to the control deviation. Therefore, within the scope of a region, only the dominant eigenvalues are modified by the controller, while the damping factor remains unchanged, which is caused essentially by the marginal tire damping coefficient. Therefore, the control performance of the EMPC based on the system (6.6) is rather restricted. In order to tackle this problem, the virtual damping coefficient proposed in [128] is applied in the present work as an auxiliary control component.

Based on (6.6), the transfer function of the system is described by

$$G_s(s) = \frac{T_{ss}}{T_{el}} = \frac{c_{ss}^*}{J_r^*} \cdot \frac{1}{s^2 + \omega_0^2}, \quad (6.7)$$

where the marginal damping coefficient k_{ss}^* is neglected. Considering the compensation block with transfer function $G_c(s)$ illustrated in Figure 6.6, the transfer function of the new system is defined by

$$G'_s(s) = \frac{G_s}{1 + G_c G_s} = \frac{\frac{c_{ss}^*}{J_r^*}}{s^2 + \frac{c_{ss}^*}{J_r^*} G_c + \omega_0^2} = \frac{\frac{c_{ss}^*}{J_r^*}}{s^2 + 2\zeta^{\text{mod}} \omega_0 s + \omega_0^2}, \quad (6.8)$$

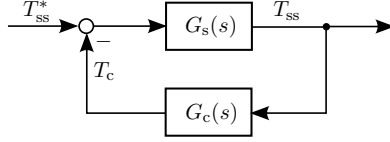


Figure 6.6: Virtual damping coefficient scheme.

where the damping factor of the new system is represented by

$$\zeta^{\text{mod}} = \frac{c_{\text{ss}}^*}{2\omega_0 J_r^*} G_c \frac{1}{s}. \quad (6.9)$$

As implied by this equation, the damping factor ζ^{mod} is modifiable by the transfer function G_c . Subsequently, the compensation torque is calculated by

$$T_c = G_c(s) \cdot T_{\text{ss}} = \frac{2\zeta^{\text{mod}}\omega_0 J_r^*}{c_{\text{ss}}^*} \cdot T_{\text{ss}} \cdot s = 2\zeta^{\text{mod}}\omega_0 J_r^* \cdot (\omega_r - \omega_w). \quad (6.10)$$

Here, the damping k_{ss}^* is neglected, since it is much smaller when compared to the virtual damping coefficient $k_{\text{ss}}^{\text{mod}}$ derived from (6.5). The virtual damping coefficient yields

$$k_{\text{ss}}^{\text{mod}} = 2\zeta^{\text{mod}} \sqrt{\frac{J_r^* J_{\text{vm}}^* c_{\text{ss}}^*}{J_r^* + J_{\text{vm}}^*}}. \quad (6.11)$$

Therefore, the new system is derived by replacing the damping coefficient k_{ss}^* by $k_{\text{ss}}^{\text{mod}}$ in (6.6). Moreover, The dynamic torque constraint discussed in section (5.4) is employed here for the IM. It has to be reconsidered by involving the compensation torque:

$$-\bar{T}_{\text{el}} + T_c \leq T_{\text{el}} \leq \bar{T}_{\text{el}} + T_c. \quad (6.12)$$

Furthermore, the objective function

$$J = \|T_{\text{ss}}^* - T_{\text{ss}}\|_Q^2 + \|T_{\text{el}}\|_R^2 \quad (6.13)$$

is specified for the optimization problem of the active damping control. The parameter vector of the optimization problem is defined by

$$\mathbf{x} = \left[\omega_r \quad \omega_w \quad T_{\text{ss}} \quad T_{\text{load}} \quad T_{\text{ss}}^* \quad \bar{T}_{\text{el}} \quad T_c \right]^T. \quad (6.14)$$

In order to access the state variables, a Kalman filter is applied by using the new state-space representation, whereat the system matrix is expressed as

$$\mathbf{C} = \begin{bmatrix} 1 & 0 & 0 & 0 \\ 0 & 1 & 0 & 0 \end{bmatrix}.$$

The structure of the control approach is illustrated in Figure 6.7.

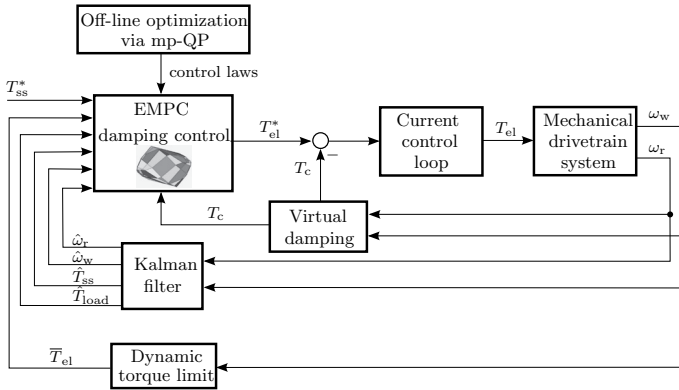


Figure 6.7: Block diagram of the active damping control approach.

6.3 Simulative and experimental results

In the simulation, the control approach is applied to a six-mass-oscillator model with the parameters described in Appendix E. Figure 6.8 illustrates the system response with/without active damping controller. The reference value is changed in step from 0 to 40 Nm. It is evident, that by means of the introduced control approach, the oscillation behavior described by the red line is significantly suppressed and the actual torque denoted by the blue line reaches promptly the reference value.

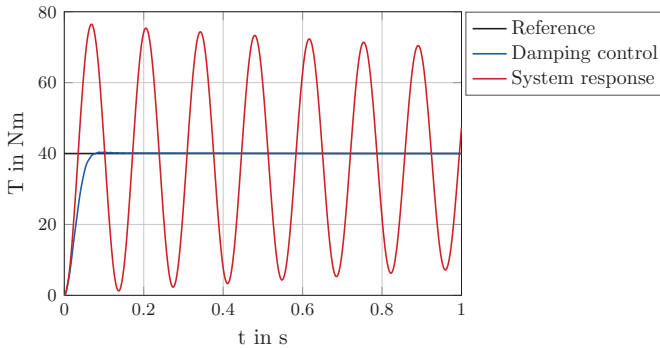


Figure 6.8: Simulation results.

In order to validate the control approach for mechanical drivetrain systems in vehicles, a test bench is set up to simulate the resonance frequency of such a drivetrain. Based on the principle of Laschet's order reduction, a two-mass-oscillator system owning a low resonance frequency is implemented. In Figure 6.9, the test

bench scheme is illustrated.

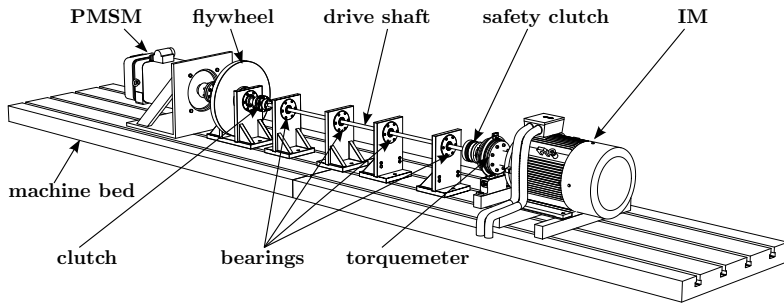


Figure 6.9: Test bench scheme.

Since no gear box is established, the stiffness of the drive shaft in the test bench must be designed much smaller than the one of the side shaft in vehicles (see (6.3b)). The torsion stiffness of a cylinder is determined by

$$c = \frac{\pi G d^4}{32l}, \quad (6.15)$$

where G is the shear modulus of the steel material, d and l the diameter and the length of the cylinder. In order to reduce the stiffness of the steel cylinder, one can either reduce the diameter or increase the length. However, since a certain torque must be transmitted without breaking the shaft, the diameter cannot be arbitrarily decreased. As a consequence, a long drive shaft is employed as shown in Figure 6.9. To ensure the straightness of the shaft, which may be deteriorated by its tare weight, the shaft is supported on several positions with the help of bearings.

The vehicle mass is simulated by means of a flywheel, whose inertia is much larger than the rotor's one. The inertia is defined according to the inertia of the vehicle mass in the two-mass-oscillator system. Moreover, for safety reasons, a safety clutch is introduced. In case that the transmitted torque exceeds the predefined threshold value, this safety clutch is released to decouple the oscillating system. The torque-controlled IM represents the traction motor in EV, while the speed-controlled PMSM simulates the wheel speed, which is given by the dSPACE *Automotive Simulation Models* (ASM) suite introduced in chapter 7. The data of the components in this test bench are given in Appendix E.

In order to attain a high dynamic active damping control, the resonance frequency of this physical system has to be checked and compared to the calculated frequency. This is achieved by applying sinusoidal drive torque with different frequencies on the IM side. This test is performed under diverse vehicle velocities, which implicates different flywheel speeds. The results are illustrated in Figure 6.10. It is important to note, that independent on the vehicle velocity, the resonance frequency of the mechanical drivetrain in combination with the vehicle simulation stays at around

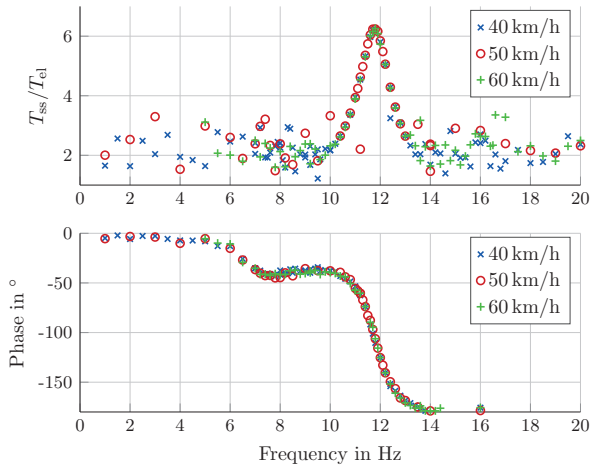


Figure 6.10: Identification of resonance frequency.

11.8 Hz, which corresponds to the calculated value according to the component data in Appendix E.

The experimental result of aforementioned system is presented in Figure 6.11. A step reference change from 0 to 40 Nm is applied at a vehicle velocity of 50 km/h. Same as in the simulation, the oscillation behavior of the system is significantly suppressed by means of the active damping control approach. The reference torque is achieved within 0.2 s. The slight overshooting of the step response is able to be diminished by the outer control loop, which has a lower dynamic and can be therefore considered as a low-pass filter for the damping control loop.

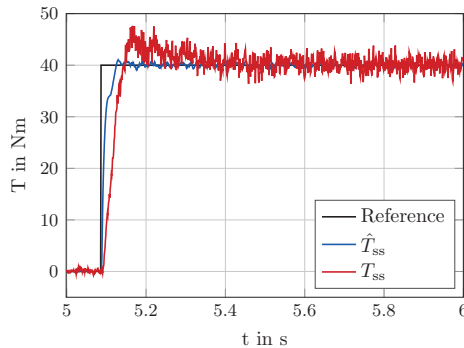


Figure 6.11: Experimental result.

6.4 Summary

In this chapter, the mechanical drivetrain in vehicles is discussed. Due to its elastic joints, the system exhibits oscillating behavior. In order to suppress such torsional oscillations and improve the system performance, an active damping control approach is implemented. In order to validate this approach and to integrate the electrical drivetrain, a drivetrain system is assembled in a test bench, in which the resonance frequency is simulated on the drive shaft and the drive torque is generated by the controlled IM and transferred to the drive shaft. In the next step, the entire drivetrain system is combined with the vehicle dynamic model. The TV application is implemented based on the assembled system.

7 High-performance torque vectoring control

Recalling the requirements and specifications introduced in chapter 2, a high-performance torque vectoring control approach is implemented in this chapter. The vehicle modeling is discussed in section 7.1. To enhance the system performance, both the active yaw rate control and the tire slip control are implemented in this work, which are explained in section 7.2. The operation strategy interacting with the driver's demand is introduced in section 7.3. Since a limited number of sensors are assumed to be applied in the present work, a set of not practically measurable quantities, which are employed for the control strategy, have to be estimated. The estimation procedure is depicted in section 7.4.

7.1 Vehicle modeling

In order to replicate the physical system as close as possible, the dSPACE ASM suite, in which vehicle dynamics and nonlinearities are comprehensively modeled [52], is applied in this work. In this section, issues are discussed, which are relevant to the design of a high-performance control.

The physical quantities in the vehicle system are based on diverse coordinate systems. Therefore, to prevent confusions, it is necessary to preliminarily introduce these coordinate systems, the definition of the transformation between them, as well as the notations of the physical quantities, before the vehicle system is analyzed. These are given in section 7.1.1. Furthermore, the pneumatic tires of a road vehicle significantly influence the dynamic interaction between vehicle and road, which further changes the overall vehicle behavior, maneuverability, and driving experience. Consequently, understanding this vehicle component from a physical point of view is essential for accurately analyzing and predicting vehicle behavior. This is in turn required for the development of capable drive dynamics control systems and is therefore discussed in section 7.1.2. In section 7.1.3 and 7.1.4, the linear single track model and dual track model applied in the control design, are introduced respectively.

7.1.1 Coordinate systems

Within the scope of the present work, Newtonian mechanical laws are appropriate to describe the motion of rigid bodies under the influence of forces in space time. As the modeling in this work heavily relies on non-inertial reference systems, a coordinate transformation is introduced that facilitates the application of Newton's laws in accelerated reference systems. In regards to the following context the international

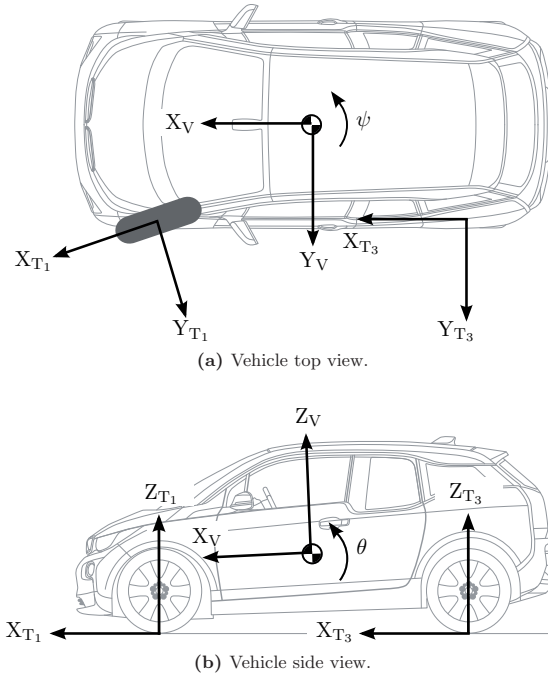


Figure 7.1: The Vehicle Coordinate System [22].

standard of the ISO 8855 Road Vehicles – Vehicle dynamics and road-holding ability – Vocabulary [6] is of high relevance and used as a reference.

Inertial reference frame

The *Inertial Reference Frame* (IRF) in the present work is defined as a special case of an inertial frame of reference with a constant speed of motion equal to zero. Accordingly, it exhibits neither linear nor rotational velocity and accelerations. Although not exactly valid for the Earth, in Newton mechanics the Earth is indeed assumed as an IRF, which offers more than sufficient accuracy for the scope of the present work. The IRF can be identified with a reference coordinate system, usually referred to as the *Earth Coordinate System* (ECS) E . The ECS enables a spacial parameterization of the IRF and unique definition of position with respect to an arbitrary but fixed reference point, denoted with the origin O . Furthermore, the ECS is composed of three orthogonal space axes $\{X, Y, Z\}$ forming a right-handed coordinate system $E = \{O, X, Y, Z\}$. Each point in space may then be identified with respect to O using a set of Cartesian coordinates $\{x, y, z\}$. The Z -axis of ECS is

oriented perpendicularly to the horizontal plane spanned by X and Y and is therefore parallel to the gravitational field.

Vehicle coordinate system

The *Vehicle Coordinate System* (VCS) represents another reference frame that is rigidly attached to the vehicle sprung mass. It is composed of a right-handed, orthogonal axis system $\{X_V, Y_V, Z_V\}$, and an origin O_V located at the vehicle body's CoG. Its X_V -axis points horizontally towards the front of the vehicle and lies on the vehicle body's longitudinal center plane. The Y_V -axis is oriented perpendicularly to this center plane, pointing to the left side of the vehicle (see Figure 7.1a). Finally, the Z_V -axis points upwards (see Figure 7.1b). Again, a set of Cartesian coordinates $\{x_V, y_V, z_V\}$ is introduced, providing means to describe positions and vector quantities with respect to the VCS E_V . To avoid the contextual ambiguities, quantities expressed in vehicle coordinates are indicated by superscript V .

Due to forces acting on the vehicle body, the VCS may exhibit angular inclinations relative to the ECS. Any rotation of the VCS relative to the ECS can be attained using a sequence of elementary rotations related to a set of angles $\{\psi, \theta, \varphi\}$, referred to as Tait-Bryan angles [76]. From six possible rotation sequences, the yaw-pitch-roll convention commonly used in engineering science is chosen for the present work [76]. In this context the set $\{\psi, \theta, \varphi\}$ denote the Kardan angles [167]. Furthermore, two intermediate axes X_H, Y_H need to be introduced (see Figure 7.2). Both axes lie on the horizontal plane (X - Y plane), where X_H is the projection of X_V onto this plane and Y_H is oriented perpendicularly to X_H .

The first rotation (1) is performed about the Z -axis until the X and X_H axes representing the yaw angle ψ . The second rotation (2) is performed by the VCS rotation about the Y_H -axis until the X_H and X_V axes constituting the pitch angle θ . Such an angle is usually induced under acceleration or braking conditions. The third rotation (3) is performed about the longitudinal X_V -axis describing the roll motion of the vehicle body. The resulting angle between the Y_H and Y_V axes is denoted by the roll angle φ .

The VCS is only subject to the previously described angular motion relative to the ECS. This means, O_V does not exhibit translational motion relative to the ECS. This observation is of great importance in the context of coordinate transformations discussed later on.

Tire coordinate systems

The set of coordinate systems $\{E, E_V\}$ is complemented by four additional *Tire Coordinate Systems* (TCS). For each tire, the origin O_{T_i} of the underlying right-handed is typically called *Contact Point* (CP), where $i \in \{1, 2, 3, 4\}$ with the definition given in Table 7.1. Both axes X_{T_i} and Y_{T_i} lie on the local road-surface plane. With X_{T_i} defined as the intersection of the tire's longitudinal center plane

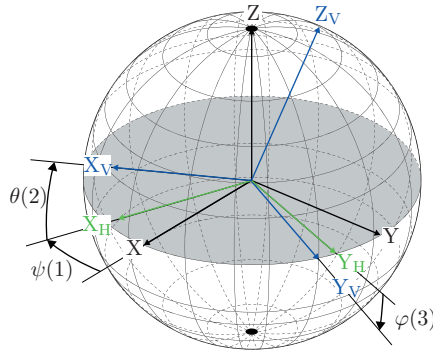


Figure 7.2: Definition of Kardan angles.

and the local road-surface, tire coordinate systems are uniquely defined. A set of Cartesian coordinates $\{x_{T_i}, y_{T_i}, z_{T_i}\}$ is introduced to describe positions and vector quantities corresponding to the four TCS. In order to avoid contextual ambiguities, quantities expressed in tire coordinates are indicated by superscript T_i . Analogous to the aforementioned VCS, the four TCS are limited to rotational motion relative to the ECS. Figures 7.1a and 7.1b illustrate these definitions for the *Front Left* (FL) and *Rear Left* (RL) tires.

T_i	1	2	3	4
Tire	Front Left (FL)	Front Right (FR)	Rear Left (RL)	Rear Right (RR)

Table 7.1: Equivalence between index i and tire position.

Coordinate transformations

Since the introduced coordinate systems are subject to motion relative to each other, it is helpful to introduce a matrix transformation that facilitates conversion of vector quantities among those coordinate systems. This can be achieved by employing the procedure used earlier to rotate the VCS with respect to the ECS based on a sequence of elementary rotations using Kardan angles. Mathematically, this can be lumped into a single matrix [76]:

$$\mathbf{R} = \begin{pmatrix} \cos \psi \cos \theta & \sin \psi \cos \theta & -\sin \theta \\ \cos \psi \sin \theta \sin \varphi - \sin \psi \cos \varphi & \sin \psi \sin \theta \sin \varphi + \cos \psi \cos \varphi & \cos \theta \sin \varphi \\ \cos \psi \sin \theta \cos \varphi - \sin \psi \sin \varphi & \sin \psi \sin \theta \cos \varphi - \cos \psi \sin \theta & \cos \theta \cos \varphi \end{pmatrix} \quad (7.1)$$

Now, let $\mathbf{q}^V = (q_x, q_y, q_z)^T$ denote a generic vector quantity expressed in ESC. Then, applying \mathbf{R} to \mathbf{q} , a representation in the VCS \mathbf{q}^V with x_V, y_V, z_V yields:

$$\mathbf{q}^V = \mathbf{R} \cdot \mathbf{q}. \quad (7.2)$$

Deriving (7.2) with respect to time gives the time derivative of \mathbf{q} expressed in Vehicle coordinates:

$$\dot{\mathbf{q}}^V = \dot{\mathbf{R}} \cdot \mathbf{q} + \mathbf{R} \cdot \dot{\mathbf{q}}. \quad (7.3)$$

Equation (7.3) may be reformulated as follows

$$\dot{\mathbf{q}}^V = \mathbf{R} \cdot \dot{\mathbf{q}} - \mathbf{R}(\boldsymbol{\omega} \times \mathbf{q}), \quad (7.4)$$

where $\boldsymbol{\omega} = \frac{d}{dt}(\theta, \varphi, \psi)^T$ denotes the instantaneous angular velocity of the vehicle body with respect to the ECS [164].

7.1.2 Tire modeling

A state-of-the-art reference on this matter, vehicle and tire dynamics [139] by Dutch engineer Hans B. Pacejka is utilized throughout the present work. The tire models derived and validated in [139], such as the *Magic Formula* (MF), are applied in various engineering disciplines and range from implementations in computer games to professional simulation tools employed in the automotive industry.

Definition of basic tire quantities

A correct application of the tire model used in this work requires a careful definition of the model input quantities. First, a pneumatic tire with rim depicted in Figure 7.3b is considered¹ with several radii, where R_0 is the unloaded or manufactured tire radius, R the loaded tire radius, and R_{dyn} the effective rolling radius. The difference between R_0 and R , denoted as the radial tire deflection $\delta_R = R_0 - R$, is the consequence of the tire's air-spring-like behavior under the influence of a wheel load force F_z . The definition of R_{dyn} is less straightforward: One considers a free-rolling² wheel dragged on an even, horizontal plane, such that it exhibits zero torque τ ³ (neglecting the small rolling resistance portion). By measuring the distance, the tire travels within one revolution U (also rolling circumference). R_{dyn} is defined as follows [139, 2]:

$$R_{\text{dyn}} = \frac{U}{2\pi}. \quad (7.5)$$

Then, in free-rolling condition, the circle with radius R_{dyn} , which is called as lip circle, rolls over an imaginary line parallel to the road plane. This line corresponds

¹ When talking about wheels, the tire-rim-entity is intended.

² Rolling motion is a combination of rotational and translational motion.

³ τ is used instead of T throughout this chapter to differ from the tire symbol.

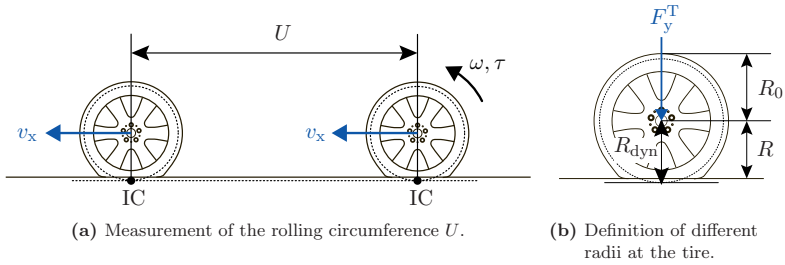


Figure 7.3: Definition of the effective rolling radius R_{dyn} .

to the locus of the *Instantaneous Center (IC)* of wheel rotation, therefore is denoted as fixed centrod of the wheel motion (see Figure 7.3a) [167]. The wheel's rotational velocity about its spindle axis is given by $\omega = v_x/R_{\text{dyn}}$, where v_x is the velocity of the CP in X_T -direction. Tire particles located at the IC exhibit zero velocity.

In the general case, the wheel is subjected to either driving or braking torque. The IC moves relative to O and the points on which slip circle and fixed centrod intersect and have $\tau = 0$ in the previous case now have a non-zero velocity. This velocity is called longitudinal slip speed and defined as $v_{\text{sx}} = v_x - \omega R_{\text{dyn}}$. More commonly, the slip ratio or longitudinal slip defined as follows is employed:

$$s_x = -\frac{v_{\text{sx}}}{v_x}. \quad (7.6)$$

Figure 7.4 gives an overview of different cases of (7.6) and depicts the relevant

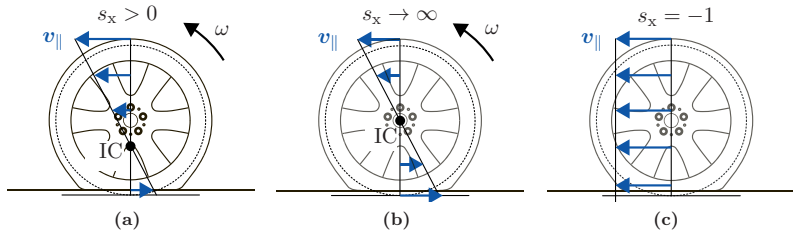


Figure 7.4: Tangential velocity distribution v_{\parallel} at the lateral tyre center plane under different slip ratios.

tangential velocity vectors v_{\parallel} at the wheel's lateral center plane, indicating the changing position of the IC. Figure 7.4a depicts the driving case. Figures 7.4b and 7.4c show the special cases of wheel spin and wheel lock, respectively. In a similar manner to (7.6), a lateral slip or side slip may be defined as

$$s_y = \tan \alpha = \frac{v_y}{v_x}, \quad (7.7)$$

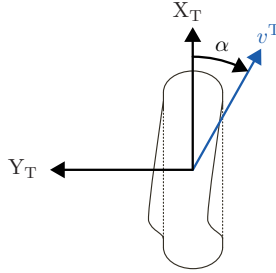


Figure 7.5: Definition of the tire slip angle α .

where v_y denotes the velocity of the CP in Y_T -direction and α the tire slip angle (see Figure 7.5). By analogy with v_{sx} , v_y describes the velocity of the rubber particles in the CP relative to the road-surface in the lateral direction. The definition of slip quantities given in this section implies that tires are only able to produce longitudinal or lateral forces at cases in which either non-zero slip ratio or side slip takes place.

Magic formula tire model

In the present work, the semi-empirical MF model is utilized and discussed in the following. Input to the MF is the (longitudinal) slip ratio s_x , side slip s_y , tire load force F_z , and wheel camber γ . Here, γ denotes the tilt angle between the longitudinal tire center plane and the local road-surface plane. Camber represents a degree of freedom in the suspension design that can be used to improve the lateral force potential of the tires [80]. The MF is applicable in the exclusively longitudinal and lateral slip cases as well as in the combined slip case. For the exclusively slip cases the tire forces are obtained from the sine-version of the MF. Its general analytical structure is

$$F_{i0}(u_i) = D_i \sin(C_i \arctan[B_i \bar{s}_i - E_i (B_i \bar{s}_i - \arctan B_i \bar{s}_i)]) + S_{V_i}, \quad (7.8)$$

where $i \in \{x, y\}$, $\bar{s}_i = s'_i + S_{H_i}$, and the input variables $s'_x = s_x \cdot \text{sgn } v_x$, $s'_y = s_y \cdot \text{sgn } v_x$. The offset parameters S_{H_i} , S_{V_i} enable a shifting of the nominal curve ($S_{H_i} = S_y = 0$) with respect to the origin in horizontal (S_{H_i}) and vertical (S_{V_i}) directions, respectively. Offset parameters usually appear as non-zero due to ply-steer or conicity, when tire pull forces are present. Both effects induce side forces at zero tire slip angle and are the consequences of tire non-uniformity [4, 30]. The peak value D_i determines the maximum (minimum) value that (7.8) may attain. The slope of (7.8) in the linear region around the origin corresponds to the product $B_i C_i D_i$. The shape factor C_i controls the influence of the sine-function in (7.8), leaving B_i to set the desired slope around the origin. Consequently, B_i is referred to as the stiffness factor and it is applied in case of $C_s = B_x C_x D_x|_{\bar{s}_x=0}$ (traction stiffness) and $C_\alpha = B_y C_y D_y|_{\bar{s}_y=0}$ (cornering stiffness). Finally, the curvature factor E_i defines the curvature of (7.8) around its extremal points as well as their horizontal

positions. The dependency of MF on F_z and γ is implied by its coefficients' relationship with these quantities. Figure 7.6 depicts the typical shape of (7.8)

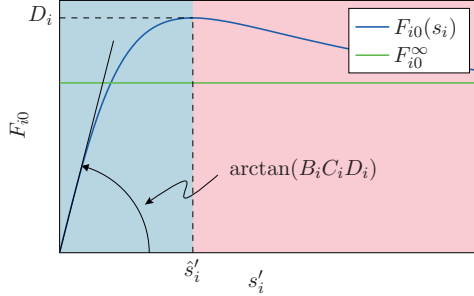


Figure 7.6: Sine-version of the Magic Formula.

without offsets: From $u_i = 0$ the MF passes through the origin, subsequently reaching its peak value by \hat{s}_i and eventually settling on a horizontal asymptote F_{i0}^{∞} . For the combined slip case MF is extended with a weighting function

$$G_{ij}(v_j) = \frac{\cos(C_{ij} \arctan[B_{ij}\bar{s}_j - E_{ij}(B_{ij}\bar{s}_j - \arctan B_{ij}\bar{s}_j)])}{\cos(C_{ij} \arctan[B_{ij}S_{Hij} - E_{ij}(B_{ij}S_{Hij} - \arctan B_{ij}S_{Hij})])}, \quad (7.9a)$$

$j \in \{x, y\}, i \neq j$ such that

$$F_x(s'_x, s'_y) = F_{x0}(s'_x) \cdot G_{xy}(s'_y) \quad (7.9b)$$

$$F_y(s'_x, s'_y) = F_{y0}(s'_y) \cdot G_{yx}(s'_x) + S_{Vyx}, \quad (7.9c)$$

and $\bar{s}_j = s'_j + S_{Hij}$. The full set of MF-equations required for the computation of longitudinal and lateral tire forces is provided in Appendix F.1.

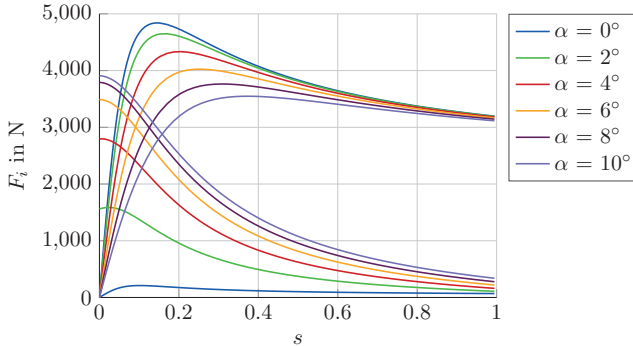


Figure 7.7: Longitudinal and lateral tire forces produced by the MF at varying α .

Figure 7.7 depicts a typical family of curves for the longitudinal and lateral tire forces depending on s_x , at varying α . It can be observed that an increasing tire slip angle

α reduces the available traction force F_x . At large longitudinal slip values ($s_x \rightarrow 1$), this reduction converges to zero as the lateral tire force vanishes. For the side force F_y , the maximum value is attained at $s_x = 0$ and it increases with α . The coherence underlying those observations is represented through the so-called *Tire-Force Ellipse* (TFE) in the following.

Tire-force ellipse

Under the assumption of exclusively longitudinal or lateral slip, the maximum force a tire is able to produce is limited by the product of the friction coefficient⁴ and tire load force:

$$F_{x,\max} = \mu_x \cdot F_z, \quad (7.10a)$$

$$F_{y,\max} = \mu_y \cdot F_z. \quad (7.10b)$$

It is important to note that the maximum force in x- or y-direction can only be fulfilled when the other is zero. Based on those limits, a peak slip ratio \hat{s}_x is attained for $F_{x,\max}$ and a peak side slip $\hat{s}_y = \tan \alpha_{\text{th}}$ for $F_{y,\max}$ exist. If the slip is increased beyond its peak value, the corresponding tire force commences to decrease and finally approaches an asymptotic value. From a drive dynamics control point of view, it is essential to obey these limits, since their violation potentially results in unstable vehicle behavior. Equations (7.10a) and (7.10b) emphasize that a real-world tire may have different friction coefficients in longitudinal (μ_x) and lateral (μ_y) directions.

In the combined slip case, both longitudinal and lateral tire forces are present. The force \mathbf{F} is composed of elements F_x and F_y , whereat the maximum available friction force remains unchanged. Under the assumption of symmetric friction coefficients $\mu_x = \mu_y = \mu$, the maximum value of \mathbf{F} may attain before the tire starts to skid. Mathematically, this relationship writes

$$F_{\max} = \mu \cdot F_z = F_{x,\max} = F_{y,\max}, \quad (7.11)$$

where $F = \|\mathbf{F}\|_2$. This circle-based representation of the limit of adhesion was first formulated and published by Wunibald I. E. Kamm and therefore named after him as *Kamm Circle* [149]. For the more general case $\mu_x \neq \mu_y$, the same notion may be employed resulting in an elliptic representation of the tire force limits [28]:

$$\frac{F_x^2}{\mu_x^2} + \frac{F_y^2}{\mu_y^2} \leq F_z^2. \quad (7.12)$$

Figures 7.8 and 7.9 depict the TFE for $\mu_x = 1.21$ and $\mu_y = 0.99$ (see Appendix F.1) in comparison to the curves produced by the MF at $F_z = 4000$ N. In Figure 7.8 the tire slip angle α is varied. Figure 7.9 shows the variation of the slip ratio s_x . Evidently, the TFE represents a quite accurate approximation of the envelope defined by

⁴ The *effective friction coefficients* $\mu_i^{\text{eff}} = \max\{F_i/F_z\}$, $i \in \{x, y\}$, introduced in this section must not be confused with the physical static and dynamic friction coefficients introduced earlier.

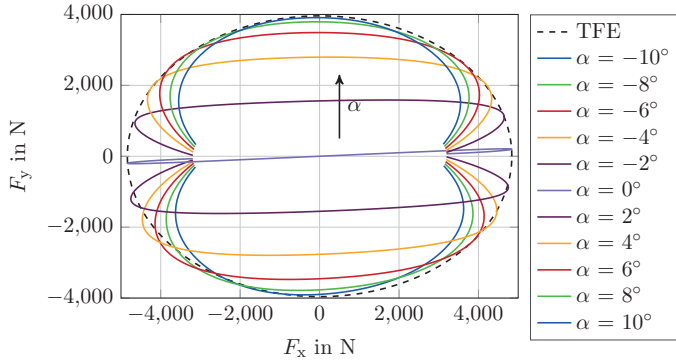


Figure 7.8: Tire-Force Ellipse at varying α .

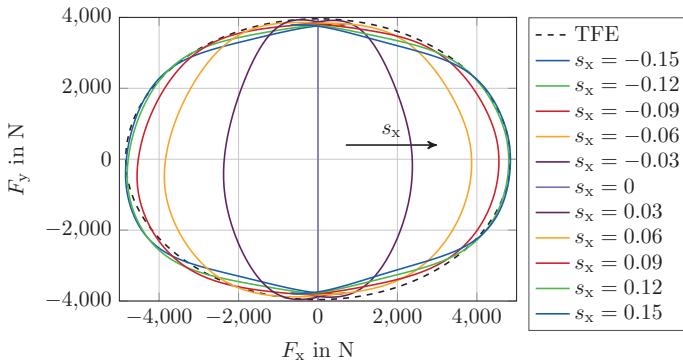


Figure 7.9: Tire-Force Ellipse at varying s_x .

the true maximum tire forces. Due to effects caused by tire non-uniformity and anisotropy, a slight discrepancy between the ideal and the real-world curves can be expected.

An important statement regarding the tire behavior can be derived from the TFE: At given lateral tire force, the occurrence of any traction force (braking or accelerating) may cause the tire to increase its slip angle. This fundamental relation becomes of a great importance when a vehicle in a heavy cornering situation is considered: If one tire is already close to its peak side slip value (e.g. due to fast cornering), a braking intervention potentially make the slip angle exceeding the peak value, which effectively diminishes the lateral tire force. Depending on the vehicle's state of motion, unstable behavior, like spin out, may be the consequence [80].

7.1.3 Linear single track model

In this section a simple vehicle model is derived with the objective to analyze and discuss basic vehicle cornering behavior. The so-called *Linear Single Track Model* (LSTM) facilitates a physically plausible and convenient approach to this matter by incorporating the following approximations [167]:

- ▷ Longitudinal vehicle dynamics are neglected, i.e. the velocity magnitude at the CoG remains constant ($v = \text{const.}$). In other words, there is no presence of the traction forces, which means the vehicle is neither subjected to braking interventions nor to accelerations ($\sum_{i=1}^4 F_x^{T_i} = 0$).
- ▷ Vertical vehicle dynamics are neglected. This includes vanishing of the vertical force at the CoG ($F_z^V = 0$), negligence of roll and pitch motion of the chassis ($\theta = \varphi = 0$), and additionally, a static wheel load distribution.
- ▷ The mass distribution of the vehicle is lumped into a point mass m located at the vehicle's CoG.
- ▷ On both vehicle axes (front and rear), the left and right tires are consolidated into one tire that is shifted to the vehicle's longitudinal center plane. Each entailed virtual tire has a stiffness that is equivalent to the sum of the individual stiffnesses of the left and right tires.
- ▷ The elasticity of the steering system is disregarded, which significantly cancels the effects due to the presence of alignment torque.
- ▷ Aerodynamic drag forces and resultant torques are neglected.

Input to the LSTM is the steer angle δ . The LSTM provides physically reasonable results up to lateral accelerations of $|a_y| = 4 \text{ m s}^{-2}$ on dry roads [12].

From the first two assumptions it may be inferred that the vehicle motion is constrained to translation in X_V - and Y_V -direction and rotation about the vertical Z_V -axis. Hence, the number of Degrees of Freedom (DOFs) is reduced from six to three⁵, whereat X_V -direction is neglected since no longitudinal acceleration exists. This information is used to define a couple of state-space variables representing those two remaining DOFs:

$$\mathbf{x}^T = \begin{bmatrix} x_1 & x_2 \end{bmatrix}^T = \begin{bmatrix} \beta & \psi \end{bmatrix}^T. \quad (7.13)$$

Symbol β denotes the angle of the velocity vector \mathbf{v} with respect to the vehicle's CoG and the longitudinal X_V -axis of the VCS and is referred to as the vehicle sideslip angle. According to this, β can be described in vehicle coordinates:

$$\beta = \arctan \left(\frac{v_y^V}{v_x^V} \right). \quad (7.14)$$

⁵ An unconstrained rigid body has six DOFs: three translational (X, Y, Z) and three rotational (θ, φ, ψ).

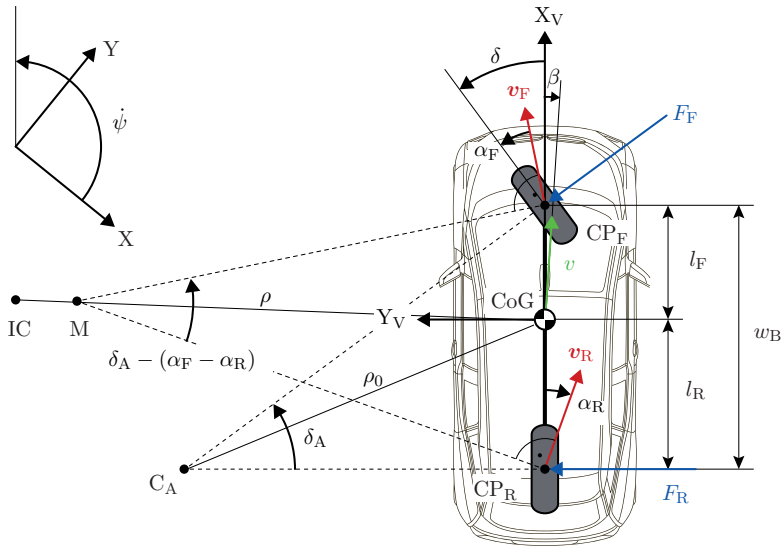


Figure 7.10: Geometry and kinematics of the LSTM.

The second state-space variable $\dot{\psi}$, named the yaw rate, denotes the time derivative of yaw angle ψ . Figure 7.10 qualitatively depicts geometric and kinematic quantities relevant for the subsequent derivation of the model. Before proceeding the LSTM, the so-called *Ackermann Angle* δ_A needs to be introduced as a measure to describe the vehicle's cornering behavior at low speeds. In these situations, tire forces vanish and the vehicle trajectory corresponds to a circle with the radius ρ_0 . In order to maintain this trajectory the front wheel has to be steered by δ_A , which is approximately given as

$$\delta_A \approx \frac{w_B}{\rho_0}, \quad (7.15)$$

with w_B denoting the wheel base [72]. The geometric path radius ρ_0 is a special case of the instantaneous path radius ρ that describes the distance between IC and CoG. The definition of ρ follows

$$\rho = \frac{v}{\dot{\psi} + \dot{\beta}}, \quad (7.16)$$

where the angle $\psi + \beta$ is referred to as the *course angle*.

For the time derivation of the first kinematic equation with respect to β , Newton's Second Law, stating that the sum of all external forces acting on a rigid body is equal to the rate of change of its linear momentum \mathbf{p} , is employed. Therefore, it is

also referred to as the *principle of linear momentum* and given as follows:

$$\mathbf{F} = \frac{d\mathbf{p}}{dt} = m \cdot \frac{d\mathbf{v}}{dt}. \quad (7.17)$$

The analysis of the vehicle cornering behavior is simplified by rewriting (7.17) in vehicle coordinates. This is achieved in two steps: First the coordinate transformation (7.2) is applied to (7.17):

$$\mathbf{F}^V = \mathbf{R} \cdot \mathbf{F} = m \cdot \mathbf{R} \cdot \frac{d\mathbf{v}}{dt}. \quad (7.18)$$

Now, Newton's Second Law is given in vehicle coordinates except for the time derivative $\frac{d\mathbf{v}}{dt}$. Using expression (7.4) this derivative can be stated in vehicle coordinates as well, such that

$$\mathbf{F}^V = m \cdot \left(\frac{d\mathbf{v}^V}{dt} + \boldsymbol{\omega} \times \mathbf{v}^V \right) \quad (7.19)$$

with

$$\boldsymbol{\omega} = \begin{bmatrix} 0 \\ 0 \\ \dot{\psi} \end{bmatrix} \quad \text{and} \quad \mathbf{R} = \begin{bmatrix} \cos \psi & \sin \psi & 0 \\ -\sin \psi & \cos \psi & 0 \\ 0 & 0 & 1 \end{bmatrix}. \quad (7.20)$$

Decomposing (7.19) to its longitudinal and lateral components (the assumption $F_z^V = 0$ holds), according to (7.14) in consideration of $v = \|\mathbf{v}\|_2 = \text{const.}$, yields:

$$\frac{F_x^V}{m} = -v \left(\dot{\psi} + \dot{\beta} \right) \sin \beta, \quad (7.21)$$

$$\frac{F_y^V}{m} = v \left(\dot{\psi} + \dot{\beta} \right) \cos \beta. \quad (7.22)$$

Now the Left-Hand-Sides (LHS) of (7.21) and (7.22) are investigated. The sums of the longitudinal and lateral forces acting on the CoG are given as follows when a steered front wheel ($\delta \neq 0$) and zero traction forces ($\sum F_x^{\text{T}_i} = 0$, $i \in \{\text{(F)ront}, \text{(R)ear}\}$) are taken into account:

$$F_x^V = -F_y^{\text{T}_F} \cdot \sin \delta, \quad (7.23)$$

$$F_y^V = F_y^{\text{T}_F} \cdot \cos \delta + F_y^{\text{T}_R}. \quad (7.24)$$

By computing the sum of (7.21) and (7.22) and then substituting corresponding terms in equations (7.23) – (7.24), a single equation for β can be obtained:

$$\dot{\beta} = \frac{F_y^{\text{T}_F} (\sin \delta + \cos \delta) + F_y^{\text{T}_R}}{mv (\sin \beta + \cos \beta)} - \dot{\psi}. \quad (7.25)$$

The lateral tire forces $F_y^{\text{T}_F}$ and $F_y^{\text{T}_R}$ are obtained from a linear tire model

$$F_y^{\text{T}_F} = C_\alpha^F \cdot \alpha_F \quad (7.26) \quad F_y^{\text{T}_R} = C_\alpha^R \cdot \alpha_R, \quad (7.27)$$

where α_F and α_R are the tire slip angles at the front and rear wheel, respectively, whereas C_α^F and C_α^R are the corresponding cornering stiffnesses. Following the definition of the tire slip angle (7.7) from Section 7.1.2 and remembering the vehicle's rotational motion yields

$$\tan(\delta - \alpha_F) = \frac{v \cdot \sin \beta + l_F \cdot \dot{\psi}}{v \cdot \cos \beta} \quad \text{and} \quad (7.28)$$

$$-\tan \alpha_R = \frac{v \cdot \sin \beta - l_R \cdot \dot{\psi}}{v \cdot \cos \beta}. \quad (7.29)$$

Here, l_F and l_R denote the distances from the front and rear axle to the CoG.

In the present work, the analysis of the vehicle behavior may be restricted to values of β below six degrees (see section 2.3.2). Hence, $\cos \beta \approx 1$ and $\sin \beta \approx \beta$ are reasonable approximations. The same approximations are applicable for the side slip ($\tan \alpha_i \approx \alpha_i$) and steer angles such that:

$$\alpha_F \approx \delta - \beta - \frac{l_F \cdot \dot{\psi}}{v}, \quad (7.30) \quad \alpha_R \approx -\beta + \frac{l_R \cdot \dot{\psi}}{v}. \quad (7.31)$$

Substituting the tire slip angles into (7.26) and (7.27) by elaborated expressions derived in (7.30) and (7.31), and subsequently inserting the results in (7.25), yields:

$$\dot{\beta} = \frac{C_\alpha^F \left(\delta - \beta - \frac{l_F \dot{\psi}}{v} \right) (\sin \delta + \cos \delta) + C_\alpha^R \left(\frac{l_R \dot{\psi}}{v} - \beta \right)}{mv (\sin \beta + \cos \beta)} - \dot{\psi}. \quad (7.32)$$

Finally, (7.32) may be further simplified by assuming $\sin x + \cos x \approx 1$, $x \in \{\beta, \delta\}$, which is implicit for the angle approximations made previously. This results in

$$\dot{\beta} \approx \frac{1}{mv} \left[C_\alpha^F \delta - \beta (C_\alpha^F + C_\alpha^R) - \frac{\dot{\psi}}{v} (mv^2 + C_\alpha^F l_F - C_\alpha^R l_R) \right]. \quad (7.33)$$

The second kinematic equation regarding $\dot{\psi}$ is derived by means of the Newton Euler Equation. This equation embodies the *principle of angular momentum* stating that the rate of change of angular momentum about a rigid body's CoG is equivalent to the sum of external torques acting on the CoG:

$$\frac{d\mathbf{L}}{dt} = \boldsymbol{\tau} = \mathbf{I} \cdot \dot{\boldsymbol{\omega}} + \boldsymbol{\omega} \times (\mathbf{I} \cdot \boldsymbol{\omega}). \quad (7.34)$$

In (7.34) \mathbf{L} denotes the angular momentum. It is assumed that the axes of the VCS coincide with the vehicle's principle axes (axes of symmetry) such that the inertia tensor \mathbf{I} reduces to a 3×3 diagonal matrix $\mathbf{I} = \text{diag}(I_x, I_y, I_z)$. The diagonal elements correspond to the inertias about the vehicle's principal axes. Due to the existence of the constraints on the LSTM only one independent equation remains from (7.34):

$$\sum \tau_z = I_z \cdot \ddot{\psi}. \quad (7.35)$$

The torque about the vehicle's vertical Z_V -axis is induced by the lateral tire forces that do not directly act on the CoG. The geometry introduces two levers l_F and l_R which are multiplied with the corresponding tire force result in $\sum \tau_z$:

$$I_z \cdot \ddot{\psi} = F_y^{\text{TF}} \cdot l_F \cdot \cos \delta - F_y^{\text{TR}} \cdot l_R. \quad (7.36)$$

Again, the tire forces can be replaced using (7.26), (7.27) in conjunction with (7.30), (7.31). Applying $\cos \delta \approx 1$ yields:

$$\ddot{\psi} \approx \frac{1}{I_z} \left[C_\alpha^{\text{F}} l_F \delta + \beta (C_\alpha^{\text{R}} l_R - C_\alpha^{\text{F}} l_F) - \frac{\dot{\psi}}{v} (C_\alpha^{\text{F}} l_F^2 + C_\alpha^{\text{R}} l_R^2) \right]. \quad (7.37)$$

Ultimately, the state-space representation of the LSTM with two DOFs is given as follows:

$$\begin{bmatrix} \dot{\beta} \\ \dot{\psi} \end{bmatrix} = \begin{bmatrix} -\frac{1}{v} \frac{C_\alpha^{\text{F}} + C_\alpha^{\text{R}}}{m} & -1 - \frac{1}{v^2} \frac{C_\alpha^{\text{F}} l_F - C_\alpha^{\text{R}} l_R}{m} \\ -\frac{C_\alpha^{\text{F}} l_F - C_\alpha^{\text{R}} l_R}{I_z} & -\frac{1}{v} \frac{C_\alpha^{\text{F}} l_F^2 + C_\alpha^{\text{R}} l_R^2}{I_z} \end{bmatrix} \begin{bmatrix} \beta \\ \psi \end{bmatrix} + \begin{bmatrix} \frac{C_\alpha^{\text{F}}}{mv} \\ \frac{C_\alpha^{\text{F}} l_F}{I_z} \end{bmatrix} \delta. \quad (7.38)$$

7.1.4 Dual track model

In the previous discussion the axle load transfer phenomenon has not been mentioned. Axle load transfer describes the effects that forces acting on the vehicle's CoG virtually always impose torque on the vehicle body. As a consequence, this leads to a change of the tire load distribution. Axle load transfer can only be explained by means of three-dimensional models that allow positioning of the CoG at a certain height. The significance of axle load transfer becomes apparent when the cornering stiffness' dependence on the tire load force is recalled. In case of the LSTM, linear tire characteristics are assumed, which also imply $C_\alpha \propto F_z^{\text{T}}$. Since the load excess at the (curve) outer tire can be compensated by the load deficit at the inner tire, the lumped cornering stiffnesses at both axles (C_α^{F} , C_α^{R}) may remain constant. While this method is valid only for lateral accelerations smaller than 0.4g, tire nonlinearities cause the cornering stiffness to increase more slowly at larger lateral accelerations, resulting in reduction of the effective cornering stiffnesses [167]. It can therefore be concluded, that an accurate simulation of cornering behavior up to the tires' limit of adhesion can only be accomplished when all four tires are treated individually.

The nonlinear Dual Track Model (DTM) employed in this work features three explicit DOFs, namely x_V , y_V and ψ , and eight implicit DOFs. Among these DOFs, four are given by the rotational velocities about each wheel's spinning axis ω_i , $i \in \{1 \dots 4\}$, entering the model implicitly through the slip ratios $s_x^{\text{T}i}$. The remaining four DOFs enter the model by means of the dynamic load forces $F_z^{\text{T}i}$, effectively incorporating the axle load transfer phenomenon.

The derivation process of the DTM's equations of motion is similar to the one performed for the LSTM. Differences occur because additional tire forces need to be included in the Newton and Euler equations (see Figure 7.11). Eventually, when a

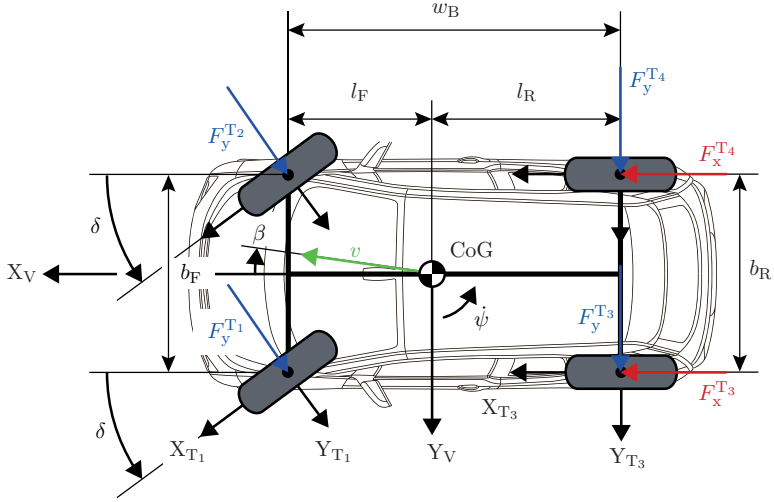


Figure 7.11: Geometry and kinematics of the Dual Track Model.

rear-wheel drive vehicle ($F_x^{T1} = F_x^{T2} = 0$) is considered in the absence of the road incline as well as lateral drag forces, the following non-linear and input affine state space equations is obtained:

$$\dot{\mathbf{x}} = \mathbf{F}(\mathbf{x}) + \mathbf{G}(\mathbf{x})\mathbf{u}, \quad (7.39) \quad \mathbf{x} = [v \quad \beta \quad \dot{\psi}]^T, \quad (7.40)$$

$\mathbf{F}(\mathbf{x}) =$

$$\begin{bmatrix} \frac{1}{m} [\sin(\beta - \delta) (F_y^{T1} + F_y^{T2}) + \sin\beta (F_y^{T3} + F_y^{T4}) - F_{x,D} \cos\beta] \\ \frac{1}{mv} [\cos(\beta - \delta) (F_y^{T1} + F_y^{T2}) + \cos\beta (F_y^{T3} + F_y^{T4}) + F_{x,D} \sin\beta] - \dot{\psi} \\ \frac{1}{l_z} [l_F \cos\delta (F_y^{T1} + F_y^{T2}) - l_R (F_y^{T3} + F_y^{T4})] \end{bmatrix}, \quad (7.41)$$

$$\mathbf{G}(\mathbf{x}) = \begin{bmatrix} \frac{\cos\beta}{m} & \frac{\sin\beta}{m} \\ -\frac{\sin\beta}{mv} & -\frac{\cos\beta}{mv} \\ -\frac{b_R}{2l_z} & \frac{b_R}{2l_z} \end{bmatrix}, \quad (7.42) \quad \mathbf{u} = [F_x^{T3} \quad F_x^{T4}]^T. \quad (7.43)$$

In the equations above, the front and rear track width b_F and b_R have been introduced. The two-dimensional system input vector \mathbf{u} is comprised of the rear left and rear right tractive tire forces. These forces are obtained from the MF-tire model together with the lateral tire forces, which requires computation of the longitudinal and lateral slip values. The main steps in this calculation is elaborated in Appendix F.1 and F.2. Thereby, the tire-specific slip angles are

derived from the following expressions:

$$\alpha_1 = \delta_1 - \arctan \frac{v_y^V + l_R \dot{\psi}}{v_x^V - \frac{1}{2} b_R \dot{\psi}}, \quad (7.44)$$

$$\alpha_2 = \delta_2 - \arctan \frac{v_y^V + l_R \dot{\psi}}{v_x^V + \frac{1}{2} b_R \dot{\psi}}, \quad (7.45) \quad \alpha_3 = \arctan \frac{v_y^V - l_R \dot{\psi}}{v_x^V - \frac{1}{2} b_R \dot{\psi}}, \quad (7.46)$$

$$\alpha_4 = \arctan \frac{v_y^V - l_R \dot{\psi}}{v_x^V + \frac{1}{2} b_R \dot{\psi}}. \quad (7.47)$$

The steer angles at the front and left tires are not identical, which is clarified later. For the rear tires, it is assumed there exists no steer angle.

The longitudinal slip values for the rear tires are directly introduced to the model. As such, information on the wheel dynamics

$$\dot{\omega}_i \cdot I_W = \tau_{D,i} - R_{\text{dyn},i} \cdot F_x^{\text{T}_i} - f_0 \cdot R_{\text{dyn},i} \cdot F_z^{\text{T}_i} \quad (7.48)$$

is – as stated before – provided implicitly. In (7.48) $\tau_{D,i}$ denotes the driving torque acting on the i -th wheel, f_0 the static rolling resistance coefficient, and I_W the wheel's inertia about its spindle axis. According to Pacejka [139], for the effective rolling radius R_{dyn} the following relation holds when the centrifugal growth of the unloaded tire radius is neglected:

$$R_{\text{dyn}} = R_0 - \frac{F_{z0}}{k_z} \left(D_R^{\text{eff}} \arctan \left(B_R^{\text{eff}} \frac{F_z^{\text{T}_i}}{F_{z0}} \right) + F_R^{\text{eff}} \frac{F_z^{\text{T}_i}}{F_{z0}} \right). \quad (7.49)$$

From the equation (7.49) the unloaded tire radius R_0 as well as the vertical tire stiffness k_z are recalled. The remaining parameters are constant coefficients which can be determined empirically.

7.2 Vehicle dynamics control

With the introduced knowledge of vehicle dynamics, the TV control approach is discussed in this section. As aforementioned, a tire slip control is applied in the present study to enhance the control performance. It is introduced in section 7.2.1. The implementation of the inverse tire model is presented in section 7.2.2, in which the nonlinearity of tire slip to tire force is described. Finally, the overlying yaw rate control is given in section 7.2.3.

7.2.1 Tire slip control

In this section the tire slip control for the rear-left and rear-right tires is derived and implemented. Two identical and independent controllers are utilized, one for each tire. In regards to the overall TV control system, the slip control's purpose is to take a reference longitudinal slip value s_x^* provided by the inverted tire model and to control the desired slip values on each side by applying certain shaft torques. The structure of the tire slip control is presented in Figure 7.12.

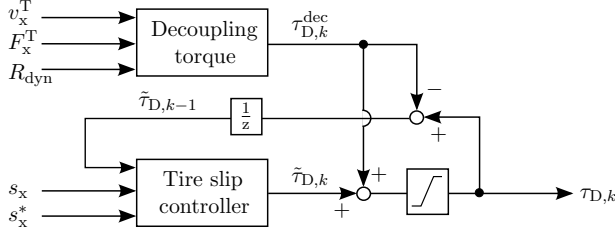


Figure 7.12: Block diagram of the tire slip control.

The prediction model employed for the tire slip control is directly derived from the definition of the longitudinal slip ratio introduced in section 7.1.2

$$s_x = \frac{\omega R_{\text{dyn}} - v_x^T}{v_x^T}, \quad (7.50)$$

along with the rotational wheel dynamics (see section 7.1.4)

$$\dot{\omega} I_W = \tau_D - R_{\text{dyn}} F_x^T. \quad (7.51)$$

In (7.51), the rolling resistance torque has been neglected. Derivating (7.50) with respect to time and substituting (7.51) yields

$$\dot{s}_x = -\frac{\dot{v}_x^T}{v_x^T} s_x + \frac{R_{\text{dyn}}}{I_W v_x^T} \tau_D - \frac{R_{\text{dyn}}^2 F_x^T}{I_W v_x^T} - \frac{\dot{v}_x^T}{v_x^T}, \quad (7.52)$$

where the longitudinal contact point velocity v_x^T and its derivative \dot{v}_x^T are considered as time-varying parameters. These quantities are constrained in this work by the following bounds:

$$30 \text{ km/h} \leq v_x^T \leq 120 \text{ km/h} \quad (7.53)$$

$$-7 \text{ m/s}^2 \leq \dot{v}_x^T \leq 7 \text{ m/s}^2 \quad (7.54)$$

To obtain a model compatible to the polytopic uncertainty description, a decoupling term is added to the input variable τ_D

$$\tau_D = \tilde{\tau}_D + \tau_D^{\text{dec}}, \quad \tau_D^{\text{dec}} = R_{\text{dyn}} F_x^T + \frac{I_W}{R_{\text{dyn}}} \dot{v}_x^T. \quad (7.55)$$

One may reformulate the tire slip model into the requested form

$$\dot{s}_x = -\frac{\dot{v}_x^T}{v_x^T} s_x + \frac{R_{\text{dyn}}}{I_W v_x^T} \tilde{\tau}_D. \quad (7.56)$$

After the discretization by the Euler discretization method, the following discrete-time representation of (7.56) can be obtained

$$x_{k+1} = \left(1 - T_s \frac{\dot{v}_x^T}{v_x^T} \right) x_k + T_s \frac{R_{\text{dyn}}}{I_W v_x^T} \tilde{u}_k, \quad (7.57)$$

where $\tilde{u}_k = \tilde{\tau}_D$ denotes the input, $x_k = s_x$ the state, and $T_s = 1$ ms the sample time.

In order to facilitate offset-free reference tracking, the model (7.57) is rewritten in differential form

$$\begin{bmatrix} \Delta x_{k+1} \\ e_{k+1} \end{bmatrix} = \underbrace{\begin{bmatrix} 1 - T_s \frac{\dot{v}_x^T}{v_x^T} & 0 \\ 1 - T_s \frac{\dot{v}_x^*}{v_x^*} & 1 \end{bmatrix}}_{A(\theta)} \begin{bmatrix} \Delta x_k \\ e_k \end{bmatrix} + \underbrace{\begin{bmatrix} T_s \frac{R_{\text{dyn}}}{J_W v_x^T} \\ T_s \frac{R_{\text{dyn}}}{J_W v_x^*} \end{bmatrix}}_{B(\theta)} \Delta \tilde{u}_k, \quad (7.58)$$

where $\Delta x_k = x_k - x_{k-1}$ denotes the change in the system state within one time step, $\Delta \tilde{u}_k = \tilde{u}_k - \tilde{u}_{k-1}$ the change in the input quantity, and $e_k = x_k - r_k$ the control deviation from the reference value $r_k = s_x^*(t = kT_s)$. In this context, it is assumed that the reference value remains constant ($r_{k+1} = r_k$) within the control horizon. Since the control law is computed off-line, the increased number of system states induced by the differential reformulation is of no concern.

The LPV prediction model (7.58) provides the basis for the formulation of the robust optimal control problem. Thereby, from the two uncertain parameters included in the system matrices, four vertices $[A_l, B_l]$, $l = 1, \dots, 4$ are defined. Additionally, the following state and input constraints are considered:

$$\tilde{x}^{\max} = \begin{bmatrix} 0.04 & 0.3 \end{bmatrix}^T \quad (7.59) \quad \tilde{u}^{\max} = 730 \quad (7.60)$$

The tire slip's rate of change is limited to 0.04/ms, which may be derived from (7.52) under the assumption that the maximum wheel torque $\tau_D^{\max} = 730$ Nm is applied. The maximum control deviation of 0.3 was chosen, since the peak value of the longitudinal tire force is attained for values of s_x in the area of 0.15. The value is doubled since it is assumed that the largest possible set point change of s_x occurs when a change from positive peak traction force to negative peak traction force is requested. Finally, the maximum difference of τ_D between two time instants is assumed to be equal to the maximum driving torque, which implies that the induction machine's torque can be controlled within 1 ms. We remark that due to the differential formulation, no absolute constraints can be imposed on the control output. Ensuring that τ_D stays below the maximum available driving torque will be the task of the overlying yaw rate control. Nevertheless, a saturation block ($-\tau_D^{\max} \leq \tau_{D,k} \leq \tau_D^{\max}$) is introduced to guarantee a bounded control output when high-dynamic changes of the slip request occur.

7.2.2 Inversed tire model

The inverted tire model represents a key component in the TV control system. It translates the longitudinal tire force requests into corresponding longitudinal slip values. Hence, an inaccurate inversion of the tire model will lead to a mismatch between requested and actual tire force. This is not critical under normal operation, since the yaw rate dynamics demonstrate strongly integrating behavior. However, a mismatch can potentially deteriorate the yaw rate control's performance.

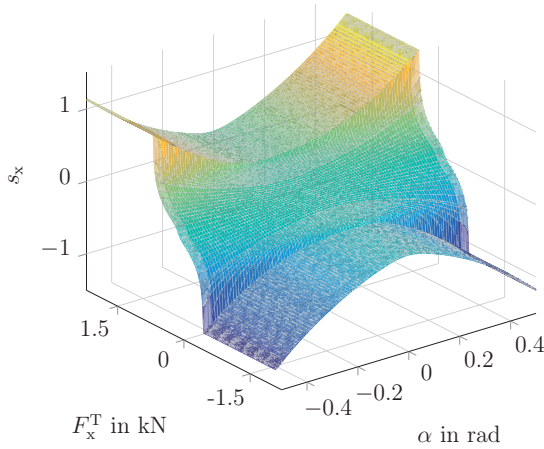


Figure 7.13: Slip ratio depending on the tire slip angle and longitudinal tire force at fixed $F_z^T = 800 \text{ N}$.

In severely combined slip driving situations, a model mismatch may lead to oscillations, as the tire may be driven beyond its peak slip value, resulting in a smaller longitudinal force than expected. This is attributed to a change of the MF's monotony occurring at large tire slip angles. Beside the combined slip case, a mismatch at large longitudinal slip values may induce oscillations for the same reason. For the vehicle considered in the present work, both critical situations occur at large lateral accelerations at the rear wheel on the inner side of the curve. In order to prevent such situations, the maximum tire force calculation $F_x^{T,\max}$ is limited to 95% of the theoretically attainable value.

The following discretization is defined experientially by the simulation to deliver accurate results for the inverted tire model's full range of applicability:

$$\begin{aligned} \Delta\alpha &= \begin{cases} 0.002 & |\alpha| \geq 0.49 \\ 0.01 & \text{else} \end{cases} \\ \Delta F_z^T &= \begin{cases} 50 \text{ N} & F_z^T \leq 2080 \text{ N} \\ 750 \text{ N} & \text{else} \end{cases} \\ \Delta F_x^T &= \begin{cases} 20 \text{ N} & |F_x^T| \geq 500 \text{ N} \\ 50 \text{ N} & \text{else.} \end{cases} \end{aligned}$$

Considering the maximum available driving torque on each side as well as the MF's domain of invertibility, the following parametric range was chosen

$$-\pi/6 \leq \alpha \leq \pi/6 \quad 800 \text{ N} \leq F_z^T \leq 8800 \text{ N} \quad -\tau_D^{\max}/R_{\text{dyn}}^{\min} \leq F_x^T \leq \tau_D^{\max}/R_{\text{dyn}}^{\min},$$

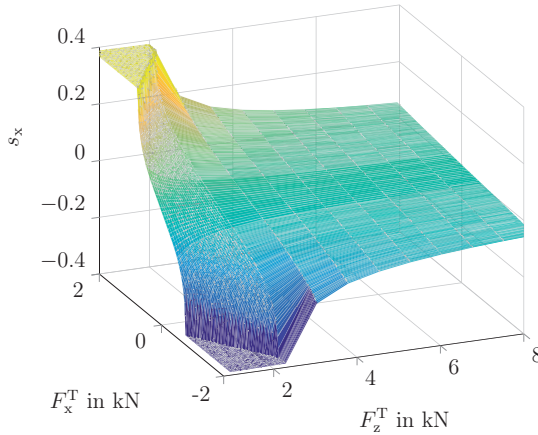


Figure 7.14: Slip ratio depending on the tire load force and longitudinal tire force at fixed $\alpha = 0$.

where a minimum effective rolling radius $R_{\text{dyn}}^{\text{min}} = 0.33 \text{ m}$ was assumed. For values of the longitudinal tire force that exceed the peak value at a given α and F_x^T , a saturation was implemented, such that an excessive force request does not lead to further instability. Figure 7.13 renders the inverted data for the most critical situation, i.e. $F_z^T = 800 \text{ N}$ and it clearly shows the aforementioned saturation. At larger load forces, the saturation vanishes, as the tire's force potential exceeds the EM's maximum torque. Figure 7.14 depicts the inverted model, where $\alpha = 0$ is fixed. The region of small tire load force emphasizes the necessity for a finer discretization in this area. Inclusion of different road surfaces is mandatory for the inverted tire model. Here, the force request input $F_x^T = (F_x^T)^*$ is simply divided by μ .

7.2.3 Yaw rate control

In the following, the implementation of the yaw rate control for the TV application is described. Beside the main aspect of controlling the vehicle's yaw rate, it is the yaw rate control's task to interpret and forward the driver's demand to the underlying slip controllers. Thus, a strategy to determine the drive forces in consideration of the driver's demand and the yaw rate control is required. In contrast to the tire slip controller, time-varying constraints are taken into account in the control design. In order to ensure a safe operation close to the tires' physical limitations, the dynamic force constraints are analyzed. The entire structure of the yaw rate control is given in Figure 7.15.

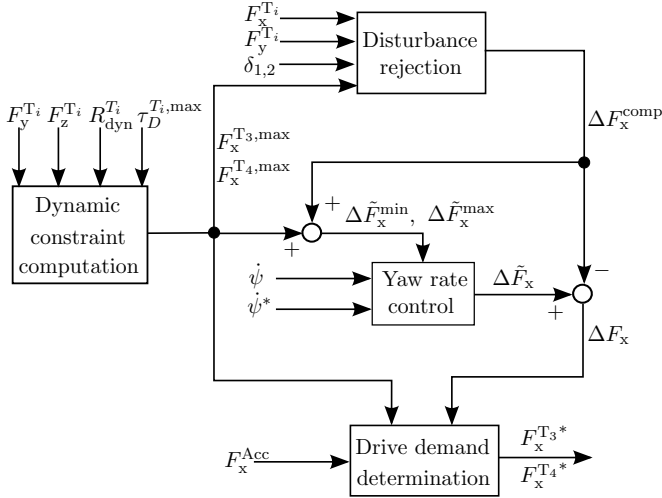


Figure 7.15: Block diagram of the yaw rate control.

Control derivation

In order to establish a model for the control design, the DTM introduced in section 7.1.4 is recalled. The continuous-time equation is again discretized using the first order approximation:

$$\dot{\psi}_{k+1} = \mathbf{A}\dot{\psi}_k + \mathbf{B}\mathbf{u}_k + \frac{T_s}{I_z}d_k. \quad (7.61)$$

The system matrices \mathbf{A} and \mathbf{B} , input vector \mathbf{u}_k , as well as the disturbance term are given as follows:

$$\mathbf{A} = 1 \quad \mathbf{B} = \frac{T_s b_R}{2I_z} \quad \mathbf{u} = \Delta F_x = F_x^{T_4} - F_x^{T_3}. \quad (7.62)$$

By means of a feed-forward disturbance compensation with

$$\begin{aligned} \Delta F_x &= \Delta \tilde{F}_x - \Delta F^{comp} \quad \text{and} \\ \Delta F^{comp} &= \frac{2}{b_R} \cdot \left(l_F \cdot (\cos \delta_1 \cdot F_y^{T_1} + \cos \delta_2 \cdot F_y^{T_2}) - l_R \cdot (F_y^{T_3} + F_y^{T_4}) \right. \\ &\quad \left. + \frac{b_F}{2} (\sin \delta_2 \cdot F_x^{T_2} - \sin \delta_1 \cdot F_x^{T_1}) \right), \end{aligned} \quad (7.63)$$

the state-space representation used for the nominal yaw rate control is then given as follows:

$$\dot{\psi}_{k+1} = \dot{\psi}_k + \frac{T_s b_R}{2I_z} \Delta \tilde{F}_x. \quad (7.64)$$

The model equation (7.64) represents the first constraint in the QP-based control problem. Additional constraints are introduced to maintain the tires within their physical limits:

$$\Delta \tilde{F}_x^{\min} \leq \Delta \tilde{F}_x \leq \Delta \tilde{F}_x^{\max}. \quad (7.65)$$

The computation of the lower and upper thresholds is clarified later. The optimization-based control problem is completed by the following cost function

$$J(k) = \sum_{i=0}^N \left\| \dot{\psi}_{k+i|k} - \dot{\psi}_k^* \right\|_Q^2 + \left\| \Delta \tilde{F}_{x, k+i|k} \right\|_R^2. \quad (7.66)$$

The QP problem based on the objective function (7.66) can be stated as a multi-parametric Quadratic Programming (mp-QP) problem

$$\begin{aligned} \min_{\mathbf{z}} J(\mathbf{z}, \mathbf{x}) \\ \text{s.t. (7.64), (7.65),} \end{aligned} \quad (7.67)$$

where the optimizer $\mathbf{z} = \tilde{\mathbf{U}}$ contains the sequence of control inputs $\tilde{\mathbf{U}} = \{\tilde{\mathbf{u}}_k^T, \dots, \tilde{\mathbf{u}}_{N-1}^T\}$. Moreover, the parameter vector is comprised of the following four elements:

$$\mathbf{x} = [\dot{\psi}_k \quad \dot{\psi}_k^* \quad \Delta \tilde{F}_x^{\min} \quad \Delta \tilde{F}_x^{\max}]^T.$$

Driver demand determination

As mentioned before, the yaw rate control is responsible for the interpretation of the driver's demand as well. Thereby, the acceleration demand of the driver is translated into symmetric longitudinal forces and is considered in the control design. The primary target of the application is to produce the asymmetrical longitudinal drive forces to get the desired yaw rate. Therefore, in order to hold the system constraint and ensure the yaw rate control performance, the drive demand is considered as a secondary requirement and has to be modified if necessary. The total longitudinal forces required are represented by

$$F_x^{\text{T}3} = -\frac{1}{2} \Delta F_x + F_x^{\text{T}3, \text{D}} \quad (7.68a)$$

$$F_x^{\text{T}4} = \frac{1}{2} \Delta F_x + F_x^{\text{T}4, \text{D}}. \quad (7.68b)$$

In Algorithm 6 the control logic to determine the acceleration forces required by the driver is shown, where F_x^{Acc} represents the unmodified acceleration longitudinal forces demanded by the driver.

Based on the equations (7.68a) and (7.68b) the total longitudinal forces required are compared to the maximum and the minimum longitudinal forces of both rear tires. If the force limitation on any tire is exceeded, the offset having the larger value, that shifts the required force within the limitation, is added to both tires. In this way,

Algorithm 6 Determination of drive forces required by the driver

-
- 1: $F_x^{T_{3,D}} = F_x^{T_{4,D}} = \frac{1}{2}F_x^{\text{Acc}}$
 - 2: $\Delta F_x^{T_i}_{\text{ub}} = \left(F_x^{T_i,\text{max}} < F_x^{T_i} \right) \cdot \left(F_x^{T_i} - F_x^{T_i,\text{max}} \right), \quad i \in \{3, 4\}$
 - 3: $\Delta F_{x,\text{ub}} = \max \left\{ \Delta F_x^{T_3}_{\text{ub}}, \Delta F_x^{T_4}_{\text{ub}} \right\}$
 - 4: $\Delta F_x^{T_i}_{\text{lb}} = \left(F_x^{T_i,\text{min}} > F_x^{T_i} \right) \cdot \left(F_x^{T_i} - F_x^{T_i,\text{min}} \right), \quad i \in \{3, 4\}$
 - 5: $\Delta F_{x,\text{lb}} = \min \left\{ \Delta F_x^{T_3}_{\text{lb}}, \Delta F_x^{T_4}_{\text{lb}} \right\}$
 - 6: $F_x^{T_i*} = F_x^{T_i,D} - \Delta F_{x,\text{ub}} - \Delta F_{x,\text{lb}};$
 - 7: **return** $F_x^{T_i*}$
-

the yaw rate control approach is not impacted in case that the force limitation is exceeded, but the total acceleration demand by the driver may be modified. However, such modification takes place temporarily in the transient procedures of certain situations and is therefore not perceived by the driver.

Dynamic constraint computation

As aforementioned, diverse force limitations are applied in the control design. In the following, the computation of the thresholds ΔF_x^{min} , ΔF_x^{max} , $F_x^{T_{3,\text{max}}}$ and $F_x^{T_{4,\text{max}}}$ is clarified.

First, the maximum longitudinal force that can be transmitted by the rear tires is computed. Here, not only the tire-force ellipse has to be considered (see section 7.1.2), but also the maximum torque on the drive shaft. Therefore, the maximum tire forces are determined by computing the minimum of both contributions

$$F_x^{T_i,\text{max}} = \min \left\{ \frac{\tau_D^{T_i,\text{max}}}{R_{\text{dyn}}^{T_i}}, 0.95\mu_x \sqrt{\left(F_z^{T_i} \right)^2 - \frac{\left(F_y^{T_i} \right)^2}{\mu_y^2}} \right\} \quad i \in \{3, 4\}. \quad (7.69)$$

In (7.69) the factor 0.95 represents a safety margin, which was mentioned in the previous section.

Based on the maximum longitudinal tire forces, the difference between RR and RL tires is constrained by

$$-F_x^{T_{3,\text{max}}} - F_x^{T_{4,\text{max}}} \leq \Delta F_x \leq F_x^{T_{3,\text{max}}} + F_x^{T_{4,\text{max}}}. \quad (7.70)$$

Subsequently, the force thresholds of the yaw rate controller are computed by

$$-F_x^{T_{3,\text{max}}} - F_x^{T_{4,\text{max}}} + \Delta F_x^{\text{comp}} \leq \tilde{\Delta F}_x \leq F_x^{T_{3,\text{max}}} + F_x^{T_{4,\text{max}}} + \Delta F_x^{\text{comp}}. \quad (7.71)$$

7.3 Operation strategy

Recalling the software specification defined in section 2.3.3, an operation strategy is implemented, which manages the interaction between driver and control software. In addition, road situations such as cross slope and inhomogeneous frictions are considered in the operation strategy as well. The entire SW structure is illustrated in Figure 7.16 and its components are introduced in the following.

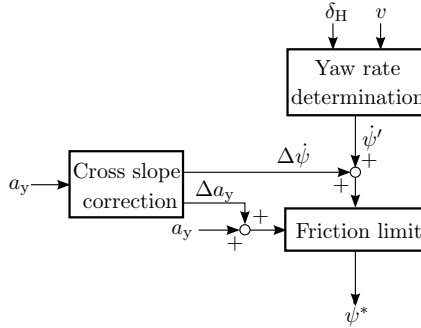


Figure 7.16: SW structure of operation strategy.

7.3.1 Determination of reference yaw rate

The steady-state yaw rate reference can be determined for the yaw rate control by using the steady-state equation derived from (7.38) with $\ddot{\psi} = 0, \dot{\beta} = 0$. Mathematically, this formulation follows

$$\frac{\dot{\psi}}{\delta} = \frac{v}{w_B + \eta \cdot v^2} \quad (7.72)$$

with

$$\eta = \frac{m}{w_B} \left(\frac{l_R}{C_\alpha^F} - \frac{l_F}{C_\alpha^R} \right). \quad (7.73)$$

Here, η is referred to as the self-steer gradient and describes the steady-state steering behavior of vehicles [144]. Figure 7.17 depicts typical shapes of the yaw gain for different self-steer gradients. The stable and unstable regions for an over-steered vehicle are highlighted with blue and red, respectively. Under-steered vehicles ($\eta \geq 0$) experience a peak yaw gain occurring at the characteristic velocity $v_{ch} = \sqrt{1/\eta}$. Typically, v_{ch} ranges from 18 m/s to 35 m/s [129]. For an over-steered vehicle such a maximum does not exist. Equation (7.72) rather exhibits a singularity at $v = v_{cr} = \sqrt{-1/\eta}$, which renders an infinite yaw gain. Obviously, this phenomenon cannot be of any physical nature and is therefore attributed to the model failure. However, eigenvalue analysis shows that this singularity is related to the unstable vehicle behavior [139].

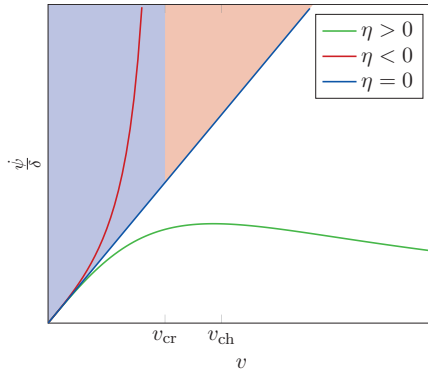


Figure 7.17: Typical yaw gain curves of understeer $\eta > 0$, neutral steer $\eta = 0$ and oversteer $\eta < 0$.

If η takes positive values, the car is considered to have under-steering behavior as the steering effort increases with increasing lateral acceleration. Contrarily, vehicles with negative self-steer gradient exhibit over-steering behavior, i.e. the necessary steering effort decreases at increasing lateral accelerations. A vehicle exhibits neutral steer if $\eta = 0$ [138].

The self-steering behavior is essential for the drivability and maneuverability of a vehicle. Most passenger cars are designed to show under-steering behavior as it is most drivers' natural response to increase the steering wheel angle when the vehicle is drifting away from the desired trajectory [129, 144]. Furthermore, an under-steered vehicle inhibits unstable steady-state cornering behavior. Consequently, under-steered vehicles are inherently safer to operate by normal drivers and less likely to exhibit instabilities in comparison to over-steered vehicles. Unfortunately, under-steering behavior may lead to unsatisfactory agility and limited cornering performance. Hence, sports cars are designed towards a more neutral behavior. Racing cars, usually operated by trained and experienced drivers, may in fact exhibit an over-steering characteristic at relatively low velocities. In contrast to these common cases, this characteristic line can be freely modified by means of a yaw rate controller. This is achieved by determining a reference yaw rate at a certain velocity and a certain steer angle. In order to attain a satisfying agility and simultaneously ensure the vehicle's stability, the neutral steering behavior line ($\eta = 0$) is pursued in the present work.

Equation (7.72) and Figure 7.17 give the relationship between yaw rate and steer angle. The input signal to the operation strategy is the steering wheel angle, though. Therefore, the steering system is introduced in the following. Initially, the idealized steering system depicted in Figure 7.18a is considered. This system is typically consisted of a steering wheel (1), a steering column (2), a steering gear (3, 4), two tire rods (5), steering arms (6), king-pins and stub axles (7). Any joints or active

support systems are neglected and the overall stiffness of the steering system is lumped into an ideal torsional spring C_δ , disregarding any damping ($d_\delta = 0$).

Assuming an infinitely rigid steering system ($C_\delta \rightarrow \infty$), the steer angle is simply given by the ratio of steering wheel angle and kinematic steering ratio i_s :

$$\delta = \frac{\delta_H}{i_s}. \quad (7.74)$$

In practice, the resulting hypothetical steer angle (7.74) is reduced when longitudinal or lateral tire forces exist. This is caused by the fact that the CP no longer lies in the middle of the tire, and induces torques acting on the steering system's finite stiffness C_δ . In that case, the sum of the pneumatic and kinematic trails t, n_y constitutes the lever, on which the lateral tire force $F_y^{T_i}$ acts (see Figure 7.18b). With the same principle, the steer angle is affected by the longitudinal tire force $F_x^{T_i}$, whereat no pneumatic trail exists. For the sake of brevity, only effects attributed to the lateral tire force are considered, since it is much greater than the longitudinal one. Neglecting the system's exact geometry, the true steer angle is given as follows [129]:

$$\delta_i = \frac{\delta_H}{i_s} - \frac{F_y^{T_i}(t + n_y)}{C_\delta} - \gamma_i, \quad i \in \{1, 2\}. \quad (7.75)$$

In other words, elasticity in the steering system requires the driver to turn the steering-wheel beyond the geometrically necessary angle increasing the vehicle's tendency to behave under-steered [129]. In (7.75) γ_i denotes the toe angle describing the offset of wheel's steer angle at neutral steering-wheel position. It provides another constructive means to improve the cornering behavior by maximizing the tires' lateral force potential [80]. Typically, it is defined $\gamma_1 = -\gamma_2$. As aforementioned, the steer angles on the rear tires are idealized as zero.

Therefore, the reference yaw rate resulting from the steering wheel angle in steady-state is derived by substituting the average steer angle from (7.75) in (7.72):

$$\dot{\psi}' = \frac{v}{w_B + \eta \cdot v^2} \cdot \frac{\delta_1 + \delta_2}{2}. \quad (7.76)$$

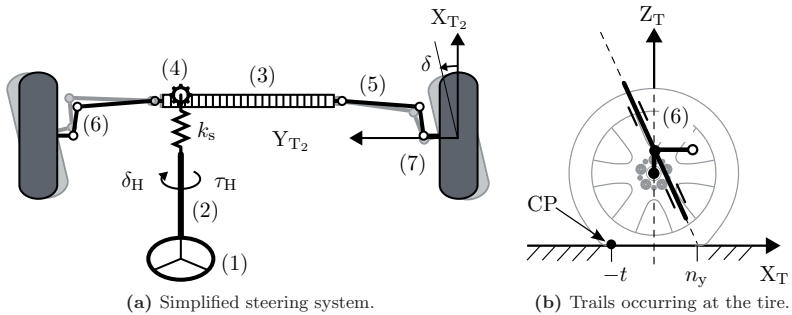


Figure 7.18: Overview of the simplified steering system's geometry and components.

7.3.2 Cross slope correction

The determination of reference yaw rate is considered so far on flat surfaces. However, roads may also show a lateral gradient. This lateral gradient, denoted by the bank angle φ , significantly influences the vehicle's motion.

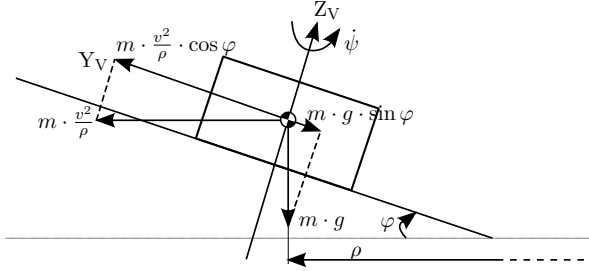


Figure 7.19: Steady-state cornering with cross slope.

Figure 7.19 shows the steady-state cornering with cross slope from the front/rear view of the vehicle. The effective radius of the drive circle is now $\rho' = \rho / \cos \varphi$ on the Y_V -axis. Therefore, the following equation is obtained:

$$m \cdot a_y = m \cdot \frac{v^2}{\rho'} - m \cdot g \cdot \sin \varphi. \quad (7.77)$$

Substituting (7.16) with $\dot{\beta} = 0$ and applying ρ' as effective radius in (7.77) yields

$$a_y = v \cdot \dot{\psi} - g \cdot \sin \varphi. \quad (7.78)$$

Therefore, the correction of the lateral acceleration is represented by [190]

$$\Delta a_y = v \cdot \dot{\psi} - a_y = g \cdot \sin \varphi. \quad (7.79)$$

Recalling the LSTM and considering the equilibrium of the moment on both tires around Z_V -axis in Figure 7.20 as a simplification of Figure 7.10 yields

$$F_y^F \cdot \cos \delta \cdot w_B = m \cdot \frac{v^2}{\rho} \cdot \cos \beta \cdot l_R = m \cdot a_y \cdot l_R \quad (7.80a)$$

$$F_y^R \cdot w_B = m \cdot \frac{v^2}{\rho} \cdot \cos \beta \cdot l_F = m \cdot a_y \cdot l_F, \quad (7.80b)$$

where $\cos \delta \approx 1$, $\cos \beta \approx 1$ and the tire forces are calculated by means of (7.26), (7.27) (7.30), and (7.31):

$$F_y^F = C_\alpha^F \cdot \left(\delta - \beta - \frac{l_F \cdot \dot{\psi}}{v} \right) \quad (7.81a)$$

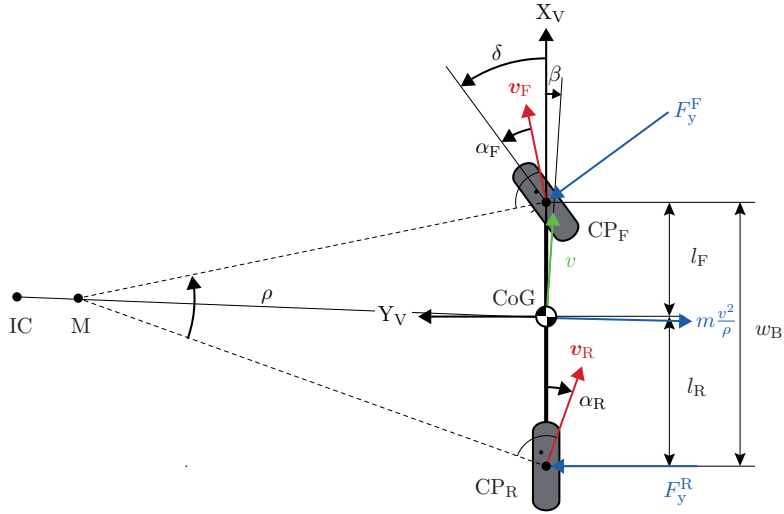


Figure 7.20: Simplified kinematics of LSTM.

$$F_y^R = C_\alpha^R \cdot \left(-\beta + \frac{l_R \cdot \dot{\psi}}{v} \right). \quad (7.81b)$$

Eliminating β by subtracting (7.81b) from (7.81a) and substituting them in (7.80a), (7.80b) yields

$$\delta = \frac{w_B}{v} \cdot \dot{\psi} + \eta \cdot a_y. \quad (7.82)$$

Substituting (7.79) in (7.82) results in

$$\delta = \frac{w_B}{v} \cdot \dot{\psi} + \eta \cdot \left(v \cdot \dot{\psi} - \Delta a_y \right). \quad (7.83)$$

Reformulating (7.83) it is obtained

$$\dot{\psi} = \frac{v}{w_B + \eta \cdot v^2} \cdot \delta + \frac{\eta \cdot v \cdot \Delta a_y}{l + \eta \cdot v^2}. \quad (7.84)$$

Comparing equation (7.84) with (7.76), the correction term due to cross slope is represented by

$$\Delta \dot{\psi} = \frac{\eta \cdot v}{l + \eta \cdot v^2} \cdot \Delta a_y. \quad (7.85)$$

7.3.3 Friction limit

The reference yaw rate cannot be set to an arbitrarily large value, since friction on the tires has physical limits. The following condition has to be held:

$$|m \cdot a_y| \leq \left| \sum_{i=1}^4 F_y^{T_i} \cdot \cos \delta_i \right|. \quad (7.86)$$

Assuming $\cos \delta_i \approx 1$ and introducing the maximum admissible tires' lateral force described in Figure 7.8, the lateral acceleration is limited by

$$|a_y| \leq \left| \sum_{i=1}^4 \mu_{y,\max}^{T_i} \cdot g \right| \quad (7.87)$$

where $\mu_{y,\max}^{T_i}$ represents the maximum friction coefficient of each tire given by the Kamm Circle. Therefore, the reference yaw rate is limited by substituting (7.79) in (7.87)

$$|\dot{\psi}| \leq \left| \frac{\sum_{i=1}^4 \mu_{y,\max}^{T_i} \cdot g}{v} + \frac{\Delta a_y}{v} \right|. \quad (7.88)$$

7.4 Parameter estimation

The aforementioned control approaches as well as the operation strategy are based on a sequence of vehicle quantities, some of which are not measurable. Therefore, a reliable estimator is required to ensure the control performance and safety of the TV application. In order to provide an overview, the signals regarding the vehicle dynamics control are categorized. The measured quantities are associated with the specification given in section 2.3.3 and summarized by

- ▷ Steering wheel angle δ_H ;
- ▷ Wheel speeds ω_i ;
- ▷ Yaw rate $\dot{\psi}$;
- ▷ Lateral acceleration a_y .

The other unmeasurable quantities required for the vehicle dynamics control are represented by

- ▷ Steer angle δ ;
- ▷ Tire forces $F_x^{T_i}$, $F_y^{T_i}$ and $F_z^{T_i}$;
- ▷ Vehicle's longitudinal velocity v_x^V ;
- ▷ Tires' longitudinal slips $s_x^{T_i}$;
- ▷ Overall cornering stiffness C_{α_i} ;
- ▷ Vehicle's lateral velocity v_y^V ;
- ▷ Vehicle sideslip angle β ;
- ▷ Tire slip angles α_i ;
- ▷ Friction coefficients μ^{T_i} .

The estimation of the steer angle δ according to the steering wheel angle δ_H was derived in section 7.3.1 and therefore is not presented here.

Tire force estimation

In a moving vehicle, a tire transfers all the desired forces: longitudinal forces to compensate resistances and to accelerate or to brake, lateral forces to turn the vehicle in other directions and vertical forces to bear the vehicles weight.

The calculation of the longitudinal tire forces is based on the momentum equilibrium around the wheel rotation axis:

$$I_W^{T_i} \cdot \dot{\omega}_i = \tau_D^{T_i} - F_x^{T_i'} \cdot R_{\text{dyn}}^{T_i}. \quad (7.89)$$

Since the resistance force is neglected in the control strategy, the effective longitudinal tire force in consideration of a rolling resistance coefficient is calculated by

$$F_x^{T_i} = F_x^{T_i'} - F_{x,R}^{T_i} = \frac{1}{R_{\text{dyn}}^{T_i}} \cdot \left(\tau_D^{T_i} - I_W^{T_i} \cdot \dot{\omega}_i \right) - f_R \cdot F_z^{T_i}, \quad (7.90)$$

where f_R describes the rolling resistance coefficient, which is empirically fixed to $f_R = 0.01$ in this work. The lateral tire forces are determined by

$$F_y^{T_i} = C_{\alpha_i} \cdot \alpha_i, \quad (7.91)$$

where C_{α_i} denotes the overall cornering stiffness and α_i the tire slip angle. The calculation of both parameters is derived later.

In order to calculate the vertical tire forces, some preconditions are required. In the simple case of uniform motion, the wheel forces are determined by the vehicle's CoG. Given the vehicle's geometric dimensions and the location of the CoG, it is uncomplicated to calculate, for a given wheel, which forces acting on it are induced by the vehicle's total mass:

$$F_{z0}^{T1} = F_{z0}^{T2} = \frac{l_R}{2w_B} \cdot m \cdot g, \quad (7.92a)$$

$$F_{z0}^{T3} = F_{z0}^{T4} = \frac{l_F}{2w_B} \cdot m \cdot g. \quad (7.92b)$$

In dynamic conditions the wheel forces in general will not be parallel to gravity any more. In the calculations it is assumed that only lateral accelerations cause a lateral wheel load transfer. According to Figure 7.21a the equilibrium of the moment in the roll-axis (φ) is given by

$$m \cdot a_y \cdot h = (F_z^{T2} - F_z^{T1}) \cdot \frac{b_F}{2} + (F_z^{T4} - F_z^{T3}) \cdot \frac{b_R}{2}, \quad (7.93)$$

which results in

$$2 \cdot m \cdot a_y \cdot h = \Delta F_{z,\text{roll}}^F \cdot b_F + \Delta F_{z,\text{roll}}^R \cdot b_R. \quad (7.94)$$

The symbol h denotes the height of the vehicle's CoG referred to the driving surface. The following representations are given: $\Delta F_{z,\text{roll}}^F = F_z^{T2} - F_z^{T1}$, $\Delta F_{z,\text{roll}}^R = F_z^{T4} - F_z^{T3}$. The lateral wheel load transfer concerns both, the front and the rear axle and the

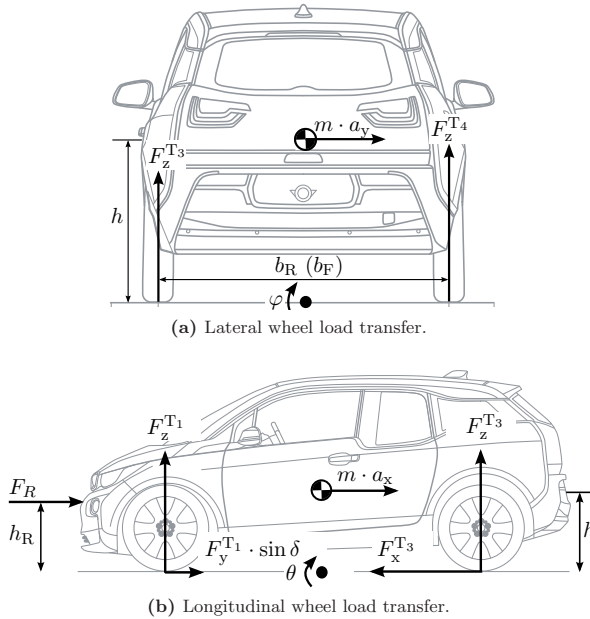


Figure 7.21: Wheel load transfer.

distribution, which is caused by the suspension's springs together with anti-roll-bars. These effects are represented in the calculation by the parameters k_F and k_R with $k_F + k_R = 1$. Therefore, the vertical tire force changes due to lateral wheel load transfer in case of roll motion are represented by

$$F_{z,\text{roll}}^{\text{T}1} = -\frac{h}{b_F} \cdot k_F \cdot m \cdot a_y; \quad F_{z,\text{roll}}^{\text{T}2} = \frac{h}{b_F} \cdot k_F \cdot m \cdot a_y, \quad (7.95\text{a})$$

$$F_{z,\text{roll}}^{\text{T}3} = -\frac{h}{b_R} \cdot k_R \cdot m \cdot a_y; \quad F_{z,\text{roll}}^{\text{T}4} = \frac{h}{b_R} \cdot k_R \cdot m \cdot a_y. \quad (7.95\text{b})$$

An overlying wheel load transfer is caused by longitudinal forces, such as drag forces, acceleration or braking forces. These forces result in a pitch motion. Furthermore, a simplification is made in such a way, that drag forces are set as a force parallel to the vehicle's longitudinal axis, affecting the car at its CoG. The calculation respects the longitudinal effects of lateral tire forces in cornering maneuvers. Figure 7.21b shows the effect of the longitudinal wheel load transfer. The equilibrium of the longitudinal force is given by

$$F_R + m \cdot a_x = F_x^{\text{T}3} + F_x^{\text{T}4} - F_y^{\text{T}1} \cdot \sin \delta_1 - F_y^{\text{T}2} \cdot \sin \delta_2, \quad (7.96)$$

where F_R represents the resistance and h_R the effective height of the resistance. For simplification it is assumed that $h_R = h$.

Furthermore, the equilibrium of the moment in the pitch-axis (θ) is described by

$$(F_R + m \cdot a_x) \cdot h + (F_z^{T1} + F_z^{T2}) \cdot l_F = (F_z^{T3} + F_z^{T4}) \cdot l_R. \quad (7.97)$$

Substituting (7.96) yields

$$(F_x^{T3} + F_x^{T4} - F_y^{T1} \sin \delta_1 - F_y^{T2} \sin \delta_2) \cdot h = \Delta F_z \cdot (l_F + l_R) + (F_z^{T1} + F_z^{T4}) \cdot (l_R - l_F), \quad (7.98)$$

where $\Delta F_z = F_z^{T3} - F_z^{T1} = F_z^{T4} - F_z^{T2}$ with the assumption that only longitudinal acceleration takes place. Additionally, $F_z^{T1} + F_z^{T4} = \frac{1}{2} \cdot m \cdot g$. Therefore,

$$\Delta F_z = \frac{h}{w_B} (F_x^{T3} + F_x^{T4} - F_y^{T1} \sin \delta_1 - F_y^{T2} \sin \delta_2) - \frac{l_R - l_F}{2w_B} \cdot m \cdot g. \quad (7.99)$$

Considering the difference of the vertical tire forces $\Delta F_{z0} = F_{z0}^{T3} - F_{z0}^{T1} = F_{z0}^{T4} - F_{z0}^{T2}$ in uniform motion (see (7.92)), the tire difference between front and rear wheels due to longitudinal wheel load transfer is calculated by

$$\Delta F_{z,\text{pitch}}^{T1,T3} = \Delta F_{z,\text{pitch}}^{T2,T4} = \Delta F_z - \Delta F_{z0} = \frac{h}{w_B} (F_x^{T3} + F_x^{T4} - F_y^{T1} \sin \delta_1 - F_y^{T2} \sin \delta_2). \quad (7.100)$$

A further assumption refers to the movements of the vehicle's chassis. In reality the vehicle's chassis will not be steady, but instead will show (random) movements, even in the case of uniform motion. Such movements for example are induced by the road's surface, which is not perfectly plain, furthermore by the vehicle's engine and also by the passengers inside the vehicle. The forces onto the wheels induced by such movements are ignored in the following calculation.

Finally, the calculation of the vertical tire forces according to the uniform, roll and pitch motions results in

$$F_z^{T1} = \frac{l_R}{2w_B} \cdot m \cdot g - \frac{h}{b_F} \cdot k_F \cdot m \cdot a_y - \frac{h}{2w_B} \cdot (F_x^{T3} + F_x^{T4} - F_y^{T1} \sin \delta_1 - F_y^{T2} \sin \delta_2), \quad (7.101a)$$

$$F_z^{T2} = \frac{l_R}{2w_B} \cdot m \cdot g + \frac{h}{b_F} \cdot k_F \cdot m \cdot a_y - \frac{h}{2w_B} \cdot (F_x^{T3} + F_x^{T4} - F_y^{T1} \sin \delta_1 - F_y^{T2} \sin \delta_2), \quad (7.101b)$$

$$F_z^{T3} = \frac{l_F}{2w_B} \cdot m \cdot g - \frac{h}{b_R} \cdot k_R \cdot m \cdot a_y + \frac{h}{2w_B} \cdot (F_x^{T3} + F_x^{T4} - F_y^{T1} \sin \delta_1 - F_y^{T2} \sin \delta_2), \quad (7.101c)$$

$$F_z^{T4} = \frac{l_F}{2w_B} \cdot m \cdot g + \frac{h}{b_R} \cdot k_R \cdot m \cdot a_y + \frac{h}{2w_B} \cdot (F_x^{T3} + F_x^{T4} - F_y^{T1} \sin \delta_1 - F_y^{T2} \sin \delta_2). \quad (7.101d)$$

Longitudinal velocity and slip estimation

A precise and reliable knowledge of the longitudinal velocity is necessary for the longitudinal slip estimation. The calculation is mainly based on the measured wheel speed and yaw rate.

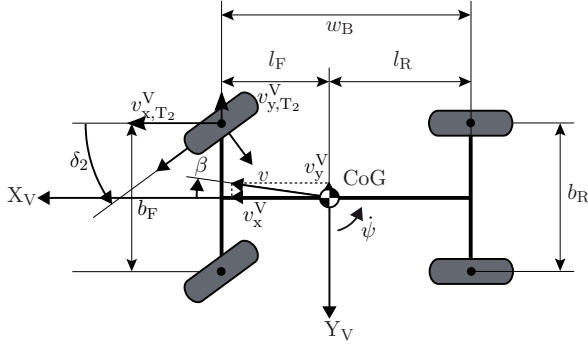


Figure 7.22: Relationship among the velocities.

Starting from the product of wheel speed and tire radius, values of the longitudinal velocity at four positions are obtained. Unfortunately, these values cannot be directly used at this stage. There are the longitudinal slip, changing tire radius and yawing. As the longitudinal slip is not known yet, a rough guess has to be performed initially. The resulting tire radius is a function of the vertical tire force. Considering the yaw rate, the longitudinal vehicle velocity at the portions of the four wheels can be transferred to the vehicle's center of mass to receive four possible values. Finally, one of them or an arithmetic mean has to be chosen.

Figure 7.22 illustrates the relationship between vehicle velocity and wheel speed. The front right wheel (T_2) is taken as an example for the computation. Since the velocity on the wheel consists of translational motion and rotational motion in the yaw-axis(ψ), the tire velocity on the X_V - and Y_V -axis is represented by

$$v_{x,T_2}^V = v_x^V + \dot{\psi} \cdot \frac{b_F}{2}, \quad (7.102a)$$

$$v_{y,T_2}^V = v_y^V - \dot{\psi} \cdot l_F. \quad (7.102b)$$

Moreover, the longitudinal tire velocity $v_x^{T_2}$ is depicted by

$$v_x^{T_2} = \frac{\omega_2 \cdot R_{\text{dyn}}}{1 + \frac{F_{x,T_2}^{T_2}}{F_z^{T_2}} \cdot C_s}, \quad (7.103)$$

where the linear tire characteristic is assumed. Therefore, the following equation results

$$\frac{\omega_2 \cdot R_{\text{dyn}}^{T_2}}{1 + \frac{F_{x,T_2}^{T_2}}{F_z^{T_2}} \cdot C_s} = v_x^{T_2} = v_{x,T_2}^V \cdot \cos \delta_2 - v_{y,T_2}^V \cdot \sin \delta_2. \quad (7.104)$$

Subsequently, the equation of vehicle's longitudinal velocity calculation is derived

by substituting (7.102a) and (7.102b) in (7.104) and reformulating the equation to

$$v_x^V|_{T_2} = \frac{\frac{\omega_2 \cdot R_{\text{dyn}}^{T_2}}{1 + \frac{F_x^{T_2}}{F_z^{T_2}} C_s} + v_y^V \cdot \sin \delta_2 - \dot{\psi} \cdot l_F \cdot \sin \delta_2 - \frac{b_F}{2} \dot{\psi} \cdot \cos \delta_2}{\cos \delta_2}. \quad (7.105)$$

The vehicle's longitudinal velocity can be derived by considering the other tires in an analogous manner. They are summarized by

$$v_x^V|_{T_1} = \frac{\frac{\omega_1 \cdot R_{\text{dyn}}^{T_1}}{1 + \frac{F_x^{T_1}}{F_z^{T_1}} C_s} + v_y^V \cdot \sin \delta_1 - \dot{\psi} \cdot l_F \cdot \sin \delta_1 + \frac{b_F}{2} \dot{\psi} \cdot \cos \delta_1}{\cos \delta_1}, \quad (7.106a)$$

$$v_x^V|_{T_3} = \frac{\omega_3 \cdot R_{\text{dyn}}^{T_3}}{1 + \frac{F_x^{T_3}}{F_z^{T_3}} C_s} + \frac{b_R}{2} \dot{\psi}, \quad (7.106b)$$

$$v_x^V|_{T_4} = \frac{\omega_4 \cdot R_{\text{dyn}}^{T_4}}{1 + \frac{F_x^{T_4}}{F_z^{T_4}} C_s} - \frac{b_R}{2} \dot{\psi}. \quad (7.106c)$$

Subsequently, the longitudinal vehicle velocity can be represented by these four velocities with the weighting factors g_i :

$$v_x^V = \sum_{i=1}^4 g_i \cdot v_x^V|_{T_i} \quad \text{with} \quad \sum_{i=1}^4 g_i = 1. \quad (7.107)$$

Since the slip ratios s_x on the front tires are much smaller than those on the rear tires in rear-wheel-drive vehicles, a larger weighting factor is commonly defined for $v_x^V|_{T_1}$ and $v_x^V|_{T_2}$. In the present work, $g_1 = g_2 = 0.75/2$ and $g_3 = g_4 = 0.25/2$ are set as default. Furthermore, a strategy is implemented to eliminate the effect of the skidding wheel in order to obtain a reliable longitudinal velocity estimation.

The longitudinal slip estimation works by comparing wheel speed and longitudinal velocity and considering the vehicle's yaw rate:

$$s_x^{T_1} = \frac{\omega_1 R_{\text{dyn}}^{T_1} - \left(v_x^V - \frac{b_F}{2} \dot{\psi}\right) \cos \delta_1 + \left(v_y^V - l_F \cdot \dot{\psi}\right) \sin \delta_1}{\omega_1 \cdot R_{\text{dyn}}^{T_1}}, \quad (7.108a)$$

$$s_x^{T_2} = \frac{\omega_2 \cdot R_{\text{dyn}}^{T_2} - \left(v_x^V + \frac{b_F}{2} \dot{\psi}\right) \cos \delta_2 + \left(v_y^V - l_F \cdot \dot{\psi}\right) \sin \delta_2}{\omega_2 \cdot R_{\text{dyn}}^{T_2}}, \quad (7.108b)$$

$$s_x^{T_3} = \frac{\omega_3 \cdot R_{\text{dyn}}^{T_3} - \left(v_x^V - \frac{b_R}{2} \dot{\psi}\right)}{\omega_3 \cdot R_{\text{dyn}}^{T_3}}, \quad (7.108c)$$

$$s_x^{T_4} = \frac{\omega_4 \cdot R_{\text{dyn}}^{T_4} - \left(v_x^V + \frac{b_R}{2} \dot{\psi}\right)}{\omega_4 \cdot R_{\text{dyn}}^{T_4}}. \quad (7.108d)$$

Overall cornering stiffness estimation

The overall cornering stiffness describes the relation between tire slip angle and lateral force on each wheel. It should ideally consider all the influences, such as the friction coefficient, vertical force, longitudinal slip, steering and suspension elasticities and camber angle. Depending on the situation, there are different ways to obtain the overall cornering stiffness.

The HSRI tire model in [54, 139] allows a relation between slip, tire slip angle, longitudinal and lateral forces:

$$\frac{F_y^{T_i}}{F_x^{T_i}} = \frac{C_\alpha \cdot \alpha_i}{C_s \cdot s_x^{T_i}} \quad (7.109)$$

with the linear traction stiffness C_s and the linear cornering stiffness C_α introduced in section 7.1.2. Introducing the aforementioned steering stiffness C_{δ_i} , and the pneumatic trail $t + n_y$ the overall cornering stiffness is obtained, which is derived in [54]:

$$C_{\alpha_i} = \frac{C_{\delta_i} \frac{C_\alpha \cdot F_x^{T_i}}{C_s \cdot s_x^{T_i}}}{C_{\delta_i} + \frac{C_\alpha \cdot F_x^{T_i}}{C_s \cdot s_x^{T_i}} d_i}. \quad (7.110)$$

However, a very small slip causes a division by nearly zero in equation (7.110). Thus, the overall cornering stiffness can also be read out of a LUT with the relative friction coefficient and the vertical load as inputs.

Lateral velocity estimation

Obtaining the lateral velocity is a key element of this estimator. An EKF is implemented for this purpose with the state vector and input

$$\mathbf{x} = \begin{bmatrix} v_y^V & \dot{\psi} & a_y & d \end{bmatrix}^T, \quad u = \delta_H, \quad (7.111)$$

where d denotes the process disturbance. The matrices \mathbf{A} and \mathbf{B} of the discrete system are

$$\begin{bmatrix} v_y^V \\ \dot{\psi} \\ a_y \\ d \end{bmatrix}_{k+1} = \begin{bmatrix} 1 & -v_x^V \cdot T_s & T_s & 1 \\ \epsilon \cdot T_s & 1 + \chi \cdot T_s & 0 & 1 \\ 0 & 0 & 1 & 1 \\ 0 & 0 & 0 & 1 \end{bmatrix} \cdot \begin{bmatrix} v_y^V \\ \dot{\psi} \\ a_y \\ d \end{bmatrix}_k + \begin{bmatrix} 0 & 0 \\ \xi \cdot T_s & \zeta \cdot T_s \\ 0 & 0 \\ 0 & 0 \end{bmatrix} \cdot \begin{bmatrix} \delta_1 \\ \delta_2 \end{bmatrix}_k \quad (7.112)$$

where ϵ , χ , ξ and ζ are derived in Appendix G.1. The sample time is $T_s = 1$ ms.

In this system, $\dot{\psi}$ and a_y are available as measurement variables. Since the calculation of the lateral velocity v_y^V in (7.112) is derived from the kinematic equations in the form of an integrator as shown in G.1), the estimation errors of the applied variables are integrated simultaneously during the calculation. In

order to eliminate these errors, the lateral velocity is considered in the EKF as a 'measurement variable' in such a manner, that it is derived from the force equilibrium and is described by

$$\begin{aligned} \tilde{v}_y^V = & \frac{v_x^V}{C_{\alpha_1} \cdot \cos \delta_1 + C_{\alpha_2} \cdot \cos \delta_2 + C_{\alpha_3} + C_{\alpha_4}} \\ & \cdot \left(m \cdot a_y - \frac{C_{\alpha_1} \cdot l_F \cdot \cos \delta_1 + C_{\alpha_2} \cdot l_F \cdot \cos \delta_2 - C_{\alpha_3} \cdot l_R - C_{\alpha_4} \cdot l_R}{v_x^V} \cdot \dot{\psi} \right) \\ & + C_{\alpha_1} \cdot \cos \delta_1 \cdot \delta_1 + C_{\alpha_2} \cdot \cos \delta_2 \cdot \delta_2. \end{aligned} \quad (7.113)$$

The derivation is given in Appendix G.2. As (7.113) does not contain any integrator, it is applied as a measurement variable to correct the integration errors. Consequently, the output vector of the system is defined by

$$\mathbf{y} = \begin{bmatrix} \tilde{v}_y^V & \dot{\psi} & a_y \end{bmatrix}^T. \quad (7.114)$$

Vehicle sideslip angle and tire slip angle estimation

Based on the knowledge of the longitudinal and lateral velocity as well as the yaw rate, the calculation of the vehicle sideslip angle is performed geometrically. For the vehicle sideslip angle, the steer angle of each wheel is required in addition.

$$\beta = \frac{v_y^V}{v_x^V}. \quad (7.115)$$

According to Figure 7.22, the tire slip angles are therefore calculated by

$$\alpha_1 = \frac{v_y^V - l_F \cdot \dot{\psi}}{v_x^V - \frac{b_F}{2} \dot{\psi}} + \delta_1, \quad (7.116a)$$

$$\alpha_2 = \frac{v_y^V - l_F \cdot \dot{\psi}}{v_x^V + \frac{b_F}{2} \dot{\psi}} + \delta_2, \quad (7.116b)$$

$$\alpha_3 = \frac{v_y^V + l_R \cdot \dot{\psi}}{v_x^V - \frac{b_R}{2} \dot{\psi}}, \quad (7.116c)$$

$$\alpha_4 = \frac{v_y^V + l_R \cdot \dot{\psi}}{v_x^V + \frac{b_R}{2} \dot{\psi}}. \quad (7.116d)$$

Friction coefficient estimation

The estimation of the friction coefficient has been an important subject in automotive research in the recent years. Publications present a large variety on ideas and approaches to estimate the friction coefficient, however up to now, to the best knowledge of the author, no method with satisfying results has been established. Some ideas, for instance the analysis of the slip stiffness at a small slip, are presented in [59, 133, 189].

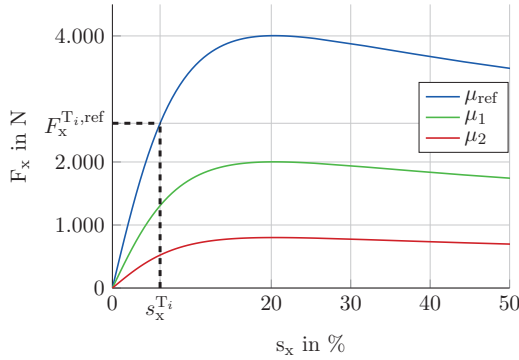


Figure 7.23: Characteristic line (longitudinal) of Pacejka tire model with constant slip angle and vertical tire force.

In the present work, the friction coefficient is obtained by comparing the estimated force to a reference value calculated from the tire model. Firstly, the friction at the actual operating point is to be found, which means the slip ratio $s_x^{T_i}$, the tire slip angle α_i and the vertical tire force $F_z^{T_i}$ are given. The characteristic line of the Pacejka tire model in the longitudinal direction is illustrated in Figure 7.23, where the tire vertical force and the slip angle are constant. According to the characteristic line, a reference force $F_x^{T_i,ref}$ is determined by selecting a certain reference friction coefficient μ_x^{ref} (typically with a properly large value) and the current slip ratio. Therefore, a relative friction coefficient is identified by

$$\mu_{rel}^{T_i} = \frac{F_x^{T_i}}{F_x^{T_i,ref}} = \frac{s_x \cdot C_s(\mu_x^{T_i}) \cdot F_z^{T_i}}{s_x \cdot C_s(\mu_x^{ref}) \cdot F_z^{T_i}} = \frac{C_s(\mu_x^{T_i})}{C_s(\mu_x^{ref})}. \quad (7.117)$$

In the Pacejka tire model, it is assumed that the traction stiffness $C_s(\mu_x)$ changes linear to the friction coefficient μ_x in case that other factors remain the same. Therefore, equation (7.117) is described by

$$\mu_{rel}^{T_i} = \frac{F_x^{T_i}}{F_x^{T_i,ref}} = \frac{\mu_x^{T_i}}{\mu_x^{ref}}. \quad (7.118)$$

With the knowledge of μ_x^{ref} , the current longitudinal friction coefficient $\mu_x^{T_i}$ is determined. Analogously, the lateral friction coefficient $\mu_y^{T_i}$ can be derived by comparing the lateral forces.

Under the assumption of symmetric friction coefficients ($\mu = \mu_x = \mu_y$), the friction coefficient μ is determined either by μ_x or μ_y . The relative friction coefficient can only be estimated when forces are applied on the tire. Therefore, friction coefficients on both axes are compared and the more appropriate one is chosen. In this approach, it is assumed that the tire model is entirely known to the software. The implementation is achieved by storing the characteristics of the tire model in the LUT.

In Figure 7.24 the entire structure of the estimator with implicated estimation sequence is summarized.

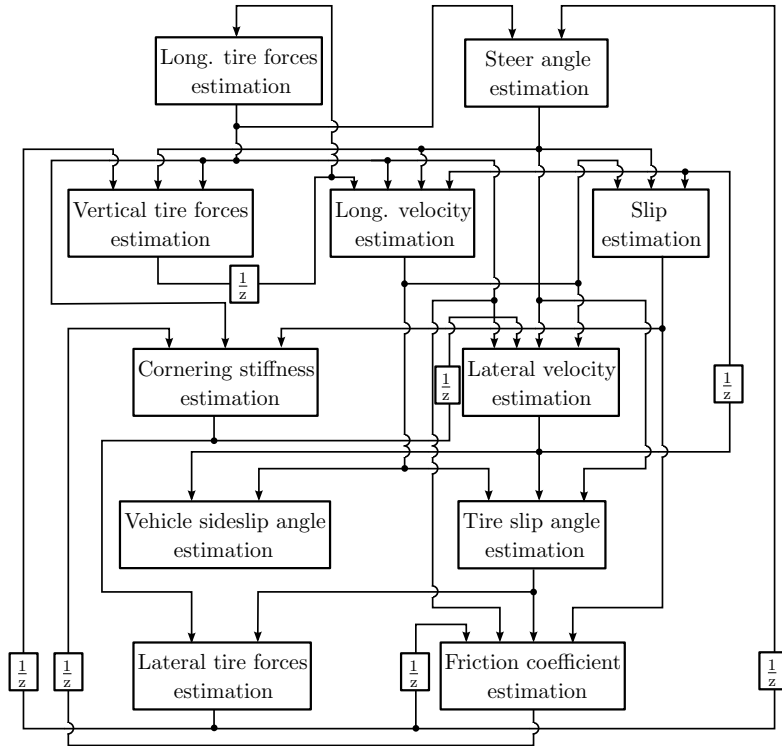


Figure 7.24: Structure of the parameter estimator.

7.5 Summary

The TV application is studied in this chapter. In order to prevent wheel spin and enhance the reliability of the application, both tire slip control and yaw rate control are implemented. Furthermore, the operation strategy and the approach of parameter estimation are introduced. In the next chapter, these approaches are integrated with the drivetrain system and the validated control approaches presented in the previous chapters, and tested in the Hardware-in-the-Loop (HiL).

8 Integration and Validation of the entire application

In this chapter, the robust current control and the active damping control, which are validated in the corresponding subsystems with results presented in section 5.6 and 6.3, are integrated in the TV control. By means of the dSPACE ASM suite mentioned in section 7.1, the entire control SW is applied to the real-time vehicle dynamics simulation. Two different simulation approaches applied in the present work are introduced in section 8.1. In section 8.2, the performance of the TV application is evaluated. In addition, the standardized test maneuvers specified in section 2.3.1 are performed.

8.1 Simulation approaches

In order to test the control SW in a proper way, two different simulation approaches are applied in the present work. The first one is called Processor-in-the-Loop (PiL) simulation. In the PiL simulation, the control SW to be tested is compiled and downloaded to the target real-time platform. In this way, the control SW is stand-alone and is executed in real-time. Unlike the standard PiL test, the simulation environment – the vehicle model and the driving situation – is simulated in the present work on another real-time platform and communicates with the control SW via I/O interfaces of both systems.

Another approach is the HiL simulation. According to the V-model in the industry, the implemented TV application is validated on a HiL test bench before it is integrated in the entire physical vehicle system. Safety functions in particular have to be tested in a simulated environment to avoid potential dangers. The setup of the test bench is schemed in Figure 8.1.

As shown in the figure, the entire system consists of the simulation and the physical components, and depicts a close-loop system. The physical component is represented by the mechanical drivetrain introduced in chapter 6 as the RR drivetrain in the vehicle and the IM as the RR drive motor (shown as ①). The simulation component consists of the RL drivetrain, the vehicle dynamics and the driving environment (shown as ②). The control unit, on which the simulation runs, is referred to as slave thereafter.

The work flow as well as the interaction between the physical and the simulative systems are described as follows: The operation strategy on the control unit referred to as master determines the reference yaw rate according to the steering wheel angle and the driving situations in the simulation. In order to obtain the yaw rate, the TV controller manipulates in both drivetrains the shaft torques, which are considered as

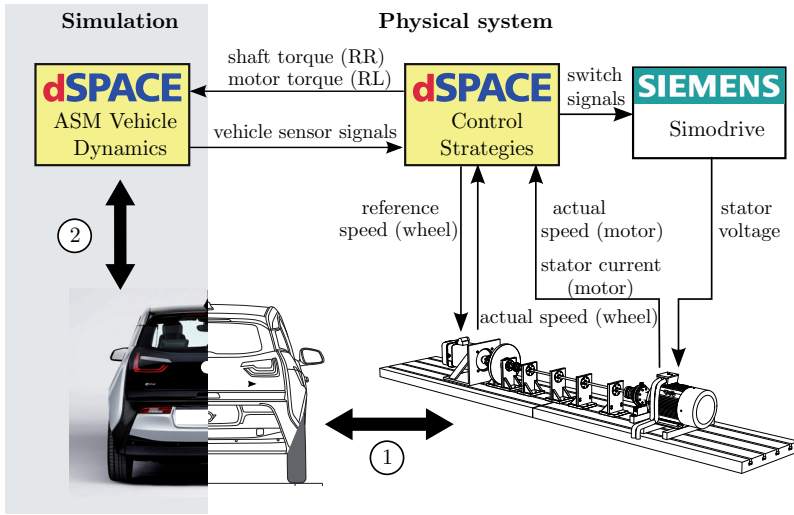


Figure 8.1: scheme of the HiL test bench.

reference values for the damping controllers. So far, there is no difference between both drivetrains.

Subsequently, both damping controllers compute the control output – the motor torque – in order to obtain a dynamic shaft torque response without oscillation. Here, the RL damping control is based on the wheel speed and the rotor speed from the simulation, while the RR damping control uses the values from the physical systems. The RR wheel speed in the simulation is implemented in the physical system by applying this speed as reference value to the PMSM. The RL motor torque is transferred to the slave, whereas the RR motor torque is translated as reference value to the current controller. By using the SIEMENS Simodrive system introduced in chapter 5, the IM provides an electromagnetic torque enforced on the rotor and the mechanical drivetrain. The resulted shaft torque is measured and transferred as RR shaft torque to the slave. In the simulation, the vehicle dynamics are influenced by the RR shaft torque and the RL motor torque. As feedback, the sensor signals are sent to the master.

Both the simulation and the control strategies are operated in real-time. The sample time of the current control loop is $T_s^1 = 0.1\text{ms}$, while for the vehicle dynamics simulation as well as for the rest part of the control strategies the sample time is defined by $T_s^2 = 1\text{ms}$.

8.2 Results and evaluations

In order to evaluate the application in a proper way, the following properties with their measures are considered in the present work as essential evaluation criteria for the performance analysis of the TV application [185]:

- ▷ **Stability:** The vehicle sideslip angle β is applied to evaluate the vehicle stability.
- ▷ **Maneuverability:** The time delay between the steering wheel angle and the yaw rate, and the time delay between the steering wheel angle and the lateral acceleration, are defined as the criterion to present the steerability [3]. In addition, the driving trajectories are considered as another reference.
- ▷ **Agility:** The agility is exhibited by the maximum admissible lateral acceleration a_y .

SW integration test

The first test is performed in the PiL simulation. In this test, it is aimed to validate the SW integration as well as to roughly present the performance of the TV application. The driving maneuver is defined as follows: The vehicle velocity is kept constantly at 60 km/h. A step change of steering wheel angle from 0° to 90° is applied.

The yaw rate responses are shown in Figure 8.2. The yaw rate reference of the system without TV is derived from the natural steering behavior of the vehicle introduced in section 7.3.1, while the operation strategy of the TV application determines the reference value based on the neutral steering behavior. Therefore, a higher reference value is required by the system with TV as shown in Figure 8.2a. Unlike the system without TV that the actual yaw rate converges to the reference value, a steady-state control deviation is noticed in the figure. This issue can be clarified in Figure 8.2b. It is important to note, at around the 2nd second, that the upper bound of the input constraint of the yaw rate controller is reached. For this reason, a larger force to increase the yaw rate is impossible and the reference value cannot be reached. However, the reference yaw rate determined by the operation strategy is only a steering behavior to be pursued. More important is that, the actual yaw rate by the same steering wheel angle is increased by the TV application, which implicates that the cornering behavior is improved.

In Figure 8.3 and 8.4, the performances of the tire slip control and the active damping control are presented. Apparently, the reference tracking of slips and torques are satisfying. Because of the asymmetrical torque distribution of TV, a positive tire slip is required on the RR wheel, while a negative slip is applied on the RL wheel. It is important to notice, the slip value of the RL wheel is greater compared to the

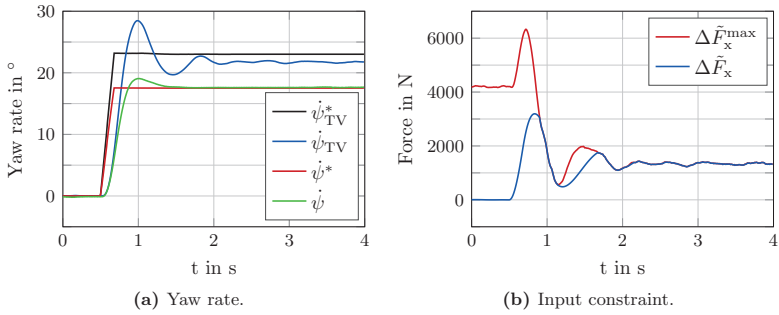


Figure 8.2: Comparison of yaw rate responses.

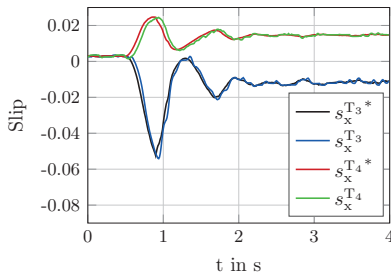


Figure 8.3: Slip control.

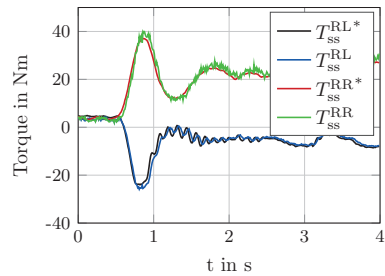


Figure 8.4: Active damping control.

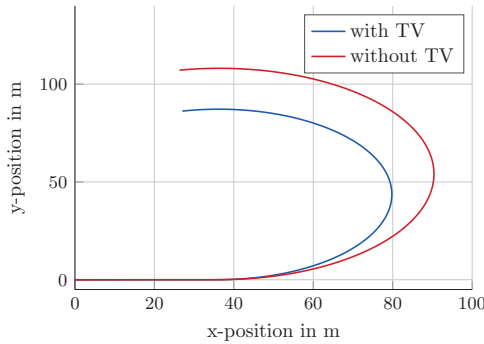


Figure 8.5: Vehicle trajectory.

value of the RR wheel, although the force/torque value on the RL wheel is smaller. This phenomenon is clarified as follows: The vertical load forces on the left and the right wheels are differently distributed due to the roll motion of the vehicle as

introduced in section 7.4. In case of left cornering as in the simulation, the vertical load forces on the right tire is higher than on the left tire. According to the Pacejka tire model, with the same slip, the corresponding force is proportional to $\mu \cdot F_z$. Therefore, in order to obtain the same force, higher slip is applied in case of smaller $\mu \cdot F_z$.

Figure 8.5 illustrates the TV performance in an intuitive way, that the vehicle trajectories are delineated. Apparently, under the condition that the vehicle drives at the same velocity and is steered with the same steering wheel angle, the vehicle with TV requires a shorter duration and path to be steered in the desired direction. It means, assisted by the TV application, that the vehicle steering behavior is improved. This features a great importance in certain emergencies: For instance, the vehicle is steered due to an obstacle appearing abruptly in the driving path. The TV application facilitates the vehicle to drive quickly around the obstacle, while the vehicle with natural steering behavior may drive against it.

Furthermore, another driving situation is simulated: a step change of steering wheel angle from 0° to 180° at 60 km/h is employed. The vehicle behavior with/without TV is illustrated in Figure 8.6 and 8.7.

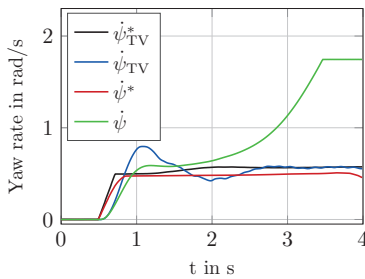


Figure 8.6: Yaw rate.

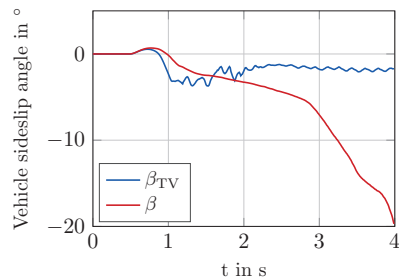


Figure 8.7: Vehicle sideslip angle.

Due to the large step change of the steering wheel angle, large side forces on the tires are produced and result in the instability of the vehicle without TV. Figure 8.6 shows that the actual yaw rate does not match the reference value compared to Figure 8.2a. The peak value of the vehicle sideslip angle in Figure 8.7 is around -20° , which deviates far away from the admissible extreme value of $\pm 6^\circ$ specified in section 2.3.2. In the vehicle with TV in contrast, the actual yaw rate is maintained near to its reference value by means of the yaw rate controller and the vehicle sideslip angle is kept under 4° . This simulation result implicates the fact, that despite of the overreaction of the driver, TV ensures a stable vehicle behavior as long as enough system resource is available for the control application.

As has been introduced, the TV application is validated in the present work by means of the standardized test maneuvers.

Lateral transient response test

As specified in the standard ISO 7401, the driving torque and the steering wheel angle are chosen in such a manner, that the lateral acceleration a_y in steady-state is kept to 4 m/s^2 and the vehicle velocity at 80 km/h . The target of this test is to evaluate the lateral dynamic behavior of the driving system. Figure 8.8 shows the results of the significant measures on the HiL test bench.

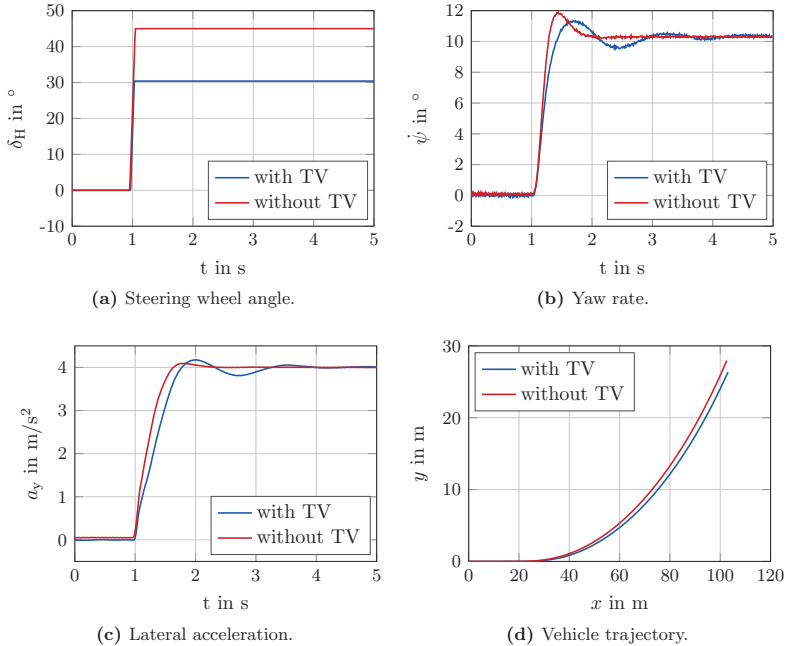


Figure 8.8: Lateral transient response test.

In order to obtain a constant lateral acceleration in the amount of 4 m/s^2 , a larger steering wheel angle is required for the vehicle without TV as presented in Figure 8.10a. The yaw rate responses of both systems are illustrated in Figure 8.10b. The response time of the vehicle without TV is smaller than the vehicle with TV. Furthermore, The yaw rate of the vehicle with TV exhibits an oscillating behavior. The reason of a slower response with TV is clarified as follows: The dynamic of the TV control is limited to the system dynamics in the inner loops. The system response time of the uncontrolled yaw rate in the present work is around 200 ms . However, due to the limited measurement resolution and noises on the test bench, the dynamics of the controllers are restricted, so that the time constant of the entire control system is greater than this response time. As a consequence, additional

longitudinal forces, which are applied by the TV controller to the vehicle system for yaw rate enhancement, have a slower effect on the vehicle compared to the response time of the yaw rate and cause therefore oscillations. In analogy, the transient behavior of the lateral acceleration without TV is better than the one with TV, which is presented in Figure 8.8c. According to ISO 7401, the values of the assessment criteria in this test are measured and given in Table 8.1.

Criterion	Symbol	without TV	with TV
Yaw gain in steady-state	$\left(\dot{\psi}/\delta_H\right)_{ss}$	0.2288 /s	0.3426 /s
Response time of lateral accel.	T_{a_y}	0.469 s	0.633 s
Response time of yaw rate	$T_{\dot{\psi}}$	0.215 s	0.331 s
Time to the maximum lateral accel.	$T_{a_y,max}$	0.818 s	1.01 s
Time to the maximum yaw rate	$T_{\dot{\psi},max}$	0.384 s	0.701 s
Overshooting value of lateral accel.	U_{a_y}	1.0237	1.0311
Overshooting value of yaw rate	$U_{\dot{\psi}}$	1.1473	1.0947

Table 8.1: Values of the assessment criteria of the lateral transient response test.

The yaw gain with TV in steady-state is greater than the one without TV, since the vehicle with TV has a neutral steering behavior, while the vehicle without TV owns the natural under-steering behavior. For this reason, the steady-state steering behavior of the vehicle is improved by means of TV. Subject to ISO 7401, the response time of the quantity is defined by the duration from the time, when 50 % of the steering wheel angle is reached, to the time, when 90 % of the quantity in steady-state is achieved. The time to the maximum quantity is give by the duration from the time, when 50 % of the steering wheel angle is reached, to the time, when the peak value of the quantity is attained. Both the response time and the time to the maximum quantity without TV are shorter when compared to those with TV. The reason was clarified above. The overshooting of the lateral acceleration U_{a_y} with/without TV is comparable. Unlike to the lateral acceleration, the overshooting of the yaw rate without TV is 5 % higher when compared to those with TV. Since the yaw damping coefficient decreases with the vehicle velocity, this overshooting becomes greater at higher velocity without TV and may cause vehicle instability.

As shown above, the dynamic steering behavior with TV is not satisfied when compared to the one without TV. In order to show the effect of this drawback, the vehicle trajectories of both cases are illustrated in Figure 8.8d. Apparently, the vehicle trajectories in both cases deviate little from each other. Since the yaw rates of both cases in steady-state are identical, the slight discrepancy of the trajectories is caused by the yaw rate difference in the transient procedure, which has a marginal effect as shown. Therefore, the drawback of the TV in the transient procedure does not significantly deteriorate the maneuverability of the vehicle.

In Figure 8.9, the essential estimation values are presented. The estimated slip ratios are close to the physical values. The slip ratio of the RR drivetrain has a larger ripple compared to the RL drivetrain, since the driving torque on the former

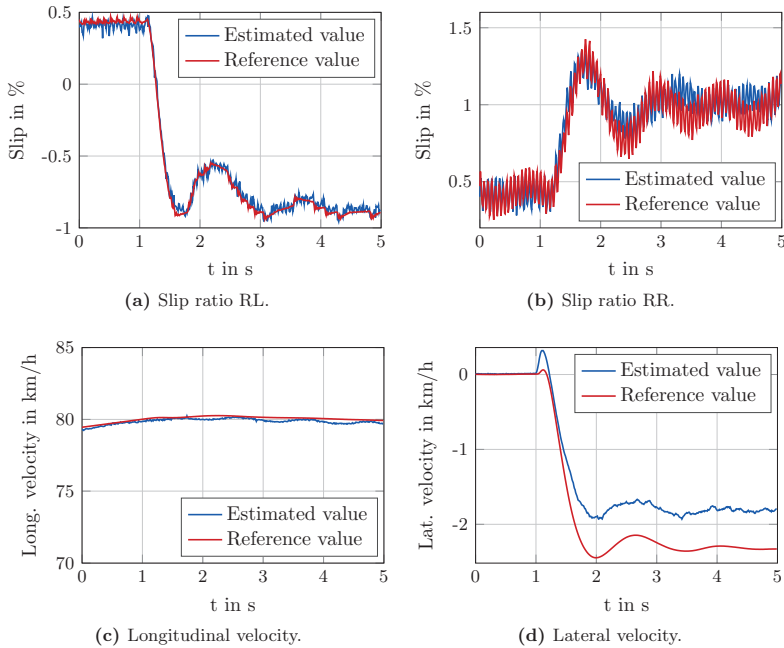


Figure 8.9: Estimation values.

drivetrain is performed by the mechanical components. The longitudinal velocity is well estimated. Since the lateral velocity is marginal, an estimation error is present. The estimation values of other relevant quantities are presented in Appendix I.1.

Sine-steer test

The sine-steer test is performed by a complete period of sinusoidal steering wheel angle with 0.5 Hz as input. The vehicle velocity is kept around 80 km/h by a constant gas pedal position. The magnitude of the steering wheel angles are selected in such a way, that comparable lateral accelerations (around 4 m/s^2) are obtained with/without TV. The results of the HiL simulation are described in Figure 8.10.

Since the comparable yaw rate and lateral acceleration should be attained with/without TV, a higher magnitude of the steering wheel angle is required in the case without TV as described in Figure 8.10a. Similar to the lateral step response test, the transient behaviors of the yaw rate and the lateral acceleration without TV shown in Figure 8.10b and 8.10c are better compared to the ones with TV. According to ISO 7401, the necessary measures of this test are given in Table 8.2.

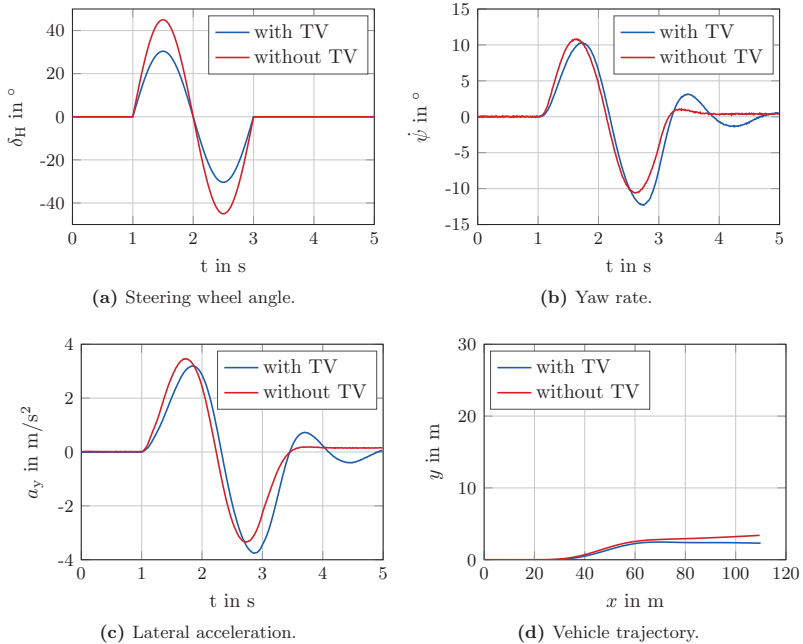


Figure 8.10: Sine-steer test.

Criterion	Symbol	without TV	with TV
Time delay of lateral accel.	$T(\delta_H - a_y)$	0.23 s	0.36 s
Time delay of yaw rate	$T(\delta_H - \dot{\psi})$	0.14 s	0.23 s
Lateral accel. gain	a_y/δ_H	0.0768 (m/s ²)/°	0.1065 (m/s ²)/°
Yaw gain	$\dot{\psi}/\delta_H$	0.240 s	0.342 s

Table 8.2: Values of the assessment criteria of the sine-steer test.

The time delay of a quantity is defined by the duration between the peak values of the steering wheel angle and the quantity. As presented in the table, the delay time of both the lateral acceleration and the yaw rate without TV is smaller compared to those with TV. In contrast, assisted by the TV, the lateral acceleration gain and the yaw gain are greater. As the former test, the vehicle trajectories are illustrated in Figure 8.10d. A similar result is obtained here as in the lateral transient response test, the vehicle trajectory is slightly impacted. The estimation results of the essential values are illustrated in Figure 8.11. Other estimation results are given in Appendix I.2.

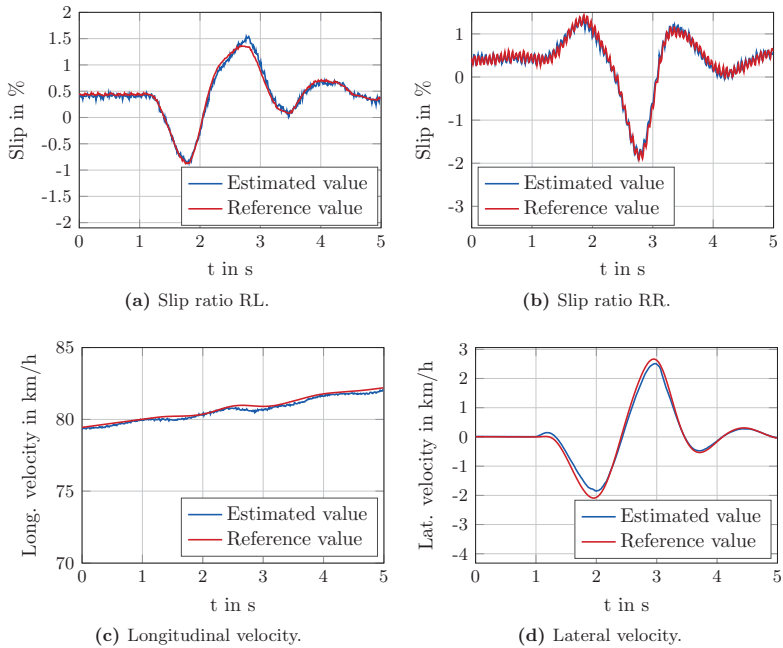


Figure 8.11: Estimation values.

Sine-steer with dwell test

The sine-steer with dwell test is the most appropriate driving maneuver to excite an unstable vehicle behavior. The maneuver is specified in H.3. According to the specification, no gas pedal is applied during the test. The initial vehicle velocity is 80 km/h. Since the safety clutch on the test bench is activated in case of vehicle instability, the test can only be performed in the PiL simulation. Figure 8.12 presents the essential results.

As shown in Figure 8.12a, the same steering wheel angle is applied in both cases. The peak value of the steering wheel angle is 200° . In the first half of the period, the vehicle in both cases is stable. A large yaw rate is obtained by the steering wheel angle. Although only a small force range is available for the TV application due to the large portion of the lateral force, a greater yaw rate is attained assisted by TV. However, in the second half of the period, the vehicle in both cases reaches the system limit. The vehicle without TV exhibits an instability. Both, the yaw rate and the lateral acceleration deviate significantly from the values of the stable behavior, which are described in Figure 8.12b and 8.12c. Figure 8.12e emphasizes this phenomenon: Despite of the reset steering wheel angle, the vehicle slides further

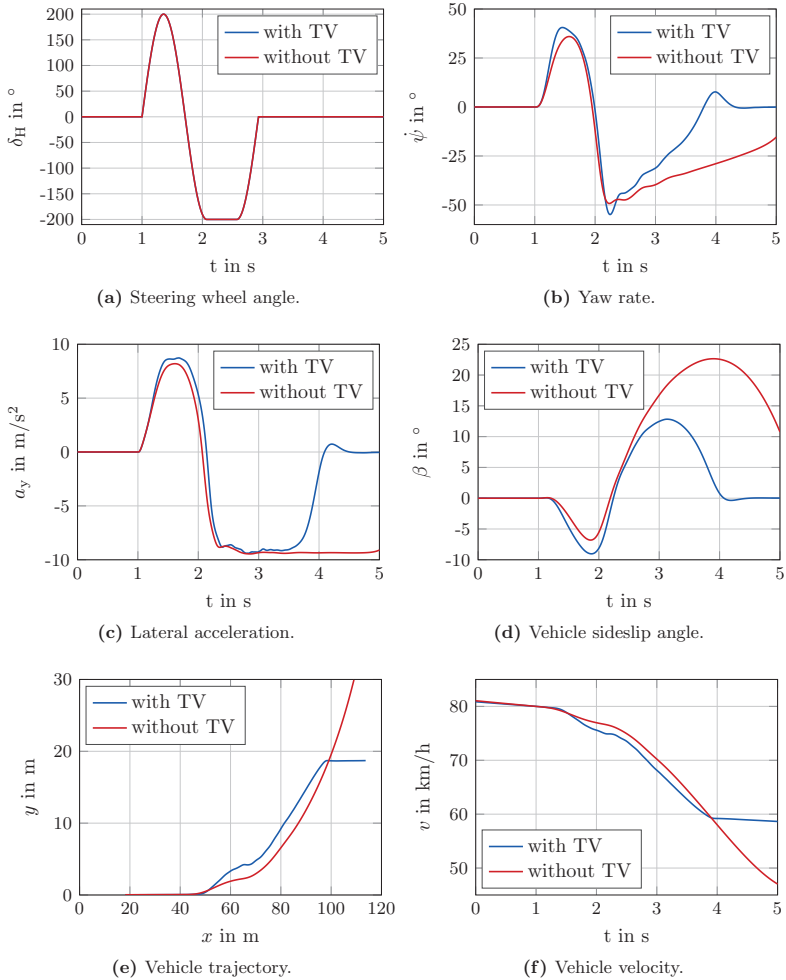


Figure 8.12: Sine-steer with dwell test.

in the same direction. Due to the resistance caused by the large tire slip angles on the front axle, the vehicle velocity decreases significantly as depicted in Figure 8.12f.

In comparison to the case without TV, the vehicle assisted by TV is kept stable. In the second half of the period, the yaw rate is reset slowly. The reason is explained as follows: Restricted by the TFE, not sufficient longitudinal force is available for TV

to control the yaw rate to the reference value, since the lateral forces of both rear tires are large. Once the lateral forces decrease, the control deviation is reduced. In the end, the actual yaw rate is controlled to zero corresponding to the steering wheel angle. The same result is implicated by the vehicle trajectory in Figure 8.12e as well. The vehicle is able to drive straightly in the end of this test since the yaw rate is corrected to zero. It is important to notice, that the vehicle slip angle without TV exceeds 20° , while the slip angle with TV is maintained in an acceptable range compared with the large steering wheel angle. The vehicle velocity is kept at around 60 km/h with TV, while in case without TV the vehicle is able to return to a stable state first at a much lower velocity. This test shows evidently, that the vehicle stability is enhanced significantly by the TV application.

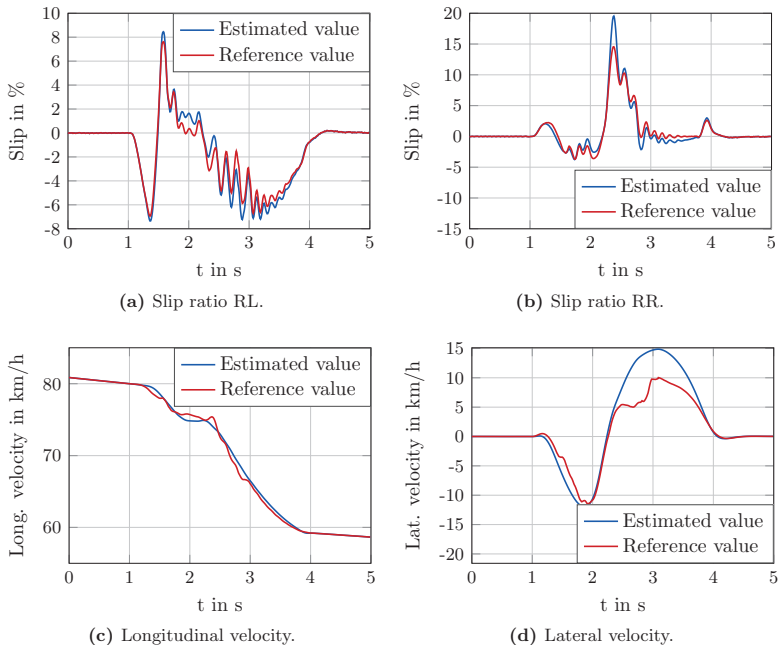


Figure 8.13: Estimation values.

Figure 8.13 illustrates the estimation quality. Although the vehicle dynamics and the tire modeling are far away beyond the linear operation range, the estimation errors are acceptable. These results validate the reliability of the estimator. More estimation results can be found in Appendix I.3.

9 Conclusions and perspectives

Motivated by the increase of the customer requirements in the automotive market, vehicles possessing safety systems are becoming particularly critical. Amongst these safety systems, TV exhibits a reliable facilitation of cornering behavior without significantly deteriorating the drive dynamics. TV exploits the possibility of producing additional yaw moment by applying asymmetric tire forces on either vehicle side. Assisted by this additional yaw moment, the driver's steering effort can be either supported or corrected, so that the vehicle is kept in the desired trajectory. Taking advantage of individual drive wheel control, unlike conventional vehicles with ICE, TV is achieved in EVs without active differential. Furthermore, the response time of torque produced by electric motors is much smaller compared to the response time of ICEs. These features make EV appealing for TV applications.

As preliminaries of the present work, a hypothetical vehicle is defined as the platform for the TV application. The cost, the mass, the installation/HW and SW complexity, the adaptability for TV as well as the vehicle stability are taken into account as the critical criteria. Furthermore, the functional requirements and SW specifications are taken as guidance for the SW development and validation.

The requirements of safety and reliability of TV emphasize a high dynamic and robust control application. For this reason, the optimization-based MPC theories are applied as fundamentals of the present work. Technical reviews are stated in regard to the current control in the IM, the active damping control in the mechanical drivetrain and the torque vectoring control, which constitute the control objective of the present work. In contrast to other works, the potential benefits of MPC theories are further exploited in order to attain a high-performance control application.

In the current control of the IM, the system uncertainties and the system constraints are among the most critical issues, which influence the robustness and the dynamic of the system. Two approaches are implemented to tackle the system uncertainties: In the former case, the system is described as a LPV system with polytopic uncertainties. The optimization problem is represented by minimizing the maximum objective function inside the polytopic uncertainty set, which is bounded by Lyapunov functions. For the purpose of real-time application, the approximated multi-parametric SemiDefinite Programming (mp-SDP) is applied for the orthogonal partition, which is executed off-line, and the quad-tree search is implemented for efficient on-line computation. Due to expensive off-line computational efforts and therefore the inconvenience of tuning control parameters, the latter approach is proposed and implemented in the present work. It is based on a nominal prediction model and restricts the errors between the nominal and the uncertain systems by a RPI set. By determining the minimal Robust Positively Invariant (mRPI) set and the tightened sets of the state and input variables, both of which are polyhedrons, the optimization problem can be formulated as a QP problem. To obtain the real-time application, the QP problem is reformulated into a mp-QP problem, in which

the piecewise affine control laws are expressed explicitly by the vector parameters. Despite the significant reduction of the computational costs in the latter approach compared to the former one, the robustness and the optimality of the system are seldom deteriorated. The simulation and the experimental results show, that both approaches achieve a high control performance despite of parameter mismatches. Meanwhile, in comparison to the approaches based on MPC and Kalman filter with disturbance modeling, the control performance and the robustness of both approaches do not depend on the quality of the disturbance estimation. That means, as can be observed from the results, the overshooting in transient states due to slow estimation is eliminated.

Besides the system uncertainties, the system constraints of IM are taken into account in the control design as well. Instead of directly handling the current and voltage constraints, they are reformulated as torque constraint. The advantage of such reformulation is that, no approximation of quadratic current and voltage constraints is required, since the torque constraint formulation is linear. By appending the time varying torque limit to the vector parameters and applying mp-QP, the approach is applicable for the entire operation range in real-time. It is presented in the results that neglecting the approximation of the system constraints entails a sufficient utilization of the system resource and promotes thus the optimality of the system.

In the mechanical drivetrain, the main control issue is depicted by the oscillating behavior due to the elastic joints among the mechanical components. In order to suppress such torsional oscillations and improve the system performance, an active damping control approach is implemented. Since the control objective is to prevent the natural dominant resonance frequency of the system, which is barely impacted by the potential parameter variations, the explicit MPC approach with underlying mp-QP is applied according to the approximated two-mass-oscillator model. To enhance the control performance, a feedback compensation based on the speed difference between motor and wheel is adopted. By means of this compensation, which is essentially a derivative controller, the damping factor of the closed-loop system can be modified. The system constraint is represented by the torque capacity of the IM as input constraint, whereat the compensation torque has to be factored as well.

To validate the active damping controller by measurements, a test bench is designed, in which the resonance frequency of a mechanical drivetrain in vehicles is simulated. On this test bench, the set-point of the speed-controlled PMSM as a load machine is determined by the wheel speed obtained from the vehicle simulation model. In this manner, the repercussion of the vehicle to the mechanical drivetrain is taken into account.

In the vehicle dynamic system, the LSTM and the DTM are applied as fundamentals for the TV control. Unlike numerous TV control approaches, a tire slip controller is implemented in the present work. The primary advantage of the tire slip control is that the tires' physical limitations can be systematically considered in the control approach. Particularly under low friction conditions, the skidding is suppressed. The tire model is described as a LPV system, in which the longitudinal

velocity and acceleration are considered as time-varying parameters. This system can be dealt with by either the min-max control method based on mp-SDP or the tube-based MPC method. In order to translate the required longitudinal tire forces into the corresponding longitudinal slips, an inverse tire model is implemented by means of LUTs. However, model mismatch can be caused in certain critical situations discussed in the present work. In order to avoid such situations, the maximum tire force limitation is applied by 95 % of the potentially available value. The yaw rate control is composed of a yaw rate controller based on mp-QP and several auxiliary components responsible for the disturbance rejection, the dynamic constraint computation as well as the driving force determination. For the purpose of reference tracking of the yaw rate, the force difference between both drive wheels is overlapped to the symmetrical driving force demanded by the driver in such a way, that the total driving force remains a constant. However, in some extreme situations, where the tire force limitation is reached, either the TV force or the force demanded by the driver must be modified. In the present work, the TV force is kept unchanged to guarantee that the control performance and the driving force from the driver is adapted according to the tire force limitation. Nevertheless, the driver cannot sense this change, since it takes place transiently.

In order to enhance the reliability of the TV application, an operation strategy is proposed. According to it, the maximum admissible yaw rate and the road situations such as cross slope and inhomogeneous frictions are considered. In this way, a proper situation-dependent yaw rate reference can be determined for the TV control. Furthermore, a systematical estimation strategy is developed to provide the unmeasurable signals used by the TV application.

According to the development procedure of the V-model, the validated controlled IM and the damped mechanical drivetrain subsystems are finally integrated into the vehicle system with TV. The entire system is validated through both the PiL and the HiL simulation. The evaluation of the TV application is performed according to the vehicle stability, steerability and agility. Due to the equipment limitations such as resolution and noises, the dynamic of the active damping control is limited. As a consequence, the dynamic of the entire TV application is slower than the tire dynamic. Slight contribution is made by the TV application to enhance the transient behavior. According to the evaluation criterion specified in ISO 7401, the transient maneuverability in case of absence of the TV application is therefore better. However, since the TV application enables a neutral steering behavior, more yaw rate is attained by the identical steering effort of the driver. Therefore, the steering behavior assisted by the TV application is usually better than the natural steering behavior. The results of the sine-steer with dwell test show, that the TV application ensures a stable vehicle behavior in critical driving situations, while the vehicle without TV application becomes completely unstable. Furthermore, a higher agility is achieved by means of the TV application. Ultimately, the cornering behavior and the vehicle safety are evidently enhanced by the TV application.

Although the test results prove that a high-performance torque vectoring is attained by means of the optimization-based control approaches, several works can be performed in the future. The primary work to be expected is to apply and test

the entire SW in a real vehicle system. This means, the control parameters and the estimation parameters have to be newly calibrated. Moreover, several control issues can be anticipated in such a system: So far the Pacejka tire model is adopted both in the control SW and in the vehicle model. However, such model is an approximation of real tires' property. As a consequence, the estimation quality of the friction coefficient μ based on the tire model is limited. Another factor, which influences the estimation accuracy of the friction coefficient, is the tire wear. Since the physical properties may change with the wearing and the aging of the tire, it is reasonable to assume that the characteristic line obtained from a used tire is significantly different from the one obtained from a new tire. This phenomenon emphasizes the necessity and importance of the friction coefficient estimation in the practice.

Furthermore, in the present work, a neutral steering behavior ($\eta = 0$) is pursued. However, depending on the requirement of the TV application, the characteristic line can be modified. For instance, an over-steering characteristic ($\eta < 0$) can be specified for sports cars. The impact of this change over the control strategy should be also carefully investigated.

Finally, the redundancy of the signals and the failure tolerance of the TV application are worthy to be studied. In case of sensor failures, the failed signal can be replaced by the value derived from other signals. In the most critical cases, the TV application should be either switched to the limp modus or completely switched off and the overlying ESC system takes on the responsibility to ensure the vehicle stability.

A Definitions and notations of optimization problems

Definition A.0.1 (Closed Set [42]) A set S is closed if every point outside S has a neighborhood disjoint from S .

Definition A.0.2 (Bounded Set [42]) A set in \mathbb{R}^n is bounded if it is contained inside a ball $\{\mathbf{x} \in \mathbb{R}^n : \|\mathbf{x}\| \leq R\}$ of finite radius R .

Definition A.0.3 (Compact Set [42]) A set in \mathbb{R}^n is compact if it is both bounded and closed.

Definition A.0.4 (Convex Set [27]) A set C is convex if the line segment between any two points in C lies in C , i.e., if for any $\mathbf{x}_1, \mathbf{x}_2 \in C$ and any θ with $0 \leq \theta \leq 1$, it holds

$$\theta \mathbf{x}_1 + (1 - \theta) \mathbf{x}_2 \in C. \quad (\text{A.1})$$

Definition A.0.5 (Hyperplane and Halfspace [27]) A hyperplane is a set of the form

$$\{\mathbf{x} \mid \mathbf{a}^T \mathbf{x} = b\}, \quad (\text{A.2})$$

where $\mathbf{a} \in \mathbb{R}^n$, $\mathbf{a} \neq 0$, and $b \in \mathbb{R}$.

A hyperplane divides \mathbb{R}^n into two halfspaces. A (closed) halfspace is a set of the form

$$\{\mathbf{x} \mid \mathbf{a}^T \mathbf{x} \leq b\}, \quad (\text{A.3})$$

where $\mathbf{a} \neq 0$.

Definition A.0.6 (Polyhedron [27]) A polyhedron is defined as the solution set of a finite number of linear equalities and inequalities:

$$\mathcal{P} = \{\mathbf{x} \mid \mathbf{a}_i^T \mathbf{x} \leq b_i, i = 1, \dots, m, \mathbf{c}_j^T \mathbf{x} = d_j, j = 1, \dots, p\}. \quad (\text{A.4})$$

Obviously, a polyhedron is the intersection of a finite number of halfspaces and hyperplanes.

Definition A.0.7 (Polyhedral Partition [25]) A collection of sets $\mathcal{P}_1, \dots, \mathcal{P}_N$ is a partition of a set Θ if $\bigcup_{i=1}^N \mathcal{P}_i = \Theta$ and $\mathcal{P}_i \cap \mathcal{P}_j = \emptyset, \forall i \neq j$. Moreover, $\mathcal{P}_1, \dots, \mathcal{P}_N$ is a polyhedral partition of a polyhedral set Θ if $\mathcal{P}_1, \dots, \mathcal{P}_N$ is a partition of Θ and the $\overline{\mathcal{P}_i}$ are polyhedral sets, where $\overline{\mathcal{P}_i}$ denotes the closure of the set \mathcal{P}_i .

Definition A.0.8 (Polytope [27]) A bounded polyhedron $\mathcal{P} \in \mathbb{R}^n$

$$\mathcal{P} = \{\mathbf{x} \in \mathbb{R}^n : \mathbf{H}\mathbf{x} \leq \mathbf{d}\}, \quad (\text{A.5})$$

is called a polytope, where $\mathbf{H} \in \mathbb{R}^{q \times n}$, $\mathbf{d} \in \mathbb{R}^q$, where q represents the number of halfspaces defining \mathcal{P} and all inequalities are interpreted in an element-wise manner.

Definition A.0.9 (Convex Hull [27]) The convex hull of a set $\mathcal{S} \subseteq \mathbb{R}^n$, denoted $\text{Co}\{\mathcal{S}\}$, is the set of all convex combinations of points v_i , $i \in \{1, \dots, M\}$ in \mathcal{S} :

$$\text{Co}\{\mathcal{S}\} = \left\{ \sum_{l=1}^L \theta_l v_l, 0 \leq \theta_l \leq 1, \sum_{l=1}^L \theta_l = 1 \right\}. \quad (\text{A.6})$$

The points v_i represent the vertices of this convex hull.

Definition A.0.10 (Robust Positively Invariant Set [19]) A set $\Theta \subset \mathbb{R}^n$ is said to be robust positively invariant (RPI) for a system $\mathbf{x}(k+1) = f(\mathbf{x}(k), \mathbf{w}(k))$, if for all $\mathbf{x}(0) \in \Theta$ and all $\mathbf{w}(k) \in \mathcal{W}$ the solution $\mathbf{x}(k) \in \Theta$ for all $k > 0$.

Definition A.0.11 (Minimal Robust Positively Invariant Set [154]) A robust positively invariant set \mathcal{F}_∞ is said minimal robust positively invariant (mRPI) for a system $\mathbf{x}(k+1) = f(\mathbf{x}(k), \mathbf{w}(k))$, if it is contained in every closed RPI set of this system.

Definition A.0.12 (Convex Function [27]) A function $f: \mathbb{R}^n \rightarrow \mathbb{R}$ is convex if its domain is a convex set and if for all \mathbf{x}_1 and \mathbf{x}_2 in its domain and any scalar θ with $0 \leq \theta \leq 1$ the following inequality is satisfied

$$f(\theta \mathbf{x}_1 + (1 - \theta) \mathbf{x}_2) \leq \theta f(\mathbf{x}_1) + (1 - \theta) f(\mathbf{x}_2). \quad (\text{A.7})$$

Definition A.0.13 (Convex Quadratic Function [27]) A quadratic function $f(\mathbf{x}) = \mathbf{x}^T \mathbf{Q} \mathbf{x} + 2\mathbf{c}^T \mathbf{x} + d$ is convex if and only if $\mathbf{Q} \succeq 0$, and a quadratic function $f(\mathbf{x}) = \mathbf{x}^T \mathbf{Q} \mathbf{x} + 2\mathbf{c}^T \mathbf{x} + d$ is strictly convex if and only if $\mathbf{Q} \succ 0$.

Definition A.0.14 (Affine Function [27]) A function $f: \mathbb{R}^n \rightarrow \mathbb{R}^m$ is affine if it is a sum of a linear function and a constant, i.e., if it has the form $f(\mathbf{x}) = \mathbf{A}\mathbf{x} + \mathbf{b}$, where $\mathbf{A} \in \mathbb{R}^{m \times n}$ and $\mathbf{b} \in \mathbb{R}^m$.

Definition A.0.15 (Piecewise Affine Function [25]) A function $f: \mathbb{R}^n \rightarrow \mathbb{R}^n$, is piecewise affine (PWA) if there exists a partition $\mathcal{R}_1, \dots, \mathcal{R}_N$ of the domain in \mathbb{R}^n , and $f^i(\mathbf{x}) = \mathbf{A}^i \mathbf{x} + \mathbf{b}^i, \forall \mathbf{x} \in \mathcal{R}_i, i = 1, \dots, N$

Piecewise quadratic (PWQ) functions are defined analogously.

Definition A.0.16 (Minkowski Set Addition [166]) *The Minkowski set addition is defined as follows:*

$$\mathcal{A} \oplus \mathcal{B} := \{\mathbf{x} + \mathbf{y} \mid \mathbf{x} \in \mathcal{A}, \mathbf{y} \in \mathcal{B}\}, \quad (\text{A.8})$$

where $\mathcal{A} \subset \mathbb{R}^n$ and $\mathcal{B} \subset \mathbb{R}^n$.

Definition A.0.17 (Pontryagin Set Difference [99]) *The Pontryagin set difference is defined as follows*

$$\mathcal{A} \ominus \mathcal{B} := \{\mathbf{x} \in \mathbb{R}^n \mid \mathbf{x} + \mathbf{y} \in \mathcal{A}, \forall \mathbf{y} \in \mathcal{B}\}, \quad (\text{A.9})$$

where $\mathcal{A} \subset \mathbb{R}^n$ and $\mathcal{B} \subset \mathbb{R}^n$.

The indispensable relationship between Pontryagin set difference and Minkowski set addition is that the former one is not exactly the complement of the latter one. Actually, instead of $(\mathcal{A} \ominus \mathcal{B}) \oplus \mathcal{B} = \mathcal{A}$, $(\mathcal{A} \ominus \mathcal{B}) \oplus \mathcal{B} \subset \mathcal{A}$ [24].

Notation A.0.1 *The description $\mathbf{F} \in \mathbb{S}^n$ denotes that matrix \mathbf{F} is symmetric, where \mathbb{S}^n represents the set of symmetric matrices in $\mathbb{R}^{n \times n}$. Analogously, $\mathbf{F} \in \mathbb{S}_+^n$ and $\mathbf{F} \in \mathbb{S}_{++}^n$ denote that the matrix is positive semidefinite ($\mathbf{F} \succeq 0$) and positive definite ($\mathbf{F} \succ 0$) respectively.*

Notation A.0.2 *The subscripts r , b , l associated with the state vector \mathbf{x} , input vector \mathbf{u} and output vector \mathbf{y} denote real, binary and logical value, respectively.*

Notation A.0.3 *The subscripts i , k associated with the state vector \mathbf{x} , input vector \mathbf{u} and output vector \mathbf{y} denote the index for the prediction horizon and the current time instant respectively.*

B Technical data of electric drivetrain

Component	Model type
Drive motor	Siemens 1LA5186-4AA10
Load machine	Siemens Servomotor 1FT6134-6SF71-1EH0
Supply module	Simodrive 1P 6SN1145-1BA02-0CA1
Power module (drive motor)	Simodrive 1P 6SN1123-1AA00-0EA2
Power module (load machine)	Simodrive 6SN1123-1AA01-0FA1
Control module (load machine)	Simodrive 611 universal HRS
DSP system	dSPACE 1103
Interface between Simodrive and dSPACE	Sidi board

Table B.1: Electrical component list.

Model type	Siemens 1LA5186-4AA10
Rated voltage	400 V
Rated current	41.5 A
Rated power	22 kW
Rated torque	144 Nm
Stator frequency at rated point	50 Hz
Rated slip	2,67%
Pole pair number	2
Stator resistance	0.18 Ω
Rotor resistance (referred to stator side)	0.1232 Ω
Stator leakage inductance	1.94 mH
rotor leakage inductance (referred to stator side)	1.27 mH
Mutual inductance	40.11 mH
Rotor inertia	0.15 kgm ²
Topology	star connection

Table B.2: Parameters of the drive motor.

Model type	Siemens 1LA5186-4AA10
Rated voltage	283 V
Rated current	23.1 A
Rated torque	56 Nm
Stator frequency at rated point	50 Hz

Table B.3: Modified rated point of the drive motor.

Model type	Siemens Servomotor 1FT6134-6SF71-1EH0
Rated voltage	324 V
Rated current	72 A
Rated power	35 kW
Rated torque	110 Nm
Rated speed	3000 rpm
Pole pair number	3
Maximum speed	3600 rpm
Maximum torque	316 Nm
Peak current	264 A
Constant of torque	1.68 Nm/A
Winding resistance	0.039 Ω
Rotating field inductance	1.3 mH
Electrical time constant	33 ms
Mechanical time constant	2.3 ms
Inertia (with brake mechanism)	0.0625 kgm ²
Inertia (without brake mechanism)	0.0547 kgm ²
Encoder	EQN 1325

Table B.4: Parameters of the load machine.

Model type	Simodrive 1P 6SN1145-1BA02-0CA1
Rated power	36 kW
Rated voltage	400 V
dc link voltage	600 V

Table B.5: Parameters of the supply module.

Model type	Simodrive 1P 6SN1123-1AA00-0EA2
dc link voltage	600 V
Rated current	60 A
Peak current	160 A
Carrier frequency	3.2 kHz

Table B.6: Parameters of the power module for the drive motor.

Model type	Simodrive 6SN1123-1AA01-0FA1
dc link voltage	600 V
Rated current	70 A
Peak current	200 A
Number of axles	1

Table B.7: Parameters of the power module for the load machine.

Model type	Simodrive 611 universal HRS
Resolution	switchable 14/12 bit
Pole pair number	1-6
Maximum operating frequency	108/432 Hz
TTL-sensor for IM	until 420 kHz
Analoge I/O	2
Digitale I/O	4
Operation mode	speed- or torque-controlled

Table B.8: Parameters of control module for the load machine

Model type	dSPACE 1103 PPC Controller Board
CPU clock frequency	1 GHz
Memory (local)	32 MB
memory (global)	96 MB
A/D converter	20 channels
D/A converter	8 channels
Timers	8
Digital I/O	32-bit
Encoder interface	8 (digital), 1 (analog)
Slave DSP	Texas Instruments TMS320F240
Relevant software	Real-Time Library/Interface

Table B.9: Data of DSP system.

Model type	Heidenhain ROD 420
Teeth number	2000
Sampling rate	≤ 300 kHz
Maximum speed	16 000 rpm

Table B.10: Data of Encoder for the drive motor.

Model type	HBM T10F 500
Rated torque	500 Nm
Voltage output (positive)	10 V
Voltage output (negative)	-10 V
Residual ripple (peak-to-peak)	0.4 %
Frequency output delay time	0.15 ms
Voltage output delay time	0.9 ms
Inertia of rotor	$13.2 \times 10^{-3} \text{kgm}^2$

Table B.11: Data of torque meter.

C Measurement of the characteristic curve of the stator inductance

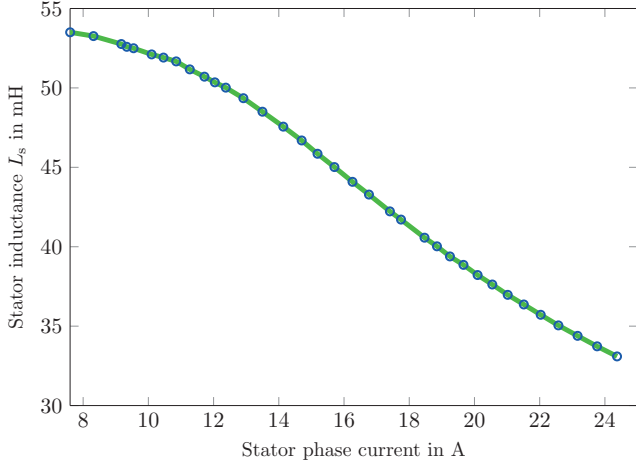


Figure C.1: Characteristic curve of stator inductance.

In order to obtain the characteristic curve of the stator inductance, the measurement is performed in no-load operation at high speed. In this case, the current on the q-axis is marginal and the voltage drop on the stator resistance can be neglected. Therefore, the stator voltage equations in steady-state are simplified by

$$\begin{aligned} u_{sd} &= -\omega_{\mu} \cdot \sigma \cdot L_s \cdot i_{sq} \\ u_{sq} &= \omega_{\mu} \cdot L_s \cdot i_{sd}. \end{aligned} \quad (\text{C.1})$$

By means of the power-invariant transformation, it follows

$$u_{sd}^2 + u_{sq}^2 = 3 \cdot U_1^2. \quad (\text{C.2})$$

Assuming $\omega_{\mu} \approx \omega_r$, the stator inductance is calculated by

$$L_s = \sqrt{\frac{3 \cdot U_1^2}{(\omega_r \cdot \sigma \cdot i_{sq})^2 + (\omega_r \cdot i_{sd})^2}}. \quad (\text{C.3})$$

D Dynamic torque constraint calculation

Torque constraint in the basic speed area is derived from the following equations:

$$\begin{aligned} I_{\text{dq,max}}^2 &= i_{\text{sd}}^2 + i_{\text{sq}}^2 \\ i_{\text{sd}} &= i_{\text{sd,n}} \\ \bar{T}_{\text{el}} &= \frac{pL_{\text{m}}^2}{L_{\text{r}}} i_{\text{sd}} i_{\text{sq}}. \end{aligned}$$

Substituting i_{sd} for i_{sq} , the torque constraint is expressed as

$$\bar{T}_{\text{el}} = \frac{pL_{\text{m}}^2}{L_{\text{r}}} i_{\text{sd,n}} \sqrt{I_{\text{dq,max}}^2 - i_{\text{sd,n}}^2}. \quad (\text{D.1})$$

Torque constraint in the field-weakening area is calculated as follows: First, the rotor flux speed ω_{μ} in case that the voltage constraint is active, is derived by solving the equations

$$\begin{aligned} i_{\text{sd}} &= \frac{\omega_{\text{n}}}{\omega_{\text{r}}} i_{\text{sd,n}} \\ U_{\text{dq,max}}^2 &= (\omega_{\mu} L_{\text{s}} i_{\text{sd}})^2 + (\sigma \omega_{\mu} L_{\text{s}} i_{\text{sq}})^2 \\ \omega_{\mu} &= \omega_{\text{r}} + \frac{i_{\text{sq}}}{\tau_{\text{r}} i_{\text{sd}}}, \end{aligned}$$

which result in a fourth-order polynomial equation according to ω_{μ} :

$$U_{\text{dq,max}}^2 = \left(\frac{\omega_{\text{n}} L_{\text{s}} i_{\text{sd,n}}}{\omega_{\text{r}}} \right)^2 \cdot \omega_{\mu}^2 + \left(\frac{\omega_{\text{n}} \tau_{\text{r}} \sigma L_{\text{s}} i_{\text{sd,n}}}{\omega_{\text{r}}} \right)^2 \cdot (\omega_{\mu} - \omega_{\text{r}})^2 \cdot \omega_{\mu}^2. \quad (\text{D.2})$$

Second, the maximum torque is calculated by solving the equations

$$\begin{aligned} U_{\text{dq,max}}^2 &= (\omega_{\mu} L_{\text{s}} i_{\text{sd}})^2 + (\sigma \omega_{\mu} L_{\text{s}} i_{\text{sq}})^2 \\ i_{\text{sd}} &= \frac{\omega_{\text{n}}}{\omega_{\text{r}}} i_{\text{sd,n}} \\ \bar{T}_{\text{el}} &= \frac{pL_{\text{m}}^2}{L_{\text{r}}} i_{\text{sd}} i_{\text{sq}}. \end{aligned}$$

Finally, the torque constraint in the field-weakening area is expressed as

$$\bar{T}_{\text{el}} = \frac{pL_{\text{m}}^2}{L_{\text{r}}} \frac{\omega_{\text{n}}}{\omega_{\text{r}}} i_{\text{sd,n}} \sqrt{\left(\frac{U_{\text{dq,max}}}{\sigma \omega_{\mu} L_{\text{s}}} \right)^2 - \left(\frac{\omega_{\text{n}}}{\sigma \omega_{\text{r}}} i_{\text{sd,n}} \right)^2} \quad (\text{D.3})$$

with ω_{μ} as the solution of (D.2) and L_{s} from the LUT illustrated in Figure C.1. L_{m} and L_{r}' are derived from L_{s} assuming that σ , σ_1 and σ_2 are constant.

E Technical data of mechanical drivetrain

Parameter	Symbol	Value
Inertia of the rotor	J_r	0.15 kg · m ²
Inertia of the torquemeter	J_{tm}	0.0132 kgm ²
Inertia of the safety clutch	J_{cl}	0.012 kgm ²
Inertia of the flywheel	J_{fw}	2.2677 kgm ²
Effective length of the drive shaft	l_{eff}	1.55 m
Stiffness of the drive shaft	c	837.8 Nm/rad

Table E.1: Parameters of the mechanical drivetrain.

F Technical data of the hypothetical vehicle

Vehicle parameter	Symbol	Value
Mass	m	1525 kg
Wheelbase	w_B	2.57 m
Axle track (front / rear)	b_F / b_R	1.544 m / 1.544 m
Wheel load distribution (front / rear)	l_F / l_R	1.438 m / 1.132 m
Height of CoG	h	0.543 m
Vehicle inertia	I_x	548 kgm ²
	I_y	1732 kgm ²
	I_z	1809 kgm ²
Manufactured tire radius	R_0	0.35 m
Transmission ratio of speed $\frac{\Omega_t}{\Omega_w}$	i_v	2
Transmission ratio of torque $\frac{T_w}{T_{el}}$	i_t	18
Transmission ratio of steering $\frac{\delta_H}{\delta}$	i_s	25.13

Table F.1: Parameters of the hypothetical vehicle.

F.1 The Magic Formula Tire Model: Full Set of Equations

All relevant equations utilized to adapt the MF in this work are stated below. In order to simplify the notation an auxiliary input, $\Delta F_z = (F_z - F_{z0})/F_{z0}$, denoting the normalized change in tire load force with respect to the nominal load force F_{z0} , is introduced. Numerical stability over MF's full range of applicability is achieved by including a small offset $\epsilon = 0.01$ in some critical denominators. Due to the assumption of zero wheel camber ($\gamma = 0$), terms involving γ do not appear in the subsequent formulation. Furthermore, it is useful to redefine slip quantities for use with the MF slightly deviating from the definitions given in (7.6) and (7.7):

$$s'_x = -\frac{v_{sx}}{|v_s|} = s_x \cdot \text{sgn } v_x \quad (\text{F.1})$$

$$s'_y = \tan \alpha \cdot \text{sgn } v_x = \frac{v_y}{|v_s|} = s_y \cdot \text{sgn } v_x \quad (\text{F.2})$$

F.1.1 Longitudinal Tire Force

The full set of equations for the longitudinal tire force F_x ($i = x, j = y$) is given below. Values for the coefficients p_* , that are introduced in this section are provided in Table F.2.

F.1.1.1 Main Equations

$$F_x(s'_x, s'_y, F_z, \Delta F_z) = F_{x0}(s'_x, F_z, \Delta F_z) \cdot G_{xy}(s'_y, F_z, \Delta F_z) \quad (\text{F.3a})$$

$$F_{x0} = D_x \sin(C_x \arctan[B_x \tilde{s}_x - E_x(B_x \tilde{s}_x - \arctan B_x \tilde{s}_x)]) + S_{Vx} \quad (\text{F.3b})$$

$$G_{xy} = \frac{\cos(C_{xy} \arctan[B_{xy} \tilde{s}_y - E_{xy}(B_{xy} \tilde{s}_y - \arctan B_{xy} \tilde{s}_y)])}{\cos(C_{xy} \arctan[B_{xy} S_{Hxy} - E_{xy}(B_{xy} S_{Hxy} - \arctan B_{xy} S_{Hxy})])} \quad (\text{F.3c})$$

$$\tilde{s}_x = s'_x + S_{Hx} \quad (\text{F.3d})$$

$$\tilde{s}_y = s'_y + S_{Hxy} \quad (\text{F.3e})$$

F.1.1.2 Main Parameters

$$B_x = \frac{K_x}{C_x \cdot D_x + \epsilon} \quad (\text{F.4a})$$

$$C_x = p_{Cx1} \quad (\text{F.4b})$$

$$D_x = \mu_x \cdot F_z \quad (\text{F.4c})$$

$$E_x = (p_{Ex1} + p_{Ex2} \cdot \Delta F_z + p_{Ex3} \cdot \Delta F_z^2) \cdot (1 - p_{Ex4} \cdot \text{sgn}(s'_x + S_{Hx})) \quad (\text{F.4d})$$

$$S_{Hx} = p_{Hx1} + p_{Hx2} \cdot \Delta F_z \quad (\text{F.4e})$$

$p_{C_{x1}} = 1.685$			
$p_{D_{x1}} = 1.21$	$p_{D_{x2}} = -0.037$		
$p_{E_{x1}} = 0.344$	$p_{E_{x2}} = 0.095$	$p_{E_{x3}} = -0.02$	$p_{E_{x4}} = 0$
$p_{H_{x1}} = 0$	$p_{H_{x2}} = 0$		
$p_{V_{x1}} = 0$	$p_{V_{x2}} = 0$		
$p_{B_{xy1}} = 12.35$	$p_{B_{xy2}} = -10.77$		
$p_{C_{xy1}} = 1.092$			
$p_{E_{xy1}} = 0$	$p_{E_{xy2}} = 0$		
$p_{H_{xy1}} = 0.007$			
$p_{K_{x1}} = 21.51$	$p_{K_{x2}} = -0.163$	$p_{K_{x3}} = 0.245$	

Table F.2: Coefficients used for longitudinal tire force computation.

$$S_{V_x} = F_z \cdot (p_{V_{x1}} + p_{V_{x2}} \cdot \Delta F_z) \quad (\text{F.4f})$$

$$B_{xy} = p_{B_{xy1}} \cdot \cos(\arctan(p_{B_{xy2}} \cdot s'_x)) \quad (\text{F.4g})$$

$$C_{xy} = p_{C_{xy1}} \quad (\text{F.4h})$$

$$E_{xy} = p_{E_{xy1}} + p_{E_{xy2}} \cdot \Delta F_z \quad (\text{F.4i})$$

$$S_{H_{xy}} = p_{H_{xy1}} \quad (\text{F.4j})$$

F.1.1.3 Auxiliary Parameters

$$\mu_x = \lambda_\mu \cdot (p_{D_{x1}} + p_{D_{x2}} \cdot \Delta F_z) \quad (\text{F.5a})$$

$$K_x = F_z \cdot (p_{K_{x1}} + p_{K_{x2}} \cdot \Delta F_z) \cdot \exp(p_{K_{x3}} \cdot \Delta F_z) \quad (\text{F.5b})$$

F.1.2 Lateral Tire Force

The full set of equations for the lateral tire force F_y ($i = y, j = x$) is given below. Values for coefficients p_* introduced in this section are provided in Table F.3.

F.1.2.1 Main Equations

$$F_y(s'_x, s'_y, F_z, \Delta F_z) = F_{y0}(s'_y, F_z, \Delta F_z) \cdot G_{yx}(s'_x, F_z, \Delta F_z) + S_{V_{yx}} \quad (\text{F.6a})$$

$$F_{y0} = D_y \sin(C_y \arctan[B_y \tilde{s}_y - E_y (B_y \tilde{s}_y - \arctan B_y \tilde{s}_y)]) + S_{V_y} \quad (\text{F.6b})$$

$$G_{yx} = \frac{\cos(C_{yx} \arctan [B_{yx} \bar{s}_x - E_{yx} (B_{yx} \bar{s}_x - \arctan B_{yx} \bar{s}_x)])}{\cos(C_{yx} \arctan [B_{yx} S_{Hyx} - E_{yx} (B_{yx} S_{Hyx} - \arctan B_{yx} S_{Hyx})])} \quad (\text{F.6c})$$

$$\tilde{s}_y = s'_y + S_{Hy} \quad (\text{F.6d})$$

$$\bar{s}_x = s'_x + S_{Hyx} \quad (\text{F.6e})$$

F.1.2.2 Main Parameters

$$B_y = \frac{K_y}{C_y \cdot D_y + \epsilon} \quad (\text{F.7a})$$

$$C_y = p_{Cy1} \quad (\text{F.7b})$$

$$D_y = \mu_y \cdot F_z \quad (\text{F.7c})$$

$$E_y = (p_{Ey1} + p_{Ey2} \cdot \Delta F_z) \cdot (1 - p_{Ey3} \cdot \text{sgn}(s'_y + S_{Hy})) \quad (\text{F.7d})$$

$$S_{Hy} = p_{Hy1} + p_{Hy2} \cdot \Delta F_z \quad (\text{F.7e})$$

$$S_{Vy} = F_z \cdot (p_{Vy1} + p_{Vy2} \cdot \Delta F_z) \quad (\text{F.7f})$$

$$B_{yx} = p_{Byx1} \cdot \cos(\arctan [(p_{Byx2} \cdot (s'_y - p_{Byx3}))]) \quad (\text{F.7g})$$

$$C_{yx} = p_{Cyx1} \quad (\text{F.7h})$$

$$E_{yx} = p_{Eyx1} + p_{Eyx2} \cdot \Delta F_z \quad (\text{F.7i})$$

$$S_{Hyx} = p_{Hyx1} + p_{Hyx2} \cdot \Delta F_z \quad (\text{F.7j})$$

$$S_{Vyx} = \mu_y \cdot F_z \cdot (p_{Vyx1} + p_{Vyx2} \cdot \Delta F_z) \cdot \cos(\arctan(p_{Vyx4} \cdot s'_y)) \cdot \sin p_{Vyx5} \cdot (\arctan(p_{Vyx6} \cdot s'_x)) \quad (\text{F.7k})$$

F.1.2.3 Auxiliary Parameters

$$\mu_y = \lambda_\mu \cdot (p_{Dy1} + p_{Dy2} \cdot \Delta F_z) \quad (\text{F.8a})$$

$$K_y = p_{Ky1} \cdot F_{z0} \cdot \sin\left(p_{Ky4} \cdot \arctan\left(\frac{F_z}{F_{z0} \cdot p_{Ky2}}\right)\right) \quad (\text{F.8b})$$

F.1.3 Scaling of the Friction Coefficient

For the longitudinal and lateral tire forces a scaling parameter λ_μ was incorporated into the equations defining μ_x and μ_y (F.5a), (F.8a). In order to account for changing road surface conditions λ_μ may be varied according to Table F.4, effectively scaling the maximum available friction forces in both directions.

$p_{Cy1} = 1.193$				
$p_{Dy1} = -0.99$		$p_{Dy2} = 0.145$		
$p_{Ey1} = -1.003$		$p_{Ey2} = -0.532$		$p_{Ey3} = -0.083$
$p_{Hy1} = 0$		$p_{Hy2} = 0$		
$p_{Vy1} = 0$		$p_{Vy2} = 0$		
$p_{Byx1} = 6.4615$		$p_{Byx2} = 4.196$		$p_{Byx3} = -0.015$
$p_{Cyx1} = 1.081$				
$p_{Eyx1} = 0$		$p_{Eyx2} = 0$		
$p_{Hyx1} = 0.009$		$p_{Hyx2} = 0$		
$p_{Vyx1} = 0.053$		$p_{Vyx2} = -0.073$		$p_{Vyx4} = 35.44$
				$p_{Vyx5} = 1.9$
				$p_{Vyx5} = -10.71$
$p_{Ky1} = 14.95$		$p_{Ky2} = 2.13$		$p_{Ky4} = 2$

Table F.3: Coefficients used for lateral tire force computation.

Road Condition	Dry	Damp	Wet	Icy
λ_μ	1	0.75	0.5	0.25

Table F.4: Adjustment of the friction coefficients μ_x , μ_y for different road conditions.

G Derivation of the computations in the operation strategy

G.1 Derivation of system matrices of the EKF

$$I_z \cdot \ddot{\psi} = \sum F_y^{T_i} \cdot \cos \delta_i \cdot l_i + \sum F_x^{T_i} \cdot \sin \delta_i \cdot l_i + \sum F_y^{T_i} \cdot \sin \delta_i \cdot \frac{b_i}{2} + \sum F_x^{T_i} \cdot \cos \delta_i \cdot \frac{b_i}{2}. \quad (\text{G.1})$$

Under the conditions that $F_x^{T_1}$, $F_x^{T_2}$, δ_3 and $\delta_4 = 0$, the equation is described by

$$I_z \cdot \ddot{\psi} = F_y^{T_1} \cdot \cos \delta_1 \cdot l_F + F_y^{T_2} \cdot \cos \delta_2 \cdot l_F - F_y^{T_3} \cdot l_R - F_y^{T_4} \cdot l_R - F_y^{T_1} \cdot \sin \delta_1 \cdot \frac{b_F}{2} + F_x^{T_2} \cdot \sin \delta_2 \cdot \frac{b_F}{2} - F_x^{T_3} \cdot \frac{b_R}{2} + F_x^{T_4} \cdot \frac{b_R}{2}. \quad (\text{G.2})$$

Considering $F_y^{T_i} = -C_{\alpha_i} \cdot \alpha_i$ and $\alpha_i = \frac{v_y^i}{v_x^i} - \delta_i \approx \frac{v_y^i}{v_x^i} - \delta_i$ and substituting $v_y^{1,2} = v_y^V + l_F \cdot \dot{\psi}$, $v_y^{3,4} = v_y^V - l_R \cdot \dot{\psi}$ in (G.2), it results in

$$I_z \cdot \ddot{\psi} = -C_{\alpha_1} \cdot \left(\frac{v_y^V + l_F \cdot \dot{\psi}}{v_x^V} - \delta_1 \right) \cdot \cos \delta_1 \cdot l_F - C_{\alpha_2} \cdot \left(\frac{v_y^V + l_F \cdot \dot{\psi}}{v_x^V} - \delta_2 \right) \cdot \cos \delta_2 \cdot l_F + C_{\alpha_3} \cdot \frac{v_y^V - l_R \cdot \dot{\psi}}{v_x^V} \cdot l_R + C_{\alpha_4} \cdot \frac{v_y^V - l_R \cdot \dot{\psi}}{v_x^V} \cdot l_R + C_{\alpha_1} \cdot \left(\frac{v_y^V + l_F \cdot \dot{\psi}}{v_x^V} - \delta_1 \right) \cdot \sin \delta_1 \cdot \frac{b_F}{2} - C_{\alpha_2} \cdot \left(\frac{v_y^V + l_F \cdot \dot{\psi}}{v_x^V} - \delta_2 \right) \cdot \sin \delta_2 \cdot \frac{b_F}{2} + (F_x^{T_4} - F_x^{T_3}) \cdot \frac{b_R}{2}. \quad (\text{G.3})$$

The equation is sorted and expressed as

$$I_z \cdot \ddot{\psi} = \frac{(-C_{\alpha_1} \cdot \cos \delta_1 - C_{\alpha_2} \cdot \cos \delta_2) \cdot l_F + (C_{\alpha_3} + C_{\alpha_4}) \cdot l_R + (C_{\alpha_1} \cdot \sin \delta_1 - C_{\alpha_2} \cdot \sin \delta_2) \cdot \frac{b_F}{2}}{v_x^V} \cdot v_y^V + \frac{(-C_{\alpha_1} \cdot \cos \delta_1 - C_{\alpha_2} \cdot \cos \delta_2) \cdot l_F^2 - (C_{\alpha_3} + C_{\alpha_4}) \cdot l_R^2 + (C_{\alpha_1} \cdot \sin \delta_1 - C_{\alpha_2} \cdot \sin \delta_2) \cdot \frac{b_F \cdot l_F}{2}}{v_x^V} \cdot \dot{\psi} + \left(C_{\alpha_1} \cdot \cos \delta_1 \cdot l_F - C_{\alpha_1} \cdot \sin \delta_1 \cdot \frac{b_F}{2} \right) \cdot \delta_1 + \left(C_{\alpha_2} \cdot \cos \delta_2 \cdot l_F + C_{\alpha_2} \cdot \sin \delta_2 \cdot \frac{b_F}{2} \right) \cdot \delta_2 + (F_x^{T_4} - F_x^{T_3}) \cdot \frac{b_R}{2}. \quad (\text{G.4})$$

The discrete description of (G.4) is given by

$$\dot{\psi}_{k+1} = \epsilon \cdot T_s \cdot v_{y_k}^V + (1 + \chi \cdot T_s) \cdot \dot{\psi}_k + \xi \cdot T_s \cdot \delta_{1k} + \zeta \cdot T_s \cdot \delta_{2k} + \frac{b_R \cdot T_s}{2I_z} \cdot (F_x^{T_4} - F_x^{T_3})_k, \quad (\text{G.5})$$

where

$$\begin{aligned} \epsilon &= \frac{(-C_{\alpha_1} \cdot \cos \delta_1 - C_{\alpha_2} \cdot \cos \delta_2) \cdot l_F + (C_{\alpha_3} + C_{\alpha_4}) \cdot l_R + (C_{\alpha_1} \cdot \sin \delta_1 - C_{\alpha_2} \cdot \sin \delta_2) \cdot \frac{b_F}{2}}{I_z \cdot v_x^V} \\ \chi &= \frac{(-C_{\alpha_1} \cdot \cos \delta_1 - C_{\alpha_2} \cdot \cos \delta_2) \cdot l_F^2 - (C_{\alpha_3} + C_{\alpha_4}) \cdot l_R^2 + (C_{\alpha_1} \cdot \sin \delta_1 - C_{\alpha_2} \cdot \sin \delta_2) \cdot \frac{b_F \cdot l_F}{2}}{I_z \cdot v_x^V} \\ \xi &= \frac{C_{\alpha_1} \cdot \cos \delta_1 \cdot l_F - C_{\alpha_1} \cdot \sin \delta_1 \cdot \frac{b_F}{2}}{I_z} \end{aligned}$$

$$\zeta = \frac{C_{\alpha_2} \cdot \cos \delta_2 \cdot l_F + C_{\alpha_2} \cdot \sin \delta_2 \cdot \frac{b_F}{2}}{I_z}. \quad (\text{G.6})$$

G.2 Analytical calculation of the vehicle lateral velocity \tilde{v}_y^V

The force equilibrium is given by

$$m \cdot a_y = \sum F_y^{\text{T}i} \cdot \cos \delta_i + \sum F_x^{\text{T}i} \cdot \sin \delta_i. \quad (\text{G.7})$$

With the assumption that $F_x^{\text{T}1}$, $F_x^{\text{T}2}$, δ_3 , $\delta_4 = 0$, it follows:

$$m \cdot a_y = F_y^{\text{T}1} \cdot \cos \delta_1 + F_y^{\text{T}2} \cdot \cos \delta_2 + F_y^{\text{T}3} + F_y^{\text{T}4}. \quad (\text{G.8})$$

Substituting $F_y^{\text{T}i} = C_{\alpha_i} \cdot \alpha_i$, it yields:

$$m \cdot a_y = C_{\alpha_1} \cdot \alpha_1 \cdot \cos \delta_1 + C_{\alpha_2} \cdot \alpha_2 \cdot \delta_2 + C_{\alpha_3} \cdot \alpha_3 + C_{\alpha_4} \cdot \alpha_4. \quad (\text{G.9})$$

Considering $\alpha_i = \frac{v_y^{\text{T}i}}{v_x^{\text{T}i}} - \delta_i \approx \frac{v_y^{\text{T}i}}{v_x^{\text{T}i}} - \delta_i$ and substituting $v_y^{\text{T}1,2} = v_y^V + l_F \cdot \dot{\psi}$, $v_y^{\text{T}3,4} = v_y^V - l_R \cdot \dot{\psi}$, (G.9) is represented by

$$\begin{aligned} m \cdot a_y &= C_{\alpha_1} \cdot \left(\frac{v_y^V}{v_x^V} + \frac{l_F \cdot \dot{\psi}}{v_x^V} - \delta_1 \right) \cdot \cos \delta_1 + C_{\alpha_2} \cdot \left(\frac{v_y^V}{v_x^V} + \frac{l_F \cdot \dot{\psi}}{v_x^V} - \delta_2 \right) \cdot \cos \delta_2 \\ &+ C_{\alpha_3} \cdot \left(\frac{v_y^V}{v_x^V} - \frac{l_R \cdot \dot{\psi}}{v_x^V} \right) + C_{\alpha_4} \cdot \left(\frac{v_y^V}{v_x^V} - \frac{l_R \cdot \dot{\psi}}{v_x^V} \right) \\ &= \left(\frac{C_{\alpha_1} \cdot \cos \delta_1}{v_x^V} + \frac{C_{\alpha_2} \cdot \cos \delta_2}{v_x^V} + \frac{C_{\alpha_3}}{v_x^V} + \frac{C_{\alpha_4}}{v_x^V} \right) \cdot v_y^V \\ &+ \left(\frac{C_{\alpha_1} \cdot l_F \cdot \cos \delta_1}{v_x^V} + \frac{C_{\alpha_2} \cdot l_F \cdot \cos \delta_2}{v_x^V} - \frac{C_{\alpha_3} \cdot l_R}{v_x^V} - \frac{C_{\alpha_4} \cdot l_R}{v_x^V} \right) \cdot \dot{\psi} \\ &- (C_{\alpha_1} \cdot \cos \delta_1 \cdot \delta_1 + C_{\alpha_2} \cdot \cos \delta_2 \cdot \delta_2). \end{aligned} \quad (\text{G.10})$$

Therefore, the lateral velocity is calculated by

$$\begin{aligned} \tilde{v}_y^V &= \frac{v_x^V}{C_{\alpha_1} \cdot \cos \delta_1 + C_{\alpha_2} \cdot \cos \delta_2 + C_{\alpha_3} + C_{\alpha_4}} \\ &\cdot \left(\frac{m \cdot a_y - \frac{C_{\alpha_1} \cdot l_F \cdot \cos \delta_1 + C_{\alpha_2} \cdot l_F \cdot \cos \delta_2 - C_{\alpha_3} \cdot l_R - C_{\alpha_4} \cdot l_R}{v_x^V} \cdot \dot{\psi}}{v_x^V} \right) \\ &+ C_{\alpha_1} \cdot \cos \delta_1 \cdot \delta_1 + C_{\alpha_2} \cdot \cos \delta_2 \cdot \delta_2. \end{aligned} \quad (\text{G.11})$$

H Test maneuvers

H.1 Lateral Transient Response Test (ISO 7401)

The Lateral Transient Response Test according to ISO 7401 is an open-loop test will be employed to compare the open-loop vehicle response to quasi-step inputs of the steering wheel angle against the closed-loop vehicle response with activated yaw rate control [3]. The final value of δ_H is chosen in three cases such that the resulting steady-state value of a_y^V corresponds to 2 m s^{-2} , 4 m s^{-2} or 6 m s^{-2} , respectively. As δ_H cannot change instantaneously in practice, it is increased at a ramp of 500 deg/s . The three test runs are repeated for positive and negative steering wheel angles.

H.2 Sine-Steer Test (ISO 7401)

In order to analyze the frequency domain behavior of the TV-algorithm the open-loop Sine-Steer Test according to ISO 7401 is adapted. In this test the steering wheel frequency is altered logarithmically in a range from 0 Hz to 4 Hz. The amplitude of δ_H is chosen such that $a_y^{V,ss} = 4 \text{ m s}^{-2}$ at 0 Hz. Each test run is considered complete when harmonic steady-state is reached (meaning the amplitudes settle to constant values), with three periods being the minimum run time.

H.3 Sine-steer Test with dwell input (UN 13-H)

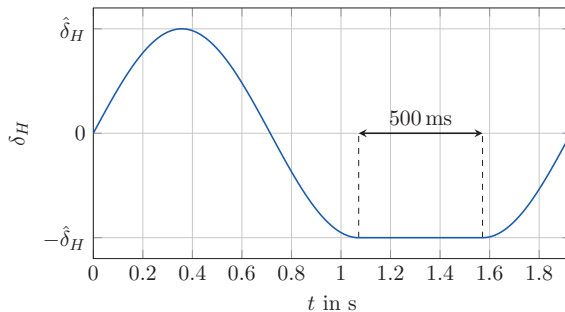


Figure H.1: Sine-steer with dwell steering-wheel input.

According to the NHTSA's *Light Vehicle Handling and ESC Effectiveness Research Program* the *Sine-Steer with Dwell* maneuver is the best suited test procedure to

asses the effectiveness of ESC-systems as it is superior in regards to the excitation of transient over-steer responses [57]. This is manifested in the UN Regulation 13-H, Addendum 12-H where this maneuver is part of the approval tests for passenger vehicles equipped with ESC-systems [5]. Although TV-systems are rather considered performance enhancement functions than safety functions [165], they are still related to ESC-systems. While ESC-systems make use of asymmetrically distributed braking forces to excite additional yaw, TV uses tractive forces for the same purpose instead. Hence, the open-loop sine-steer with dwell maneuver provides an adequate test procedure to evaluate the TV-system's performance in extreme lateral conditions and to prove that it implicitly enhances vehicle safety as well.

The sine-steer with dwell procedure is based on the steering-wheel input depicted in Figure H.1, being comprised of a sine function with $f = 0.7\text{ Hz}$ and variable amplitude as well as a dwell time of 500 ms introduced in the second half-cycle. This hold-time causes the steering wheel angle to be reversed close to peak value of $\dot{\psi}$, effectively provoking an over-steer and as such hardly controllable vehicle response [185].

I Estimation results

I.1 Lateral transient response test

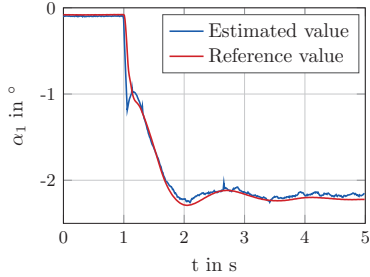


Figure I.1: Estimation of Slip angle FL.

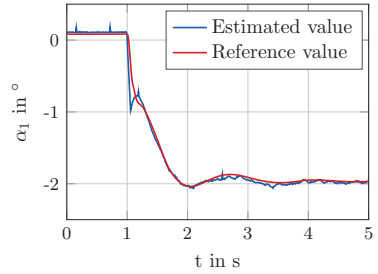


Figure I.2: Estimation of Slip angle FR.

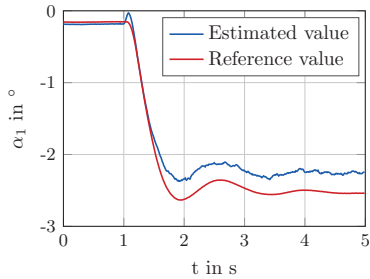


Figure I.3: Estimation of Slip angle RL.

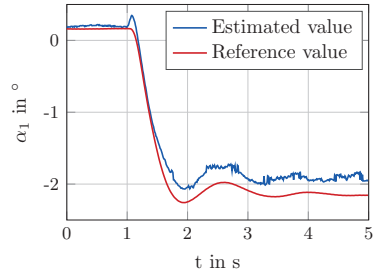


Figure I.4: Estimation of Slip angle RR.

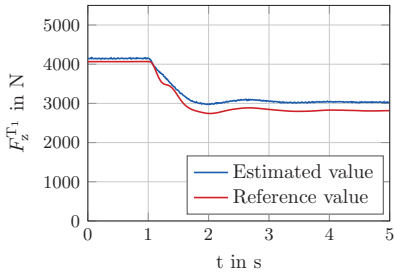


Figure I.5: Estimation of Vertical force FL.

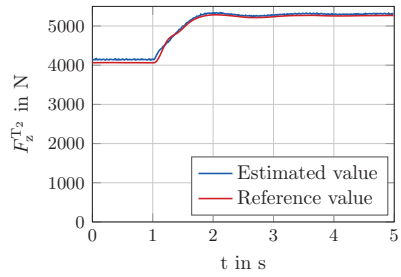


Figure I.6: Estimation of Vertical force FR.

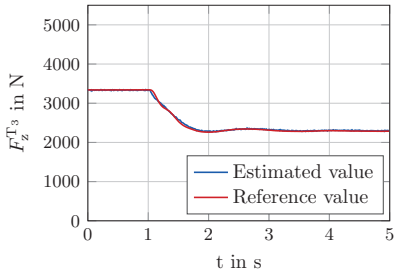


Figure I.7: Estimation of Vertical force RL.

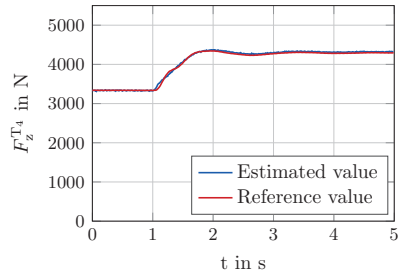


Figure I.8: Estimation of Vertical force RR.

I.2 Sine-steer test

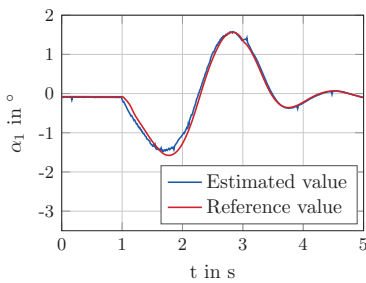


Figure I.9: Estimation of Slip angle FL.

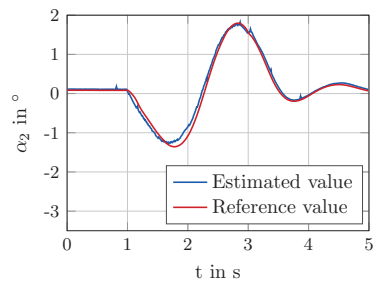


Figure I.10: Estimation of Slip angle FR.

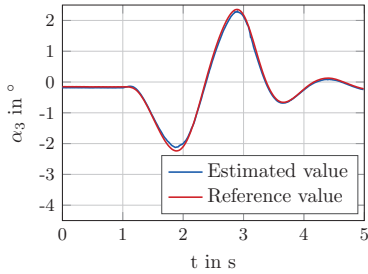


Figure I.11: Estimation of Slip angle RL.

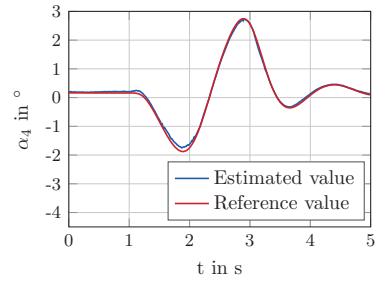


Figure I.12: Estimation of Slip angle RR.

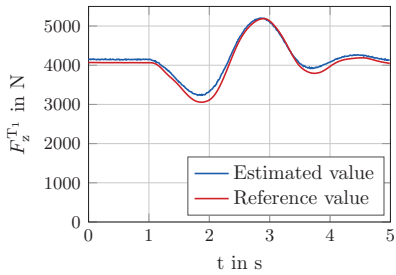


Figure I.13: Estimation of Vertical force FL.

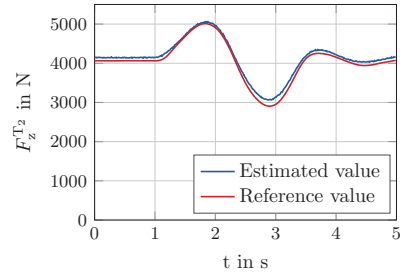


Figure I.14: Estimation of Vertical force FR.

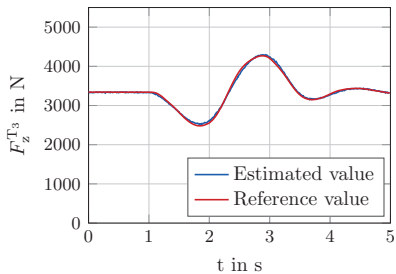


Figure I.15: Estimation of Vertical force RL.

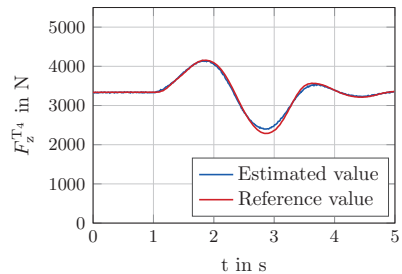


Figure I.16: Estimation of Vertical force RR.

I.3 Sine-steer with dwell test

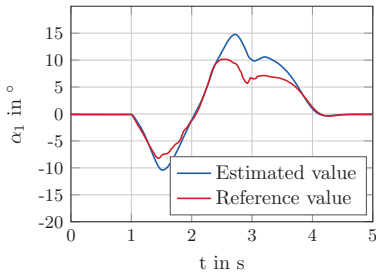


Figure I.17: Estimation of Slip angle FL.

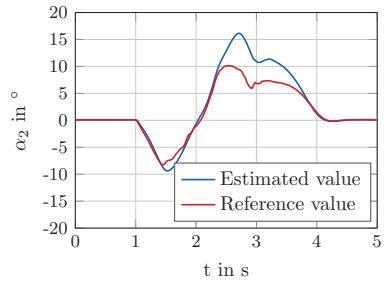


Figure I.18: Estimation of Slip angle FR.

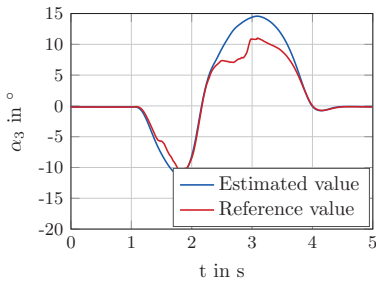


Figure I.19: Estimation of Slip angle RL.

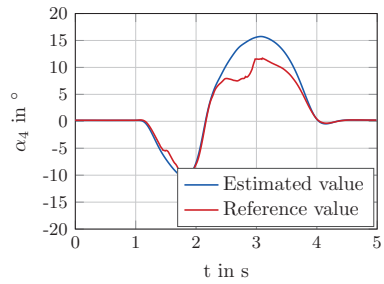


Figure I.20: Estimation of Slip angle RR.

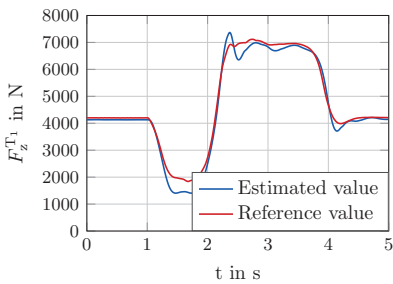


Figure I.21: Estimation of Vertical force FL.

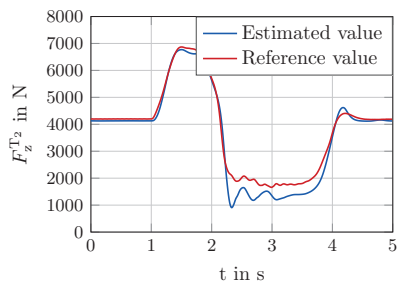


Figure I.22: Estimation of Vertical force FR.

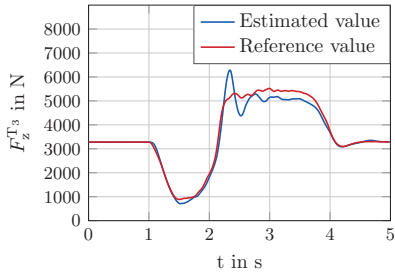


Figure I.23: Estimation of Vertical force RL.

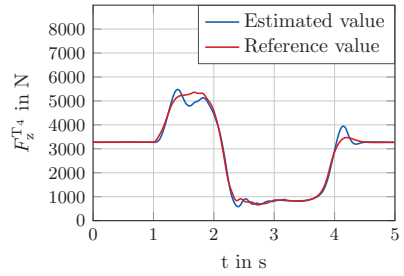


Figure I.24: Estimation of Vertical force RR.

J Abbreviation

4WD	4-Wheel Drive
ABS	Anti-lock Braking
ac	alternative current
AD	Analog-Digital
ASM	Automotive Simulation Models
AYC	Yaw Rate Control
CCS-MPC	Continuous Control Set Model Predictive Control
CoG	Center of Gravity
CP	Contact Point
dc	direct current
DOFs	Degrees of Freedom
DSP	Digital Signal Processor
DTM	Dual Track Model
ECG	Earth Coordinate System
EM	Electrical Machine
EMF	Electromotive Force
EMPC	Explicit Model Predictive Control
ESC	Electronic Stability Control
EV	Electric Vehicle
FCS-MPC	Finite-Control-Set Model Predictive Control
FL	Front Left
FOC	Field Oriented Control
FR	Front Right
FWD	Front-Wheel Drive
GPC	Generalized Predictive Control
HiL	Hardware-in-the-Loop
HW	Hardware
I/O	Input/Output
IC	Instantaneous Center
ICE	Internal Combustion Engine
IM	Induction Motor
IRF	Inertial Reference Frame

ISO	International Organization for Standardization
KKT	Karush-Kuhn-Tucker
LMI	Linear Matrix Inequality
LP	Linear Programming
LPV	Linear Parameter-Varying
LQR	Linear Quadratic Regulator
LSTM	Linear Single Track Model
LTI	Linear Time Invariant
LUT	Look Up Table
MF	Magic Formula
MPC	Model Predictive Control
mp-LP	multi-parametric Linear Programming
mp-QP	multi-parametric Quadratic Programming
mp-SDP	multi-parametric Semi-Definite Programming
MPT	Multi-Parametric Toolbox
mRPI	minimal Robust Positively Invariant
MRPI	Maximal Robust Positively Invariant
NEKF	Nonlinear Extended Kalman Filter
NHTSA	National Highway Traffic Safety Administration
NP	Non-deterministic Polynomial-time
PD	Primal Dual
PI	Proportional Integral
PID	Proportional Integral Derivative
PiL	Processor-in-the-Loop
PMSM	Permanent-Magnet Synchronous Motor
PWA	Piece-wise Affine
PWQ	Piece-wise Quadratic
QP	Quadratic Programming
RHC	Receding Horizon Control
RL	Rear Left
RMPC	Robust Model Predictive Control
RPI	Robust Positively Invariant
RR	Rear Right
RWD	Rear-Wheel Drive
SDP	Semi-Definite Programming
Sidi	Simodrive-dSPACE-interface
SVM	Space Vector Modulation
SW	Software
TCS	Tire Coordinate System
TFE	Tire-Force Ellipse
TV	Torque Vectoring
VCS	Vehicle Coordinate System

VSI Voltage Source Inverter

K Nomenclature

Greek Symbols

α	parameter denoting the size different between the ellipsoid and the mapped one
α	coordinate after the Clark transformation
α	tire slip angle
β	coordinate after the Clark transformation
β	nonnegative scalar parameter in LMI
β	vehicle sideslip angle
γ	upper bound of Lyapunov function
γ	toe angle
δ	steer angle and steering wheel angle
θ	parameter of time-varying matrix
θ	pitch angle
ϵ	induced voltage
μ	friction coefficient
τ	time constant
τ	torque
φ	position angle of the masses
φ	bank angle
ψ	yaw angle
ω	rotational speed
σ	leakage factor
ζ	damping factor
Ω	mechanical speed
Θ	unit simplex set
Ψ	matrix parameter
Θ	matrix parameter

Latin Symbols

\mathbf{a}	vector parameter
\mathbf{A}	matrix parameter
a_x	longitudinal acceleration
a_y	lateral acceleration
\mathbf{b}	vector parameter
b	track width
\mathbf{B}	matrix parameter
\mathbb{B}	set of unit ball
c	torsional stiffness
\mathbf{c}	vector parameter
C	tire stiffness
\mathbf{C}	matrix parameter
\mathcal{C}	convex set
\mathbf{d}	vector variable of disturbance
\mathbf{D}	matrix parameter
\mathbf{e}	vector variable of error
\mathbf{E}	matrix parameter
\mathbb{E}	set of invariant ellipsoid
F	force
\mathbf{F}	matrix parameter
\mathbf{F}	vector parameter of force
\mathbf{g}	vector parameter
\mathbf{G}	matrix parameter
\mathbf{h}	vector parameter
\mathbf{H}	matrix parameter
H	H-polyhedral representation
i	current
I	moment of inertia
\mathbf{I}	unit matrix
\mathbb{I}	set of unit matrices
J	moment of inertia
J	objective function
k	damping coefficient
\mathbf{K}	Kalman gain
l	track length
L	inductance
\mathbf{L}	angular momentum
\mathbb{L}	set of vertex indices
\mathbf{M}	matrix parameter
\mathbf{N}	matrix parameter

\mathbb{N}	set of natural numbers
\mathbf{P}	matrix parameter
\mathbb{P}	predecessor set
\mathcal{P}	partition set
\mathcal{P}	Polyhedron
\mathbf{Q}	weighting matrix parameter
\mathbf{R}	covariance matrix parameter
\mathbf{R}	weighting matrix parameter
R	resistance
R	radius of wheel
\mathbf{R}	matrix parameter
\mathbf{R}	covariance matrix parameter
\mathbb{R}	set of real numbers
s	tire slip
\mathbf{S}	matrix parameter
p	linear momentum
\mathbf{q}	vector quantity
\mathbf{r}	reference vector
\mathbf{s}	steady state vector
\mathbb{S}	set of symmetric matrices
T	torque
T	time
\bar{T}	torque threshold
\mathbf{T}	matrix parameter
u	voltage
\mathbf{u}	vector variable of control system output
\mathbf{U}	matrix variable of control system input
\mathbb{U}	system input constraint set
v	velocity
\mathbf{v}	velocity vector
\mathbf{v}	vector variable of measurement noises
\mathbf{w}	vector variable of system disturbance
\mathbf{W}	matrix parameter
\mathbb{W}	disturbance constraint set
w_B	wheel base
\mathbf{x}	vector variable of system states
\mathbf{X}	matrix variable of system states
\mathbb{X}	state constraint set
\mathbb{X}_f	state terminal constraint set
\mathbf{y}	vector variable of system output
\mathbf{Y}	matrix variable of system output
\mathbb{Y}	output constraint set

z	vector variable of optimizer
Z	set of unpartitioned regions

superscript

$\hat{}$	estimated value
*	reference value
-	nominal value
+	successor
'	quantities of the rotor referred to the stator side
'	representation value
c	compensated
dec	decoupling
F	front
max	maximum
min	minimum
mod	modified
R	rear
T_i	tire
V	vehicle

subscript

a,b,c	phase index
d	dead time
dyn	dynamic
eq	equality
el	electromagnetic
F	front
FL	front left
FR	front right
g,in	gearbox input
g,out	gearbox output
gw	gear wheel
inf	infinity
k	time instant
k	time instant
l	vertex index
m	mutual
min	minimum

max	maximum
ms	machine shaft
n	nominal
r	rotor
R	rear
rd	rotor d-value
RL	rear left
rq	rotor q-value
RR	rear right
s	stator
s	artificial steady-state value
sd	stator d-value
sq	stator q-value
ss	side shaft
tb	tire belt
tp	tire profile
ts	tire side
v	vertex
vm	vehicle mass
wr	wheel rim

Bibliography

- [1] INTERNATIONAL ELECTROTECHNICAL COMMISSION: „IEC Standard 34-2: Methods for determining losses and efficiency of rotating electrical machinery from tests (excluding machines for traction vehicles)“. Genf, Switzerland, 1972. – STANDARD.
- [2] DEUTSCHES INSTITUT FÜR NORMIERUNG: „DIN 70020-5. Automotive Engineering; Tyres and Wheels; Concepts and Measuring Conditions“. Berlin, Germany, 1986. – STANDARD.
- [3] INTERNATIONAL ORGANIZATION FOR STANDARDIZATION: „ISO 7401:1989. Road vehicles – Lateral transient response test methods – Open-loop test methods“. Geneva, Switzerland, 1989. – STANDARD.
- [4] SAE INTERNATIONAL: „SAE J2047 (Issued 1998). Tire Performance Terminology“. Warrendale, US, 1998. – STANDARD.
- [5] UNITED NATIONS: „Uniform provisions concerning the approval of passenger cars with regard to braking“. Geneva, Switzerland, 2011. – UN-REGULATION.
- [6] INTERNATIONAL ORGANIZATION FOR STANDARDIZATION: „ISO 8855:2011. Road Vehicles - Vehicle Dynamics and Road-holding Ability - Vocabulary“. Geneva, Switzerland, 2013. – STANDARD.
- [7] ALKORTA, P ; BARAMBONES, O ; CORTAJARENA, J. A. ; ZUBIZARRETA, A: „Efficient Multivariable Generalized Predictive Control for Sensorless Induction Motor Drives“. *IEEE Transactions on Industrial Electronics* 61 (2014), September, Nr. 9, pages 5126–5134.
- [8] ALVARADO, I: *Model predictive control for tracking constrained linear systems*, University de Sevilla, Dissertation., 2007.
- [9] ALVARADO, I ; LIMON, D ; ALAMO, T ; CAMACHO, E. F.: „Output feedback robust tube based MPC for tracking of piece-wise constant references“. *Proceedings of IEEE Conference on Decision and Control*. New Orleans, LA, 2007, pages 2175–2180.
- [10] ALVARADO, I ; LIMON, D ; ALAMO, T ; FIACCHINI, M ; CAMACHO, E. F.: „Robust tube based MPC for tracking of piece-wise constant references“. *Proceedings of IEEE Conference on Decision and Control*. New Orleans, LA, 2007, pages 1820–1825.
- [11] ALVARADO, I ; LIMON, D ; ALAMO, T ; CAMACHO, E. F.: „On the Design of Robust Tube-Based MPC for Tracking“. *Proceedings of the World Congress*. Seoul, Korea, 2008, pages 15333–15338.

- [12] AMMON, D: *Modellbildung und Systementwicklung in der Fahrzeugdynamik (Leitfäden der angewandten Mathematik und Mechanik)*. 1st Edition. Vieweg+Teubner Verlag, 1997.
- [13] ANGELI, D ; CASAVOLA, A ; FRANZÈ, G ; MOSCA, E: „An ellipsoidal off-line MPC scheme for uncertain polytopic discrete-time systems“. *Automatica* 44 (2008), December, Nr. 12, pages 3113–3119.
- [14] AUBIN, J.-P: *Viability Theory*. 1st Edition. Birkhäuser Basel, 2009.
- [15] BEMPORAD, A ; BORRELLI, F ; MORARI, M: „Min-max control of constrained uncertain discrete-time linear systems“. *IEEE Transactions on Automatic Control* 48 (2003), September, Nr. 9, pages 1600–1606.
- [16] BEMPORAD, A ; MORARI, M: „Robust Model Predictive Control: A Survey“. *Robustness in Identification and Control* 245 (1999), pages 207–226.
- [17] BEMPORAD, A ; FILIPPI, C: „An Algorithm for Approximate Multiparametric Convex Programming“. *Journal of Computational Optimization and Applications* 35 (2006), September, Nr. 1, pages 87–108.
- [18] BEMPORAD, A ; MORARI, M ; DUA, V ; PISTIKOPOULOS, E. N.: „The explicit linear quadratic regulator for constrained systems“. *Automatica* 38 (2002), January, Nr. 1, pages 3–20.
- [19] BLANCHINI, F: „Survey Paper: Set Invariance in Control“. *Automatica* 35 (1999), November, Nr. 11, pages 1747–1767.
- [20] BLANCHINI, F ; MIANI, S: *Set-Theoretic Methods in Control*. 2nd Edition. Birkhäuser Basel, 2015.
- [21] BMW AG: *Aktives M Differential*, 2016. – <http://www.bmw.de/de/neufahrzeuge/M/m2-coupe/2015/fahrdynamik-effizienz.html>, accessed 15.08.2016.
- [22] BMW AG: *Der BMW i3*. Munich, Germany, 2016. – http://www.bmw.com/com/de/newvehicles/i/i3/2015/showroom/technical_data.html, accessed 15.08.2016.
- [23] BOCCIA, A ; GRÜNE, L ; WORTHMANN, K: „Stability and feasibility of state constrained MPC without stabilizing terminal constraints“. *System & Control Letters* 72 (2014), October, pages 14–21.
- [24] BORRELLI, F ; BEMPORAD, A ; MORARI, M: *Constrained optimal control and predictive control*. Springer, 2010.
- [25] BORRELLI, F: *Constrained optimal control of linear and hybrid systems*. 1st Edition. Springer, 2003.
- [26] BOYD, S ; EL GHAOU, L ; FERON, E ; BALAKRISHNAN, V: *Studies in Applied Mathematics*. volume 15: *Linear Matrix Inequalities in System and Control Theory*. 1st Edition. SIAM, 1994.

- [27] BOYD, S ; VANDENBERGHE, L: *Convex Optimization*. Cambridge University Press, 2009.
- [28] BRACH, R ; BRACH, M: „The Tire-Force Ellipse (Friction Ellipse) and Tire Characteristics“. *Proceedings of Tire and Wheel Technology*. Warrendale, US, 2011.
- [29] BRACHERT, J. D. I. ; HADELER, R. D. I. D. ; LEIBELING, F ; MUELLER, E. D. I. ; SCHUBERT, M. D. I. ; SCHUH, J. D. I.: *Fahrdynamikregelsystem*. June. 17. 2004. – DE Patent DE4446534.
- [30] BREWER, H. K. (Eds.) ; CLARK, S. K. (Eds.) ; GENT, A. N. (Eds.) ; GINGO, J. M. (Eds.) ; HERMANN, C (Eds.) ; HOCHSCHWENDER, J. M. (Eds.) ; STEPHENS, D. R. (Eds.) ; WALTER, J. D. (Eds.): *The Pneumatic Tire*. Washington D.C., US : National Highway Traffic Safety Administration (NHTSA), 2006.
- [31] BURG, H (Eds.) ; MOSER, A (Eds.): *Handbuch Verkehrsunfallrekonstruktion - Unfallaufnahme, Fahrdynamik, Simulation*. Vieweg+Teubner Verlag, 2009.
- [32] CAIRANO, S. D. ; TSENG, H. E. ; BERNARDINI, D ; BEMPORAD, A: „Vehicle Yaw Stability Control by Coordinated Active Front Steering and Differential Braking in the Tire Sideslip Angles Domain“. *IEEE Transactions on Control Systems Technology* 21 (2012), July, Nr. 4, pages 1236–1248.
- [33] CAMACHO, E. F. ; BORDONS, C: *Model Predictive Control*. 2nd Edition. Springer, 2013.
- [34] CAO, Y ; LIN, Z: „Min-max MPC algorithm for LPV systems subject to input saturation“. *IEE Proceedings – Control Theory and Applications* 152 (2005), May, Nr. 3, pages 266–272.
- [35] CASADEI, D ; PROFUMO, F ; SERRA, G ; TANI, A: „FOC and DTC: Two Viable Scheme for Induction Motor Torque Control“. *IEEE Transactions on Power Electronics* 17 (2002), September, Nr. 5, pages 779–787.
- [36] CHEN, H ; ALLGÖWER, F: „A Quasi-Infinite Horizon Nonlinear Model Predictive Control Scheme with Guaranteed Stability“. *Automatica* 36 (1998), October, Nr. 10, pages 1205–1217.
- [37] CHU, L ; XU, M ; ZHANG, Y ; OU, Y ; SHI, Y: „Vehicle Dynamics Control Based on Optimal Sliding Mode Control Theory“. *Proceedings of International Conference on Computer, Mechatronics, Control and Electronic Engineering*. Changchun, China, 2010, pages 486–491.
- [38] CHU, W ; LOU, Y ; DAI, Y ; LI, K: „Traction system coordinated allocation control for four wheel independently driven electric vehicle“. *Proceedings of International Symposium on Advanced Vehicle Control*. Seoul, Korea, 2012, pages 1–6.

- [39] CUZZOLA, F. A. ; GEROMEL, J. C. ; MORARI, M: „An improved approach for constrained robust model predictive control“. *Automatica* 39 (2002), July, Nr. 7, pages 1183–1189.
- [40] CYCHOWSKI, M. T. ; DING, B ; O'MAHONY, T: „An Orthogonal Partitioning Approach to Simplify Robust Model Predictive Control“. *Proceedings of IEEE International Symposium on Mediterrean Conference on Control Automation Intelligent Control*. Limassol, Cyprus, 2005, pages 877–882.
- [41] CYCHOWSKI, M. T. ; O'MAHONY, T: „Efficient approximate robust MPC based on quad-tree partitioning“. *Proceedings of IEEE Conference on Control Applications*. Toronto, Ont., 2005, pages 239–244.
- [42] CYCHOWSKI, M: *Robust Model Predictive Control*. 1st Edition. VDM Verlag Dr. Müller, 2006.
- [43] CYCHOWSKI, M ; SZABAT, K ; ORLOWSKA-KOWALSKA, T: „Constrained Model Predictive Control of the Drive System With Mechanical Elasticity“. *IEEE Transactions on Industrial Electronics* 56 (2009), June, Nr. 6, pages 1963–1973.
- [44] DIAB, A. A. Z. ; KOTIN, D. A. ; PANKRATOV, V. V.: „A comparative study of speed control based on MPC and PI-controller for Indirect Field oriented control of induction motor drive“. *Proceedings of International Conference on Actual Problems of Electronics Instrument Engineering*. Novosibirsk, 2014, pages 728–732.
- [45] DIAB, A. A. Z. ; KOTIN, D. A. ; PANKRATOV, V. V.: „Speed Control of Sensorless Induction Motor Drive Based On Model Predictive Control“. *Proceedings of International Conference of Young Specialists on Micro/Nanotechnologies and Electron Devices*. Novosibirsk, 2013, pages 269–274.
- [46] DIAB, A. A. Z. ; PANKRATOV, V. V.: „Model predictive control of vector controlled induction motor drive“. *Proceedings of International Forum on Strategic Technology*. Tomsk, 2012, pages 1–6.
- [47] DIEZ, W: *Automobil-Marketing: Erfolgreiche Strategien, praxisorientierte Konzepte, effektive Instrumente*. 6th Edition. Vahlen, 2015.
- [48] DING, B ; XI, Y ; CYCHOWSKI, M ; O'MAHONY, T: „Improving off-line approach to robust MPC based-on nominal performance cost“. *Automatica* 43 (2007), January, Nr. 1, pages 158–163.
- [49] DING, B ; XI, Y ; LI, S: „A synthesis approach of on-line constrained robust model predictive control“. *Automatica* 40 (2004), January, Nr. 1, pages 163–167.
- [50] DORF, R. C. ; BISHOP, R. H.: *Modern Control Systems*. 12th Edition. Prentice Hall, 2011.

- [51] DOUMIATI, M ; SENAME, O ; DUGARD, L ; MARTINEZ-MOLINA, J.-J ; GASPAR, P ; SZABO, Z: „Integrated vehicle dynamics control via coordination of active front steering and rear braking“. *European Journal of Control* 19 (2013), March, Nr. 2, pages 121–143.
- [52] DSPACE GMBH: *ASM Vehicle Dynamics*. Paderborn, Germany, 2016. – https://www.dspace.com/de/gmb/home/products/sw/automotive_simulation_models/produkte_asm/vehicle_dynamics_models.cfm, accessed 15.08.2016.
- [53] EDWARDS, C ; SPURGEON, S: *Sliding mode control: theory and applications*. CRC Press, 1998.
- [54] EHRET, T ; HARTMANN, U ; LUTZ, A: *Method of Determining the Oblique-motion Angle of a Braked Vehicle and/or the Lateral Motion Force Acting on the Vehicle*. January 1995. – Europäische Patentschrift EP 0503026 B1.
- [55] FALLAH, S ; KHAJEPOUR, A ; FIDAN, B ; CHEN, S.-K ; LITKOUHI, B: „Vehicle Optimal Torque Vectoring Using State-Derivative Feedback and Linear Matrix Inequality“. *IEEE Transactions on Vehicular Technology* 62 (2013), May, Nr. 4, pages 1540–1552.
- [56] FÖLLINGER, O: *Regelungstechnik*. 10th Edition. Hüthig GmbH Verlag, 2008.
- [57] FORKENBROCK, G. J. ; ELSASSER, D ; O’HARRA, B: „NHTSA’s Light Vehicle Handling and ESC Effectiveness Research Program“. *Proceedings of International Technical Conference on Enhanced Safety of Vehicles*. Washington, D.C., 2005, pages 05–0221:1–16.
- [58] FUENTES, E ; KALISE, D ; RODRIGUEZ, J ; KENNEL, R: „Cascade-Free Predictive Speed Control for Electric Drives“. *IEEE Transactions on Industrial Electronics* 61 (2014), May, Nr. 5, pages 2176–2184.
- [59] FURUKAWA, K ; HORI, Y: „Advanced Estimation Techniques of Road Surface Condition and Their Experimental Evaluation using Test Electric Vehicle ’UOT March I and II‘“. *Proceedings of EVS-20*, 2003.
- [60] GAN, L ; WANG, L: „Cascaded continuous-time model predictive control of induction motor“. *Proceedings of Annual Conference of the IEEE Industrial Electronics Society*. Montreal, QC, 2012, pages 1696–1701.
- [61] GAN, L ; WANG, L: „Cascaded model predictive position control of induction motor with constraints“. *Proceedings of Annual Conference of the IEEE Industrial Electronics Society*. Vienna, 2013, pages 2656–2661.
- [62] GAN, Y ; XIONG, L ; MARTINEZ, F: „A Torque Vectoring Control System for Maneuverability Improvement of 4WD EV“. *Proceedings of International Conference on Computer Science and Electronics Engineering*. Hangzhou, China, 2013, pages 2729–2732.

- [63] GAYEK, J. E.: „A survey of techniques for approximating reachable and controllable sets“. *Proceedings of IEEE Decision and Control*. Brighton, 1991, pages 1724–1729.
- [64] GENG, C ; MOSTEFAI, L ; DENAI, M ; HORI, Y: „Direct Yaw-Moment Control of an In-Wheel-Motored Electric Vehicle Based on Body Slip Angle Fuzzy Observer“. *IEEE Transactions on Industrial Electronics* 56 (2009), May, Nr. 5, pages 1411–1419.
- [65] GEYER, T ; OIKONOMOU, N ; PAPAFOITIU, G ; KIEFERNDORF, F. D.: „Model Predictive Pulse Pattern Control“. *IEEE Transactions on Industrial Applications* 48 (2012), March, Nr. 2, pages 663–676.
- [66] GEYER, T ; QUEVEDO, D. E.: „Multistep direct model predictive control for power electronics - Part 1: Algorithm“. *Proceedings of IEEE Energy Conversion Congress and Exposition*. Denver, CO, 2013, pages 1154–1161.
- [67] GEYER, T ; QUEVEDO, D. E.: „Multistep direct model predictive control for power electronics - Part 2: Analysis“. *Proceedings of IEEE Energy Conversion Congress and Exposition*. Denver, CO, September 2013, pages 1162–1169.
- [68] GEYER, T ; QUEVEDO, D. E.: „Performance of Multistep Finite Control Set Model Predictive Control for Power Electronics“. *IEEE Transactions on Power Electronics* 30 (2015), March, Nr. 3, pages 1633–1644.
- [69] GEYER, T: „Model predictive direct current control for multi-level converters“. *Proceedings of IEEE Energy Conversion Congress and Exposition*. Atlanta, GA, 2010, pages 4305–4312.
- [70] GEYER, T ; PAPAFOITIOUS, G ; MORARI, M: „Model Predictive Direct Torque Control—Part I: Concept, Algorithm, and Analysis“. *IEEE Transactions on Industrial Electronics* 56 (2009), June, Nr. 6, pages 1894–1905.
- [71] GILBERT, E. G. ; TAN, K. T.: „Linear systems with state and control constraints: the theory and application of maximal output admissible sets“. *IEEE Transactions on Automatic Control* 36 (1991), September, Nr. 9, pages 1008–1020.. – ISSN 0018–9286
- [72] GILLEPSIE, T. D.: *Fundamentals of Vehicle Dynamics*. Warrendale, US : SAE International, 1992.
- [73] GIRARD, A: „Reachability of Uncertain Linear Systems Using Zonotopes“. *Proceedings of International Conference on Hybrid Systems: Computation and Control*. Berlin, Heidelberg, 2005, pages 291–305.
- [74] GOGGIA, T ; SORNIOTTI, A ; NOVELLIS, L. D. ; FERRARA, A: „Integral Sliding Mode for the Torque-Vectoring Control of Fully Electric Vehicles: Theoretical Design and Experimental Assessment“. *IEEE Transactions on Vehicular Technology* 64 (2015), May, Nr. 5, pages 1701–1715.

- [75] GOLDFARB, D ; SCHEINBERG, K: „On parametric semidefinite programming“. *Applied Numerical Mathematics* 29 (1999), March, Nr. 3, pages 361–377.
- [76] GOLDSTEIN ; POOLE ; SAFKO: *Classical Mechanics*. 3rd Edition. San Francisco, US : Addison-Wesley, 2000.
- [77] GUZMAN, H ; DURAN, M ; BARRERO, F ; ZARRI, L ; BOGADO, B ; PRIETO, I. G. ; ARAHAL, M. R.: „Comparative Study of Predictive and Resonant Controllers in Fault-Tolerant Five-Phase Induction Motor Drives“. *IEEE Transactions on Industrial Electronics* 63 (2016), January, Nr. 1, pages 606–617.
- [78] GUZMAN, H ; DURAN, M. J. ; BARRERO, F ; BOGADO, B ; TORAL, S: „Speed Control of Five-Phase Induction Motors With Integrated Open-Phase Fault Operation Using Model-Based Predictive Current Control Techniques“. *IEEE Transactions on Industrial Electronics* 61 (2014), September, Nr. 9, pages 4474–4484.
- [79] HABIBULLAH, M ; LU, D. D.-C: „A Speed-Sensorless FS-PTC of Induction Motors Using Extended Kalman Filters“. *IEEE Transactions on Industrial Electronics* 62 (2015), November, Nr. 11, pages 6765–6778.
- [80] HEISSING, B (Eds.) ; ERSOY, M (Eds.): *Chassis Handbook: Fundamentals, Driving Dynamics, Components, Mechatronics, Perspectives*. Wiesbaden, Germany : Vieweg+Teubner Verlag, 2011.
- [81] HEISSING, B ; ERSOY, M ; GIES, S (Eds.): *Fahrwerkhandbuch: Grundlagen, Fahrdynamik, Komponenten, Systeme, Mechatronik, Perspektiven*. 3rd Edition. Berlin, Germany : Vieweg+Teuber Verlag, 2011.
- [82] HERCEG, M ; KVASNICA, M ; JONES, C ; MORARI, M: „Multi-Parametric Toolbox 3.0“. *Proceedings of the European Control Conference*. Zürich, Switzerland, 2013, pages 502–510.
- [83] HU, Z ; HAMEYER, K: „Robust Predictive Current Control for Performance Improvement of Induction Motors with Parameter Variation“. *Proceedings of Annual Conference of the IEEE Industrial Electronics Society*. Yokohama, 2015, pages 451–456.
- [84] HU, Z ; HAMEYER, K: „A Method of Constraint Handling for Speed-Controlled Induction Machines“. *IEEE Transactions on Industrial Electronics* 63 (2016), July, Nr. 7, pages 4061–4072.
- [85] HUANG, H ; LI, D ; LIN, Z: „An improved robust model predictive control design in the presence of actuator saturation“. *Automatica* 47 (2011), April, Nr. 4, pages 861–864.
- [86] ISERMANN, R (Eds.): *Fahrdynamik-Regelung: Modellbildung, Fahrerassistenzsysteme, Mechatronik*. 1st Edition. Vieweg+Teuber Verlag, 2006.

- [87] JAMES B. RAWLINGS, D. Q. M.: *Model Predictive Control: Theory and Design*. Nob Hill Publishing, 2009.
- [88] JEONG, S. C. ; PARK, P: „Constrained MPC Algorithm for Uncertain Time-Varying Systems With State-Delay“. *IEEE Transactions on Automatic Control* 50 (2005), February, Nr. 2, pages 257–262.
- [89] JILES, D: *Introduction to Magnetism and Magnetic Materials*. 3rd Edition. CRC Press, 2015.
- [90] JOHANSEN, T. A. ; GRANCHAROVA, A: „Approximate explicit constrained linear model predictive control via orthogonal search tree“. *IEEE Transactions on Automatic Control* 48 (2003), May, Nr. 5, pages 810–815.
- [91] KAISER, G: *Torque Vectoring - Linear Parameter-Varying Control for an Electric Vehicle*, Technische Universität Hamburg, Dissertation., 2015.
- [92] KAISER, G ; HOLZMANN, F ; CHRETIEN, B ; KORTE, M: „Torque Vectoring with a feedback and feed forward controller - applied to a through the road hybrid electric vehicle“. *Proceedings of IEEE Intelligent Vehicles Symposium*. Baden-Baden, Germany, 2011, pages 448–453.
- [93] KARAMANAKOS, P: *Model Predictive Control Strategies For Power Electronics Converters And Ac Drives*, National Technical University of Athens, Dissertation., 2013.
- [94] KARAMANAKOS, P ; GEYER, T ; OIKONOMOU, N ; KIEFERNDORF, F. D. ; MANIAS, S: „Direct Model Predictive Control: A Review of Strategies That Achieve Long Prediction Intervals for Power Electronics“. *IEEE Industrial Electronics Magazine* 8 (2014), March, Nr. 1, pages 32–43.
- [95] KARAMUK, M: „A Survey on Electric Vehicle PowerPower Systems“. *Proceedings of International Aegean Conference on Electrical Machines and Power Electronics and Electromotion*. Istanbul, 2011, pages 315–324.
- [96] KASINATHAN, D ; KASAIEZADEH, A ; WONG, A ; KHAJEPOUR, A ; CHEN, S.-K ; LITKOUHI, B: „An Optimal Torque Vectoring Control for Vehicle Applications via Real-Time Constraints“. *IEEE Transactions on Vehicular Technology* 65 (2016), June, Nr. 6, pages 4368–4378.
- [97] KERRIGAN, E. C.: *Robust Constraint Satisfaction: Invariant Sets and Predictive Control*, University of Cambridge, Dissertation., 2000.
- [98] KHOSRAVANI, S ; KASAIEZADEH, A ; KHAJEPOUR, A ; FIDAN, B ; CHEN, S.-K ; LITKOUHI, B: „Torque-Vectoring-Based Vehicle Control Robust to Driver Uncertainties“. *IEEE Transactions on Vehicular Technology* 64 (2015), August, Nr. 8, pages 3359–3367.
- [99] KOLMANOVSKY, I ; GILBERT, E. G.: „Theory and Computation of Disturbance Invariant Sets for Discrete-Time Linear Systems“. *Mathematical Problems in Engineering* 4 (1998), Nr. 4, pages 317–367.

- [100] KOTHARE, M. V. ; BALAKRISHNAN, V ; MORARI, M: „Robust constrained model predictive control using linear matrix inequalities“. *Automatica* 32 (1996), October, Nr. 10, pages 1361–1379.
- [101] KOURAMAS, K. I. ; RAKOVIC, S. V. ; KERRIGAN, E. C. ; ALLWRIGHT, J. C. ; MAYNE, D. Q.: „On the Minimal Robust Positively Invariant Set for Linear Difference Inclusions“. *Proceedings of IEEE Conference on Decision and Control*. Seville, 2005, pages 2296–2301.
- [102] KOURO, S ; CORTÉS, P ; VARGAS, R ; AMMANN, U ; RODRÍGUEZ, J: „Model Predictive Control—A Simple and Powerful Method to Control Power Converters“. *IEEE Transactions on Industrial Electronics* 56 (2009), June, Nr. 6, pages 1826–1838.
- [103] KRAUSE, P. C. ; THOMAS, C. H.: „Simulation of Symmetrical Induction Machinery“. *IEEE Transactions on Power Apparatus and Systems* 84 (1965), November, Nr. 11, pages 1038–1053.
- [104] KRAUSE, P. C. ; WASYNCZUK, O ; SUDHOFF, S. D.: *Analysis of Electric Machinery and Drive Systems*. 2nd Edition. Wiley Inter-Science, 1986.
- [105] KUTASI, N ; KELEMEN, A ; IMECS, M: „Vector Control of Induction Motor Drives with Model Based Predictive Current Controller“. *Proceedings of IEEE International Conference on Computational Cybernetics*. Stara Lesna, 2008, pages 21–26.
- [106] LANGSON, W ; CHRYSOCHOOS, I ; RAKOVIĆ, S. V. ; MAYNE, D. Q.: „Robust Model Predictive Control Using Tubes“. *Automatica* 40 (2004), January, Nr. 1, pages 125–133.
- [107] LASCHET, A: *Simulation von Antriebssystemen*. Springer, 1988.
- [108] LASSERRE, J. B.: „Reachable, Controllable Sets and Stabilizing Control of Constrained Linear Systems“. *Automatica* 29 (1993), May, Nr. 2, pages 531–536.
- [109] LEE, J. H.: „Model predictive control: Review of the three decades of development“. *International Journal of Control, Automation and Systems* 9 (2011), June, Nr. 3, pages 415–424.
- [110] LEE, Y. I. ; CANNON, M ; KOUVARITAKIS, B: „Extended invariance and its use in model predictive control“. *Automatica* 41 (2005), December, Nr. 12, pages 2163–2169.
- [111] LEE, Y. I. ; KOUVARITAKIS, B: „Brief Robust Receding Horizon Predictive Control for Systems with Uncertain Dynamics and Input Saturation“. *Automatica* 36 (2000), October, Nr. 10, pages 1497–1504.
- [112] LI, G: *The Robustness and Stability Analysis of Model Predictive Control: using robust control and absolute stability theories*. LAP LAMBERT, 2010.

- [113] LIM, C. S. ; LEVI, E. ; JONES, M. ; RAHIM, N. A. ; HEW, W. P.: „FCS-MPC-Based Current Control of a Five-Phase Induction Motor and its Comparison with PI-PWM Control“. *IEEE Transactions on Industrial Electronics* 61 (2014), January, Nr. 1, pages 149–163.
- [114] LIM'ON, D. ; ALVARADO, I. ; ALAMO, T. ; CAMACHO, E. F.: „Robust tube-based MPC for tracking of constrained linear systems with additive disturbances“. *Journal of Process Control* 20 (2010), Nr. 3, pages 248–260.
- [115] LIMÓN, D. ; ALVARADO, I. ; ALAMO, T. ; CAMACHO, E.: „MPC for tracking piecewise constant references for constrained linear systems“. *Automatica* 44 (2008), September, Nr. 9, pages 2382–2387.
- [116] LINDER, A. ; KENNEL, R.: „Direct model predictive control - a new direct predictive control strategy for electrical drives“. *Proceedings of European Conference on Power Electronics and Applications*. Dresden, 2005, pages 1–10.
- [117] LINDER, A. ; KANCHAN, R. ; KENNEL, R. ; STOLZE, P.: *Model-Based Predictive Control of Electric Drives*. Cuvillier Verlag Göttingen, 2010.
- [118] LINDER, A. ; KENNEL, R.: „Model Predictive Control for Electrical Drives“. *Proceedings of IEEE Power Electronics Specialists Conference*. Recife, 2005, pages 1793–1799.
- [119] LÖFBERG, J.: *Linear Model Predictive Control Stability and Robustness*, Linköpings Universitet, Dissertation., 2001.
- [120] LÖFBERG, J.: „YALMIP: A toolbox for modeling and optimization in MATLAB“. *Proceedings of IEEE International Symposium on Computer Aided Control System Design*. Taipei, 2004, pages 284–289.
- [121] LU, Q.: „New Results on Robust Model Predictive Control for Time-Delay Systems with Input Constraints“. *Journal of Applied Mathematics* 2014 (2014), November, Nr. Article ID 528926, pages 12.
- [122] MACIEJOWSKI, J. M.: *Predictive control with constraints*. 1st Edition. Prentice Hall, 2002.
- [123] MAO, W.-J.: „Robust stabilization of uncertain time-varying discrete systems and comments on “an improved approach for constrained robust model predictive control”“. *Automatica* 39 (2003), June, Nr. 6, pages 1109–1112.
- [124] MARIÉTHOZ, S. ; DOMAHIDI, A. ; MORARI, M.: „High-Bandwidth Explicit Model Predictive Control of Electrical Drives“. *IEEE Transactions on Industrial Applications* 48 (2012), October, Nr. 6, pages 1980–1992.
- [125] MAYNE, D. Q. ; RAWLINGS, J. B. ; RAO, C. V. ; SCOKAERT, P. O. M.: „Constrained model predictive control: Stability and optimality“. *Automatica* 36 (2000), June, Nr. 6, pages 789–814.

- [126] MAYNE, D. Q. ; SERON, M. M. ; RAKOVIĆ, S. V.: „Robust Model Predictive Control of Constrained Linear Systems with Bounded Disturbances“. *Automatica* 41 (2005), February, Nr. 2, pages 219–224.
- [127] MAYNE, D ; RAKOVIĆ, S. V. ; FINDEISEN, R ; ALLGÖWER, F: „Robust output feedback model predictive control of constrained linear systems“. *Automatica* 42 (2006), July, Nr. 7, pages 1217–1222.
- [128] MENNE, M: *Drehschwingungen im Antriebsstrang von Electrostraßenfahrzeugen - Analyse und aktive Dämpfung*, RWTH Aachen University, Dissertation., 2001.
- [129] MITSCHKE, M ; WALLENTOWITZ, H: *Dynamik der Kraftfahrzeuge*. 5th Edition. Berlin, Germany : Springer, 2014.
- [130] MORARI, M ; LEE, J. H.: „Model predictive control: past, present and future“. *Computer & Chemical Engineering* 23 (1999), May, Nr. 4-5, pages 667–682.
- [131] MUSKE, K. R. ; BADGWELL, T. A.: „Disturbance modeling for offset-free linear model predictive control“. *Journal of Process Control* 12 (2002), August, Nr. 5, pages 617–632.
- [132] MUSLEM UDDIN AND SAAD MEKHILEF AND MUTSOU NAKAOKA: „Model Predictive Control of Induction Motor with Delay Time Compensation: An Experiment Assessment“. *Proceedings of IEEE Applied Power Electronics Conference and Exposition*. Charlotte, NC, 2015, pages 543–548.
- [133] MÜLLER, S ; UCHANSKI, M ; HEDRICK, K: „Estimation of the Maximum Tire-Road Friction Coefficient“. *Journal of Dynamic Systems, Measurement, and Control* 125 (2004), January, Nr. 4, pages 607–617.
- [134] NISHIO, K ; KASHIMA, K ; IMURA, J: „Effects of time delay in feedback control of linear quantum systems“. *Physical Review A* 79 (2009), June, Nr. 6, pages 062105:1–062105:6.
- [135] NOVELLIS, L. D. ; SORNIOTTI, A ; GRUBER, P ; PENNYCOTT, A: „Comparison of Feedback Control Techniques for Torque-Vectoring Control of Fully Electric Vehicles“. *IEEE Transactions on Vehicular Technology* 63 (2014), October, Nr. 8, pages 3612–3623.
- [136] NUSSBAUMER, T ; HELDWEIN, M. L. ; GONG, G ; ROUND, S. D. ; KOLAR, J. W.: „Comparison of Prediction Techniques to Compensate Time Delays Caused by Digital Control of a Three-Phase Buck-Type PWM Rectifier System“. *IEEE Transactions on Industrial Electronics* 55 (2008), February, Nr. 2, pages 791–799.
- [137] OKORO, O. I.: *Dynamic and Thermal Modelling of Induction Machine with NonLinear Effects*, Kassel University, Dissertation., 2002.
- [138] OLLEY: „Road manners of the modern car“. *Proceedings of the Institution of Automobile Engineers*, 1946, pages 523–551.

- [139] PACEJKA, H: *Tyre and Vehicle Dynamics*. 3rd Edition. Elsevier, 2012.
- [140] PALLADINO, L ; DUC, G ; POTHIN, R: „LPV control of road vehicle during braking action in curve“. *Proceedings of IFAC Symposium on Robust Control Design*. Toulouse, France, 2006, pages 113–118.
- [141] PANNOCCIA, G ; RAWLINGS, J. B.: „Disturbance models for offset-free model-predictive control“. *AICHE journal* 49 (2003), February, Nr. 2, pages 426–437.
- [142] PEÑA, D. M. I. ; BEMPORAD, A ; FILIPPI, C: „Robust explicit MPC based on approximate multiparametric convex programming“. *IEEE Transactions on Automatic Control* 51 (2006), August, Nr. 8, pages 1399–1403.
- [143] PETER, R ; GRANZOW, C ; SPIESS, M ; DENZLER, R: „The vector drive rear axle transmission“. *ATZ worldwide* 109 (2007), December, Nr. 12, pages 2–5.
- [144] PFEFFER, P (Eds.) ; HARRER, M (Eds.): *Lenkungshandbuch - Lenksysteme, Lenkgefühl, Fahrdynamik von Kraftfahrzeugen*. 1st Edition. Vieweg+Teuber Verlag, 2011.
- [145] PING, X ; SUN, N ; DING, B: „An off-line approach to dynamic output feedback robust model predictive control with ellipsoidal estimation error set“. *Proceedings of Chinese Control and Decision Conference*. Changsha, China, 2014, pages 1078–1083.
- [146] PLUYMERS, B ; SUYKENS, J ; MOOR, B. D.: „Robust Finite-Horizon MPC using Optimal Worst-Case Closed-Loop Predictions“. *Proceedings of IEEE Conference on Decision and Control*. Atlantis, 2004, pages 2503–2508.
- [147] POPESCU, M: *Induction motor modelling for vector control purposes*. Helsinki University of Technology, 2000.
- [148] PORSCHE AG: *Porsche Torque Vectoring Plus (PTV Plus)*, 2016. – <http://www.porsche.com/germany/models/911/911-turbo/drive/porsche-torque-vectoring-ptv-plus/>, accessed 15.08.2016.
- [149] POTTHOFF, J ; SCHMID, I. C.: *Wunibald I. E. Kamm – Wegbereiter der modernen Kraftfahrttechnik*. 1st Edition. Berlin, Germany : Springer, 2012.
- [150] POUSSOT-VASSALA, C ; SENAMEB, O ; DUGARDB, L ; SAVARES, S. M.: „Vehicle dynamic stability improvements through gain-scheduled steering and braking control“. *Vehicle System Dynamics* 49 (2011), March, Nr. 10, pages 1597–1621.
- [151] PREINDL, M ; BOLOGNANI, S: „Model Predictive Direct Torque Control With Finite Control Set for PMSM Drive Systems, Part 1: Maximum Torque Per Ampere Operation“. *IEEE Transactions on Industrial Informatics* 9 (2013), January, Nr. 4, pages 1912–1921.

- [152] QIN, J ; BADGWELL, T. A.: „An overview of industrial Model Predictive Control Technology“. *Control Engineering Practice* 93 (1997), January, Nr. 316, pages 232–256.
- [153] RAJAMANI, R ; PIYABONGKARN, D. N.: „New paradigms for the integration of yaw stability and rollover prevention functions in vehicle stability control“. *IEEE Transactions on Intelligent Transportation Systems* 14 (2012), March, Nr. 1, pages 249–261.
- [154] RAKOVIĆ, S. V. ; KERRIGAN, E. C. ; KOURAMAS, K. I. ; MAYNE, D. Q.: „Invariant Approximations of the Minimal Robust Positively Invariant Set“. *IEEE Transactions on Automatic Control* 50 (2005), March, Nr. 3, pages 406–410.
- [155] ÅSTRÖM, K. J. ; WITTENMARK, B.: *Adaptive Control*. 2nd Edition. Addison-Wesley, 1995.
- [156] RAWLINGS, J. B. ; MUSKE, K. R.: „The Stability of Constrained Receding Horizon Control“. *IEEE Transactions on Automatic Control* 38 (1993), October, Nr. 10, pages 1512–1516.
- [157] RAWLINGS, J. B. ; MAYNE, D. Q.: *Model Predictive Control: Theory and Design*. WI: Nob Hill, 2009.
- [158] RICHalet, J ; RAULT, A ; TESTUD, J. L. ; PAPON, J: „Model predictive heuristic control: Applications to industrial processes“. *Automatica* 14 (1978), September, Nr. 5, pages 413–428.
- [159] ROSSITER, J. A.: *Model-based Predictive Control - A Practical Approach*. 1st Edition. CRC Press, 2005.
- [160] RUCHIKA ; RAGHU, N: „Model Predictive Control: History and Development“. *International Journal of Engineering Trends and Technology* 4 (2013), June, Nr. 6, pages 2600–2602.
- [161] SANTOS, T. L. M. ; LIMON, D ; NORMEY-RICO, J. E. ; RAFFO, G. V.: „Dead-time compensation of constrained linear systems with bounded disturbances: output feedback case“. *IET Control Theory and Applications* 7 (2013), January, Nr. 1, pages 52–59.
- [162] SANTOS, T. L. ; LIMON, D ; NORMEY-RICO, J. E. ; ALAMO, T: „On the explicit dead-time compensation for robust model predictive control“. *Journal of Process Control* 22 (2012), January, Nr. 1, pages 236–246.
- [163] SAVARESI, S. M. ; TANELLI, M: *Active Braking Control Systems Design for Vehicles*. Springer London, 2010.
- [164] SCHECK: *Theoretische Physik 1*. 8th Edition. Springer, 2007.

- [165] SCHEUCH, V ; KAISER, G ; KORTE, M ; GRABS, P ; KREFT, F ; HOLZMANN, F: „A safe Torque Vectoring function for an electric vehicle“. *World Electric Vehicle Journal* 6 (2013), pages 731–740.
- [166] SCHNEIDER, R: *Convex Bodies: The Brunn-Minkowski Theory*. 2nd Edition. Cambridge University Press, 2014.
- [167] SCHRAMM, D ; HILLER, M ; BARDINI, R: *Modellbildung und Simulation der Dynamik von Kraftfahrzeugen*. Berlin, Germany : Springer, 2010.
- [168] SCHRÖDER, D: *Elektrische Antriebe Regelung von Antriebssystemen*. 3rd Edition. Springer, 2009.
- [169] SHI, Y. J. ; CHAI, T. Y. ; WANG, H ; SU, C. Y.: „Delay-dependent robust model predictive control for time-delay systems with input constraints“. *Proceedings of American Control Conference*. St. Louis, MO, 2009, pages 4880–4885.
- [170] SHIBAHATA, Y ; TOMARI, T: „Direct Yaw Control Torque Vectoring“. *AutoTechnology* 6 (2006), May, Nr. 3, pages 34–38.
- [171] SIAMPIS, E ; MASSARO, M ; VELENIS, E: „Electric Rear Axle Torque Vectoring for Combined Yaw Stability and Velocity Control near the Limit of Handling“. *Proceedings of IEEE Conference on Decision and Control*. Firenze, 2013, pages 1552–1557.
- [172] SIAMPIS, E ; VELENIS, E ; LONGO, S: „Model Predictive torque vectoring control for electric vehicles near the limits of handling“. *Proceedings of European Control Conference*. Linz, 2015, pages 2553–2558.
- [173] SIAMPIS, E ; VELENIS, E ; LONGO, S: „Predictive rear wheel torque vectoring control with terminal understeer mitigation using nonlinear estimation“. *Proceedings of IEEE Conference on Decision and Control*. Osaka, 2015, pages 4302–4307.
- [174] SONTAG, E. D.: *Mathematical Control Theory*. 2nd Edition. Springer, New York, 1998.
- [175] SZABAT, K ; ORLOWSKA-KOWALSKA, T: „Vibration Suppression in a Two-Mass Drive System Using PI Speed Controller and Additional Feedbacks–Comparative Study“. *IEEE Transactions on Industrial Electronics* 54 (2007), April, Nr. 2, pages 1193–1206.
- [176] SZABAT, K ; ORLOWSKA-KOWALSKA, T: „Performance Improvement of Industrial Drives With Mechanical Elasticity Using Nonlinear Adaptive Kalman Filter“. *IEEE Transactions on Industrial Electronics* 55 (2008), March, Nr. 3, pages 1075–1084.
- [177] SZABAT, K ; ORLOWSKA-KOWALSKA, T: „Application of the Kalman Filters to the High-Performance Drive System With Elastic Coupling“. *IEEE*

- Transactions on Industrial Electronics* 59 (2012), January, Nr. 11, pages 4226–4235.
- [178] SZABAT, K ; SERKIES, P ; ORLOWSKA-KOWALSKA, T ; CYCHOWSKI, M: „Robust torque constraints handling in drive systems with elastic transmission“. *Proceedings of International Conference on Industrial Technology*. Vi a del Mar, 2010, pages 398–403.
- [179] TAVASOLI, A ; NARAGHI, M: „Comparison of Static and Dynamic Control Allocation Techniques for Integrated Vehicle Control“. *Proceedings of IFAC World Congress*. Milano, 2011, pages 7180–7186.
- [180] THOMSEN, S ; HOFFMANN, N ; FUCHS, F. W.: „PI Control, PI-Based State Space Control, and Model-Based Predictive Control for Drive Systems With Elastically Coupled Loads—A Comparative Study“. *IEEE Transactions on Industrial Electronics* 58 (2011), August, Nr. 8, pages 3647–3657.
- [181] UNITED STATES. BUREAU OF STANDARDS: *Copper wire tables*. G. P. O., 1912.
- [182] VACLAVEK, P ; BLAHA, P: „Field Weakening Implementation in AC Induction Machine Predictive Control“. *Proceedings of International Conference on Power Electronics and Drive Systems*. Singapore, 2011, pages 171–176.
- [183] VAS, P: *Vector control of AC machines*. Clarendon Press, 1990.
- [184] VAZQUEZ, S ; LEON, J. I. ; FRANQUELO, L. G. ; RODRIGUEZ, J: „Model Predictive Control: A Review of Its Applications in Power Electronics“. *IEEE Industrial Electronics Magazine* 8 (2014), March, Nr. 1, pages 16–31.
- [185] VIETINGHOFF, A von: *Nichtlineare Regelung von Kraftfahrzeugen in querdynamisch kritischen Fahrsituationen*, Universität Karlsruhe, Dissertation., 2008.
- [186] WAN, Z ; KOTHARE, M. V.: „Efficient robust constrained model predictive control with a time varying terminal constraint set“. *Systems & Control Letters* 48 (2003), April, Nr. 5, pages 375–383.
- [187] WAN, Z ; KOTHARE, M. V.: „An efficient off-line formulation of robust model predictive control using linear matrix inequalities“. *Automatica* 39 (2003), May, Nr. 5, pages 837–846.
- [188] WANG, C ; YANG, M ; ZHENG, W ; LONG, J ; XU, D: „Vibration Suppression With Shaft Torque Limitation Using Explicit MPC-PI Switching Control in Elastic Drive Systems“. *IEEE Transactions on Industrial Electronics* 62 (2015), November, Nr. 11, pages 6855–6867.
- [189] WEBER, I ; WINNER, H: „Reibwertangepasste Regelstrategien bei Bremsmanövern im Kraftfahrzeug“. *Darmstädter Reifenkolloquium*, 2002, pages 151–168.

-
- [190] WINNER, H ; HAKULI, S ; WOLF, G (Eds.): *Handbuch Fahrerassistenzsysteme*. 2nd Edition. Vieweg+Teubner Verlag, 2012.
- [191] XIONG, L ; YU, Z ; MENG, Y: „Vehicle dynamic control for a 4 in-wheel-motored EV based on identification of tyre cornering stiffness“. *Proceedings of International Symposium on Advanced Vehicle Control*. Loughborough, 2010, pages 861–866.
- [192] YIN, G ; WANG, J ; PI, D: „Torque Distribution Control for Independent Wheel Drive Electric Vehicles with Varying Vertical Load“. *Proceedings of Chinese Intelligent Automation Conference*, 2013, pages 111–118.

Own Publications

Journal publications (with peer-review)

- (1) Z. Hu; Q. Liu; K. Hameyer: „Loss Minimization of Speed Controlled Induction Machines in Transient States Considering System Constraints”. *Journal of International Conference on Electrical Machines and Systems 4* (2015), Nr. 1, pages 34–41.
- (2) Z. Hu; K. Hameyer: „A Method of Constraint Handling for Speed-Controlled Induction Machines”. *IEEE Transactions on Industrial Electronics* 63 (2016), Nr. 7, pages 4061–4072.

Publications in Proceedings of international conferences (with review)

- (1) Z. Hu; Q. Liu; K. Hameyer: „Loss minimization of speed controlled induction machines in transient state considering system constraints”. *Proceedings of 17th International Conference on Electrical Machines and Systems, ICEMS*. Hangzhou, China, October 2014, pages 123–129.
- (2) Z. Hu; K. Hameyer: „Robust Predictive Current Control for Performance Improvement of Induction Motors with Parameter Variation”. *Proceedings of 41th Annual Conference of the IEEE Industrial Electronics Society, IECON*. Yokohama, Japan, November 2015, pages 451–456.
- (3) Z. Hu; Q. Liu; K. Hameyer: „A Study of Multistep Direct Model Predictive Current Control for Dynamic Drive Applications with High Switching Frequency”. *Proceedings of 8th International Conference on Power Electronics, Machine and Drives, PEMD*. Glasgow, Scotland, April 2016, 1–6.
- (4) Z. Hu; K. Hameyer: „Optimization-based Yaw Rate Control in Electric Vehicles with Integrated System Limitations of Induction Traction Motors”. *Proceedings of 10. Tag des Fahrwerks*. Aachen, Germany, October 2016, 61–71.

Supervised master theses

- (1) F. Kaumanns: „Implementation and Validation of an optimisation-oriented Drive Dynamics Control for the Application of a high-dynamic Torque Distribution in Electric Vehicles”. Institute of Electrical Machines, RWTH Aachen University, August 2016.
- (2) X.R. Li: „High-Performance Direct Control for Induction Motors Driven by Voltage Source Inverter”. Institute of Electrical Machines, RWTH Aachen University, November 2015.
- (3) X.Y. Li: „Robustness Improvement of Multi-Step Direct Current Control in Induction Machine”. Institute of Electrical Machines, RWTH Aachen University, September 2016.
- (4) P. Schönhuber: „Development of an Adaptive Operation Strategy and a Nonlinear Observer in Support of a Lateral Electronic Stability Control in Electric Vehicles Considering Road Effects”. Institute of Electrical Machines, RWTH Aachen University, August 2016.
- (5) H.M. Xu: „Echtzeitfähige optimale Regelung einer Asynchronmaschine unter Berücksichtigung von Unsicherheiten”. Institute of Electrical Machines, RWTH Aachen University, April 2015.
- (6) Y.T. Zhou: „Drehschwingungsdämpfung im elektrischen Antriebsstrang mittels modellbasierter prädiktiver Regelung am Beispiel einer Asynchronmaschine”. Institute of Electrical Machines, RWTH Aachen University, May 2014.
- (7) Z. Zhou: „Echtzeitfähige Drehzahlregelung einer Asynchronmaschine mittels modellbasierter Prädiktivregelung unter Berücksichtigung der Systembegrenzungen”. Institute of Electrical Machines, RWTH Aachen University, July 2014.

Supervised bachelor theses

- (1) M. Lorenz: „Implementierung eines dynamischen adaptiven Beobachters zur Bestimmung des Seitenwellenmoments eines Elektrofahrzeugs”. Institute of Electrical Machines, RWTH Aachen University, March 2015.
- (2) S. Sandbaumhüter: „Analyse und Regelung einer virtuellen Wellenverbindung zwischen Verbrennungsmotor und Getriebe mittels Echtzeitvernetzung von Prüfständen”. Institute of Electrical Machines, RWTH Aachen University, March 2015.

Supervised seminar theses

- (1) X.Y. Li: „Overview of Predictive Control”. Institute of Electrical Machines, RWTH Aachen University, June 2015.
- (2) G.J. Tan: „Regulation Requirement of Safety Function in Electric Vehicle”. Institute of Electrical Machines, RWTH Aachen University, June 2015.

Lebenslauf

Personalien:	Zheng Hu 15. Oktober 1982	geboren in Jiangsu Provinz, V.R. China
Schulbildung:	1988 - 1994 1995 - 1997 1997 - 2000 Juli 2000	Grundschule Yuhong, Wuxi Helie Junior Middle School, Wuxi Zhongshan Senior High School, Wuxi Abitur
Studium:	2000 - 2002 2003 - 2008 16. September 2008 2008 - 2011 24. Februar 2011	Studium der Informatik an Beijing Technology Institute, Fachrichtung Informatik Studium der Informatik an der RWTH Aachen, Fachrichtung Informatik Ausstellung der Diplomurkunde Studium der Wirtschaftswissenschaften an der RWTH Aachen, Fachrichtung Wirtschaftswissenschaften Ausstellung der Diplomurkunde
Berufliche Tätigkeit:	Juli 2007 - September 2008 Oktober 2008 - Juni 2011 Juni 2011 - Januar 2012 seit Februar 2012	Studentische Hilfskraft am Werkzeugmaschinenlabor der RWTH Aachen Softwareingenieur bei der Gesellschaft für Industrieforschung mbH Alsdorf Teamleiter bei der Gesellschaft für Industrieforschung mbH Alsdorf wissenschaftlicher Mitarbeiter am Institut für Elektrische Maschinen der RWTH Aachen

Bisher erschienene Bände in der Aachener Schriftenreihe zur Elektromagnetischen Energiewandlung

Band 1:

Christoph Schlensock

Numerische Berechnung und Optimierung einer Asynchronmaschine mit Käfigläufer zur elektrischen Lenkunterstützung im Kfz

1. Auflage 2005 - 156 Seiten - ISBN 978-3-8322-4418-7

Band 2:

Stephan Schulte

Simulationsmethoden zur Analyse und Optimierung des Betriebsverhaltens von Kraftfahrzeuggeneratoren

1. Auflage 2006 - 173 Seiten - ISBN 978-3-8322-5417-9

Band 3:

Kay Hameyer

Elektrische Maschinen II

Dynamisches Verhalten, Stromrichterspeisung, Regelung

1. Auflage 2008 - 158 Seiten

Band 4:

Marc Schöning

Virtueller Produktentwicklungsprozess für Elektromotoren

1. Auflage 2008 - 162 Seiten - ISBN 978-3-8322-7444-3

Band 5:

Kay Hameyer

Elektrische Maschinen I

Aufbau, Wirkungsweisen, Betriebsverhalten

1. Auflage 2008 - 255 Seiten

Band 6:

Mercedes Herranz Gracia

Methoden zum Entwurf von robusten Stellantrieben unter Berücksichtigung fertigungsbedingter Abweichungen

1. Auflage 2009 - 146 Seiten - ISBN 978-3-8322-7966-0

Band 7:

Kay Hameyer

Electrical Machines II

Dynamic Behaviour, Converter Supply, Control

1. Auflage 2009 - 148 Seiten

Band 8:

Benedikt Schmülling

Elektromagnetische Linearführungen für Aufzugsysteme

1. Auflage 2009 - 159 Seiten - ISBN 978-3-8322-8529-6

Band 9:

Christoph Weißbacher

Entwurf und Umsetzung von Magnetlagersystemen für schwere schnelllaufende Teilchenstrahlchopper

1. Auflage 2010 - 152 Seiten - ISBN 978-3-8322-9749-7

Band 10:

Michael van der Giet

Analysis of electromagnetic acoustic noise excitations:

A contribution to low-noise design and to the auralization of electrical machines

1. Auflage 2011 - 227 Seiten - ISBN 978-3-8322-9973-6

Band 11:

Thomas Finken

Fahrzyklusgerechte Auslegung von permanentmagneterregten Synchronmaschinen für Hybrid- und Elektrofahrzeuge

1. Auflage 2011 - 216 Seiten - ISBN 978-3-8440-0607-0

Band 12:

Thomas Finocchiaro

Untersuchung eines Linearantriebskonzeptes für ein vollständig implantierbares Kunstherz

1. Auflage 2013 - 184 Seiten - ISBN 978-3-8440-1636-9

Band 13:

Martin Hafner

Hybride Methoden zur Auslegung und Berechnung von elektrischen Maschinen in einer Virtual-Reality-Entwicklungsumgebung

1. Auflage 2013 - 196 Seiten - ISBN 978-3-8440-1948-3

Band 14:

Enno Lange

Numerische Werkzeuge zur Simulation von nichtsinusförmig gespeisten geregelten elektrischen Maschinen im dynamischen Betrieb

1. Auflage 2013 - 202 Seiten - ISBN 978-3-8440-2205-6

Band 15:

Marc Leßmann

Anforderungsgerechte Auslegung eines linearen Direktantriebs für vollständig implantierbare Herzersatzsysteme

1. Auflage 2014 - 220 Seiten - ISBN 978-3-8440-2420-3

Band 16:

André Pohlmann

Wirkungsgradoptimierte Auslegung normalkraftbehafteter BLDC Scheibenläufermotoren zum Einsatz in Herzunterstützungssystemen

1. Auflage 2014 - 180 Seiten - ISBN 978-3-8440-2567-5

Band 17:

Peter Offermann

Beitrag zur Berechnung und Übertragung von Unsicherheiten am Beispiel der Magnetisierung von permanentmagneterregten Synchronmaschinen

1. Auflage 2015 - 188 Seiten - ISBN 978-3-8440-3504-9

Band 18:

Isabel Coenen

Beitrag zur Analyse elektrischer Antriebssysteme mit toleranzbehafteten Komponenten: Vom elektromagnetischen Entwurf bis zur End-of-Line Prüfung

1. Auflage 2015 - 136 Seiten - ISBN 978-3-8440-3564-3

Band 19:

Sicong von Malottki

Elektrischer Traktionsmotor am Stromzwischenkreis-Wechselrichter

1. Auflage 2015 - 168 Seiten - ISBN 978-3-8440-3839-2

Band 20:

Rüdiger Appunn

Elektromagnetisch angetriebene und geführte Aufzugsysteme:

Berührungslose Energieübertragung

1. Auflage 2015 - 180 Seiten - ISBN 978-3-8440-3858-3

Band 21:

Thomas Herold

Simulation des elektrischen Antriebsstrangs als Hilfsmittel für die Synthese und Überprüfung von Algorithmen im Kontext der antriebsbasierten Diagnose

1. Auflage 2016 - 154 Seiten - ISBN 978-3-8440-4225-2

Band 22:

Björn Riemer

Beitrag zur Berechnung der lokalen magnetischen Kernbelastung von Phasenschiebertransformatoren großer Leistung für kritische Betriebszustände

1. Auflage 2016 - 174 Seiten - ISBN 978-3-8440-4789-9

Band 23:

David Franck

Ein effizientes transientes Antriebsakustikmodell als Werkzeug zur Simulation und Analyse elektromagnetisch erregter Schwingungen

1. Auflage 2016 - 146 Seiten - ISBN 978-3-8440-4826-1

Band 24:

Zheng Hu

Optimization-based robust control for high-performance torque vectoring in electric vehicles operated by induction traction motors

1. Auflage 2017 - 224 Seiten - ISBN 978-3-8440-5209-1